Max Planck Graduate Center
mit der Johannes Gutenberg-Universität

JG|U

UNIVERSITÄTSmedizin.
MAINZ

Analysis of zinc oxide nanoparticles as a potential mutagen of respiratory epithelia

„Dissertation

zur Erlangung des Grades

eines *‚Doktor rerum naturalium* (Dr. rer. nat.)‘

der Fachbereiche:

- o 08 Physik, Mathematik und Informatik
- o 09 Chemie, Pharmazie und Geowissenschaften
- o 10 Biologie
- o 04 Universitätsmedizin

der Johannes Gutenberg-Universität“

vorgelegt von

Dipl. Biol. Julia Heim

geb. am 02.07.1984 in Schweinfurt

Mainz, August 2015

1. Gutachter:

2. Gutachter:

Tag der mündlichen Prüfung: 6. November 2015

Dedicated in gratitude to my family and friends

Zusammenfassung

Metallische Nanopartikel und ihre Oxide (z.B. ZnO NP, TiO_2 NP und Fe_2O_3 NP) werden aufgrund ihrer chemischen und physikalischen Eigenschaften häufig als Additive in der Reifenproduktion, in Katalysatoren, Lebensmitteln, Arzneimitteln und Kosmetikprodukten verwendet. Künftig wird ein kontinuierlicher Anstieg der industriellen Anwendung (~ 1663 Tonnen im Jahr 2025) mit gesteigerter Freisetzung in die Umwelt erwartet, was zwangsläufig zu einer vermehrten Aufnahme über das respiratorische Epithel führt. Metalldampffieber ist als gesundheitsschädigender Effekt von Metalloxid-haltigen Aerosolen (z.B. ZnO) nach Inhalation bekannt. Immunreaktionen, wie beispielsweise Entzündungen, werden häufig mit der Entstehung von Sauerstoffradikalen (ROS) in Verbindung gebracht, die wiederum zu DNA-Schäden führen können. Drei mögliche Ursachen der Genotoxität werden angenommen: direkte Interaktion von Nanopartikeln mit intrazellulären Strukturen, Interaktion von Ionen dissoziierter Partikel mit intrazellulären Strukturen sowie die Entstehung von ROS initiiert durch Partikel oder Ionen.

Die vorliegende Studie befasst sich mit den Mechanismen der Genotoxizität von ZnO Nanopartikeln (ZnO NP), als Beispiel für metallische Nanopartikel, im respiratorischen Epithel. In der Studie wurde gezielt die intrazelluläre Aufnahme und Verteilung von ZnO NP, deren Toxizität, deren DNA schädigendes Potential sowie die Aktivierung der *DNA damage response* (DDR) analysiert.

Es konnten kaum internalisierte ZnO NP mittels TEM detektiert werden. Innerhalb der ersten Sekunden nach Behandlung mit ZnO NP wurde spektrofluorometrisch ein starker Anstieg der intrazellulären Zn^{2+} Konzentration gemessen. In unbehandelten Zellen war Zn^{2+} in granulären Strukturen lokalisiert. Die Behandlung mit ZnO NP führte zu einer Akkumulation von Zn^{2+} in diesen Strukturen. Im zeitlichen Verlauf verlagerten sich die Zn^{2+}-Ionen in das Zytoplasma, sowie in Zellkerne und Mitochondrien. Es wurde keine Kolokalisation von Zn^{2+} mit den frühen Endosomen und dem endoplasmatischen Retikulum beobachtet. Die Vorbehandlung der Zellen mit *Diethylen-triaminpentaessigsäure* (DTPA), als extrazellulärem Komplexbildner, verhinderte den intrazellulären Anstieg von Zn^{2+} nach Behandlung mit den Partikeln.

Die Behandlung mit ZnO NP resultierte in einer zeit- und dosisabhängigen Reduktion der zellulären Viabilität, während die intrazelluläre ROS-Konzentrationen in den ersten 30 min leicht und anschließend kontinuierlich bis zum Ende der Messung anstiegen. Außerdem verringerte sich das mitochondriale Membranpotential, während sich die Anzahl der frühapoptotischen Zellen in einer zeitabhängigen Weise erhöhte.

DNA Doppelstrangbrüche (DNA DSB) wurden mittels Immunfluoreszenz-Färbung der γH2A.X foci sichtbar gemacht und konnten nach Behandlung mit ZnO NP detektiert werden. Die Vorbehandlung mit dem Radikalfänger *N-Acetyl-L-Cytein* (NAC) resultierte in stark reduzierten intrazellulären ROS-Konzentrationen sowie wenigen DNA DSB. Die DNA Schädigung wurde durch Vorbehandlung mit DTPA ganz verhindert.

Die Aktivierung der DDR wurde durch die Analyse von ATM, ATR, Chk1, Chk2, p53 und p21 mittels Western Blot und ELISA nach Behandlung mit ZnO NP überprüft. Der ATR/Chk1 Signalweg wurde durch ZnO NP nicht aktiviert. Die Komplexierung von Zn^{2+} resultierte in einer verminderten ATM/Chk2 Signalwegaktivierung. Es zeigte sich, dass das Abfangen von ROS keinen Effekt auf die ATM/Chk2 Signalwegaktivierung hatte.

Zusammengefasst wurde festgestellt, dass die Exposition mit ZnO NP in der Entstehung von ROS, reduzierter Viabilität und vermindertem mitochondrialem Membranpotential resultiert, sowie zeitabhängig eine frühe Apoptose initiiert. ZnO NP dissoziierten extrazellulär und wurden schnell als Zn^{2+} über unbekannte Mechanismen internalisiert. Die Zn^{2+}-Ionen wurden im Zytoplasma, sowie besonders in den Mitochondrien und dem Zellkern, akkumuliert. Die DDR Signalgebung wurde durch ZnO NP aktiviert, jedoch nicht durch NAC inhibiert. Es wurde gezeigt, dass DTPA die DDR Aktivierung komplett inhibierte. Die Behandlung mit ZnO NP induzierte DNA DSB. Die Inhibition von ROS reduzierte die DNA DSB und die Komplexierung der Zn^{2+} verhinderte die Entstehung von DNA DSB.

Diese Daten sprechen für die Dissoziation der Partikel und die hierbei freigesetzten Zn^{2+} als Hauptmediator der Genotoxizität metallischer Nanopartikel.

Abstract

Metallic nanoparticles including their oxides (e.g., ZnO NP, TiO_2 NP, and Fe_2O_3 NP) are widely used as additives in rubber industry, catalysts, foods, pharmaceuticals and cosmetics, because of their chemical and physical properties. Prospectively, a continuous rise of industrial application (~1663 tons in 2025) is estimated with an increasing release into the environment, and further unavoidable intake by humans e.g., through the respiratory epithelia. Acute metal fume fever is known as an adverse health effect of aerosol inhalation containing metal oxides (e.g., ZnO). Immune responses such as inflammation are often associated with the generation of reactive oxygen species (ROS), which possibly initiate DNA damages. Three reasons of genotoxicity are assumed: direct interaction of nanoparticles with intracellular structures, interactions of dissociated ions from particles, and the generation of ROS initiated by the particles or ions.

The present study paid particular attention to the mechanisms of genotoxicity in respiratory epithelia exposed to zinc oxide nanoparticles (ZnO NP), as example for metallic nanoparticles. The study aimed to investigate the intracellular ZnO NP uptake and distribution, toxicity, DNA damaging potential, and DNA damage response (DDR) activation.

Internalized ZnO NP were infrequently detected by TEM. Strongly increased intracellular Zn^{2+} levels were measured in the first seconds after treatment with ZnO NP by spectrofluorometry. In untreated cells Zn^{2+} is located in granular structures at basal levels. Treatment with ZnO NP led to an accumulation of Zn^{2+} in these structures. In the period of time, Zn^{2+} shifted to the cytoplasm, nucleus, and mitochondria. No co-localization of Zn^{2+} with early endosomes and endoplasmatic reticulum was detected. Pretreatment of the cells with the extracellular chelator *diethylene triamine pentaacetic acid* (DTPA) prevented intracellular Zn^{2+} increase after particle treatment.

ZnO NP treatment resulted in a time- and concentration-dependent reduction of cellular viability, while ROS-levels increased slightly in first 30 min and continuously afterwards until end of measurement. Furthermore, the mitochondrial membrane potential decreased whereas the amount of early apoptotic cells raised in a time-dependent manner.

DNA double strand breaks (DNA DSB) were detected after ZnO NP treatment by visualization of γH2A.X foci. Pretreatment with the ROS scavenger *N-acetyl-L-cysteine* (NAC) resulted in strongly decreased intracellular ROS-levels as well as reduced DNA DSB. However, pretreatment with DTPA prevented DNA damages entirely.

The activation of the DDR was shown by analysis of ATM, ATR, Chk1, Chk2, p53, and p21 after ZnO NP exposure performing Western blots and ELISA measurements. In contrast, the ATR/Chk1 pathway was not activated by ZnO NP. The complexation of Zn^{2+} resulted in impaired ATM/Chk2 pathway activation. However, ROS scavenging had no effect on ATM/Chk2 pathway activation, i.e., signaling remained activated.

Altogether, it was found that ZnO NP treatment resulted in increased intracellular ROS-levels, reduced viability and decreased mitochondrial membrane potential, and they initiated early apoptosis in a time-dependent manner. ZnO NP dissociated extracellular and Zn^{2+} were quickly internalized by an unknown mechanism. The Zn^{2+} ions were accumulated in the cytoplasm, the nucleus, and the mitochondria. DDR signaling was activated by ZnO NP but not inhibited by NAC, while a completely inhibition of DDR activation was shown after pretreatment with DTPA. Treatment with ZnO NP generated DNA DSB. ROS scavenging reduced DNA DSB, and Zn^{2+} complexation prevented DNA DSB.

These data suggest particle dissociation and the released Zn^{2+} seems to be the main mechanism of metallic nanoparticle genotoxicity.

Table of contents

List of figures

List of tables

List of abbreviations

AAS	atomic absorption spectroscopy
12-LOX	12-lipooxygenase
53BP1	p53-binding protein 1
Akt	serine/threonine-protein kinase
AM	acetoxymethyl
Apaf-1	apoptotic protease activating factor 1
approx.	approximately
ATM	ataxia telangiectasia mutated
ATP	adenosine triphosphate
ATR	ataxia telangiectasia and Rad3-related protein
ATRIP	ATR Interacting Protein
AV	annexin V
Bax	Bcl-2-associated X protein
Bcl-2	B-cell lymphoma gene-2
BRCA1	Breast cancer 1
BSA	bovine serum albumine
CARD	Cytoplasmic caspase-recruiting domain
CDK	cycline-dependent kinase
cf.	*confer*
Chk1	checkpoint kinase 1
Chk2	checkpoint kinase 2
cLSM	confocal laser scanning microscopy
cyt c	cytochrome complex
DNA PK	DNA-dependent protein kinase
dATP	Deoxyadenosine triphosphate
DAXX	Death domain-associated protein 6
DCT1	divalent cation transporter 1
DDR	DNA damage response
DISC	death-inducing signaling complex
DMEM	Dulbecco´s Modified Eagles´s Medium
DMT1	divalent cation transporter
DNA DSB	DNA double strand break(s)
DNA SSB	DNA single strand break(s)
DTPA	diethylene triamine pentaacedic acid
e.g.	*exempli gratia*
E3	E3 ubiquitin-protein ligase
EE	early endosomes
EGF	epidermal growth factor
EGFR	epidermal growth factor receptor
Egr-1	early growth response protein 1
ELISA	enzyme linked immunosorbent assay
Em	emission
EMT	epithelial-mesenchymal transition
ER	endoplasmatic reticulum

Erk	extracellular signal-regulated kinase
EtOH	ethanol
Ex	excitation
F	denotes fluorescence intensity measured at a single wavelength
FasL	ligand of the Fas death receptor
FITC	fluorescein isothiocyanate
F_{max}	maximal reference level of fluorescence
F_{min}	zero reference level of fluorescence
Fpg	formamidopyrimidine DNA glycosylase
FSC	forward scatter
G2/M	cell cycle checkpoint G2/M
GI	gastrointestinal tract
GSH	glutathione
GSSG	oxidized glutathione disulfide
H2A.X	H2A histone family member X
HAUSP	herpesvirus-associated ubiquitin-specific protease
HIF-1α	hypoxia-inducible factor 1α
hPMS2	human mismatch repair endonuclease PMS2
HRP	horseradish peroxidase
HUS1	checkpoint protein HUS1
i.e.	*id est*
IL-8	Interleukin 8
kd	dissociation constant
Ku70	ATP-dependent DNA helicase II subunit 1
Ku80	ATP-dependent DNA helicase II subunit 2
kV	kilovolt
L	lysosomes
LDH	L-Lactatdehydrogenase
LE	late endosomes
LIV1	zinc transporter LIV1
LMP	lysosomal membrane permeabilization
Lys	lysine
M	molarity of a solution (mol/l)
mA	milliampere
MAPK	mitogen-activated protein kinases
MDC1	mediator of DNA damage checkpoint protein 1
MDM2	mouse double minute 2 homolog
MDM4	mouse double minute 4 homolog
MEK	mitogen-activated protein kinases
MPTP	mitochrondrial permeability transition pore
MRE	metal response element
MRE11	double-strand break repair protein MRE11
MRN	Mre11-Rad50-Nbs1 complex
mRNA	messenger ribonucleic acid
MT	Metallothionein(s)
MTF-1	metal regulatory transcription factor 1

MutLalpha	DNA mismatch repair protein
NAC	N-acetyl-L-cysteine
NADPH	nicotinamide adenine dinucleotide phosphate
NBS1	Nijmegen breakage syndrome 1 protein
NF-κB	nuclear factor kappa-light-chain-enhancer of activated B cells
NHEJ	non-homologous end joining
nm	nanometer
Noxa	phorbol-12-myristate-13-acetate-induced protein 1
NP	Nanoparticle(s)
OD	optical density
OGG1	8-Oxoguanine glycosylase
p	phosphorylated
p21Cip1	cyclin-dependent kinase inhibitor
p450	Cytochromes P450
p53	tumor suppressor p53
PARP	poly (ADP-ribose) polymerase
PCR	polymerase chain reaction
pH	negative of the logarithm to base 10 of the activity of the hydrogen ion
PI	propidium iodide
PI3K	phosphatidylinositol-4,5-bisphosphate 3-kinase
PMT	primary cells of mucosal tissue
PP2A	Protein phosphatase 2A
PS	phosphatidylserine
PTEN	phosphatase and tensin homolog deleted on Chromosome 10
Puma	p53 upregulated modulator of apoptosis
RAD1	Cell cycle checkpoint protein RAD1
RAD50	DNA repair protein RAD50
RAD9	DNA repair protein RAD9
Raf	*rapidly accelerated fibrosarcoma*
Ras	Rat sarcoma
RNS	reactive nitrogen species
ROS	reactive oxygen species
RPA	replication protein A
RT	room temperature
SD	standard deviation
SDS	sodium dodecyl sulfate
SDS-Page	sodium dodecyl sulfate polyacrylamide gel electrophoresis
Ser	serine
SG	space group
SiO_2 NP	silicon dioxide nanoparticle(s)
SOD	superoxide dismutase
SSC	side scatter
$t_{1/2}$	half-life
TEM	transmission electron microscopy
TiO_2 NP	titanium dioxide nanoparticle(s)

TNF	tumor necrosis factor
TOPBP1	DNA topoisomerase 2-binding protein 1
Ub	ubiquitination
UPR	unfolded protein response
UV	ultraviolet
UV-A	ultraviolet A
UV-B	ultraviolet B
W	watt
w/w	% weight/weight
xbp-1s	X-box binding protein 1s
x*g*	gravitational force
XPA	DNA repair protein complementing XP-A cells
XRCC4	DNA repair protein XRCC4
XRD	X-ray diffraction
Zim17	zinc finger motif protein of 17 kDa
ZIP	zinc importers
Zn	zinc
$ZnCl_2$	zinc chloride
ZnO NP	zinc oxide nanoparticle(s)
ZnT	zinc exporters
ΔΨm	mitochondrial membrane potential

1 Introduction

1.1 Nanotechnology

Nanomaterial is commonly defined as an object of 1-100 nm in one or more dimensions including nanofibers, nanogels, nanotubes, and nanoparticles[1]. The diameter of a nanoparticle is corresponding in size to approximately 500 atoms. Furthermore, in a biological view it has the dimension of enzymes and receptors[2,3]. The environmental behavior of nanoscaled material is often different to their bulked material[4–6]. Nanoparticles show changes in their properties due to an increased surface to volume ratio compared to their bulk material. The chemical reactions take place on the particle surface and in comparison to bulk material, nanoparticle have an increased chemical, biological, and catalytically behavior. In 2015, earnings of $ 1 trillion in this sector are predicted and 5.3 % of these industrial products are related to medical applications[7,8]. In the last decade 485 companies in 24 countries have been established and brought more than 1000 products to market[7,9]. In contrast to the benefits of nanoscaled materials, many scientists have increasingly concerns about the environmental release (estimated ~500 tons in 2009 in the U.S.) and linked possible adverse health effects[10].

1.1.1 Metal oxide nanomaterials

Many metals and metal oxides are able to form nanoscaled materials. Metallic nanoparticles have many useful properties and have been used since the middle ages (e.g., ornamental decoration) in the form of colloids or soils[11]. They display enhanced optical, electrical, chemical or magnetic qualities. Metal and metal oxide nanoparticles can be easily synthesized from bulk material and modified on their surface (e.g., conjugated antibodies, ligands), which opens a wide range of applications[12]. There are two main approaches for fabricating metal oxide nanoparticles or manipulating devices, the bottom up and the top down principal. The bottom up path refers to the build up of a nanomaterial from the bottom, i.e., atom by atom. In contrast the top down approach refers to slicing or cutting bulk material into nanoscaled material[13,14]. Metal oxide nanoparticles are the most highly used nanoparticles in industrial applications. The global market report for metal oxide nanoparticles (2013) estimates an increase from 270,041 tons in 2012 to 1663,168 tons in 2025[15]. The mostly used metal oxide nanoparticles in consumer products are SiO_2 NP, TiO_2 NP, and ZnO NP[16]. *Ivask et al. (2015)* showed that SiO_2 NP, TiO_2 NP, and ZnO NP have toxic effects on different cell lines[17]. *Brunner et al. (2006)* suggested that ZnO NP may easily dissolute and the particles show therefore an enhanced toxic behavior[18]. The industrial application of metal

oxide nanoparticles is booming and has promising characteristics but also possible adverse effects as hypothesized for e.g., ZnO NP.

1.1.2 Zinc oxide and its application in industrial production

The annual production of zinc oxide (ZnO) is more than 1.2 million of tons worldwide. Far East, especially China, is by far the biggest producer and processor with 38 %, followed by the European Union with 31 % (Figure 1A)[19]. ZnO is widely used as an additive in industrial production, e.g., rubber industry, ceramic and class compositions, catalysts, foods, pharmaceuticals, and cosmetics (Figure 1B)[20]. According to different sources, the global annual production of nanoscaled ZnO is estimated between ~ 500 and 33,400 tons[13,16,21]. ZnO is a multifunctional inorganic compound and has interesting chemical and physical properties such as a wide range of UV absorption, high photostability, biocompatibility and biodegradability[14,19,20,22]. Pure microcrystalline ZnO is a white inorganic salt and has a molecular weight of 81.37 g/mol. ZnO is reacting amphoterically with alkalis and acids[20]. ZnO is used in food industry as a substitute for zinc as an essential trace element. The antimicrobial and UV protective properties of ZnO make it a perfect component in industrial production of food packing material. In pharmaceuticals ZnO is often used because of its antiseptic properties in powders, creams and ointments, especially for babies. ZnO strongly absorbs UV light and is therefore applied in sunscreens. This versatile utilization in industrial production leads to an increased implementation in daily life and an increased environmental release.

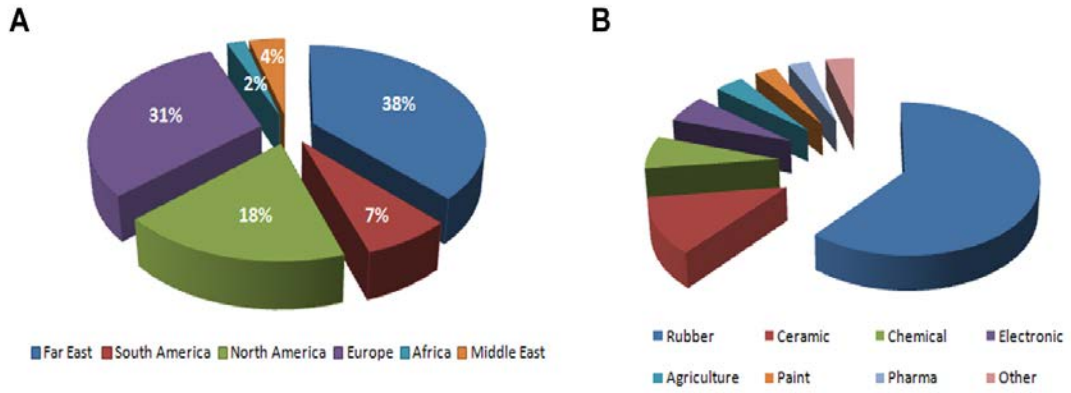

Figure 1: Application and worldwide distribution of ZnO

(A) Worldwide distribution of ZnO production and application. The Far East, especially China, is the most dominant supplier of ZnO (approx. 38 %). It is followed by Europe (approx. 31 %) and North America (approx. 18 %). (B) Rubber production is the most important application of ZnO (e.g., tires). A further utilization is the ceramic industry followed by chemical and electronic production. The total use of ZnO in pharmaceuticals is less than 10 % but is expected to increase, due to its wide range of application (adapted from:[19,20]).

1.2 Mechanisms and consequences of particle uptake

Increasing industrial manufacture and use of nanoscaled materials lead to environmental release and therefore enrichments in air, soil, water, and plants, followed by an unavoidable exposure to humans. The amounts of nanomaterial intake for humans depend on the level of deposition, injection, inhalation or ingestion over the skin, gastrointestinal- or respiratory tract (Figure 2). The nanoparticle uptake depends on particles size, concentration and surface modification.

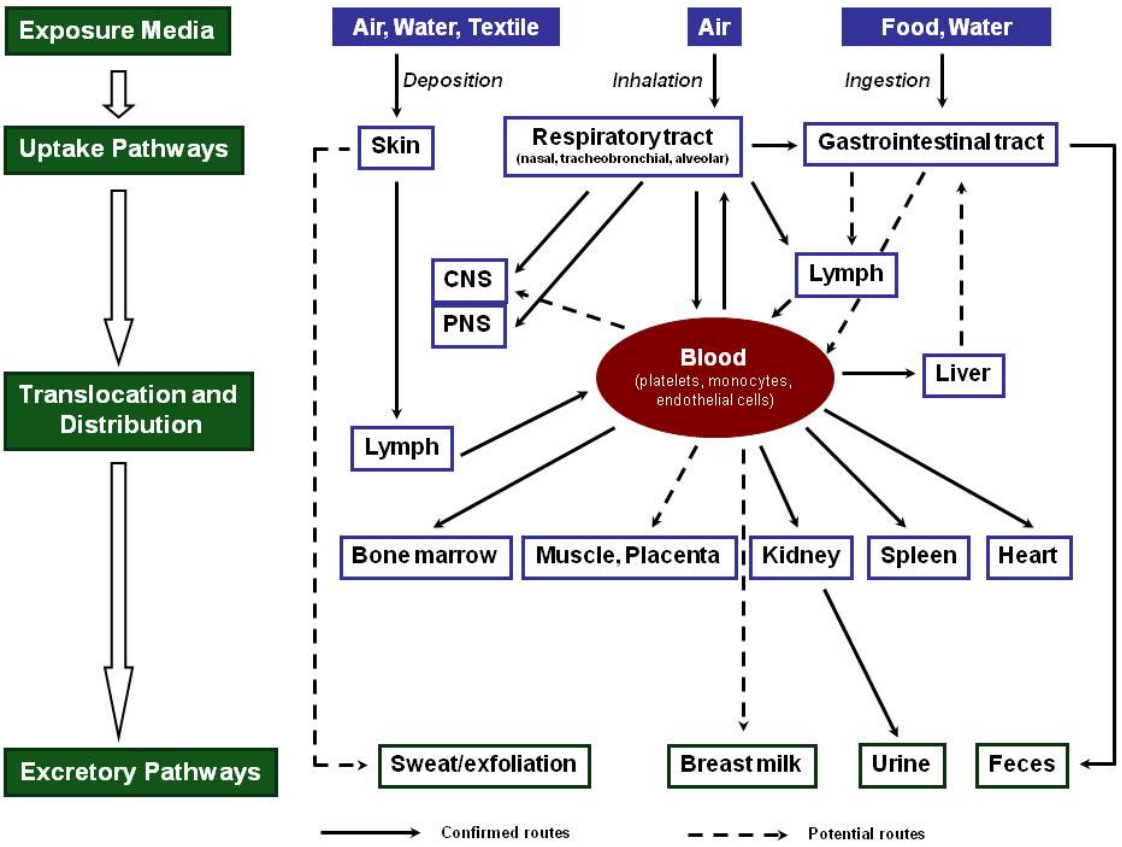

Figure 2: Uptake and translocation pathways of nanomaterial

Nanoparticles can be taken up by deposition, inhalation or ingestion. The illustration gives an overview of already investigated uptake routes (cf. confirmed ⟶) and hypothetical routes (cf. potential - - - ➔) of nanoparticles. The primary uptake pathways are through the skin, gastrointestinal and respiratory tract. After assimilation, the particles are translocated in the blood and further directly or indirectly distributed to the organs. The distribution rates are still unknown and need to be established. The uptake mechanisms as well as the translocation and distribution are dependent on physico-chemical characteristics of the nanomaterial. The affiliated particles may get excreted by sweat, exfoliation, breast milk, urine and feces (adapted from:[23]).

1.2.1 Skin

Nanoparticles are used in many cosmetics and textile products, resulting in a direct contact to the human skin. ZnO NP are utilized as inorganic filters in sunscreens like TiO_2. These compounds can reflect and absorb UV light, especially UV-A and UV-B radiation. Due to its antibacterial effects, ZnO is frequently used as a component in cosmetics, pharmaceutical creams, and shower gels. Therefore, possible deposition in the skin has been investigated in recent studies[24–26]. ZnO in sun blocker was identified as a reducer of cellular viability in keratinocytes[27]. The accumulation of particles in the skin is depending on size, surface, and skin integrity. New findings demonstrate a deposition of particles in the upper dermal layer, but single particles are penetrating to the lymph and further to the blood system[24,26,28,29]. Despite these data, ZnO NP in cosmetic products are still classified as harmless[24,26,30].

1.2.2 Gastrointestinal tract

The gastrointestinal tract (GI) represents another uptake pathway of ingested nanoparticles. The kinetics of particle distribution depend on the metabolic pathways by persorption in the extrusion zone, passage over tight junctions, and receptor-mediated endocytosis of enterocytes or transcytosis by M cells of the peyer's plaques[31–34]. An animal study, published by *Szentkuti et al. (1998)*, showed that particles with a cationic surface charge were caught by the mucosa, while the carboxylated particles were taken up by diffusion[35]. Swallowing contaminated food with nanomaterial may lead to GI damage[36]. Studies on enterocytes of *Xenopus laevis* showed an impact of metallic nanoparticles, especially ZnO NP on ROS generation, inflammation, and necrosis[37].

1.2.3 Respiratory tract

The respiratory tract, with a surface area of 1400 m^2, is besides the skin (2 m^2) and the gastrointestinal tract (200 m^2), the primary contact organ with the environment[38]. The lung has an total average lung capacity of 6 L and is therefore the main entry pathway of nanoscaled materials[33,38,39,40]. The respiratory tract is divided into the upper and lower region. The upper region includes the nose, paranasal sinuses, pharynx and a part of the larynx (above the vocal cords), known as airways. The airways comprise a distance of 2.300 km and transport the air inside and outside the human body. Due to its viscous layer, it is a barrier between air and blood[39]. The lower region includes the larynx (below the vocal cords), trachea, bronchi and bronchioles. This lower respiratory tract is also known as alveoli. $300x10^6$ alveoli are located in the lung, which are responsible for gas

exchange[39]. The area of gas exchange and the blood capillaries are separated by a thin wall of about 0.5 micron. Because of the large surface area of the alveoli, protection against the environmental intake (e.g., nanoparticles) is worse compared to the airways[39]. *Oberdoerster et al. (1995)* demonstrated significant differences between nanoparticles and larger particles (known as bulk material) of inhaled material in deposition and clearance[23]. The fractional deposition of inhaled particles in the nasopharyngeal/-laryngeal, tracheobronchial and alveolar region of respiratory tract was analyzed[23,41]. Inhaled particles between 1 nm and 50 nm are enriched in all regions, while larger particles (> 1 µm) are mainly deposited in the nasopharyngeal area (Figure 3)[23,41].

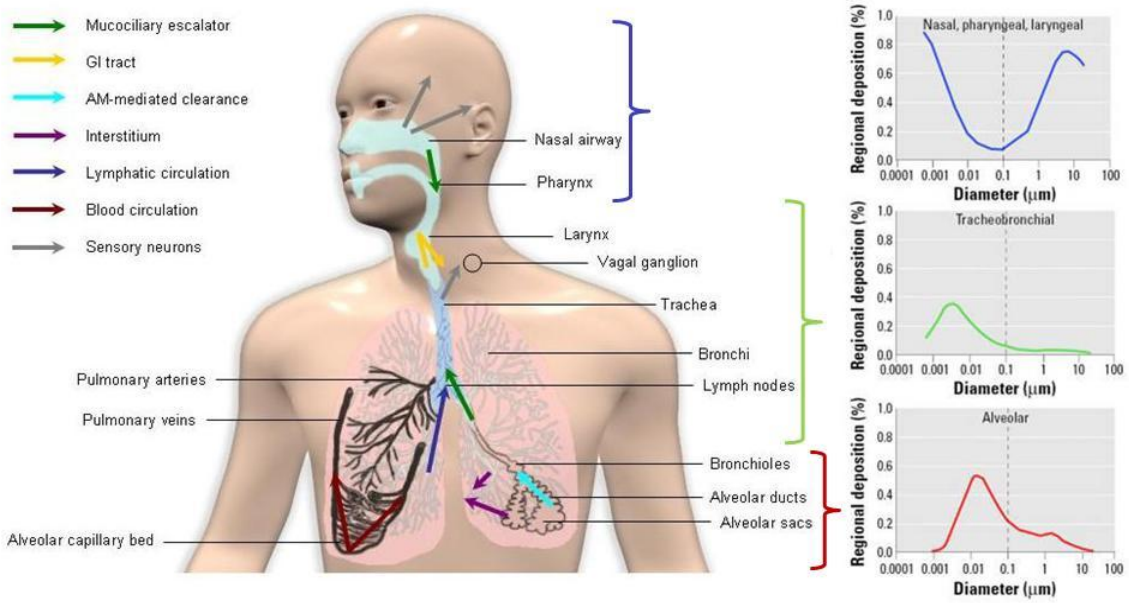

Figure 3: Pathways of nanoparticle clearance and deposition in the respiratory epithelia

The different arrows show possible clearance pathways of the respiratory epithelia. Possible depositions of inhaled nanoparticles during nose breathing are shown for the nasopharyngeal (blue), tracheobronchial (green) and alveolar region (red) of the respiratory epithelia. The clearance as well as the deposition is dependent on size and surface modifications of nanomaterial (adapted from:[18,23,41]).

The upper airways possess a mucociliary clearance that exports inhaled particles[39]. The classical clearance pathways are demonstrated in Figure 3. Biosoluble nanomaterials may undergo a chemical clearance due to extra- or intracellular milieu (pH)[23]. In the alveoli the clearance of particles smaller than 2.5 µm is cell mediated by phagocytosis of macrophages[33,39,42–46]. Alveolar epithelial cells are divided into type I cells with a direct connection to vascular endothelial cells and the surfactant producing type II cells[47]. The surfactant proteins are known for their pathogen opsonising function and affect on

phagocytosis. The activation of macrophages results in the release of immune mediators such as cytokines, chemokines and reactive oxygen species (ROS)[33,34,38,39,42,44,45]. Nanoparticles can overcome the defence mechanisms in dependence of their characteristics, concentration and exposure time. *Jachak et al. (2012)* discovered that small nanoparticles are naturally stuck in mucosa, but for some metal oxide nanoparticles, especially ZnO NP, an uptake in epithelial cells was observed[48]. The inhalation of nanoparticles may lead to lung diseases as shown for ZnO NP. The exposure to ZnO NP showed an increased occurrence of observed goblet cells and histological changes of pulmonary tissue associated with fibrosis in rats[49]. Furthermore, the inhalation of certain metal oxides (e.g., ZnO) may cause metal fume fever associated with symptoms such as fever, chills, headache and fatigue[50–52]. *Vandebriel et al. (2012)* reviewed different studies on mammalian nanoparticle toxicity and illustrated that inhalation or instillation of ZnO NP leads to lung inflammation and systemic toxicity[53].

1.2.4 Cellular uptake of nanomaterials

Mammalian cells use the energy-dependent process of endocytosis to receive energy or communicate with their biological environment by internalization of nutrients and signaling molecules[54,55]. There are four pathways for cellular uptake of nanoscaled material called clathrin/caveolar mediated endocytosis, phagocytosis, micropinocytosis and pinocytosis. Efficiency of nanoparticle internalization is dependent on their physico-chemical properties such as size, surface chemistry and shape. The clathrin/caveolar mediated endocytosis is the most important pathway for nanomaterials, because of an immediately covering of nanoparticles with plasma proteins gathering physiological solutions[55–58]. This process is receptor-mediated and enables a cellular uptake of small particles with a maximum size of 100 nm in diameter[59]. The pathway of phagocytosis is actin-dependent and used by phagocytic cells, which internalize particles larger than 0.5 µm[55,60]. The micropinocytosis and pinocytosis are an unspecific internalization mechanism of fluids and small nanoparticles (< 10 nm)[61]. The endocytic mechanism comprises distinct membrane compartments. Early endosomes (EE) are rapidly formed and usually located in the cytoplasm close to the plasma membrane, serving as a focal point of endocytosis and absorb vesicles from the cellular surface[62]. The main attributes of EE are the mildly acid environment and tubule-vesicular structure associated with their sorting function of dissociated ligands for further endocytic steps[62]. Late endosomes (LE) adhere to different membrane vesicles and proteins (e.g., acid hydrolases) receiving the pre-sorted material of the EE. The LE are acidic with a pH of 5.5 mediating a final merging prior to lysosomal transfer[63]. The pH of lysosomes (L) is at 4.8, which implodes

carbohydrates, fats, proteins and cellular waste in usable compounds for cellular functions[64]. In contrast to endocytic pathway, exocytosis involves the fusion of secretory vesicles with the inner surface of the plasma membrane and the releases of their content into the extracellular space[65]. Internalized nanomaterials can exit the cell via exocytosis by lysosomal-, vesicle-related- and non-vesicle-related secretion[55]. The regulated exocytic pathway enables a fast response of already existent vesicles and is generally triggered by a high concentration of free cytosolic Ca^{2+} [66–69]. The particle uptake is dependent on several factors such as form, size, surface charge, cell type, cell culture medium, and particle surface modification[48,53,70]. The cellular uptake of ZnO NP is rarely observed. Two possibilities are the ZnO NP upake as well as the uptake of Zn^{2+} dissociated from the particles. *Hackenberg et al. (2011)* observed an uptake of ZnO NP and an agglomeration inside the cytoplasm and nucleus but they coated the paricles with BSA reducing particle dissociation[71]. *Kao et al. (2012)* hypothesized an endosomal uptake for ZnO NP and a fast dissociation of the particles due to the acidic pH of endosomes[72].

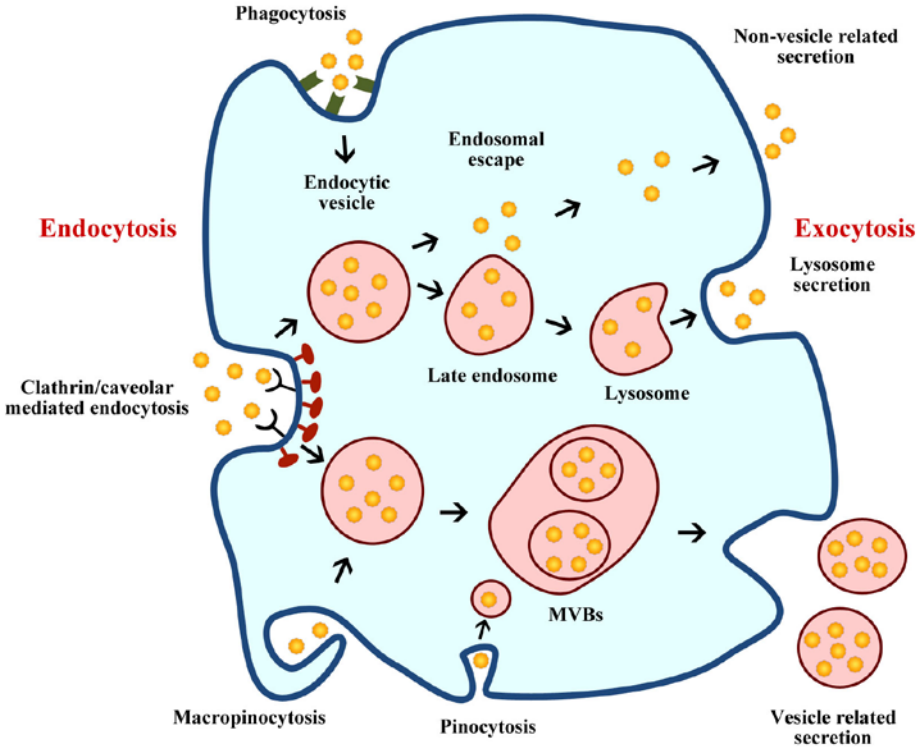

Figure 4: Cellular uptake and release of nanoparticles

Four different types of cellular nanoparticle entry are described. The nanoparticles enter the cell by clathrin/caveolar mediated endocytosis, macropinocytosis, phagocytosis and pinocytosis. After affiliation, the particles can deposit the intracellular space or can be secreted by lysosomes, by vesicles or in a non vesicle/lysosomal associated pathway (adapted from:[55]).

1.3 Nanotoxicity

Within the last two decades, the discipline of nanotoxicology has been developed in line with the rapid engineering of nanotechnology. Although the environment and humans have been exposed to respirable dust throughout their evolutionary stages, the anthropogenic sources of nanomaterials have drastically been increased during the last decade[23]. Risk assessments of nanoscaled material are still unsatisfactory investigated and more information about the safety and the potential hazards are urgently needed[23]. Therefore, the nanotoxicology is a "sub domain" of toxicology which is defined as the effects of nanosized material impacting environmental condition and human health. The toxicological effect of nanomaterial could be observed in the case of synthetically produced particles as well as in by-products of burnt and fractionated material[73,74]. The research of nanotoxicity has shown a remarkable complexity of cellular interactions with nanomaterials. Researchers address the interactions of the release focusing on the physico-chemical properties of the nanoparticles. Possible mechanisms of nano-toxicology are inflammation, ROS generation, direct structural interactions, DNA damages, apoptosis, and the effect of released ions.

1.3.1 Inflammatory potential of nanomaterial

Inflammation is a central process of nanoparticle-induced adverse health effect[75]. The inflammatory potential of inhaled metal oxides has been established for decades as acute metal fume fever syndrome[50,52]. The exposure to ZnO NP is accompanied by an impressive pulmonary cellular response, characterized by the appearance of short time symptoms after inhalation and healing of metal fume fever within 24 h[76]. The tissue inflammation is initiated and regulated by cytokines, a class of signaling molecules. Cytokines are involved in many signaling processes including cell growth, -differentiation, and the recruitment of immune cells[77–79]. *McCreanor et al. (2007)* investigated effects of diesel exhaust on respiratory epithelia and observed inflammatory responses predominantly induced by neutrophiles with increased levels of IL-8 and myeloperoxidase in the supernatant of the sputum[80]. Further, the exposure of pulmonary dendritic cells to ZnO NP as component of exhausts resulted in secretion of cytokines[81].

1.3.2 ROS generated by nanomaterials

ROS is a collective term which summarizes molecules with at least one unpaired electron assigning reactivity to a variety of biological targets. They are also defined as free radicals which naturally arise as by-product of anaerobe metabolism characterized

by a high instability. The class of ROS contains the O_2-derived free radicals called superoxide anion ($\bullet O_2^-$), hydroxyl (HO•), peroxyl ($RO_2\bullet$), and alkoxyl (RO•) as well as the O_2-derived nonradical species such as hydrogen peroxyde (H_2O_2) and hypochlorous acid (HOCl)[82–85]. High doses of ROS often induce cellular damages to DNA, proteins and lipids, which is summarized as oxidative distress, while low levels serve as regulator molecule in biological redox signaling[86,87]. Endogenous sources of ROS by-products of cellular metabolism and respiration are generated by NADPH oxidases. Organelles, such as mitochondria or peroxisomes, produce hydrogen peroxide as a by-product using enzymes (e.g., p450 cytochromes), which catalyze the oxidative reduction[88]. During the cellular respiration in mitochondria, oxygen is reduced in a gradual electron transport chain[88]. Exogenous sources of ROS are generated by chemical and physical exposures e.g., pollutants, smoke, radiation and metals[89]. Recent studies suggested possible harmful activities of metals (e.g., Zn^{2+}, Fe^{2+}) through the modulation of the intracellular redox state, at least in part of Fenton and/or Haber-Weiss reactions[52,90].

$$Fe^{2+} + H_2O_2 \rightarrow Fe^{3+} + \cdot OH + OH^-$$

$$Fe^{3+} + H_2O_2 \rightarrow Fe^{2+} + \cdot OOH + H^+$$

Figure 5: Fenton reaction as exemplified for iron ions

The dissociated ions possibly enhance the production of ROS in mitochondria through disregulated $\Delta\Psi m$ and autooxidation of thiol groups[91]. The human body has developed different defense mechanisms against ROS. Antioxidant enzymes (e.g., SOD) as well as scavengers (e.g., glutathione) are avoiding the oxidative degradation[88]. The relation between glutathione (GSH) and oxidized glutathione disulfide (GSSG) serves as sensor for an imbalance between ROS and the intracellular defense mechanisms. *Walther et al. (2000)* showed that Zn^{2+} are able to inhibit the glutathione reductase which further synergistically enhanced the oxidative stress[92]. In case of an insufficient defense the ROS sensitive MAPK- and NF-$_\kappa$B signaling is activated to induce the expression of proinflammatory cytokines, chemokines and adhesion molecules[93]. Continuously generated ROS and reduced scavenging by antioxidants lead to increased oxidative distress. This cellular situation is associated with many health impairments such as cardiovascular, neurological or psychiatric diseases and cancer[87,94–96]. However it is not proven, whether the generated oxidants trigger the disease or ROS is induced as a side effect of the disease[97].

1.3.3 Interaction of nanoparticles with intracellular structures

After cellular uptake and penetration of the particles through the plasma membrane, different interactions between the nanoparticles and the intracellular structures are conceivable. Researchers suggested the direct interaction of nanoparticles with cellular structures as possible toxic mechanism. *Moschini et al. (2013)* detected an interference of mitochondrial and lysosomal functions as well as an impairment of the mitochondrial membrane after particle treatment as evidence of a direct particle-cell-interaction[98]. Beside the generation of energy through oxidative phosphorylation of ATP, the mitochondria are necessary for important cellular regulations such as apoptosis and cellular calcium and redox homeostasis[99–101]. The effect of nanoscaled materials on mitochondria has diverse consequences to cellular viability and depends on particle size and surface chemistry. Different studies have shown that colloidal Ag-coated gold NP, black copolymer micelles and multi-walled nanotubes of approximately 50 nm are aggregated nearby or even inside the mitochondria[23,102–106]. Another study demonstrated that gold NP (3 nm, diameter) penetrate through the outer mitochondrial membrane via voltage-dependent anion channels. *Salnikov et al. (2007)* and others interpret these observations according to the mitochondrial swelling, permeability transition, morphology changes, intracellular Ca^{2+} influx and loss of cristae[93,105,107]. *Qi et al. (2005)* observed a loss of mitochondrial membrane potential ($\Delta\Psi m$) in gastric carcinoma cells induced by chitosan NP[108]. The $\Delta\Psi m$ is linked to caspase activity by initiating the cyt c release resulting in apoptosis[109]. After endocytic uptake of nanoparticles (e.g., ZnO NP), they interact with lysosomes and may impair their formation and function[110–112]. Lysosomes contain hydrolases that degrade different cellular macromolecules[113]. Liposomal overload followed by cellular generation of ROS may lead to a collapse of lysosomal membrane permeabilization (LMP). *Yuan et al. (2002)* asserted that the induction of apoptosis by primary lysosomal destabilization is p53 dependent[114]. *Cho et al. (2011)* observed a lysosomal destabilization after treatment with metal oxide particles. They suggested that a high local ion concentration led to LMP damage which results in cell death[115]. The reaction of radicals with fatty acids leads to the generation of lipid peroxyl radicals, which put a chain reaction in motion. This possibly leads to loss of membrane integrity, release of LDH, and intracellular increase of ROS. The release of LDH was observed after treatment with ZnO NP for up to 24 h indicating the loss of membrane integrity[116,117]. The nuclear internalization of nanoparticles is not completely understood yet, nevertheless some investigators refer to a nuclear uptake of small particles through nuclear pores via passive diffusion[118–120]. *Panté et al. (2002)* suggested that

nanoparticles (> 39 nm) interact with specific transport receptors to enter the nuclear envelope[119].

1.3.3.1 Programmed cell death induced by nanoparticles

Exposure to nanoparticles may lead to cellular damages resulting in apoptosis or necrosis. Apoptosis is a normal physiological process during development. Additionally, for cells with intolerant amounts of DNA damages, the apoptosis is activated by DDR[121]. The complex process of apoptosis is expired through at least two pathways, the extrinsic and the intrinsic pathway[122]. The activation of the extrinsic signal cascade occurs by receptors of the tumor necrosis factor (TNF), family binding extrinsic ligands (FasL, TNF-α), and transducing intracellular signals initiating caspase activity[122,123]. The intrinsic apoptotic process is linked to the mitochondria[122,124]. In presence of DNA damage, activated p53 promotes the expression of diverse pro-apoptotic genes such as Puma, Noxa or Bax of the Bcl-2 family[104,121,125]. The activation of the pro-apoptotic signaling results in the depolarization of $\Delta\Psi m$[126]. The emerging permeabilization of mitochondria leads to a cyt c release into the cytosol. Cyt c and dATP bind to Apaf-1 resulting in conformation changes of the Apaf-1 protein[127,128]. Therefore, the CARD domain of Apaf-1 protein is accessible for pro-caspase 9, which forms a complex referred to apoptosom, which then further initiates the caspase activation[104,121,127,128,129]. The exposition with nanoparticles can result in apoptosis through the intrinsic and extrinsic pathways. Reactive nitrogen species (RNS) can directly activate the extrinsic pathway through the Fas death receptor[130]. *Akhtar et al. (2012)* observed a ROS mediated activation of the intrinsic pathway through p53 after exposure to ZnO NP[131]. Furthermore, an induction of TNF-α expression via ROS-Erk-Egr-1 pathway activation was observed in keratinocytes after ZnO NP treatment[132]. The Raf/MEK/Erk pathway directly interacts with the Ras/PI3K/PTEN/Akt pathway regulating cellular growth, apoptosis and tumorigenesis[133]. Erk1/2 regulates apoptosis by posttranslational phosphorylation of pro-apoptotic proteins[134]. *Persons et al. (2000)* reported a function of Erk1/2 in DNA damage response which leads to stabilization of p53[135]. *Tang et al. (2002)* showed as well that Erk1/2 interacts with p53, resulting in cell cycle arrest or apoptosis[136]. Both pathways interact with p53 and may lead to an alteration of the subcellular localization and activity of pro-apoptotic proteins (e.g., Puma and Noxa)[133]. ZnO NP are able to initiate the activation of p53-signaling[137]. *Meyer et al. (2011)* showed that ZnO NP treatment of human dermal fibroblasts lead to a reduced sensitivity to ZnO NP induced apoptosis in p53-knock out cells[137]. *Wilhelmi et al. (2013)* showed the induction of apoptosis as well as necrosis in

macrophages after ZnO NP exposure[138]. Besides, the ZnO NP may directly induce mitochondrial impairments or DNA damages.

1.3.4 Nanoparticle induced genotoxicity

Various physical and chemical environmental agents (e.g., ionizing radiation, UV light, genotoxic chemicals) as well as by-products of physiological processes cause a diversity of DNA damages[139–142]. Metallic nanoparticles are able to damage the DNA indirectly by inflammation and oxidative distress[143,144]. Some DNA aberrations arise by generated ROS, from oxidative respiration, or during Fenton reactions initiated by heavy metals[142,145,146]. Furthermore, endogenous DNA damages are induced by free radicals generated through lipid peroxidation[147]. The particle diffusion inside the nucleus is thinkable due to their small size. Furthermore, positively charged particles may pass the nuclear envelope and possibly interact directly with the negatively charged DNA[148,149]. The most common types of DNA lesions are single strand breaks (SSB), DSB, mismatches, and chemical adducts[141]. The most hazardous type of DNA damages are DNA DSB[150]. SSB, generated by ROS, could be converted to DSB in case of two proximate SSBor if the DNA replication encounters SSB during S phase of the cell cycle[142,151,152]. *Hackenberg et al. (2011)* showed that a repetitive exposure of human nasal mucosa cells treated with ZnO NP leads to DNA damages[71]. Gold NP are known to interfere with DNA repair proteins such as BRCA1 or induce the expression of genes involved in cell cycle arrest or induction of apoptosis[153]. The types of DNA damage as well as the mechanism of these genotoxicity are not well established. DNA damages may lead to apoptosis or mutagenicity mediated directly by metal oxide NP or indirectly through their dissociated ions[154].

1.3.4.1 DNA damage response

The cellular response to DNA lesions is attended by a diversity of cell cycle checkpoints and activates several DNA repair pathways[139]. One of the first steps of DNA damage response (DDR) is the recognition of DNA damages initiating the phosphorylation of histone H2A.X. *Rogakou et al. (1998)* showed that H2A.X can be phosphorylated on Ser 1, ubiquitinated on Lys 119 and acetylated on Lys 5. The rapidly phosphorylation of Ser 139 occurs in presence of DNA DSB which makes the difference to other H2A family members[155]. The phosphorylation of Serine on position 139 is termed γH2A.X[155]. This phosphorylation is induced in response to DNA DSB, affected by exogenous agents, replication stress or apoptosis[155–158]. For the first time *Sedelnikova et al. (2002)*

described γH2A.X as specific DNA DSB marker, because of its fast induction and amplification around the DSB[159]. γH2A.X is dephosphorylated by the phosphatase called PP2A after DNA damage repair[160]. Main sensors of the DDR are ataxia telangiectasia mutated (ATM) and ataxia telangiectasia and Rad3-related (ATR), which are activated and recruited to the DNA DSB and replication protein A (RPA)-coated ssDNA, respectively[139,161–163]. ATM and ATR are members of the PIKK family which specifically phosphorylate serine and threonine residues of proteins[139,142]. ATM is mainly activated in presence of DSB, while ATR is activated in response to inhibit DNA replication forks or SSB[164]. The two best studied downstream targets of ATR and ATM are the effector kinases Chk1 and Chk2. ATR activates Chk1, whereas ATM activates Chk2[165,166]. Both sensors as well as their effector kinases reduce the activity of cyclin-dependent kinase (CDK) through different mechanisms, e.g., by stabilization of p53 in order to inhibit the cell cycle, promote DNA repair or initiate pro-/anti-survival signaling cascades[148,165,167-169,164]. The activation of DDR mobilizes DDR proteins to the site of damage initiating the damage repair[170].

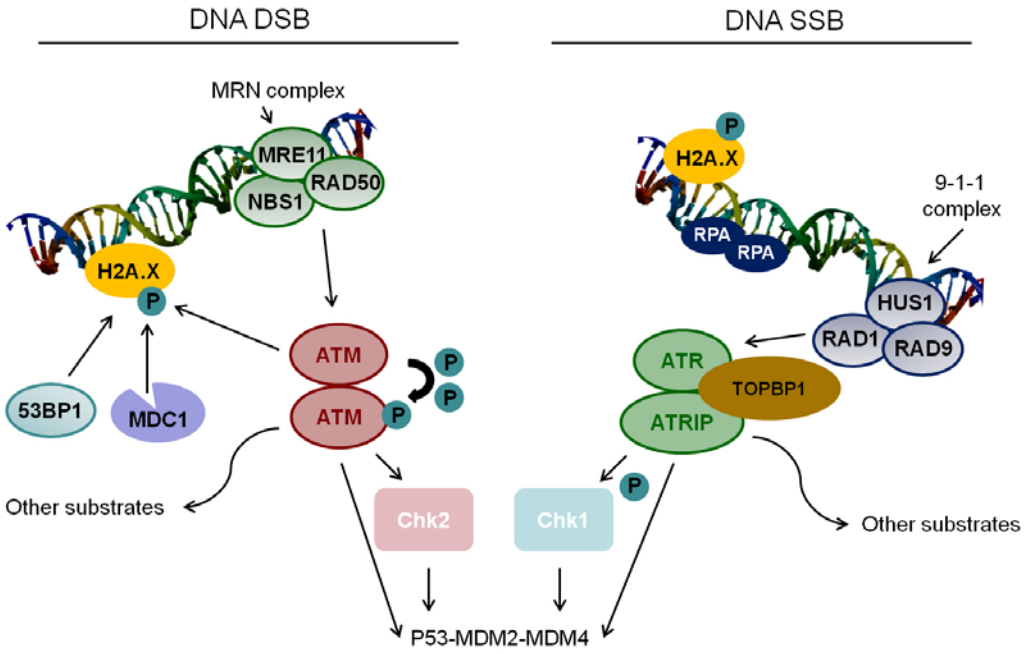

Figure 6: DNA damage response signaling

H2A.X is phosphorylated in presence of DNA damage. The DNA DSB is recognized by the MRN complex and resulting in the activation of ATM. In response to ATM phosphorylation different DDR proteins are recruited to the site of DNA damage. Furthermore, ATM activates a variety of downstream substrates such as Chk2, p53, MDM2 and MDM4. DNA SSB become coated with the RPA protein recruiting the ATR-ATRIP complex. This complex activates the 9-1-1 complex, which in turn activates ATR. Phosphorylated ATR activates their downstream proteins Chk1, p53, MDM2 and MDM4 (adapted from:[171]).

1.3.4.2 P53, the guardian of the genome

In response to DNA damage, both ATR-Chk1 as well as ATM-Chk2, induce a range of posttranslational modifications on p53, leading to cell cycle arrest and damage repair or apoptosis for instance[171,172]. In this context, the p53 is one of the main effectors of DDR. P53 is an unstable transcription factor which becomes phosphorylated and stabilized in response to cellular stresses, particularly in prescence of DNA damages[173–175]. The activity of p53 is regulated by diverse posttranscriptional and posttranslational modifications such as alternative splicing, phosphorylation and conformational changes[176]. The release of p53 from its negative regulator, mouse double minute 2 (MDM2) and mouse double minute 4 (MDM4), is the key step of p53 stabilization and connected to a feedback transcriptional regulation of MDM2[156,171,172,176]. Under normal physiological conditions, p53 is present in an instable form ($t_{1/2}$ ~30 min) and becomes ubiquitylated and proteasomal degradated by E3 ubiquitin ligases or MDM2[171,176,177]. The adapter protein DAXX interacts with the herpesvirus-associated ubiquitin-specific protease (HAUSP) and the MDM2[171,178]. This interaction reduces the auto-ubiquitylation activity of MDM2 and further enhances the degradation and turnover of p53[171]. The induction of ATM and ATR during genotoxic cellular stresses induces a wide range of p53 modification, resulting in MDM2-DAXX-HAUSP complex disruption and ubiquitylation of MDM2 and MDM4[171]. Two well investigated main consequences of p53 stabilization initiated by DNA damage are the cell cycle arrest with induction of DNA repair and apoptosis.

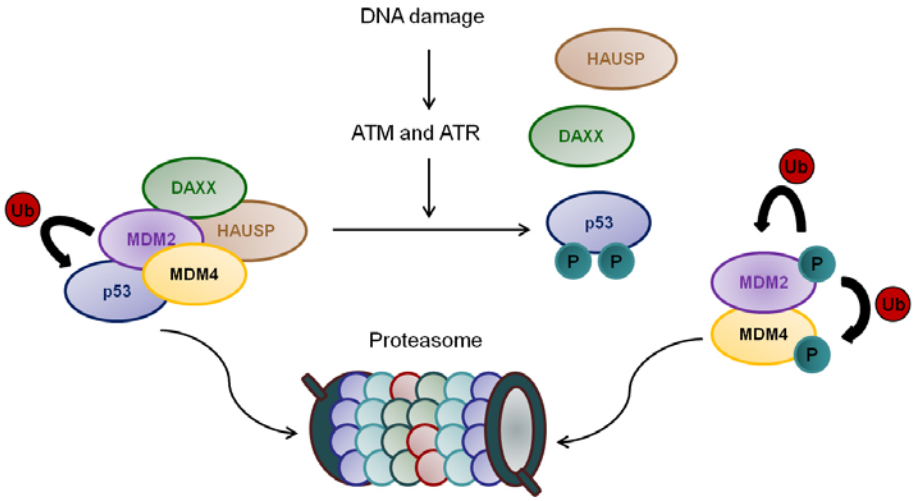

Figure 7: Degradation and stabilization of p53

Under physiological conditions p53 is proteasomal degradated after ubiquitylation. The ubiquitylation of p53 is mediated by the marking of MDM2 and MDM4. The effort of p53 could be enhanced by several proteins such as DAXX and HAUSP, which deubiquitylate MDM2 and MDM4. The activation of DDR by ATM or ATR leads to induction of p53 through MDM2-DAXX-HAUSP complex rupture and disruption of MDM2 and MDM4 (adapted from:[171]).

1.3.4.3 Repair of DNA DSB

The two major DSB repair mechanisms are the homologous recombination (HR) and non-homologous end-joining (NHEJ). The NHEJ is active during the whole cell cycle (preferred repair mode G1 and S phase) linking the break end directly and does not need the homologous template for repair[179–182]. Therefore, the Ku heterodimer (Ku70 and Ku80) binds to the ends of DNA DSB, brings the catalytic subunit of DNA PK and the Ligase4-XRCC4 to complete NHEJ[183]. DNA DSB can occur during S phase because of replication stress and replication fork collapse. Furthermore, the CDK activity during S phase is low affecting the initiation of HR[183]. The HR uses the intact sister chromatid as a template for DNA DSB repair and is therefore restricted to the late S and G2 phase[165,166,180,181,182,184] .The activation of the checkpoint control and the repair of DNA DSB, by NHEJ and HR, are important for cell cycle progression and cellular survival.

1.3.5 Possible damaging potential of dissociated Zn^{2+}

Another toxic mechanism of metalic nanoparticles is postulated as Zn^{2+} mediated by particle dissociation[185]. Changes of particle surface constitutions (i.e., using iron doping or BSA coating) reduces ion release from particles and this resulted in reduced toxic cellular effects[186,187]. Furthermore it is a question of debate in which cellular environment the ZnO NP dissociate. ZnO is often classified in material safty data sheets as insoluble in H_2O, while others reported a highly pH-dependent solubility of ZnO[188,189]. *Muller et al. (2010)* observed a pH-dependent solubility of ZnO NP and therefore rainforced toxicity. They observed particle dissociation in acidic environment suggesting the release of Zn^{2+} after endocytic uptake in endosomal vesicles[112].In many physiological processes zinc plays an essential role as functional, structural, and regulatory element. Due to this importance a potential toxicity derives from the disturbance of zinc homeostasis. The homeostasis and steady state concentrations of free intracellular Zn^{2+} are maintained by buffering systems. Therefore, the intracellular free Zn^{2+} concentration has to be tightly controlled. The involvement of deregulated Zn^{2+} homeostasis is well known for type 2 diabetes and more recently the proper regulation of the sub-cellular distribution has been shown to be relevant. Eukaryotic cells contain much more zinc than other transition metals and need to distribute them to many proteins to guarantee their functional activity[190]. The metal-response-element-binding transcription factor (MTF-1) plays a substantial role in the control of zinc homeostasis. MTF-1 serves as sensor of high levels of intracellular free Zn^{2+} and induces the transcription of MT. Low changes of the intracellular steady state Zn^{2+} concentration can be corrected by MT which is known as

regulator in buffering. ROS may lead to an increased Zn^{2+} concentration caused by the oxidation of thiol groups of the zinc-binding proteins resulting in reduced buffer capacity which leads to toxicity[190]. The second regulation mechanism of intracellular Zn^{2+}, named muffeling reaction, is organized by several zinc binding proteins and transporters distributing the free Zn^{2+} into compartements or external secretion[190]. It is quite important that Zn^{2+} has no uncontrolled access to metalloproteins, because the binding of metals to proteins follows the series of Irving-Williams showing that Zn^{2+} is highly preferred over most other metals[191,192]. *Peck et al. (1971)* investigated in the enzyme activity of phosphoglucomutases in rabbits and observed that high intracellular concentrations of free Zn^{2+} resulted in a reduced enzyme activity, because Zn^{2+} is able to displace Mg^{2+} as cofactor[192]. Zn^{2+} imbalance between mitochondria and cytoplasm, e.g., might result in insulin resistance and cell damage by induction of apoptosis[193]. The human genome encodes more than 3000 proteins comprising zinc. Due to its binding affinity to thousands of proteins, Zn^{2+} is crucial for cells differentiation, proliferation, signaling, and survival[176,190,191,194]. The functional Zn^{2+} is mostly located as catalytical unit in several enzyme classes such as ligases, hydrolases, and transferases as well as in different secretory enzymes[195]. Zinc, as a catalytical component, is located at the active site through four ligands (e.g., histidine, cysteine, aspartic- and glutamic acid)[194]. Furthermore, zinc is described as modulating coactivator together with copper (e.g., superoxide dismutases)[196]. Zinc acts also in a structural way by binding to amino acid side chains to stabilize the active tertiary structure of proteins (e.g., alcohol dehydrogenase). It serves also in histones, as DNA structure stabilizing component (e.g., histone deacetylases), which carry Zn^{2+} in their active center[197]. The functional integrity of these enzymes is substantial for proper epigenetic regulation of gene expression. Zinc is an element of transcriptionfactors and plays therefore a critical part in the regulation of DNA transcription and replication. Zinc is an essential element of zinc finger and many proteins involved in DNA repair (e.g., XPA, PARP, and Fpg). Zn^{2+} is able to cause activity loss of PARP-1 and OGG1 in subcellular systems[198,199]. Furthermore, it was shown that zinc acts as DNA repair inhibitor in presence of oxidative caused DNA base modifications[198]. The activity of DNA mismatch repair depends on a conserved Zn-binding domain of the hPMS2 subunit of the MutLalpha heterodimer. These important proteins are of great significance for maintaining DNA integrity and genomic stability. They are also associated with the hereditary form of colon cancer in case of their inactivation[200]. Zinc is essential for intra- and intercellular communication. Thus, there is evidence that Zn^{2+} serves as an intracellular signaling molecule, similar as known for Ca^{2+} [201,202]. Free Zn^{2+} is involved in neurotransmitter functions mediating intercellular communication and acting as an intracellular signaling molecule.

Yamashita et al. (2004) showed that the zinc transporter LIV1 is essential for the nuclear translocation of the Zn-finger transcription factor Snail, a master regulator of epithelial-mesenchymal transition (EMT)[203]. EMT is a key event of tissue development and cancer progression. Another function of nuclear Zn^{2+} is its participation in pre-mRNA splicing as a cofactor in spliceosomes[204,205].

Dissociation of ZnO NP into Zn^{2+} is a possible toxic mechanism of metallic oxide particle. All these many examples underscore a relevant role for Zn^{2+} in nuclear functions and consequences in the case of dysregulated sub-cellular homeostasis.

2 Aims of this work

Metal and metal oxide nanoparticles are commonly used as additives in industrial production of rubbers, catalysts, foods, pharmaceuticals and cosmetics. Prospectively, a continuous rise of industrial application is estimated, which results in an increasing release to environment and humans' exposure. Therefore, it is of importance to investigate potential adverse effects. Metallic nanoparticle intake of humans' results in inflammatory reactions known as *metal fume fever* and a multitude of publications report toxic effects in cell culture and animals. More recently genotoxic effects have been suggested to be associated with metal oxid nanoparticle intake. In this study ZnO NP were used as a model of metal oxide nanoparticles to evaluate mechanisms of genotoxicity in respiratory epithelia. The study aimed to investigate the intracellular ZnO NP uptake and distribution, their toxicity, DNA damaging potential, and DNA damage response (DDR) activation.

In particular the following questions were targeted:

- How are ZnO NP internalized by the cell and where are they accumulated?
- Is there a size dependent effect in cellular uptake, accumulation and toxicity?
- Are ZnO NP genotoxic?
- Do they activate the DNA damage response?
- What are the mechanisms of genotoxicity?

3 Materials and methods

3.1 Materials

Table 1: Equipment

Equipment	Manufacturer
Atomic absorption spectroscopy, AAS	PerkinElmer, Waltham, MA, USA
Autoclave 5050 ELV	Tuttnauer, Breda, Netherland
BD FACS Canto II	Becton Dickinson, Francklin Lakes, NJ, USA
CASY® Cell counter, Model TT	Roche Diagnostics International AG, Basel, Swiss
Centrifuge, Biofuge fresco	Heraeus, Kendro Laboratory Products, Hanau, Germany
Centrifuge, Multifuge 1L-R	Heraeus, Kendro Laboratory Products, Hanau, Germany
Combs, 1.0 mm, 10 wells	Biometra GmbH, Göttingen, Germany
Micro Centrifuge Modell: 100 VAC Fisherbrand®	Fisher Scientific, Schwerte, Germany
ChemiDoc MP system	Bio-Rad Laboratories, Inc., Hercules, CA, USA
cLSM Leica TCS SP5	Leica Camera, Solms, Germany
Digital camera	VDS Vosskühler GmbH CCD-1300, Osnabrück, Germany
Electrophoresis Chamber	Biometra GmbH, Göttingen, Germany
Fastblot B43Semi-Dry Blotter Trans-Blot® SD	Biometra GmbH, Göttingen, Germany
FluoroMax 2	Horiba Seisakusho, Kyōto, Japan
Fluoroskan Ascent™ Microplate	Thermo Fisher Scientific GmbH, Rockford, USA
Freezer (-20°C), Liebherr Premium	Liebherr, Bulle, Switzerland
Glass plates with fixed 1.0 mm spacers	Biometra GmbH, Göttingen, Germany
Hemocytometer	Paul Marienfeld GmbH & Co. KG, Lauda-Königshofen, Germany
Hera Freezer (-80°C)	Kendro Laboratory Products, Hanau, Germany
Incubator, Heracell 150i CO_2 Incubators	Thermo Scientific, Waltham, MA, USA
Irradiation equipment, Gammacell 2000, γ-source (Cs137) source	Mølgaard Medical, Risø, Denmark
Laminar flow cabinet, Herasafe Safety cabinets	Heraeus, Kendro Laboratory Products, Hanau, Germany
Magnetic stirrer, MR3001	Heidolph, Schwabach, Germany
Magnetic stirrer, Heidolph MR 3001	VWR international, Darmstadt, Germany
Microscope, Leitz Orthoplan	Leica, Wetzlar, Germany
Microscope, Nikon TMS	Nikon, Düsseldorf, Germany
Microscope fluorescence, Nikon Eclipse TE2000U	Nikon, Düsseldorf, Germany
Minicentrifuge RF	Heraeus, Kendro Laboratory Products, Hanau, Germany
Minicentrifuge Universal 16 R	Hettich Zentrifugen, Tuttlingen, Germany
Nitrogen tank	CRYO-4000, Chart Ind., Burnsville, MN, USA
Pipette	Eppendorf AG, Hamburg, Germany
Pipetus®	Hirschmann Laborgeräte, Eberstadt, Germany
Power Supply, Modell 1000/500 Constant voltage	BioRad, Hercules, CA, USA
Power Supply, Standard power pack P25	Biometra GmbH, Göttingen, Germany
Refrigerator profi line	Liebherr, Bulle, Switzerland
Rocking platform shaker WS-10	Edmund Bühler, Hechingen, Germany
Running rig Midigel + Twin G42	Biometra GmbH, Göttingen, Germany
Scale Kern PCB	Kern und Sohn GmbH, Balingen Frommern, Germany

Scale Precision Advanced DHAUS	As-Wägetechnik GmbH, Garching, Germany
Scanner, Epson Perfection 3200 Photo	Epson, Meerbusch, Germany
Semi-dry electrophoretic transfer cell	Biometra GmbH, Göttingen, Germany
Shaker, Rotor WS-10	Edmund Bühler, Hechingen, Germany
Shaker, Rocky 3D	Labortechnik Fröbel GmbH, Lindau, Germany
Silicone rubber seal, 1.0 mm	Biometra GmbH, Göttingen, Germany
Sonorex Super RK 510 H	Bandelin electronic GmbH & Co. KG, Berlin, Germany
Spectrophotometer Fluoroskan Ascent Microplate	Thermo Electron Corporation, Dreieich, Germany
StripHolder	Labcrew, Amersham Bioscience, Sunnyvale, CA, USA
Thermomixer, HLC-TM 130-6	Haep Labor Consult, Bovenden, Germany
Thermomixer comfort	Eppendorf AG, Hamburg, Germany
Transferpette® S	Brand GmbH & Co KG, Wertheim, Germany
TEM Philips EM420	Koninklijke Philips N. V., Amsterdam, Netherlands
TEM Leo 906	Carl Zeiss AG, Oberkochen, Germany
Teflon-lined stainless steel autoclave	Institute of inorganic and analytical chemistry, JGU, Mainz
Ultracut 41	Reichert-Jung, Vienna, Austria
Ultrasonic homogenisers, LABSONIC M	B. Braun Biotech International, Melsungen, Germany
Vacuum rotary evaporator	BÜCHI Labortechnik AG, Essen, Germany
Vortex, Top-Mix 11118 Fisherbrand®	Fisher Scientific, Schwerte, Germany
Vortex, VV3	VWR International, Radnor, PA, USA
Water bath	INFORS HT, Bottmingen, Swiss
Zetasizer Nano ZS	Malvern Instruments, Malvern, UK

Table 2: Chemicals

Chemicals	Manufacturer
Acetic acid	AppliChem, Inc., St. Louis, MO, USA
AlamarBlue®	BIOZOL Diagnostica Vertrieb GmbH, Eching, Germany
Ammonium acetate	Sigma-Aldrich, St. Louis, MO, USA
Albumin Fraction V, BSA	Carl Roth GmbH & Co. KG, Karlsruhe, Germany
Aprotinin	Sigma-Aldrich, St. Louis, MO, USA
Bromophenol blue	Sigma-Aldrich, St. Louis, MO, USA
Calcium chloride, $CaCl_2$	MERCK MILLIPORE, Merck KGaA, Darmstadt, Germany
Carbonyl cyanide *3*-chlorophenylhydrazone, CCCP	Sigma-Aldrich, St. Louis, MO, USA
CellLight® Early Endosomes-RFP	Molecular Probes®, life technologies™, Carlsbad, CA, USA
Casy® toner	Roche Diagnostics International AG, Basel, Swiss
Crystal violet solution	Sigma-Aldrich, St. Louis, MO, USA
Cy5	Abcam, Cambridge, UK
3,3´-Diaminobenzidine, DAB	DAKO Deutschland GmbH, Hamburg, Germany
Dimethylsulfoxid, DMSO	Carl Roth GmbH & Co. KG, Karlsruhe, Germany
Diethylene triamine pentaacetic acid, DTPA	FLUKA, Sigma-Aldrich, St. Louis, MO, USA
Dithiothreitol, DTT	Carl Roth GmbH & Co. KG, Karlsruhe, Germany
Disodium phosphate, Na_2HPO_4	Sigma-Aldrich, St. Louis, MO, USA
Western Lightning Plus ECL	PerkinElmar, Waltham, MA, USA

ER-Tracker™ Red (BODIPY® TR, glibenclamide)	Molecular Probes®, life technologies™, Carlsbad, CA, USA
Ethylenediaminetetraacetic acid, EDTA	Carl Roth GmbH & Co. KG, Karlsruhe, Germany
Epidermal growth factor, human, EGF	Sigma-Aldrich, St. Louis, MO, USA
Ethanol, EtOH	AppliChem, Inc., St. Louis, MO, USA
FITC Annexin V	BioLegend Inc., San Diego, CA, USA
Fluorescence Mounting Medium	DAKO Deutschland GmbH, Hamburg, Germany
FluoZin™-3, AM, cell permeant	Molecular Probes®, life technologies™, Carlsbad, CA, USA
Glutaraldehyde	Carl Roth GmbH & Co. KG, Karlsruhe, Germany
Glycine	Carl Roth GmbH & Co. KG, Karlsruhe, Germany
Glycerol	Carl Roth GmbH & Co. KG, Karlsruhe, Germany
ß-Glycerophosphate	Sigma-Aldrich, St. Louis, MO, USA
4-(2-Hydroxyethyl)piperazine-1-ethanesulfonic acid, HEPES	Sigma-Aldrich, St. Louis, MO, USA
2`,7`-dichlorodihydrofluorescein diacetate, H_2DFCDA	Molecular Probes®, life technologies™, Carlsbad, CA, USA
Hexane	AppliChem, Inc., St. Louis, MO, USA
Heat inactivated FCS	Sigma-Aldrich, St. Louis, MO, USA
High purity H_2O	Cayman Chemical Company, Ann Arbor, MI, USA
Hydrogen chloride	Sigma-Aldrich, St. Louis, MO, USA
Hydrogen peroxide (H_2O_2)	Sigma-Aldrich, St. Louis, MO, USA
Hämalaun solution	Carl Roth GmbH & Co. KG, Karlsruhe, Germany
Hydrocortisone	Sigma-Aldrich, St. Louis, MO, USA
Insulin	Sigma-Aldrich, St. Louis, MO, USA
Isopropyl alcohol	AppliChem, Inc., St. Louis, MO, USA
5,5′,6,6′-tetrachloro-1,1′,3,3′-tetraethylbenzimidazolocarbo-cyanine iodide, JC-1 dye	Molecular Probes®, life technologies™, Carlsbad, CA, USA
Leupeptin	Sigma-Aldrich, St. Louis, MO, USA
LR-white™	London Resin, London, UK
Methanol	AppliChem, Inc., St. Louis, MO, USA
MitoTracker® Deep Red FM	Molecular Probes®, life technologies™, Carlsbad, CA, USA
Monopotassium phosphate, KH_2PO_4	Sigma-Aldrich, St. Louis, MO, USA
N-acetyl-L-cysteine, NAC	Sigma-Aldrich, St. Louis, MO, USA
Paraformaldehyde, PFA	Sigma-Aldrich, St. Louis, MO, USA
PageRuler™ Prestained Protein Ladder	Thermo Scientific™, Carlsbad, CA, USA
Pepstatin	Sigma-Aldrich, St. Louis, MO, USA
Phosphate-buffered saline, PBS	Sigma-Aldrich, St. Louis, MO, USA
Propidium Iodide, PI	Abcam, Cambridge, UK
Picric acid	Riedel-de Haën, Sigma-Aldrich, St. Louis, MO, USA
Pluronic® F-127	Molecular Probes®, life technologies™, Carlsbad, CA, USA
Powdered milk	Carl Roth GmbH & Co. KG, Karlsruhe, Germany
Retinol	Sigma-Aldrich, St. Louis, MO, USA
Sodium dodecyl sulfate, SDS	Carl Roth GmbH & Co. KG, Karlsruhe, Germany
Sodium chloride, NaCl	Carl Roth GmbH & Co. KG, Karlsruhe, Germany
Sodium lauroyl sarcosinate	Sigma-Aldrich, St. Louis, MO, USA
Sodium azide, NaN_3	Carl Roth GmbH & Co. KG, Karlsruhe, Germany
Sodium acetate	Sigma-Aldrich, St. Louis, MO, USA
Sodium fluoride, NaF	Sigma-Aldrich, St. Louis, MO, USA

Sterillium® classic pure	Bode Chemie GmbH, Hamburg, Germany
Streptavidin/HRP	DAKO Deutschland GmbH, Hamburg, Germany
SYBR® Green	Applied Biosystems®, life technologies™, Carlsbad, CA, USA
Tocopherols	Sigma-Aldrich, St. Louis, MO, USA
TRIS buffered saline, TBS	Sigma-Aldrich, St. Louis, MO, USA
Tetramethylammonium hydroxide	Sigma-Aldrich, St. Louis, MO, USA
3,3',5,5'-Tetramethylbenzidine	Sigma-Aldrich, St. Louis, MO, USA
Transferrin	Sigma-Aldrich, St. Louis, MO, USA
Tris(hydroxymethyl)-aminomethane, TRIS	Carl Roth GmbH & Co. KG, Karlsruhe, Germany
Triton X-100	Sigma-Aldrich, St. Louis, MO, USA
Trypan Blue	Sigma-Aldrich, St. Louis, MO, USA
$Tween_{20}$	Carl Roth GmbH & Co. KG, Karlsruhe, Germany
Vectashield® Hard+Set™	Vector Laboratories, Inc., Burlingame, CA, USA
Zinc chloride	Sigma-Aldrich, St. Louis, MO, USA

Table 3: Consumables

Consumables	Manufacturer
Advanced TC Dish, Sterile, 60 x 15 mm	Greiner Bio-One GmbH, Frickenhausen, Germany
BD Falcon ™ cell scraber	BD Biosciences, Bedford, UK
Blotting paper	MACHEREY-NAGEL GmbH & Co. KG, Düren, Germany
Cell culture dishes cellstar® 96 well plate, black, 15MM REF 655090 µCLEAR®	Greiner Bio-One GmbH, Frickenhausen, Germany
ibiTreat, sterile, µ-Dish 35 mm, high	ibidi GmbH, Martinsried, Munich, Germany
TEM grids made of copper coated with carbon film	Plano GmbH, Wetzlar, Germany
ELISA microplate	Corning, Inc., Corning, NY, USA
Cell culture flask; 175 cm^2, 75 cm^2, 25 cm^2	Cellstar, Greiner, Frickenhausen, Germany
Microscope Cover Slip, 18x18 mm	IDL GmbH & Co KG, Nidderau, Germany
Microscope Cover Slip, ø10 mm	Gerhard Menzel GmbH, Braunschweig, Germany
Cryo tubes, Cryo. S™	Greiner Bio-One GmbH, Frickenhausen, Germany
Tubes, cellstar® tubes; 15 mL, 50 mL	Greiner Bio-One GmbH, Frickenhausen, Germany
Immobilon®-P-Transfer-Membran (PVDF; 0.45 µm)	Millipore Corporation, Billerica, MA, USA
Microcentrifuge tube (Eppendorf safe lock tube); 0.5 mL, 1.5 mL, 2.0 mL	Eppendorf AG, Hamburg, Germany
Nitrocellulose membrane	Immobilon®, Merck Millipore, Merck KGaA, Darmstadt, Germany
Parafilm „M"™ Laboratory Film	Pechiney, Chicago, IL, USA
Pipette, plastic disposable graduated	Carl Roth GmbH & Co KG, Karlsruhe, Germany
Pipette tip; 0.5 – 20 µL, 100 µL, 200 µL & 1000 µL	Kisker Biotech GmbH & Co. KG, Steinfurt, Germany
Protein low bind tubes; 0.5 mL, 1.5 mL	Eppendorf AG, Hamburg, Germany
Quali-PCR-Tube-Stripe	Kisker Biotech GmbH & Co. KG, Steinfurt, Germany
Serologic pipette cellstar®, 2.5 mL, 5 mL, 10 mL, 25 mL	Greiner Bio-One GmbH, Frickenhausen, Germany
6-well plate	Greiner Bio-One GmbH, Frickenhausen, Germany
Surgical blades	FEATHER Safety Razor Co., Ltd., Osaka, Japan
Tissue culture cup	Thermo Fischer Scientific (Nunc GmbH & Co. KG), Langenselbold, Germany
Tissue culture plate 96-well	Thermo Fisher Scientific (Nunc GmbH & Co.KG), Langenselbold, Germany

Welted glass	Carl Roth GmbH & Co. KG, Karlsruhe, Germany

Table 4: Culture media and sera

Material	Manufacturer
Dulbecco`s Modified Eagle`s Medium, DMEM	Sigma-Aldrich, St. Louis, MO, USA
Penicillin Streptomycin , P/S, (100 U/ml/100 µg/ml)	Sigma-Aldrich, St. Louis, MO, USA
Fetal Calfe Serum, FCS	Sigma-Aldrich, St. Louis, MO, USA
Trypsin/EDTA, T/E	Sigma-Aldrich, St. Louis, MO, USA
Trypsin inhibitor, DTI	Gibco®, life technologies™, Carlsbad, CA, USA
StemPro® Accutase® Cell Dissociation Reagent	Gibco®, life technologies™, Carlsbad, CA, USA
CnT-Prime Epithelial Cell Culture Medium	CellnTec, Geneva, Swiss

Table 5: Buffer and solutions

Buffer	Composition
10x TBS buffer	24.2 g Tris 80 g NaCl Distilled water pH 7.6 (with 10 mM HCl)
Transferring buffer	25 mM Tris 150 mM Glycine 10 % Methanol 0.037 % SDS Distilled water
1x $TBST_{20}$-washing buffer	10x TBS 0.1 % Tween $_{20}$ Distilled water
Blocking buffer	3 %, 5 % powdered milk (w/v) 1x $TBST_{20}$–washing buffer
First antibody solution	3 %, 5 % BSA (w/v) 1x $TBST_{20}$-washing buffer
Second antibody solution	3 %, 5 % powdered milk or BSA 1x $TBST_{20}$-washing buffer
4x stacking gel buffer	0.5 M Tris Distilled water pH 6.8 (with 10 mM HCl)
4x resolving gel buffer	1.5 M Tris Distilled water pH 8.8 (with 10 mM HCl)
5x running buffer	30 g/L Tris 144 g/L Glycine Distilled water
1x running buffer	5x running buffer 10 % SDS Distilled water
Stripping buffer	25 mM Glycine Distilled water pH 2.2 (10 mM HCl)
4x lysis buffer	2 M Tris 0.08 g SDS 460 µL Glycine (87 %) 2.5 M DTT Distilled water ad 40 mL pH 6.8 – 7.5 (with 10 mM HCl)
1x lysate buffer	4x lysate buffer Distilled water
Cell culture buffer	100 mM NaCl 10 mM Tris Distilled water pH 7.4 (with 10 mM HCl)

Cell staining buffer	PBS 2 % heat inactivated FCS 0.09 % NaN_3
10x Annexin V Binding buffer	100 mM HEPES 1.4 M NaCl 25 mM $CaCl_2$ Distilled water pH 7.4 (with 10 mM HCl)
1x Annexin V Binding buffer	10x Annexin V Binding Buffer Distilled water
ELISA Wash buffer	0.05 % $Tween_{20}$ PBS pH 7.2 - 7.4 (with 10 mM HCl)
ELISA Blocking buffer	1 % BSA 0.05 % NaN_3 PBS pH 7.2 - 7.4 (with 10 mM HCl)
IC Diluent #1	1 % BSA PBS pH 7.2 - 7.4 (with 10 mM HCl)
IC Diluent #4	1 mM EDTA 0.05 %Triton X-100 PBS pH 7.2 - 7.4 (with 10 mM HCl)
ELISA Lysis buffer #13	1 mM EDTA 0.5 % Triton X-100 10 µg/mL Leupeptin 10 µg/mL Pepstatin 3 µg/mL Aprotinin 150 mM NaCl 10 mM NaF 20 mM ß-glycerophosphate PBS pH 7.2 - 7.4 (with 10 mM HCl)
ELISA Substrate Solution	1:1 H_2O_2 und Tetramethylbenzidine
Stop Solution	2 N H_2SO_4
Sørensen buffer	0.1 M Na_2HPO_4 0.1 M KH_2PO_4 Distilled water pH 7.4 (with 10 mM HCl)
BSA-T-PBS buffer	1 % BSA (w/v) 0.2 %Triton X-100 (v/v) PBS
Fixation buffer	4 % Paraformaldehyde 0.1 % Glutardialdehyde 0.2 % Picric acid in 0.1 M Sørensen buffer
Stripping buffer	25 mM Glycine 1 % SDS Distilled water pH 2.2 (with 10 mM HCl)
1 % BSA /PBS	1 % BSA (w/v) 0.1 % NaN_3 PBS
5 % BSA/PBS	5 % BSA (w/v) 0.1 % NaN_3 PBS
Crystal violet dilution	0,2 % Crystal violet PBS
10 % acetic acid	10 % Acetic acid Distilled water
10x TBS	302,85 g Tris 430,50 g NaCl 4 L Distilled water pH 7.6 (with 10mM HCl)
5 % $Tween_{20}$	25 mL $Tween_{20}$ 475 mL Distilled water
TBS/$Tween_{20}$	200 mL 10x TBS 20 mL 5 % $Tween_{20}$ Distilled water pH 7.6 (with 10mM HCl)

FAD complete medium	150 mL DMEM 40 mL FCS (20 %) 4 mL P/S (2 %) 2 mg/mL Hydrocortisone 1 mg/mL Transferrin 1 mg/mL Insulin 100 µg/mL Tocopherol 1 mg/mL Retinol 200 µg/mL EGF 1 M HEPES (2 %)

Table 6: Antibodies

Antibody	Species	Application	Block-ing	(kDa)	Detection	SDS-page	Manufacturer
pH2A.X (Ser139), clone JBW301, #05-636	Mouse	1:500 in PBS with 0.3 % Triton X-100, 1 h at RT	5 % BSA/PBS, 0.3 % Triton X-100, 1 h at RT	139	ECL+	10 %	MERCK MILLIPORE, Merck KGaA, Darmstadt, Germany
pH2A.X (Ser139) (20E3) #9718	Rabbit	1:1000 in 3 % BSA, overnight at 4°C	3 % MP	15	ECL +	12.5 %	Cell Signaling Inc., Danver, MA, USA
pChk2 (Thr68) #2661	Rabbit	1:1000 in 3 % BSA, overnight at 4°C	3 % MP	62	ECL +	12.5 %	Cell Signaling Inc., Danver, MA, USA
Chk2 #2662	Rabbit	1:1000 in 3 % BSA, overnight at 4°C	3 % MP	62	ECL +	12.5 %	Cell Signaling Inc., Danver, MA, USA
pChk1 (Ser296) #2349	Rabbit	1:1000 in 3 % BSA, overnight at 4°C	3 % MP	56	ECL +	12.5 %	Cell Signaling Inc., Danver, MA, USA
p53 #P5813	Mouse	1:500 in 3 % BSA, overnight at 4°C	3 % MP	53	ECL +	12.5 %	Sigma-Aldrich, St. Louis, Missouri, USA
p21 Waf1/Cip1 (DCS60) #2946	Mouse	1:2000 in 3 % BSA, overnight at 4°C	3 % MP	21	ECL +	12.5 %	Cell Signaling Inc., Danver, MA, USA
pATR (Ser428) #2853	Rabbit	1:1000 in 3 % BSA, overnight at 4°C	3 % MP	300	ECL +	5 %	Cell Signaling Inc., Danver, MA, USA
ATR #2790	Rabbit	1:1000 in 3 % BSA, overnight at 4°C	3 % MP	300	ECL +	5 %	Cell Signaling Inc., Danver, MA, USA
pErk1(T202/Y204)/Erk2 (T185/Y187)	Rabbit	0.5µg/mL in 3 % BSA, overnight at 4°C	3 % MP	44	ECL +	12.5 %	R&D Systems, Minneapolis, MN, USA
pAkt (Ser473) Antibody #9271	Rabbit	1:1000 in 3 % BSA, overnight at 4°C	3 % MP	60	ECL +	12.5 %	Cell Signaling Inc., Danver, MA, USA
ß-actin Antibody	Mouse	1:10000 in 5 % MP, 1 h at RT	5 % MP	42	ECL +	-	Abcam, Cambridge, UK
Anti-mouse IgG, HRP-linked #7076	Horse	1:5000 in 5 % BSA, 1 h at RT	Secondary antibody			-	Cell Signaling Inc., Danver, MA, USA
Anti-rabbit IgG, HRP-	Goat	1:5000 in 5 % BSA, 1	Secondary antibody			-	Cell Signaling Inc., Danver, MA, USA

linked #7074		h at RT			
Alexa Fluor® 488 Goat Anti-Mouse IgG #A-11029	Goat	1:500 in 5 % BSA/PBS with 0.3 % Triton X-100, 1 h at RT	Secondary antibody	-	Molecular Probes®, life technologies™, Carlsbad, CA, USA
Anti-Cytoceratin 13 #ab92551	Rabbit	1:100 in PBS/BSA overnight at 4°C	Primary antibody	-	Abcam, Cambridge, UK
Anti-FGFR4 #44971	Mouse	1:50 in PBS/BSA overnight at 4°C	Primary antibody	-	Abcam, Cambridge, UK
Polyclonal Goat Anti-Rabbit #E0432	Goat	1:300 in PBS/BSA	Secondary antibody	-	DAKO Deutschland GmbH, Hamburg, Germany
Phospho-ATM (S1981) Capture Antibody #841928	Kit System			-	R&D Systems, Minneapolis, MN, USA
Phospho-ATM (S1981) Detection #841929 Antibody	Kit System			-	R&D Systems, Minneapolis, MN, USA
Phospho-ATM (S1981) Standard #841930	Kit System			-	R&D Systems, Minneapolis, MN, USA
Streptavidin-HRP #890803	Kit System			-	R&D Systems, Minneapolis, MN, USA

Table 7: SDS-page

SDS-page	Composition
5 % resolving gel	7. 5 mL 4x resolving gel buffer 3.75 mL 40 % AA/BIS 150 µL 10 % APS 379 µL 10 % SDS 15 µL TEMED 18.75 mL Distilled water
10 % resolving gel	7. 5 mL 4x resolving gel buffer 7.5 mL 40 % AA/BIS 150 µL 10 % APS 379 µL 10 % SDS 15 µL TEMED 15 mL Distilled water
12.5 % resolving gel	7. 5 mL 4x resolving gel buffer 9.4 mL 40 % AA/BIS 150 µL 10 % APS 379 µL 10 % SDS 15 µL TEMED 13.1 mL Distilled water

Table 8: Commercial available Kit systems

Kit systems	Manufacturer
Bio-Rad DC™ Protein assay	Bio-Rad Laboratories, Inc., Hercules, CA, USA
Human Phospho-ATM (S1981) DuoSet IC #DYC1655-2	R&D Systems, Minneapolis, MN, USA

Table 9: Cell lines

Cell line	Manufacturer
A549	American Type Culture Collection (ATCC), Manassas, VA, USA
NIH/3T3	American Type Culture Collection (ATCC), Manassas, VA, USA
HNSCCUM-02T	ENT department of University Medical Center, Mainz, Germany

Table 10: Software

Software	Reference/Manufacturer/Homepage
Blender 2.75a	Blender Foundation, Amsterdam, Netherlands
GraphPad Prism 5	GraphPad Software, Inc., La Jolla, CA, USA
Adobe Photoshop CS4	Adobe Systems GmbH, Munich, Germany
Citavi 4	Swiss Academic Software GmbH, Wädenswil, Switzerland
Image J 1.47f	NIH, Bethesda, MA, USA
Microsoft Office 2003/2007	Microsoft Deutschland GmbH, Unterschleißheim, Germany
LAS AF lite	Leica Camera, Solms, Germany
FlowJo 7.6.3	FlowJo, LLC, Ashland, OR, USA
ACD/ChemSketch 2012 v. 14.01	Advanced Chemistry Development, Inc. (ACD/Labs), Toronto, ON, Canada

3.2 Methods

3.2.1 Synthesis of ZnO nanoparticles

The ZnO NP were synthesized by the [redacted]. Two different sizes of ZnO NP (4-5 nm and 15-18 nm) were used in this study. ZnO NP in a size of 15-18 nm were synthesized with slight modifications, following a procedure reported by *Cheng et al. (2006)*[206]. $Zn(Ac)_2$ x 2 H_2O (1.09 g) was dissolved in 10 mL of methanol. Tetramethylammonium hydroxide (25 % w/w) in water and tetramethyl-ammonium hydroxide (25 % w/w in methanol) were added in a ratio of 1 to 3 (total volume of 20 mL) under stirring conditions at RT. The solution was transferred to a teflon-lined stainless steel autoclave and heated to 50°C for 24 h. The white precipitate was collected and purified by washing with high purity H_2O and dried afterwards at RT. ZnO NP in a size of 4-5 nm were synthesized using a procedure developed and reported by *Tahir et al. (2009)*[207]. A batch of ZnO colloids was synthesized by dissolving 110 mg (0.5 mM) of $Zn(AC)_2$ x 2 H_2O in 25 mL of ethanol (EtOH) with sonication at 0°C for 15 min. 21 mg (0.5 mM) of Li(OH) x H_2O were added to ZnO colloid solution and sonicated at 0°C for 15 min. The solvent of the obtained stable and optically transparent ZnO solution was removed using a vacuum rotary evaporator. Then ZnO NP were redispersed in high purity H_2O and dialysed against H_2O to remove excess of base Li(OH).

3.2.2 Analytical characterization of ZnO NP

The particles were characterized by transmission electron microscopy (TEM), ζ-potential and atomic absorption spectroscopy (AAS).

3.2.2.1 Transmission electron microscopy

The size and shape of the ZnO NP were determined using TEM with an acceleration voltage of 120 kV. Samples were prepared by dropping ZnO NP in high purity H_2O on a TEM grid.

3.2.2.2 ζ-potential measurement

Nanoparticles possess a specific positive or negative electrostatic charge with influence on cellular particle uptake. The measurement of the ζ-potential of the ZnO NP was

performed using a Zetasizer. The ZnO NP dispersion was applied to a disposable capillary cell and the particles migrated in the applied electrical field. 1 mL aliquots of each sample were injected into the capillary cell and 5−10 measurement per sample were performed at 25°C.

3.2.2.3 Atomic absorption spectroscopy

The atomic absorption spectroscopy (AAS) is a spectroanalytical method using the absorption of light by free atoms in the state of gas to quantify chemical elements (e.g., Zn). ZnO NP (4-5 nm, 15-18 nm) were prepared in high purity H_2O (pH 5.8) or in cell culture medium (pH 7.4) as mentioned below (see 3.2.4.1). A 50 mL tube was filled with 35 mL of high purity H_2O and another with 35 mL cell culture medium. ZnO NP were diluted in high purity H_2O to a final concentration of 100 µg/mL. 5 mL of each tube were transferred to another tube and centrifuged at 12,000x*g* for 5 min. 4 mL of the supernatants were transferred to a welted glass after 1 min, 5 min, 15 min, 30 min, 1 h and 4 h. Solutions were stored at RT on a rocking platform shaker until analysis. The dissociated Zn were measured using AAS at the [redacted].

3.2.3 Cell culture

3.2.3.1 Cell lines and conditions

Three different cell lines and primary cells of mucosa were used. A549 is an adenocarcinomic human alveolar epithelial-like type-II cell line that has been established in 1979 after removal of cancerous lung tissue of a 58 years old Caucasian male. NIH/3T3 cells have been established in 1962 from swiss albino mouse embryo tissue and are used as standard model for fibroblasts. HNSCCUM-02T is a human squamous cell carcinoma cell line from the base of the tongue, which has been established 2003 from *Welkoborsky et al. (2003)* in the lab of the [redacted][208]. The primary cells of mucosa were isolated from the gingiva of patients operated at the [redacted] and cultivated at the [redacted].

The cells were maintained in cell culture medium using *Dulbecco´s Modified Eagles´s Medium* (DMEM), supplemented with 5 % fetal calf serum (FCS) and 1 % penicillin/streptomycin (P/S). All used cell lines were cultivated at 37°C, 5 % CO_2, and

humidified atmosphere. For detailed cultivation conditions of cell lines please refer to 3.2.3.2 and for primary cells of mucosa 3.2.3.5, and 3.2.3.6.

3.2.3.2 Cell line cultivation

The culture medium was replaced every second day. After confluence of 80 %, cells were splitted for further cultivation. For passaging of A549, NIH/3T3, and HNSCCUM-02T cells, Trypsin/EDTA (T/E) was used (1:10 dilution). The confluent cells were rinsed with phosphate-buffered saline (PBS) and 2 mL of the ready to use mixture of T/E was added and incubated at 37°C until the cells were detached. Cells were transferred to a 15 mL tube and culture medium was added in a 1:1 ratio. Afterwards, cells were centrifuged at 300x*g* for 5 min. Supernatant was discarded and the cell pellet resuspended in 5 mL cell culture medium. In order to determine the cell amount, 20 µL of the cell suspension was mixed with 20 µL of trypan blue (1:1 ratio) and counted in a hemycytometer. The cells were systematically counted under a microscope. The total number of viable cells in the prepared cell suspension was calculated using the following formula:

$$\text{Total number of viable cells} = \left(\frac{A}{B}\right) \times C \times D \times E$$

Formula 1: Calculation of total cell counts

A: viable cells; B: number of squares; C: dilution factor (2); D: volume of cell suspension; E: chamber factor (10,000)

3.2.3.3 Viability measurement with CASY TT®

Viability was measured by the use of CASY TT®, an electric field multi-channel cell counting system. CASY TT® measures cell amount, cell size and cell viability and is based on a pulse surface analysis. The cells were sucked with a constant speed into a capillary between to electrodes. The magneto-resistance of the capillary equates to the cell volume. The cell membrane of a dead or injured cell is more permeable than those of an intact cell and causes less change in magneto-resistance. The cells were treated with 100 µg/mL ZnO NP. The cellular viability of the cells was determined after 24 h of ZnO NP exposure or BSA stabilized ZnO NP (see 3.2.4). After incubation cells were trypsinized and centrifuged at 450x*g* for 8 min. The cells were resuspended with 750 µL cell culture medium. Afterwards, 4 tubes with 10 mL of CASY-toner were supplied with 200 µL (50:1) cell suspension of each time point and were measured by CASY TT®.

3.2.3.4 Freezing and thawing procedure of cells

Freezing: The cells were washed with PBS and detached from cell culture flask as mentioned above (see 3.2.3.2). After detaching, cells were centrifuged and the supernatant was replaced by FCS containing 10 % dimethyl sulfoxide (DMSO). The cell pellet was resuspended and 1 mL (approx. $1x10^6$ cells) was transferred to cryo tubes. Then, the cryo tubes were stored at -80°C overnight and finally transferred into liquide nitrogen.

Thawing: Frozen cells, were thawed in a 37°C tempered water bath and resuspended in prewarmed fresh cell culture medium. Afterwards, cells were centrifuged at 300x*g* and the pellet was resuspended in fresh cell culture medium before the cells were cultivated at 37°C and 5 % CO_2.

3.2.3.5 Isolation of primary cells of mucosa from gingiva

Before starting with cell isolation the fresh mucosa tissue was slewed for 1 min each in 70 % EtOH, Sterillium® classic pure and again in EtOH. First, the connective tissue was separated from the epithelial layer by cutting at the line between red (connecting tissue) and white (epithelial layer) tissue. Afterwards, the fresh tissue pieces were transferred with the epithelial layer up into a 6-well plate and covered with 1 mL of FAD complete medium.

3.2.3.6 Cultivation of primary cells of mucosa

After 24 h, the FAD complete medium of the epithelial cells was replaced by CnT-Prime medium (specialized medium for epithelial cells). The tissue was incubated and cultivated at 37°C and 5 % CO_2 until epithelial cells covered 70 % of the well. Then, the medium was discared and the cells were incubated with T/E for 5 min. Afterwards, the cells were transferred to a tube with DMEM and a trypsin inhibitor (DTI) was added at RT for 5 min to neutralize the T/E reaction. The cell suspension was centrifuged at 300x*g* for 5 min. Supernatant was removed and the pellet was resuspended in cell culture medium and counted as mentioned in 3.2.3.2 and afterwards prepared for further experiments.

3.2.4 Pretreatments and treatments with ZnO NP, ZnO bulk, and $ZnCl_2$

3.2.4.1 Preparation of ZnO NP, ZnO bulk, and $ZnCl_2$ dispersion

The synthesized ZnO NP, ZnO bulk material or $ZnCl_2$ were weighted on the day of experiment and suspended in high purity H_2O to get a stock concentration of 1 mg/mL. The ZnO NP, ZnO bulk dispersions, and $ZnCl_2$ solutions were sonicated using an ultrasonic homogeniser for 5 min at 32 W. The cells were treated immediately with a final concentration of 0.1 µg/mL, 10 µg/mL or 100 µg/mL. The concentrations were chosen according to values measured in sun protection (up to 100 mg/mL[209]) and drinking water (10 µg/mL[210]) of daily used products.

3.2.4.2 Pretreatment with DTPA

Diethylene triamine pentaacetic acid (DTPA) was used as a chelator of Zn^{2+}, released from extracellular dissociated ZnO NP. Cells were seeded in 6-well plates and incubated at 37°C and 5 % CO_2 for 24 h. The next day, cells were pretreated with 0.06 mM DTPA for 1 h before ZnO NP were added (see 3.2.4.1).

3.2.4.3 Pretreatment with NAC

N-acetyl-L-cysteine (NAC) was used to scavenge reactive oxygen species (ROS). After seeding, the cells were incubated at 37°C and 5 % CO_2 for 24 h. The culture medium was replaced with fresh cell culture medium containing 5 mM NAC. After another 24 h of incubation the cells were incubated with cell culture medium containing NAC (5 mM) and ZnO NP in a final concentration of 100 µg/mL (see 3.2.4.1).

3.2.4.4 Stabilization of ZnO NP with BSA

Bovine serum albumin (BSA) was used for ZnO NP stabilization. A stock solution of BSA (5 mg/mL) in high purity H_2O was prepared. 20 mg of ZnO NP were weighted and incubated in 1 mL of a BSA stock solution at 4°C for 1 h. After incubation, the dispersion was sonicated using an ultrasonic homogeniser at 32 W for 5 min. Afterwards, the ZnO NP dispersion was centrifuged at 12,000x*g* for 10 min and the supernatant was replaced by high purity H_2O. This step was repeated three times. The BSA coated ZnO NP were used as described above (see 3.2.4.1).

3.2.4.5 Cell incubation with ZnO NP, ZnO bulk, and $ZnCl_2$

ZnO NP, ZnO bulk or $ZnCl_2$ were weighted on the day of experiment and suspended in high purity H_2O with a final concentration of 0.1, 10 or 100 µg/mL. The ZnO NP, ZnO bulk or $ZnCl_2$ dispersion was sonicated using an ultrasonic bath at 32 W for 5 min. The cells were treated directly with ZnO NP, ZnO bulk or $ZnCl_2$ for several minutes up to maximal 24 h depending on the performed assay. Further details are mentioned in the corresponding chapter.

3.2.5 Analysis of cellular ZnO NP uptake

3.2.5.1 TEM analysis of cellular ZnO NP uptake

For the ultra structural analysis of ZnO NP uptake, A549 cells were treated with ZnO NP (100 µg/mL; exposure time 1 min, 15 min, 30 min, 1 h and 4 h) and analyzed by TEM. After treatment, cells were centrifuged at 300x*g* for 5 min and the pellet was washed with PBS. This step was repeated three times. Afterwards, cell pellets were incubated for 15 min in fixation buffer and washed two times for 5 min in 0.1 M Sørensen buffer. Cells were dehydrated in a concentration series of ethanol (70 %, 80 %, 90 %, and 99.5 %), for 5 min, each. Afterwards, they were embedded for 10 min in a 1:1 suspension of 99.5 % ethanol and LR-White™ and further two times for 30 min in LR-White™. After embedding the pellets were then polymerised at 58°C overnight. Finally, ultrathin slides were prepared (approx. 80-100 nm) and the intracellular accumulation of ZnO NP was evaluated by TEM.

3.2.5.2 Measurement of intracellular Zn^{2+}

The free intracellular Zn^{2+} concentration after ZnO NP or $ZnCl_2$ treatment was monitored by spectrofluorimetric analysis as well as by cLSM using a Zn^{2+} specific fluorophore, FluoZin™-3 (dissociation constant (kd) of FluoZin™-3: ~ 15 nM).

3.2.5.2.1 Cell loading with FluoZin™-3

The cells were preloaded with 1 µM (FluoZin™-3 diluted in DMSO) of the cell permeable acetoxymethoxy derivate of FluoZin™-3 in 2 mL cell culture buffer in the dark at RT for 45 min.

3.2.5.2.2 Spectrofluorimetric measurement of intracellular Zn^{2+}

After 45 min of incubation, cells (appox. $1x10^6$) were washed, trypsinized, centrifuged and resuspended in 3 mL of cell culture buffer. The cell suspension was stored in the dark at RT for 30 min to allow cleavage of the acetoxymethyl (AM) ester. Afterwards, the changed intensity of FluoZin™-3 after binding to Zn^{2+} was measured by a spectrofluorometer at 494 nm (Ex) and 514 nm (Em). After 5 min of basal level measurement, ZnO NP were injected in a final concentration of 100 µg/mL. F_{max} was determined by incubation with 10 mM $ZnCl_2$ and F_{min} by complexation of free Zn^{2+} by the use of 100 µM EDTA. The intracellular Zn^{2+} concentration was then calculated using the following formula:

$$[Zn^{2+}] = kd \times \frac{(F - F_{min})}{(F_{max} - F)}$$

Formula 2: Calculation of intracellular Zn^{2+} concentration

kd: dissociation constant; F: denotes fluorescence intensity measured at a single wavelength; F_{min}: zero reference level of fluorescence; F_{max}: maximal reference level of fluorescence.

3.2.5.2.3 Confocal laser scanning microscopy

The confocal laser scanning microscopy (cLSM) facilitates the analysis and visualization of processes in living cells. The light or fluorescence microscopy is based on parallel pixel generation, while the cLSM creates each pixel separately. The cLSM uses point illumination and the light from the focus plane is conducted to the detectors by the detector pinhole **aperture**. Between the detectors and the pinhole aperture resides the fluorescence barrier filter which enables the detection of different wavelength depending on the fluorophore that is linked to the analyzing sample. The biological sample became scanned from the laser beam line by line in xy-direction. The generated fluorescence was then measured with detectors (photomultipliers) pixel by pixel. With this method a sharp image at a single focal plane of a sample can be excited (see Figure 8). Advantages of cLSM in cell live imaging are the high resolution, the depth in focus, and the visualization of 3D structures. It is possible to measure simultaneous several fluorescence dyes simultaneously co-localization experiments that can be calculated quantitatively.

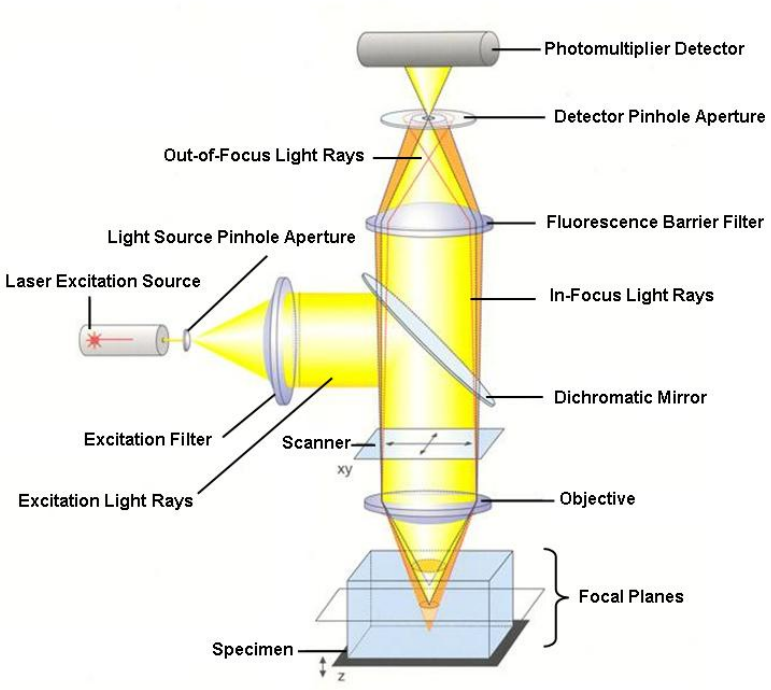

Figure 8: Setup of confocal laser scanning microscope

The cLSM permits 3D localization of labeled target molecules in cells. The principle of this method is described in 3.2.5.2.3. (adapted from:[211,212]).

3.2.5.2.4 Preparation of cLSM samples

200,000 cells were seeded in an ibiTreat cell culture dish and incubated overnight at 37°C and 5 % CO_2. The cells were stained with an organelle tracker (see 3.2.5.2.5, 3.2.5.2.6, and 3.2.5.2.7) followed with the replacement of medium by 2 mL cell culture buffer including 1 µM FluoZin™-3 (see 3.2.5.2.1). After 5 min of basal level measurement, ZnO NP or $ZnCl_2$ were injected at a final concentration of 100 µg/mL. Afterwards, the changed intensity of FluoZin™-3 after binding to Zn^{2+} was measured and documented by cLSM over a period in time of 60 min. Fluorescence was excited at 488 nm and detected in the spectral range of 505-600 nm using hybrid detector.

3.2.5.2.5 MitoTracker® Deep Red FM

The mitochondria were labeled using MitoTracker® Deep Red FM, which contains a thiol-reactive chloromethyl moiety for specific targeting. The cells were pretreated with 500 nM MitoTracker® at 37°C and 5 % CO_2 for 45 min. After incubation, the cells were rinsed three times with cell culture buffer, prior loading with FluoZin™-3 (see 3.2.5.2.1). After further washing steps (3x 5 min) with cell culture buffer, cLSM measurement started.

Table 11: cLSM settings of FluoZin™-3 and MitoTracker® Deep Red FM

	Dye	Laser (Em)	Laser line (Ex)	Line-/Frame-average
Sequential setting 1	FluoZin™-3	PMT 2 (505 nm – 600 nm)	8 % (488)	8/1
Sequential setting 2	MitoTracker® Deep Red FM	PMT 3 (656 nm- 739 nm)	8 % (633)	

3.2.5.2.6 ER-Tracker™ Red (glibenclamide BODIPY® TR)

The endoplasmatic reticulum (ER) was stained using ER-Tracker™ Red. The dye is a drug conjugate of glibenclamide BODIPY® TR. Glibenclamide is able to bind directly to the sulphonylurea receptor of ATP-sensitive K^+ channels localized on the ER. Cells were pretreated with 1 µM ER-Tracker™ Red at cell culture conditions for 45 min. Afterwards the cells were washed three times with cell culture buffer and loaded with FluoZin™-3 (see 3.2.5.2.1). After three washing steps for 5 min with cell culture buffer, cLSM measurement started.

Table 12: cLSM settings of FluoZin™-3 and ER-Tracker™ Red

	Dye	Laser (Em)	Laser line (Ex)	Line-/Frame-average
Sequential setting 1	FluoZin™-3	HyD 2 (505 nm – 550 nm)	8 % (488)	8/1
Sequential setting 2	ER-Tracker™ Red	HyD 4 (587 nm - 631 nm)	8 % (561)	

3.2.5.2.7 CellLight® Reagent *BacMam 2.0* - early endosomes

The used BacMam technology avails an insect cell virus (baculovirus), which is linked to a mammalian promoter. The CellLight® reagent for early endosomes is a fluorescent protein-signal peptide regulated by a promoter fused to the Rab5a sequence targeting the early endosomes. 200,000 cells in 2 mL medium were treated with CellLight®, according to the manufacturer´s data sheet. For one cell, 30 particles of the CellLight® Reagent were used. The cells were incubated with 12 µL CellLight® Reagent at 37°C and 5 % CO_2 for 20 h. Afterwards, cells were washed three times with cell culture buffer and labeled with FluoZin™-3 as mentioned before (see 3.2.5.2.1). Then the cells were wasched with cell culture buffer (3x for 5 min), before cLSM measurement started. Transfection efficiencies were between 30 and 40 %.

Table 13: cLSM settings of FluoZin™-3 and CellLight® Reagent *BacMam 2.0* - early endosomes

	Dye	Laser (Em)	Laser line (Ex)	Line-/Frame-average
Sequential setting 1	FluoZin™-3	PMT 2 (500 nm – 560 nm)	5 % (488)	16/1
Sequential setting 2	CellLight® Reagent *BacMam 2.0* - early endosomes	PMT 3 (580 nm - 633 nm)	15 % (561)	

3.2.6 Flow cytometry

Flow cytometry facilitates rapid analysis of optical and fluorescence characteristics of single cells counted in a fluidic stream by a laser and electronic detection hardware. This technique provides simultaneous analysis of physical properties such as cell size and granularity as well as bound or intercalated fluorescence conjugated molecules of thousands of cells per second[213,214]. These features are dissected using an optical-to-electronic coupling system that observed the cell scatters incident laser light and emitted fluorescence (BD Bioscience learning guide). The single cell suspension, in a hydrodynamic focused stream, is percolated by a laser of a single wavelength. The laser excites the electrons of the fluorescent dye to an advanced energy level. Afterwards, the electrons decline to their basal level under release of energy in terms of photons. The value of emitted photons recorded by a photon detector is proportional to the value of labeled molecules or antibodies per cell. The forward scatter (FSC) detector is in line

with the laser beam and its magnitude is roughly proportional to the cell size and volume. The side scatter (SSC) detector gives information about the granularity and complexity of the cell. The contemporaneous measurement of several fluorescence dyes is possible, if the used dyes became excited by the same laser (Argon laser, 488 nm) but emitted differentially at the specific emission spectra of the dye. If the emission spectra of the used dyes overlap, the signal of the detectors has to be compensated in order to avoid wrong positive or negative results.

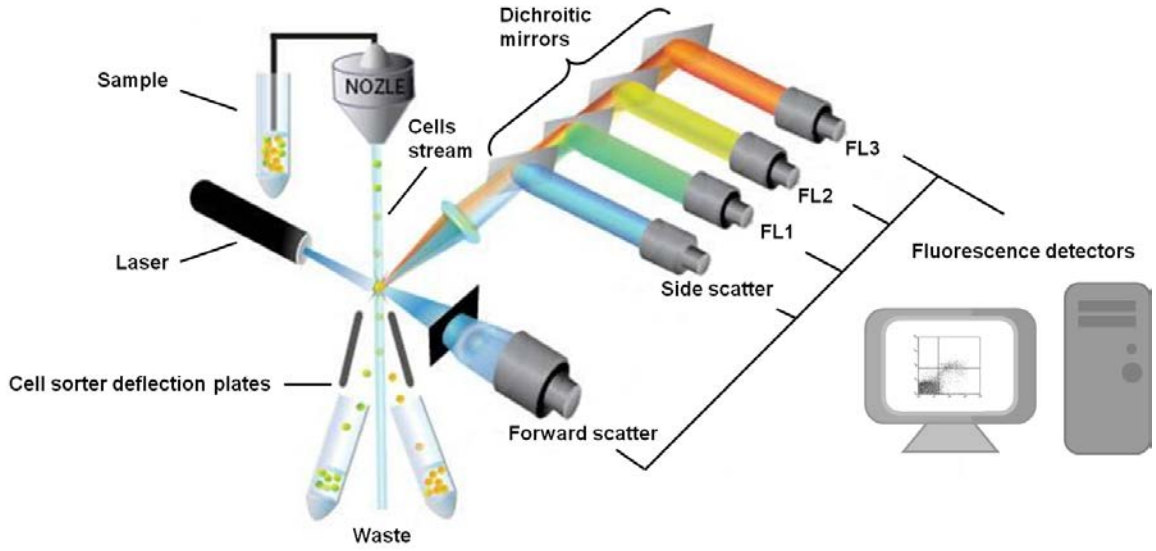

Figure 9: Setup of flow cytometer

The sample becomes hydrodynamic focused in a liquid stream and disposed to laser of a single wavelength. The incidental fluorescent and scattered light is conducted by dichroitic mirrors and optical filters to photomultipliers. The detectors convert this energy to electric signals that can be analyzed (adapted from:[215]).

3.2.6.1 Analysis of apoptosis and necrosis

Specific changes in the plasma membrane can be described as early events of apoptosis. In this state of apoptosis, phosphatidylserine (PS) lost its asymmetric distribution across the phospholipid bilayer and is translocated from the inner leaflet of the plasma membrane to the extracellular leaflet at the cell surface[216,217]. This process marks the cell for phagocytosis. Annexin V belongs to a family of calcium-dependent phospholipid-binding proteins which preferentially bind to PS and can be used as fluorescence marker, in a calcium dependent manner[217,218]. The described translocation of PS occurres as well during necrosis, but in case of necrosis the cell membrane loses integrity. Therefore, apoptosis and necrosis can be differentiated by the use of propidium iodide (PI) staining the DNA in necrotic cells (see Figure 10).

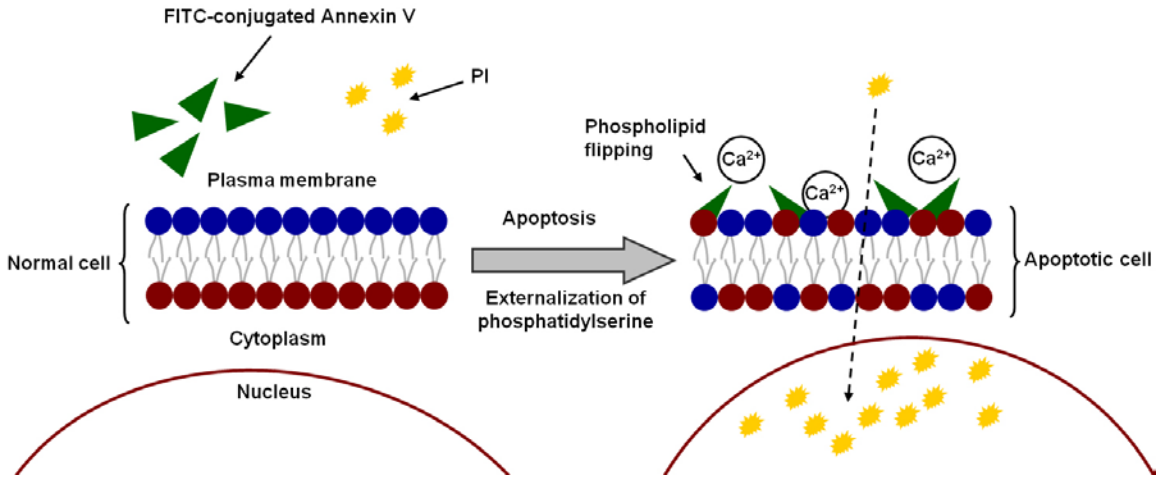

Figure 10: Schematic illustration of apoptosis and necrosis detection using Annexin V

Reorganization of plasma membrane develops in the early process of apoptosis. Annexin V stained cells that are used to indicate cell membrane changes. The early initiation of apoptosis disrupted the characterized cell surface phospholipid asymmetry. Then the phosphatidylserine, presented in the inner cell membrane, migrates through the plasma membrane. Annexin V specifically bound to phosphatidylserine in the presence of protein-dependent Ca^{2+} representing the early apoptotic process (adapted from: [219]).

To analyze, if the treatment of ZnO NP initiates apoptosis or necrosis, 650,000 cells per flask were counted, seeded and incubated overnight for adherence. Afterwards, cells were treated with ZnO NP (15-18 nm) with a final concentration of 100 µg/mL for 1 min, 15 min, 30 min, 1 h, 2 h, 3 h, 4 h, 5 h and 6 h. The staining of apoptosis was controlled by FITC Annexin V and necrosis by PI, respectively. After incubation, the medium was gathered in a tube and PBS after cells washing, respectively. Cells were detached using 1 mL StemPro® Accutase® Cell Dissociation Reagent for 5 min at 37°C. The cells were centrifuged for 5 min at 300x*g*, then the supernatant was discarded and the pellet was washed for two times with cell staining buffer. The cells were resuspended in 100 µL 1x Annexin V Binding Buffer containing 5 µL FITC Annexin V and 10 µL PI and were incubated at RT in the dark for 15 min. Prior to the measurement, 400 µL of the 1x Annexin V Binding Buffer were added to the cells. The cells were analyzed by the use of a flow cytometer with wavelength at 488 nm and emission wavelength for FITC at 518 nm and PI between 562 and 588 nm. FACS analysis was performed with a BD FACS Canto II apparatus and data were analyzed by using the FlowJo 7.6.3 software.

3.2.7 Fluorimetric assays

3.2.7.1 ROS Assay

The generation of reactive oxygen species (ROS) at different points in time was assessed in A549 cells using 2,7-dichlorofluorescin diacetate (H_2DFCDA). The non-fluorescent compound H_2DCFDA is de-esterified and oxidized in presence of ROS to fluorescent 2´,7´- dichlorofluorescein (DCF). ROS generation was studied by fluorimetric analysis analogous the publication of *Wan et al. (1993)*[220]. Cells (200,000 per well) were seeded in 6-well plates and allowed them to adhere for 24 h. Five different treatments were investigated: single treatment with ZnO NP, $ZnCl_2$, ZnO NP + NAC, ZnO NP + DTPA, and ZnO NP + BSA (see 3.2.4.1, 3.2.4.2, 3.2.4.3, 3.2.4.4, and 3.2.4.5). As positive control of ROS, 500 nM and 1 mM of H_2O_2 were used and the cells were incubated with H_2O_2 in cell culture medium until the end of measurement. The cells were incubated with H_2DCFDA (100 µM) at 37°C for 30 min. The reaction mixture was removed and the cells were washed with 2 mL PBS. Afterwards, the cells were covered with 2 mL cell culture medium containing ZnO NP or $ZnCl_2$ (100 µg/mL). Fluorescence intensities were measured after 1 min, 15 min, 30 min, 1 h, 2 h, 3 h, 4 h, 5 h, and 6 h using a fluorescent microplate reader at an excitation wavelength of 485 nm and emission wavelength of 528 nm. The values were expressed as percentage of fluorescence intensities relative to the controls.

3.2.7.2 Measurement of mitochondrial membrane potential

The impairment of the mitochondria is a distinctive characteristic of early stages of apoptosis. This mitochondrial damage is further associated with changes in the mitochondrial membrane potential (ΔΨm). The mitochondrial permeability transition pore (MPTP) enable ions and small molecules the passage from the mitochondrion to the cytoplasm. The JC-1 dye is taken up from cells due to its lipophilic and cationic nature and selectively accumulates insight the electronegatively charged interior of mitochondria. JC-1 accumulates as J-aggregates in healthy mitochondria (Em: 590 nm) and after depolarisation the changes in ΔΨm cause the release of monomers of JC-1 through the MPTP into the cytoplasm resulting in a shifting of emitted light to 530 nm. To analyze the changes of ΔΨm after ZnO NP and $ZnCl_2$ treatment, 200,000 cells were seeded in a 6-well plate and treated with 2 µM JC-1 at 37°C for 30 min. The positive control was treated additionally with 100 mM CCCP, a protonophore, to depolarize the mitochondrial membrane. After incubation, the cells were washed three times with PBS. The cells were covered with 2 mL cell culture medium and the data were obtained using

a fluorescent microplate reader (Ex: 485 nm, Em: 538 nm and 600 nm). The measurement was performed after 1 min, 15 min, 30 min, 1 h, 2 h, 3 h, 4 h, 5 h, and 6 h, and values were expressed as percentage of mitochondrial membrane potential (ΔΨm) calculated by following formula:

$$(\Delta\Psi\mathrm{m})\ \% = \frac{\text{Fluorescence JC} - 1\ (600\ \text{nm}) \Big/ \text{Fluorescence JC} - 1\ (538\ \text{nm})}{\text{Fluorescence CCCP}\ (600\ \text{nm}) \Big/ \text{Fluorescence CCCP}\ (538\ \text{nm})} * 100$$

Formula 3: Calculation of mitochondrial membrane potential

(ΔΨm) = mitochondrial membrane potential, JC-1 = 5,5′,6,6′-Tetrachloro-1,1′,3,3′-tetraethyl-imidacarbocyanine iodide, CCCP = Carbonyl cyanide *m*-chlorophenyl hydrazone

3.2.7.3 Fluorescence microscopy of ΔΨm

The changes of the mitochondrial membrane potential were performed using a fluorescence microscopy. The cells (approx. 200,000) were seeded on cover slips in a 6-well plate and treated with 2 µM JC-1 at 37°C for 30 min. CCCP was used as positive control and the cells were treated additionally with 100 mM of the protonophore. After incubation, the cells were washed three times with PBS and incubated with 100 µg/mL of ZnO NP or $ZnCl_2$ for 1 min, 15 min, 30 min, 1 h, 2 h, 3 h, 4 h, 5 h and 6 h. The cells were washed three times with PBS and fixed with 4 % paraformaldehyde for 15 min. After another washing step with PBS the cover slips were mounted on slides using fluorescence mounting medium. The slides were examined using an inverted fluorescence microscope.

3.2.7.4 AlamarBlue® Assay

The AlamarBlue® Assay serves for analysis of cellular viability. The assay is based on a redox indicator that provides a colorimetric change and fluorescent signal in response to metabolic activity of cells [221]. In order to investigate the effects of ZnO NP on the cellular viability 15,000 cells/well were seeded in a 96-well plate and cultivated overnight. The cells were treated with ZnO NP (see 3.2.4.1) at three different concentrations (0.1, 10 or 100 µg/mL), respectively. The negative control for viability was incubated with 100 µL of 100 % ice cold EtOH for 10 min. Afterwards, the medium was replaced with 200 µL fresh cell culture medium containing 10 % AlamarBlue® (10 % v/v). Subsequently, the cells were incubated at 37°C for 3 h. The data were obtained using a plate reader (Ex: 540 nm, Em: 600 nm).

3.2.7.5 Crystal violet Assay

After measurement of cellular viability using AlamarBlue® Assay the results have to be compared to the total cell amount per well. For this, the cells were washed three times with PBS and a 0.2 % crystal purple solution (50 µL/well) was added to each well and incubated at 37°C for 10 min. After incubation time the cells were washed again and treated with 40 µL of 10 % acetic acid for lysation. The cell amount was measured on a microplate reader at 540 nm. Results of AlamarBlue® Assay were related to results of Crystel violet Assay and then the treated cells were referred to the untreated controls. Untreated control is set as 100 % of viability.

3.2.7.6 γH2A.X immunofluorescence Assay

The γH2A.X immunofluorescence assay is based on the fast phosphorylation of the histone H2A.X as a sensitive marker for DNA DSB[222,223]. The DNA damaging potential of ZnO NP, ZnO bulk and $ZnCl_2$ was analyzed using the γH2A.X immunofluorescence assay. Cells (approx. 200,000) were cultivated on cover slips in 6-well plates. Three different concentrations of ZnO NP (0.1, 10 or 100 µg/mL) were investigated as well as two pretreatments (see 3.2.4.2), and BSA stabilized ZnO NP (see 3.2.4.4), $ZnCl_2$, and ZnO bulk (see 3.2.4.5). After 1 min, 15 min, 30 min, 1 h, 4 h, and 24 h cells were fixed (15 min with 4 % paraformaldehyde and 10 min with methanol) and then washed with PBS. Nonspecific staining was blocked by incubation with 5 % BSA/PBS, 0.3 % Triton X-100 for 60 min. The cells were incubated with the primary antibody, anti-phospho-Histone H2A.X (Ser139, 1:500) diluted 1:500 in PBS with 0.3 % Triton X-100 at RT following by washing two times with PBS. The secondary antibody (Alexa Fluor 488 goat anti-mouse IgG) was applied at RT for 1 h. Then cells were washed two times in PBS, incubated in TBS with 400 mM NaCl for 2 min before getting washed again in PBS. The cover slips were mounted on slides using Vectashield® Hard+Set™ Mounting Medium with DAPI. All slides were examined using an inverted microscope. For quantitative analysis foci were counted using the software Image J 1.47f[224]. At least, 60 cells were analyzed for each preparation. The foci amounts of each point in time were referred to the untreated control. The untreated control is set as 100 % of viability.

3.2.7.7 Immunostaining of primary cells of mucosa

Primary cells were seeded on a cover slip (approx. 200,000 cells) and incubated at 37°C and 5 % CO_2 overnight. The cells were washed three times with PBS and afterwards fixed with 4 % paraformaldehyde for 15 min. After this fixation step, cells were washed again three times with PBS and incubated for 5 min with TBS/Tween$_{20}$. To block nonspecific interactions, cells were incubated with 1 % BSA/PBS (1:10) for 60 min. The cells were incubated with a primary antibody for epithelial cells (anti-cytokeratin 13, 1:100) or fibroblasts (anti-FGFR4, 1:50) diluted in 1 % BSA/PBS at 4°C overnight. Cells were washed twice with TBS/Tween$_{20}$ for 5 min. The secondary antibody (Goat-anti-rabbit, biotinylated) was incubated in a dilution of 1:250 in 1 % BSA/PBS at RT for 30 min. Afterwards, cells were washed two times with TBS/Tween$_{20}$ and were incubated with Streptavidin/HRP conjugated in a dilution of 1:200 in 1 % BSA/PBS at RT for 30 min. The negative control was incubated with 2 mL of hämalaun solution for 5 min; afterwards the cells were washed with tap water for 5 min. In the next step, cells were washed again with TBS/Tween$_{20}$ for two times and covered on a slide with 3,3´- diaminobenzidine (DAB). The staining was analyzed using an inverted light microscope.

3.2.8 Biochemical methods

3.2.8.1 Total protein extraction

Cells were pretreated with NAC or DTPA (see 3.2.4.2, 3.2.4.3) and ZnO NP or were single treated with ZnO NP and $ZnCl_2$ (see 3.2.4.1, 3.2.4.5). The epidermal growth factor (EGF) served as positive control just for Erk and Akt activation. The cells were treated with 10 nM EGF for 15 min, prior lysation. The cells were scratched and the cellular proteins were extracted in 200 µL 4x lysis buffer after ZnO NP incubation after 1 min, 15 min, 30 min, 1 h, and 4 h. The cellular protein extracts were transferred to a 1.5 mL tube and sonicated for 30 sec. Then, the extracts were centrifuged at 12,000x*g* and 4°C for 20 min. The supernatants were transferred to a new 1.5 mL tube and used for protein determination.

3.2.8.2 Protein determination

The protein determination was carried out using the Bio-Rad *DC*™ (detergent compatible) protein assay kit, which is based on colorimetric reactions following the Lowry assay[225]. The protein determination kit was used according to the Bio-Rad manufacturer's instructions.

3.2.8.3 Sodium dodecyl sulfate polyacrylamide gel electrophoresis

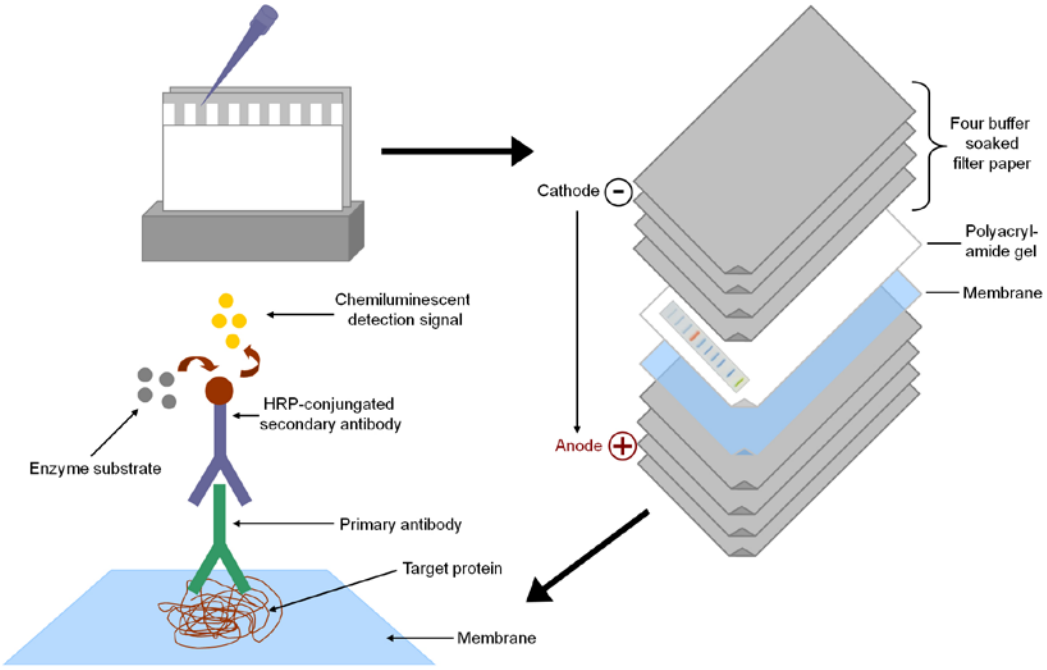

Figure 11: Illustration of gel electrophoresis, western blot and protein detection

Western blotting is used to detect the amount or activation level of a specific protein. The proteins were separated by electrophoresis in a polyacrylamide gel, known as SDS-Page. Then the gel was placed on a membrane between four buffer soaked filter papers in a blotting tank. The proteins in the gel were transferred to the membrane from cathode to anode by electrical current. Afterwards, the membrane was incubated with a specific antibody against to protein of interest. The secondary antibody is conjugated to HRP enabling the protein detection after reaction of HRP with a luminescent compound (adapted from:[226,227]).

3.2.8.3.1 Preparation of acrylamide gel

Protein samples were analyzed by protein separation using a sodium dodecyl sulfate polyacrylamide gel electrophoresis (SDS-Page) with a vertical electrophoresis chamber. Depending on the molecular weight of the analyzed protein, different acrylamide concentrations were used for the running gel (see Table 5). The prepared running gel solution was filled to three fourth between two glass plates with fixed 1.0 mm spacers and polymerized after covering with 70 % isopropyl alcohol at RT for 30 min. After gel curing the isopropanol was poured off and washed with distilled water. The 4 % stacking gel was added above the running gel. A silicone rubber comb was placed between the plates to create slots. After further 30 min of incubation, the acrylamide gel was ready to use for SDS-Page.

3.2.8.3.2 Gel electrophoresis

After removing the silicone rubber comb and seal, the glass plates were fixed in a vertical electrophoresis chamber and filled up with 1x running buffer. In the first slot, 5 µL of PageRuler™ Prestained Protein Ladder was loaded. The protein samples were added to 4x lysis buffer with 2.5 mM dithiothreitol (DTT) and denaturized at 95°C for 10 min before the lysates were carefully loaded (final concentration: 30 µg/30 µL) into the slots of the stacking gel. The acrylamide gel ran at 15 mA/gel for the first 30 min and afterwards at 30 mA/gel with maximal voltage until the bromphenol blue band reached the bottom of the running gel.

3.2.8.3.3 Western blot analysis

The acrylamide gel was blotted to a nitrocellulose membrane using an electrophoresis blotter [226]. The gel was replaced between the nitrocellulose membrane and four slides of blotting paper on each side (see Figure 11) presoaked with transferring buffer in an electrophoresis blotter. The proteins were transferred to the nitrocellulose membrane at 1.5 mA/cm^2 of acrylamide gel at RT for 1.25 h. The membrane was washed once in washing buffer and was then blocked with blocking buffer (3 % or 5 % powdered milk concentration depending on protein, which has been analyzed), at RT for 1 h (see Table 6). After three washing steps for 5 min each, the membrane was incubated with the primary antibody diluted in blocking buffer under shaking conditions at 4°C overnight. The membrane was washed again 3x 5 min with washing buffer prior to incubation with a horseradish peroxidase (HRP)-linked secondary antibody at RT for 1 h. Then the membrane was washed again 3x 5 min with washing buffer. The used antibodies and dilutions are listed in Table 6. The respective antibodies were detected using enhanced chemiluminescent reagent (Western Lightning Plus - ECL) in a dilution 1:1 ratio by addition to the blotting membrane for 3 min. The immunostained proteins were recorded by the use of a ChemiDoc MP system. Band densities were normalized to the housekeeping protein β-actin or the total amount of protein and expressed as percentage of the respective controls.

3.2.8.3.4 Membrane stripping

For detection of additional proteins (e.g., housekeeping protein), the used membranes were stripped with stripping buffer for 30 min and further by 1 % SDS in distilled water for 30 min again, both at RT. The membranes were then washed 3x 5 min with washing buffer. The membrane was further treated with additional antibodies as mentioned before (see 3.2.8.3.3).

3.2.8.4 Human Phospho-ATM (S1981) ELISA

The biological impact of ZnO NP and $ZnCl_2$ on DNA damage signaling was further analyzed using the phosphorylation status of the respective phosphatidylinositol-3-kinases related kinases ATM, the main sensor of DNA DSB and activator of DNA damage response. The ELISA Kit Duo Set® IC Human Phospho-ATM was used to determine the phosphorylated amount of ATM in dependence of ZnO NP and $ZnCl_2$ treatment. The measurement of phosphorylated human ATM in cell lysates was performed according to the standard protocol of the manufacturer. The cells were lysed in ELISA lysis buffer# 13 after incubation with 100 µg/mL of ZnO NP and $ZnCl_2$ and the following time steps: 1 min, 15 min, 30 min, 1 h and 4 h. Samples were then frozen until use. After dilution of the Phospho-ATM (S1981) capture antibody in PBS (final concentration 10 µg/mL) a 96- ELISA microplate was immediately coated with 100 µL/well at RT for 24 h. Next day, the capture antibody was replaced by PBS and each well was washed two times with PBS. The ELISA microplate was further blocked with 300 µL blocking buffer at RT for 1 h. After washing three times for 5 min with PBS, 100 µL of cell lysates or standard in IC Diluent# 4 were added and incubated at RT for 2 h. After the third washing step, 100 µL of the Phospho-ATM (S1981) detection antibody (final concentration: 200 ng/mL) was incubated at RT for 2 h. After another washing step, 100 µL of the streptavidin-HRP-solution was added and incubated at RT in the dark for 20 min. The ELISA microplate was washed again and 100 µL of substrate solution was added and incubated at RT in the dark for staining development for 20 min. Finally, 50 µL of stop solution was added and the optical density was measured using a microplate reader set at 450 nm and a wavelength correction of 540 nm.

3.2.9 Statistics

The experiments were reproduced at least three times with the exception of primary cells of mucosa data. Mean values as well as standard errors or standard deviation for all experiments were calculated. The statistical analysis of the cell experiments was carried out using a one-way analysis of variance (ANOVA) with Bonferroni post-hoc test, two-way analysis of variance (ANOVA), or student's t-test (for paired samples). The p-values provided are only descriptive: p-values ≤ 0.05 (*) were termed significant, p-values ≤ 0.01(**) were termed highly significant and p-values ≤ 0.001(***) extremely significant. The analysis was performed using GraphPad Prism 5.

4 Results

The following chapter facilitates insights into the genotoxic mechanisms of ZnO NP in a model of respiratory epithelia as results of this work. The chapter is subdivided into six parts. The first section deals with the characterization and solubility of the synthesized ZnO NP. In the second part the internalization, intracellular accumulation, and distribution of ZnO NP is documented. The third section outlines the toxicity of ZnO NP. In the fourth and fifth part the genotoxicity of ZnO NP is shown, especially the induction of DNA damages and the activation of DNA damage response. Finally, data concerning the genotoxicity of ZnO NP in primary cells of the mucosa are described.

4.1 ZnO NP preparation and characterization

The ZnO NP were prepared by the *Institute of Inorganic and Analytical Chemistry of Johannes Gutenberg University Mainz,* fabricating two different sizes of ZnO NP (4-5 nm and 15-18 nm). Characterization of the synthesized ZnO NP was performed using transmission electron microscopy (TEM) for size and X-ray diffraction (XRD) for ZnO NP crystallisation. The surface charge of the particles was analyzed using ζ-potential measurement. The solubility of ZnO NP was measured using atomic absorption spectroscopy (AAS). Results are detailed in the following sections.

4.1.1 TEM, XRD and ζ-potential measurements

The TEM images showed the presence of non-aggregated spherical particles homogeneously dispersed in high purity H_2O. The size distribution obtained from TEM showed an average size value of ZnO NP centered at 4-5 nm (Figure 12A) and 15-18 nm (Figure 12C). The phase identity and crystallinity of the ZnO NP was certified using XRD (Figure 12B and D). All reflections can be indexed to the ZnO structure (wurtzite) with the lattice parameters *a* = 3.24 Å, *c* = 5.20 Å and space group (SG) $P6_3mc$. The ζ-potential of ZnO NP (4-5 nm) was defined as -1 mV and of ZnO NP (15-18 nm) as + 40 mV.

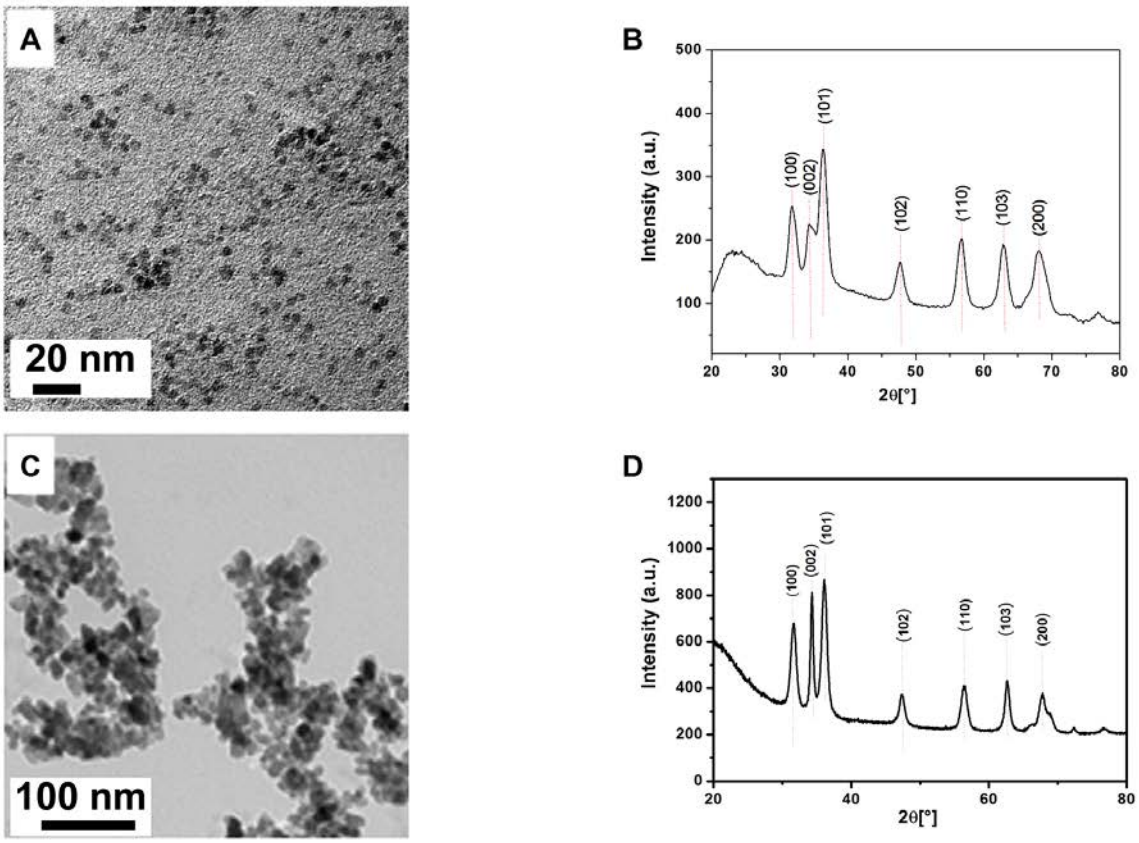

Figure 12: ZnO NP characterization by TEM and XRD measurement

(A) TEM image of synthesized ZnO NP (4-5 nm) and the corresponding (B) XRD pattern. (C) Shows the TEM image of ZnO NP (15-18 nm) and the corresponding (C) XRD pattern.

4.1.2 Solubility of ZnO NP

The concentration of Zn^{2+} in the supernatants after dispersion in high purity H_2O or cell culture medium was measured by AAS at different points in time (Figure 13). In Figure 13A the cumulated levels of released Zn^{2+} dissociated from ZnO NP (4-5 nm) are shown in a time-dependent manner. It could be observed that ZnO NP (4-5 nm) dissociated faster in high purity H_2O than in cell culture medium (~ 100 mg/L in high purity H_2O and ~ 50 mg/L in cell culture medium after 4 h). Figure 13B shows enrichment of Zn^{2+} in high purity H_2O and cell culture medium released from ZnO NP (15-18 nm) in a time-dependent manner. The larger particles (15-18 nm) showed as well a time-dependent release of Zn^{2+} in both solutions but in a smaller dimension in contrast to ZnO NP (4-5 nm). The Zn^{2+} concentration after ZnO NP (15-18 nm) treatment increased continuously in both solutions (~ 25 mg/L in high purity H_2O and ~ 35 mg/L in cell culture medium after 4 h). Furthermore, the larger particles were more dissociated in cell culture medium than in high purity H_2O.

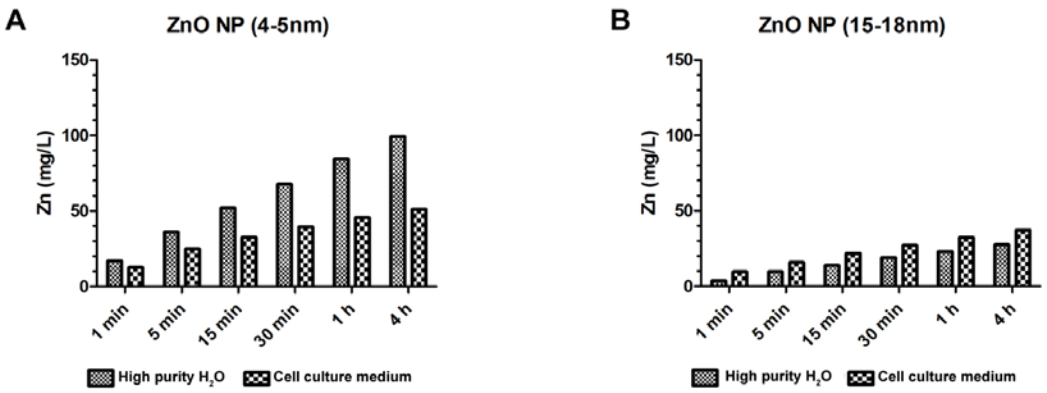

Figure 13: Cumulated solubility of ZnO NP in high purity H_2O and cell culture medium

The solubilities of ZnO NP (4-5 nm) and ZnO NP (15-18 nm) in high purity H_2O and cell culture medium are shown. (A) Time-dependent increase of Zn^{2+} in high purity H_2O and cell culture medium after incubation with ZnO NP (4-5 nm). The smaller particles dissociated faster in high purity H_2O than cell culture medium. (B) Time-dependent enrichment of Zn^{2+} in high purity H_2O and cell culture medium after treatment with ZnO NP (15-18 nm). The larger particles showed a reduced dissociation in comparison to the smaller particles. They further dissociated faster in cell culture medium than in high purity H_2O. N=1.

4.2 Intracellular localization and distribution of ZnO NP

4.2.1 Intracellular localization of ZnO NP measured by TEM

Transmission electron microscopy (TEM) gives information about cellular morphology, particle incorporation and cellular distribution. To investigate the intracellular localization of ZnO NP, TEM was performed after particle treatment for several points in time. Incorporated and distributed ZnO NP (4-5 nm) and ZnO NP (15-18 nm) after 1 h of exposure are shown in Figure 14 and Figure 15. Figure 14 shows the morphology and cellular uptake of ZnO NP (4-5 nm). Agglomerated ZnO NP (4-5 nm) were detected in the cytoplasm. As shown in Figure 15F, E, and G, incorporated ZnO NP (15-18 nm) were rarely localized in the cytoplasm, nucleus, mitochondria and nuclear envelope.

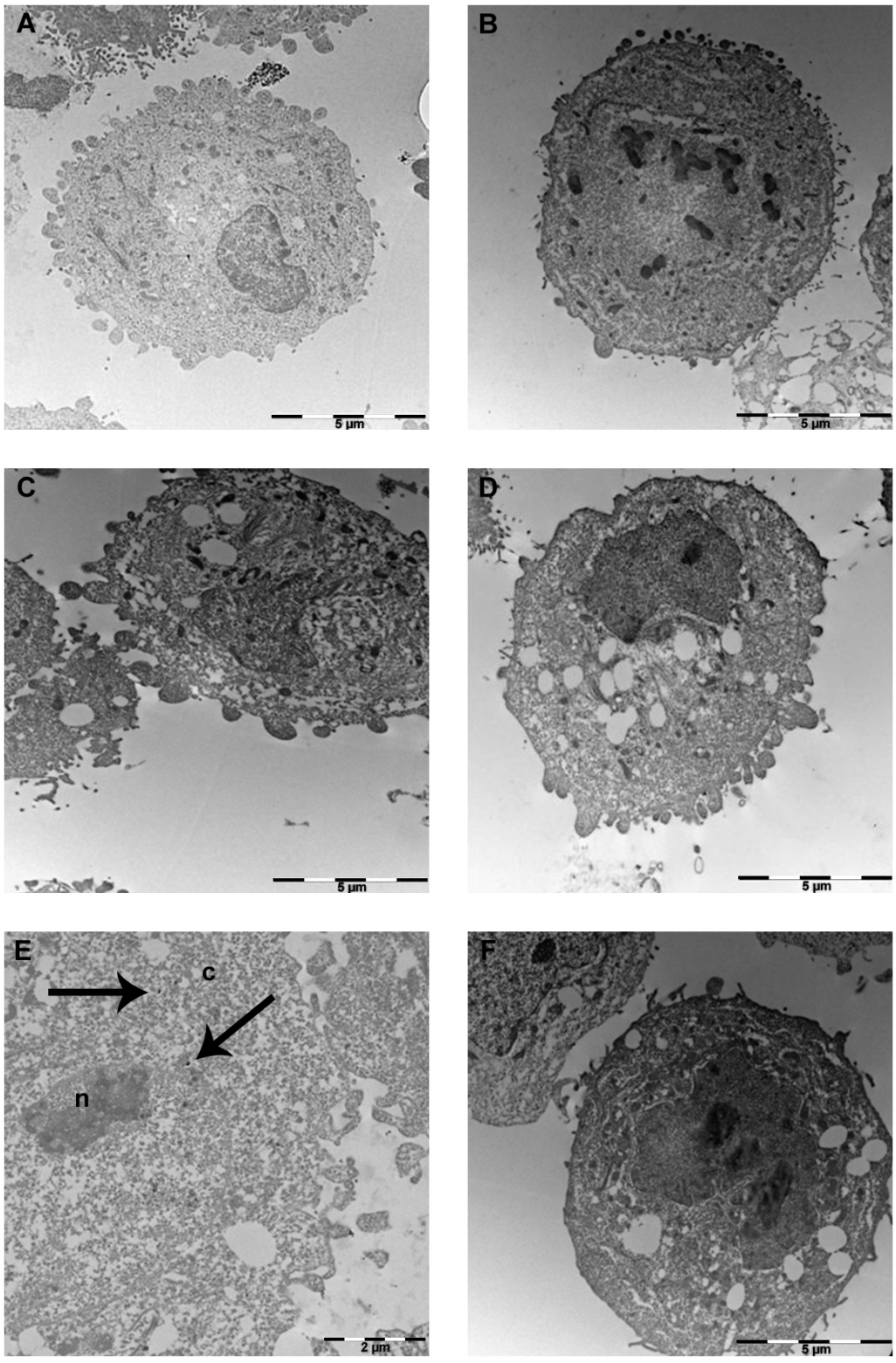

Figure 14: TEM analysis of ZnO NP (4-5 nm) treated A549 cells

A549 cells were incubated with 100 µg/mL ZnO NP. (A) Control without ZnO NP treatment. (B) 1 min, (C) 15 min, (D) 30 min, (E) 1 h and (F) 4 h incubation with ZnO NP. (E) Arrows point to the ZnO NP localized in the cytoplasm. Scale bar A, B, C, D, F: 5 µm; E: 2 µm; n = nucleus, c = cytoplasm. Magnification A-F: 2784x.

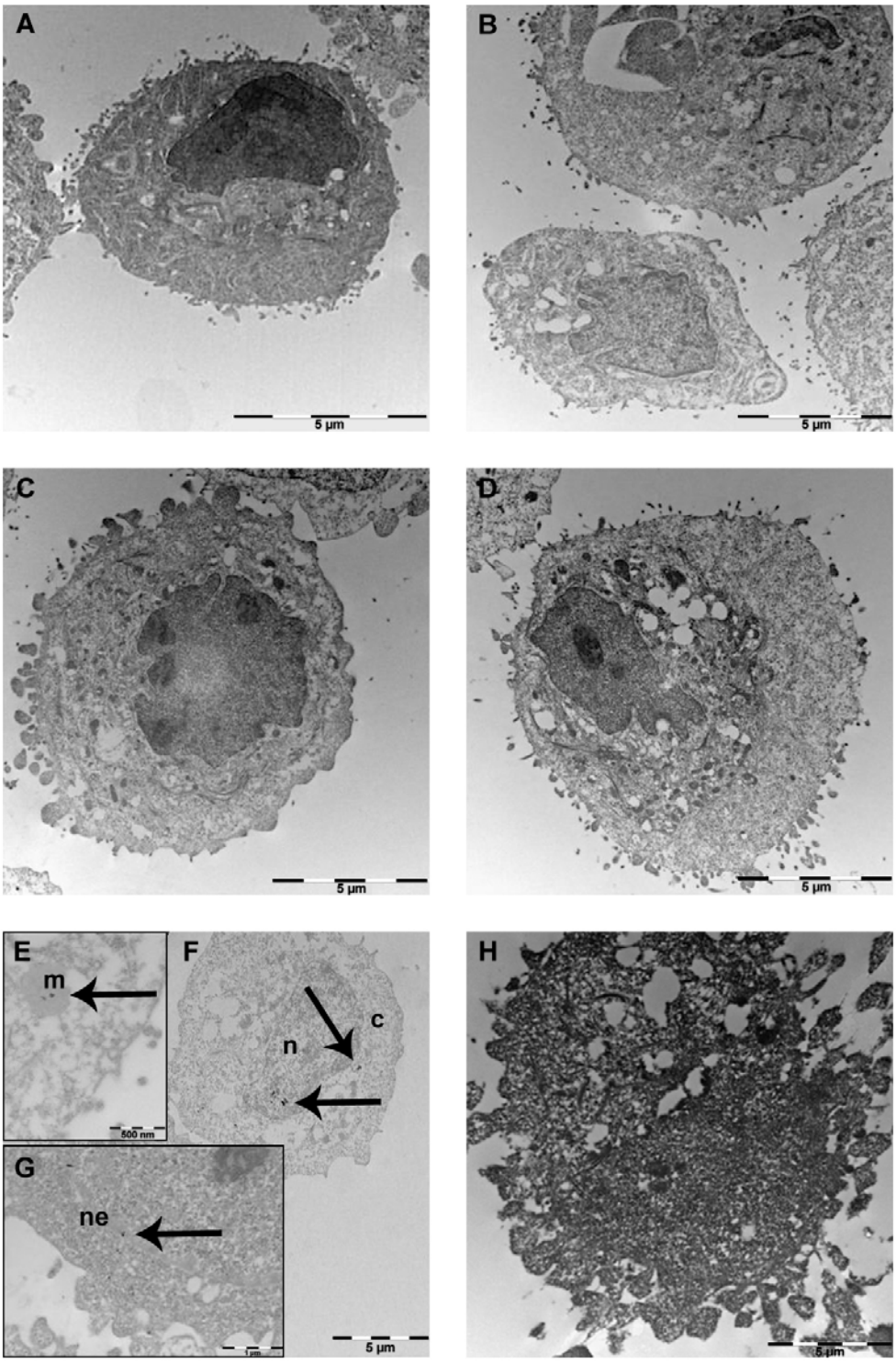

Figure 15: TEM analysis of ZnO NP (15-18 nm) treated A549 cells

A549 cells were exposed to 100 µg/mL ZnO NP. (A) Control without ZnO NP treatment. (B) 1 min, (C) 15 min, (D) 30 min, (E) (F) (G) 1 h and (H) 4 h incubation with the particles. (F) Arrows mark the aggregated ZnO NP, which are intracellular localized in cytoplasm and nuclear region. (E) Arrow points to the particles in mitochondria. (G) Arrow points to the particles between the cytoplasm and the nucleus in the nuclear envelope. Scale bar A, B, C, D, E, F: 5 µm; E: 500 nm; G: 1 µm. n = nucleus, c = cytoplasm, m = mitochondira and ne = nuclear envelope. Magnification A-G: 2784x, H: 6000x.

4.2.2 Intracellular increase of Zn^{2+} after ZnO NP treatment

The extra- or intracellular dissociation of ZnO NP as mechanism of genotoxicity is hypothesized. The cells were loaded with FluoZin^{TM}-3, a detector of intracellular free zinc, and afterwards treated with ZnO NP (4-5 nm) or ZnO NP (15-18 nm). The intracellular accumulation of Zn^{2+} was analyzed by spectrofluorometer. Cells were pretreated with the cell impermeable chelator DTPA to complex Zn^{2+} specifically. Furthermore, the ZnO NP were stabilized by BSA to prevent dissociation. ZnO NP (4-5 nm) treatment entailed to a slight intracellular increase of Zn^{2+} concentration from 1 nM in the first seconds to a maximum of 2.5 nM after 60 min (Figure 16A). The exposure to ZnO NP (15-18 nm) showed a fast intracellular increase of Zn^{2+} (Figure 17A). The intracellular Zn^{2+} concentration enhanced in the first seconds to 10 nM and increased continuously to a level of 35 nM after 60 min (Figure 17A). The extracellular chelation of Zn^{2+} by DTPA resulted in a residual intracellular increase of Zn^{2+} to a maximum of 0.5 nM after 10 min, as seen after treatment with both sizes of ZnO NP (4-5 nm and 15-18 nm) (Figure 16B and Figure 17B). BSA stabilization of ZnO NP (4-5 nm) resulted in a slight increase of intracellular Zn^{2+} with a maximal level of 2.5 nM after 60 min (Figure 16C). Figure 17C shows an intracellular increase of Zn^{2+} up to 3 nM in the first seconds keeping this level constant until the end of measurement (Figure 17C). In summary, the ZnO NP (4-5 nm) as well as ZnO NP (15-18 nm) dissociate quickly extracellular and were taken up by the cells as Zn^{2+}.

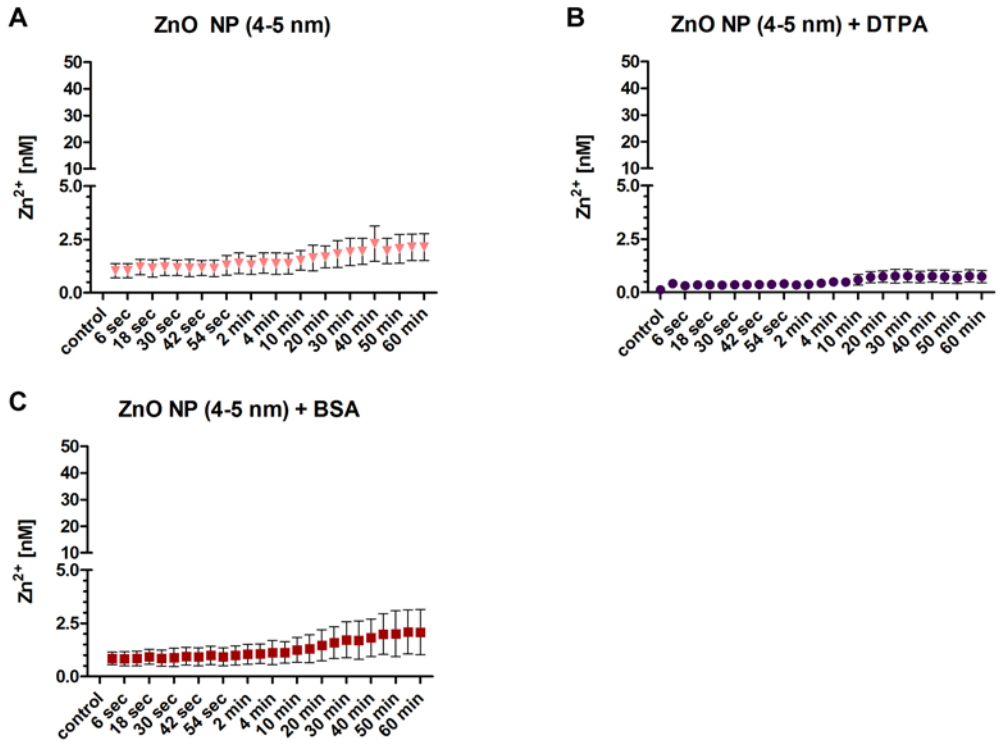

Figure 16: Spectrofluorimetric analysis of intracellular Zn^{2+}-levels after ZnO NP (4-5 nm) exposure

Spectrofluorometric measurements of intracellular Zn^{2+} after ZnO NP, ZnO NP + DTPA and ZnO NP + BSA treatment. (A) The intracellular Zn^{2+} level increased in the first seconds of exposure from 0.1 nM to ~ 1 nM and increased afterwards continuously to a level of 2.5 nM after 60 min. (B) Pretreatment with DTPA resulted in no intracellular increase of Zn^{2+}. (C) BSA stabilized ZnO NP (4-5 nm) showed an intracellular increase of Zn^{2+} comparable to treatment with pure particles. N=3.

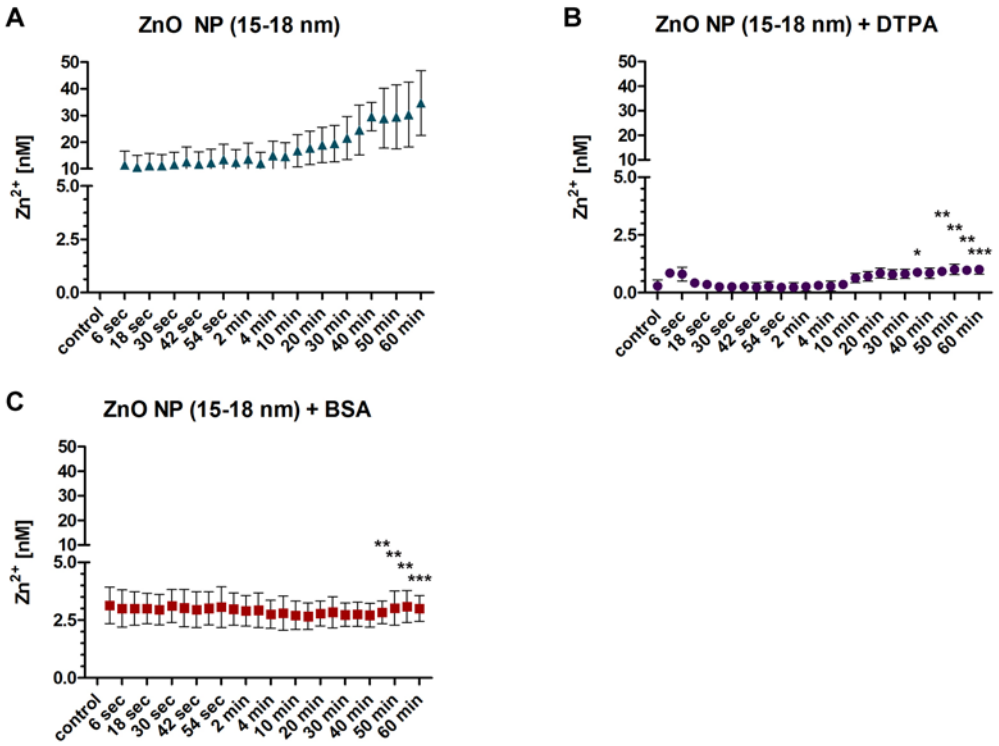

Figure 17: Spectrofluorimetric analysis of intracellular Zn^{2+} after ZnO NP (15-18 nm) exposure

Spectrofluorometric measurements of intracellular Zn^{2+} after ZnO NP, ZnO NP + DTPA and ZnO NP + BSA treatments. (A) ZnO NP (15-18 nm) exposure led to an increased intracellular Zn^{2+}-level. The Zn^{2+}-level raised to 10 nM in the first seconds and increased continuously to 35 nM after 60 min. (B) The pretreatment with DTPA resulted in no intracellular increase of Zn^{2+}. (C) The BSA stabilized ZnO NP exposure led to an intracellular increase of Zn^{2+} up to 3 nM in the first seconds and retaining this level over the measurement. * = $p<0.05$, ** = $p<0.01$, *** = $p<0.001$ (ZnO NP (15-18 nm) + DTPA and ZnO NP (15-18 nm) + BSA in comparison to ZnO NP (15-18 nm)), at least N=3.

4.2.3 Intracellular distribution of Zn^{2+} after ZnO NP or $ZnCl_2$ treatment

To further evaluate the observed influx of Zn^{2+} (Figure 16 and Figure 17) cLSM live imaging of A549 cells was performed. FluoZin™-3 was used as detector of free intracellular Zn^{2+} after ZnO NP or $ZnCl_2$ treatment. The cells were loaded with FluoZin™-3 as mentioned in 3.2.5.2.1 and three compartments (early endosomes, endoplasmatic reticulum, and mitochondria) were co-localized by fluorescent dyes as described in 3.2.5.2.5, 3.2.5.2.6, and 3.2.5.2.7. The cells were treated with ZnO NP (4-5 nm), ZnO NP (15-18 nm) or $ZnCl_2$ and the localization of Zn^{2+} was detected each minute for finally 1 h.

4.2.3.1 Zn^{2+} distribution after ZnO NP (4-5 nm) treatment

The Zn^{2+}-level did not increase in the early endosomes after particle treatment. Detected Zn^{2+} was of endogenous sources (Figure 18). In the endosplasmatic reticulum (ER) no Zn^{2+} was detected after ZnO NP (4-5 nm) exposure (Figure 19). The treatment with ZnO NP resulted in a mitochondrial accumulation of Zn^{2+} after 10 min persisting until the end of measurement (Figure 20).

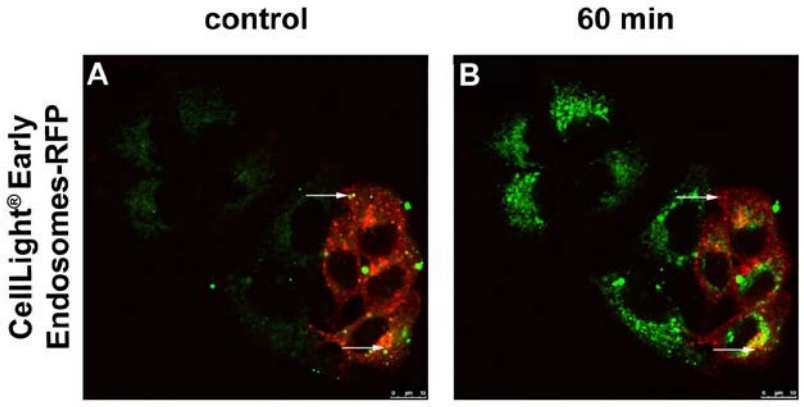

Figure 18: cLSM images of early endosomes after ZnO NP (4-5 nm) exposure

(A) Untreated A549 cells, loaded with FluoZin™-3 and CellLight® Early Endosomes-RFP. Arrows point to Zn^{2+} accumulation in early endosomes under physiological conditions in untreated cells. (B) A549 cells loaded with FluoZin™-3 and CellLight® Early Endosomes-RFP after 60 min of ZnO NP (4-5 nm) treatment. No accumulation of Zn^{2+} in early endosomes after ZnO NP (4-5 nm) exposure was detected. Arrows point to the Zn^{2+} accumulation in early endosomes before the particles were exposed. Green = FluoZin™-3, red = CellLight® Early Endosomes-RFP, yellow = co-localization of Zn^{2+} with early endosomes. Scale bar: 10 µm.

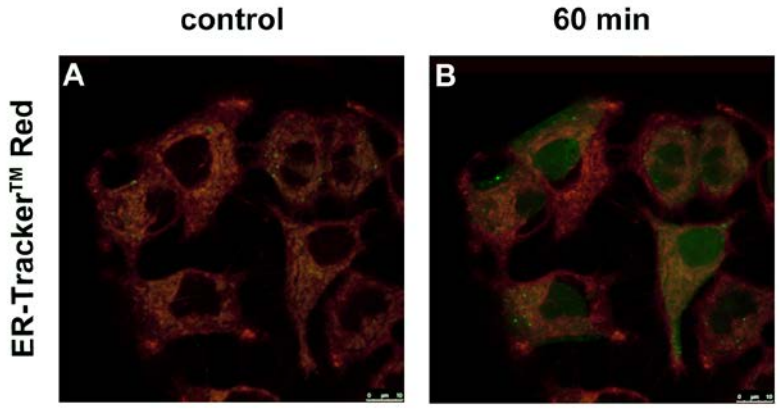

Figure 19: cLSM images of ER after ZnO NP (4-5 nm) treatment

(A) Untreated A549 cells, loaded with FluoZin™-3 and ER-Tracker™ Red. (B) A549 cells loaded with FluoZin™-3 and ER-Tracker™ Red after 60 min of ZnO NP (4-5 nm) treatment. No distribution of Zn^{2+} in the ER was detectable after ZnO NP (4-5 nm) treatment. Green = FluoZin™-3, red = ER-Tracker™ Red. Scale bar: 10 µm.

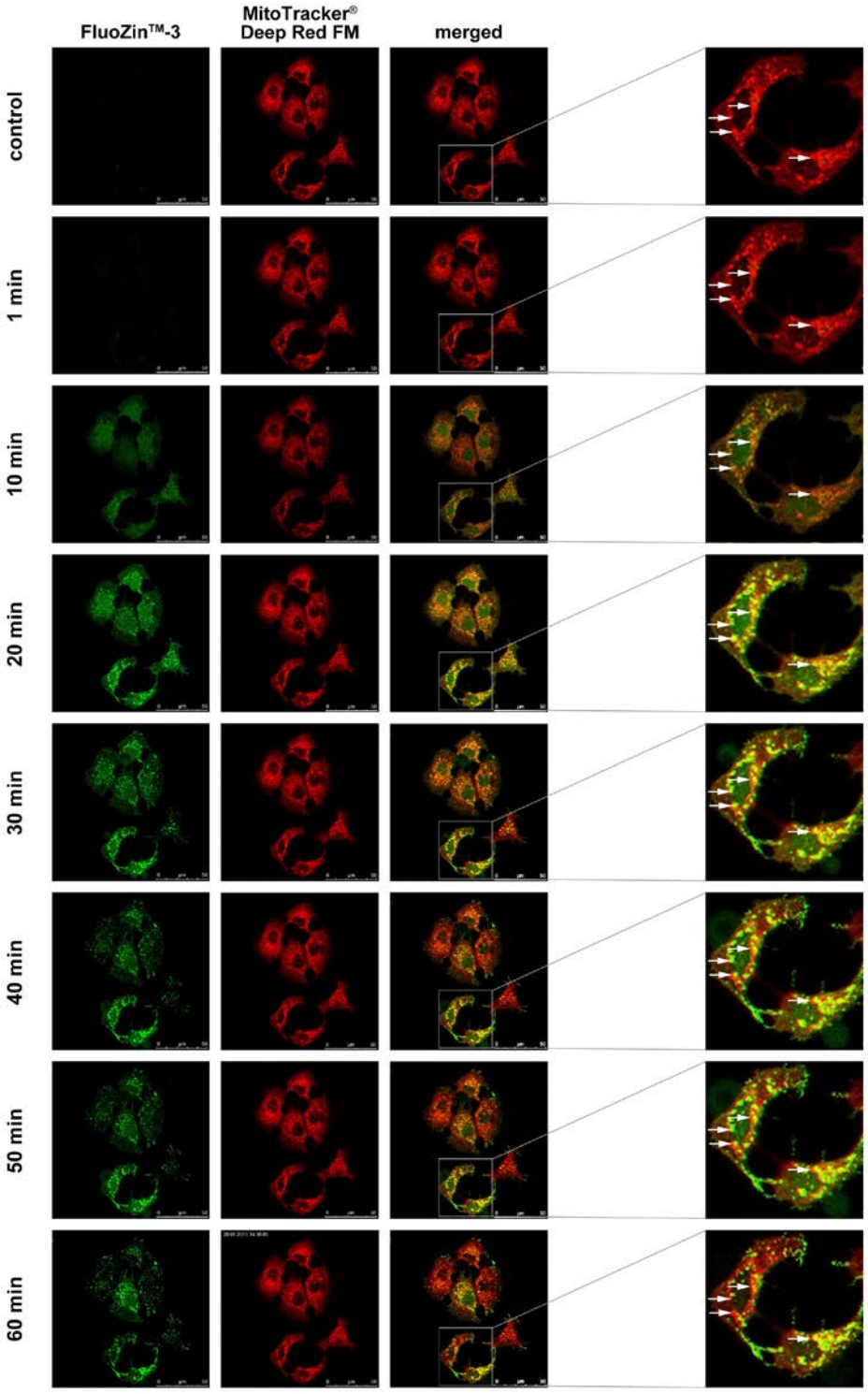

Figure 20: cLSM images of mitochondria after ZnO NP (4-5 nm) treatment

Live imaging of A549 cells loaded with FluoZin™-3 and MitoTracker® Deep Red FM and treated with ZnO NP (4-5 nm). The images show an increase of Zn^{2+} in mitochondria after 10 min keeping this Zn^{2+}-level in the period of time. The images on the right show an enlargement of the overlay images. Arrows point to the Zn^{2+} accumulation inside mitochondria. Co-localization of Zn^{2+} and mitochondria is indicated in the image as yellow overlay. Green = FluoZin™-3, red = MitoTracker® Deep Red FM. Scale bar: 50 µm.

4.2.3.2 Zn^{2+} distribution after ZnO NP (15-18 nm) treatment

The stained cells with FluoZin™-3 and CellLight® Early Endosomes-RFP showed no co-localization of Zn^{2+} in early endosomes after ZnO NP (15-18 nm) treatment (Figure 21). No Zn^{2+} accumulation was detected in the endosplasmatic reticulum after ZnO NP (15-18 nm) treatment (Figure 22). The exposure to ZnO NP (15-18 nm) resulted in a continuous mitochondrial Zn^{2+} accumulation until 20 min of exposure. Afterwards, the Zn^{2+}-level is kept constant until the end of measurement (Figure 23).

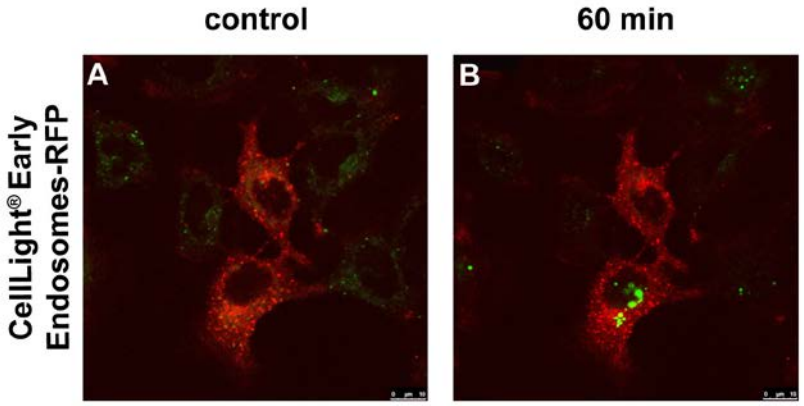

Figure 21: cLSM images of early endosomes after ZnO NP (15-18 nm) exposure

(A) Untreated A549 cells loaded with FluoZin™-3 and CellLight® Early Endosomes-RFP. (B) A549 cells loaded with FluoZin™-3 and CellLight® Early Endosomes-RFP after 60 min of ZnO NP (15-18 nm) treatment. No accumulation of Zn^{2+} in early endosomes could be observed. Green = FluoZin™-3, red = CellLight® Early Endosomes-RFP. Scale bar: 10 µm.

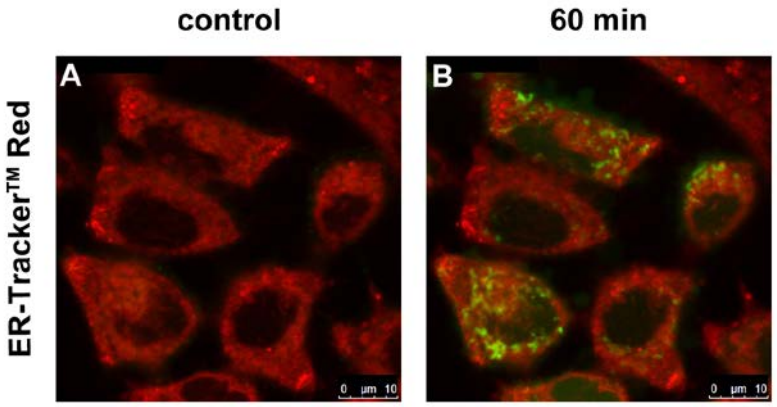

Figure 22: cLSM images of ER after ZnO NP (15-18 nm) treatment

(A) Untreated A549 cells, loaded with FluoZin™-3 and ER-Tracker™ Red. (B) A549 cells loaded with FluoZin™-3 and ER-Tracker™ Red after 60 min of ZnO NP (15-18 nm) treatment. No accumulation of Zn^{2+} in ER after ZnO NP (15-18 nm) treatment was detected in A549 cells. Green = FluoZin™-3, red = ER-Tracker™ Red. Scale bar: 10 µm.

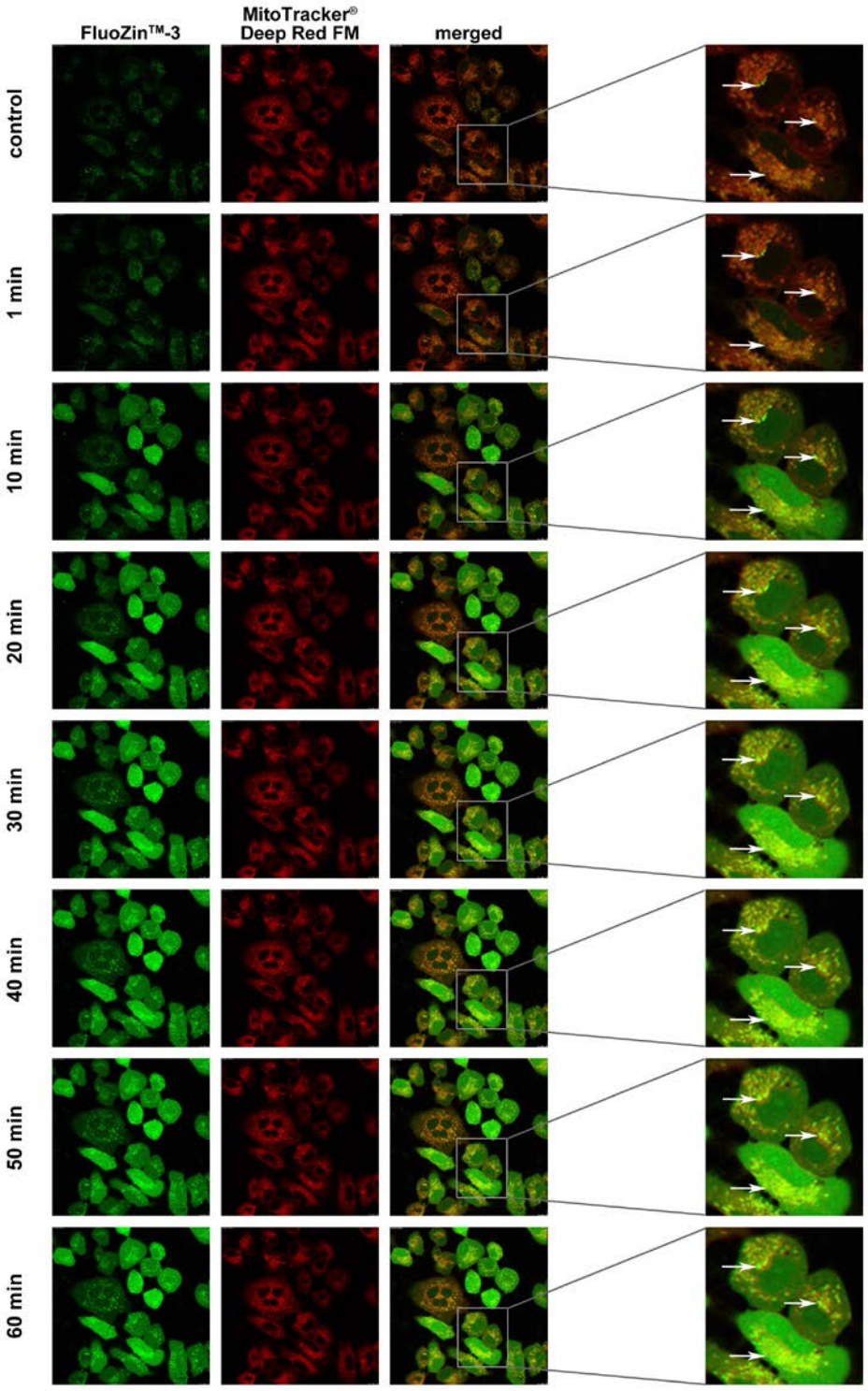

Figure 23: cLSM images of mitochondria after ZnO NP (15-18 nm) treatment

Live imaging of A549 cells loaded with FluoZin™-3 and MitoTracker® Deep Red FM and treated with ZnO NP (15-18 nm). The images show a continuous increase of Zn^{2+} in mitochondria until 20 min keeping this Zn^{2+}-level to the end of measurement. The images on the right show an enlargement of the overlay images. Arrows point to the Zn^{2+} distribution inside the mitochondria. Co-localization of Zn^{2+} and mitochondria is indicated in the image as yellow overlay. Green = FluoZin™-3, red = MitoTracker® Deep Red FM. Scale bar: 50 µm.

4.2.3.3 Zn^{2+} accumulation in A549 cells after $ZnCl_2$ exposure

The involvement of an appropriate reference material, (e.g., $ZnCl_2$) is essential in order to assess specific nanoparticle risks. As positive control for dissociated ZnO NP to Zn^{2+}, the treatment with $ZnCl_2$ was investigated. Treatment with $ZnCl_2$ resulted in strong FluoZin^{TM}-3 increments. Zn^{2+} in early endosomes could be observed in single endosomes after 1 min of $ZnCl_2$ treatment following by reinforced accumulation over the period in time (Figure 24). $ZnCl_2$ exposure resulted in a fast Zn^{2+} distribution at the ER after 1 min and increased until 10 min, keeping this level over the period in time (Figure 25). The accumulation of Zn^{2+} after $ZnCl_2$ treatment resulted in a fast mitochondrial accumulation until 1 min, keeping this high level of Zn^{2+} until the end of measurement (Figure 26). Some cells showed small constructed bodies containing FluoZin^{TM}-3 after 10 min. The bodies enlarged their size continuously (Figure 26, light blue arrow), suggesting the beginning of apoptosis or maybe autophagy.

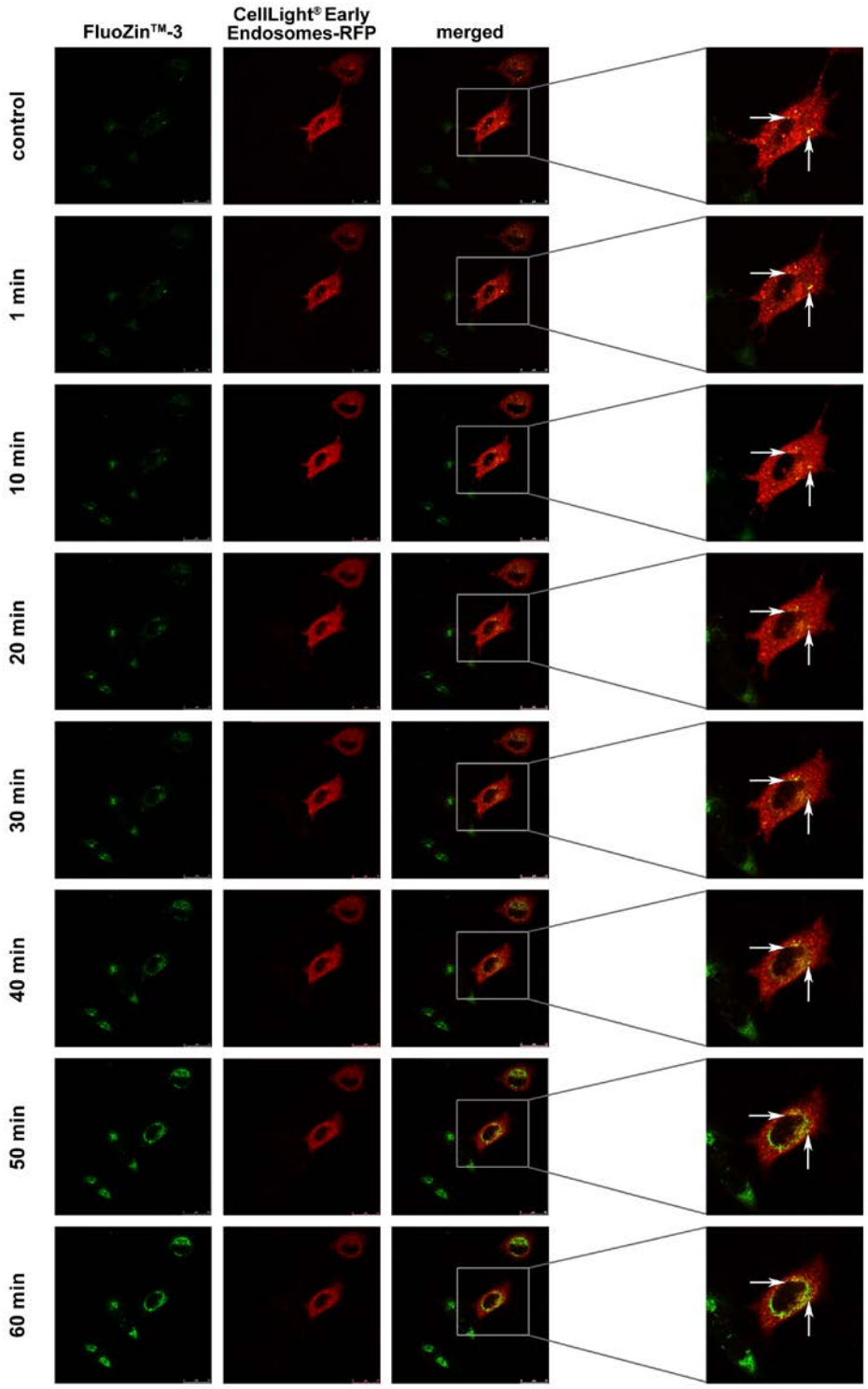

Figure 24: cLSM images of early endosomes after $ZnCl_2$ exposure

Live imaging of A549 cells loaded with FluoZin™-3 and CellLight® Early Endosomes-RFP and treated with $ZnCl_2$. Zn^{2+} in early endosomes could be observed in single endosomes after 1 min of $ZnCl_2$ treatment following by reinforced distribution over the period in time. The images on the right show an enlargement of the overlay images. Arrows show the Zn^{2+} accumulation inside the early endosomes. Co-localization of Zn^{2+} and early endosomes is indicated in the image as yellow overlap. Green = FluoZin™-3, red = CellLight® Early Endosomes-RFP. Scale bar: 25 µm.

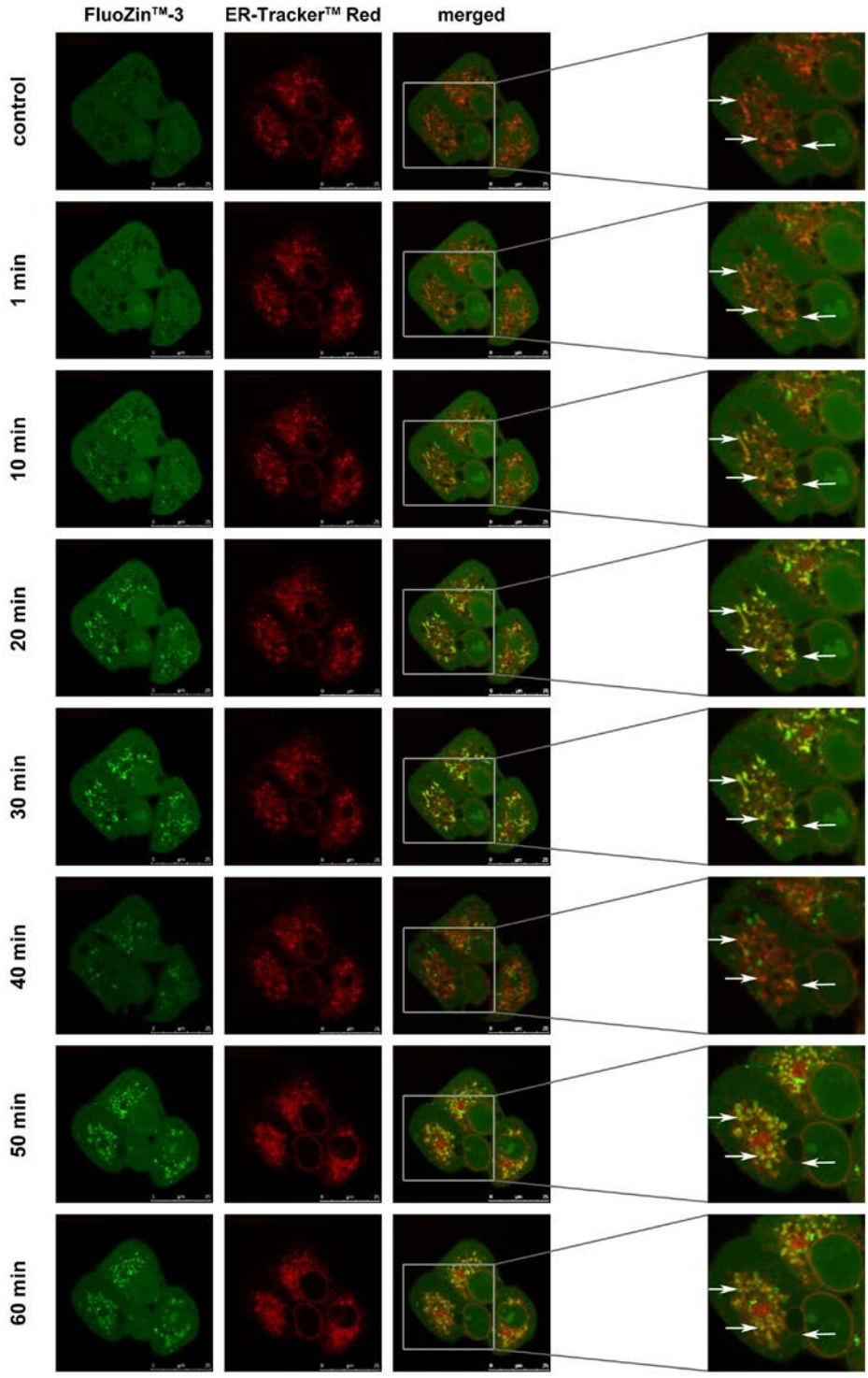

Figure 25: cLSM images of ER after $ZnCl_2$ exposure

Live imaging of A549 cells loaded with FluoZin™-3 and ER-Tracker™ Red and then treated with $ZnCl_2$. $ZnCl_2$ exposure resulted in a fast Zn^{2+} accumulation in the ER after 1 min and increased until 10 min, keeping this level until the end of measurement. The images on the right show an enlargement of the overlay images. Arrows show the Zn^{2+} accumulation inside the ER. Co-localization of Zn^{2+} and ER is indicated in the image as yellow overlap. Green = FluoZin™-3, red = ER-Tracker™ Red. Scale bar: 25 µm.

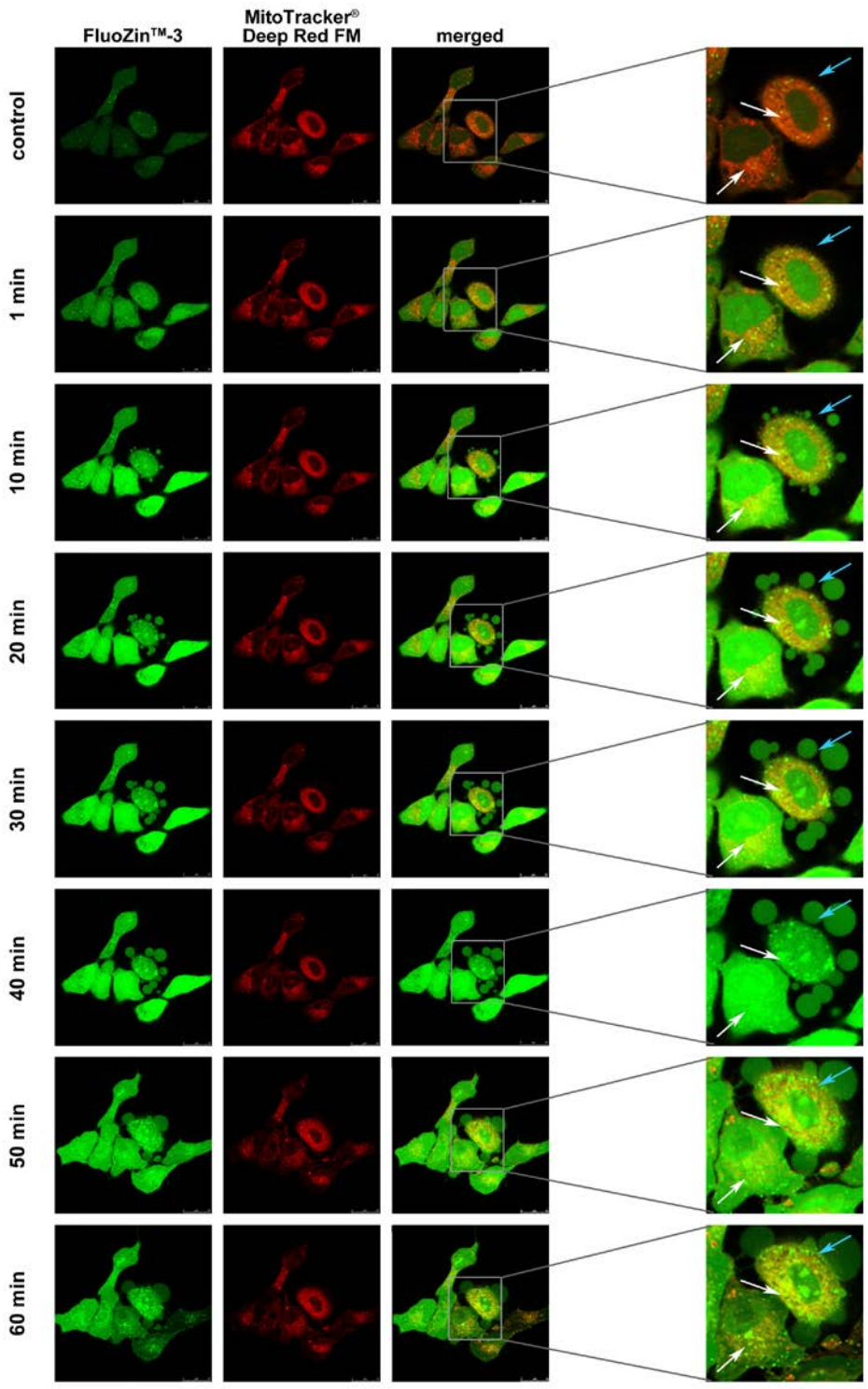

Figure 26: cLSM images of mitochondria after $ZnCl_2$ exposure

Live imaging of A549 cells loaded with FluoZin™-3 and MitoTracker® Deep Red FM and then exposed to $ZnCl_2$. $ZnCl_2$ treatment led to a fast accumulation of Zn^{2+} in mitochondria of A549 cells. The distribution of Zn^{2+} after $ZnCl_2$ treatment resulted in a fast mitochondrial accumulation until 1 min, holding this high Zn^{2+}-level until the end of measurement. The images on the right show an enlargement of the overlay images. White arrows show the Zn^{2+} accumulation inside the mitochondria. The blue arrow points to the supposed apoptotic bodies. Co-localization of Zn^{2+} and mitochondria is indicated in the image as yellow overlap. Green = FluoZin™-3, red = MitoTracker® Deep Red FM. Scale bar: 25 µm.

4.2.4 Strong accumulation of Zn^{2+} in the nucleus

The cLSM measurement of intracellular Zn^{2+} accumulation illustrated a fast increase inside the nucleus after treatment with ZnO NP (4-5 nm, 15-18 nm) and $ZnCl_2$ (Figure 27). The treatment with ZnO NP (4-5 nm) resulted in a strong nuclear Zn^{2+} distribution after 10 min (+ 1062 %) and + 1729 % after 20 min. This level remained largely unchanged until the end of measurement (Figure 27A). ZnO NP (15-18 nm) treatment showed as well a fast Zn^{2+} distribution in the nucleus. FluoZin™-3 enriched continuously in the nucleus after 10 min of treatment with ZnO NP (15-18 nm) achieving a maximum of + 611 % after 40 min compared to the control (Figure 27B). Figure 27C shows the Zn^{2+} accumulation in the nucleus after treatment with $ZnCl_2$. This exposure results as well in a fast nuclear increase of Zn^{2+} after 1 min, but not with the same intensity as shown for ZnO NP. This Zn^{2+} level was increased up to + 261 % after 10 min and remained until the end of measurement (Figure 27C). The cells of cLSM measurement in Figure 18-27 were analyzed using software Image J 1.47f and the intensity of FluoZin™-3 in the nucleus of each point in time was referred to the untreated control. The control was set as 100 %.

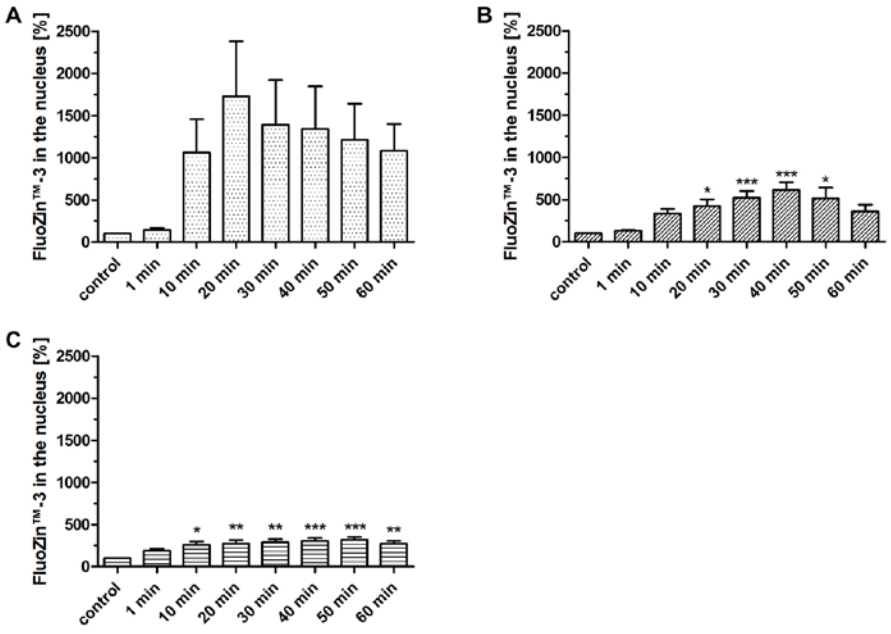

Figure 27: Measurement of nuclear Zn^{2+} accumulation

Live imaging of A549 cells loaded with FluoZin™-3, indicating Zn^{2+}, and exposed to ZnO NP (4-5 nm, 18-15 nm) and $ZnCl_2$. All treatments resulted in a fast accumulation of FluoZin™-3 in the nucleus. (A) Exposure to ZnO NP (4-5 nm) resulted in a fast and strong distribution of Zn^{2+} up to 1062 % after 10 min and with a maximum of + 1729 % after 20 min. (B) ZnO NP (15-18 nm) exposure resulted in a continuous Zn^{2+} distribution in the nucleus after 10 min with a maximum of + 611 % after 40 min compared to the control. (C) Treatment to $ZnCl_2$ led to a fast accumulation of Zn^{2+} in the nucleus after 1 min. This Zn^{2+}-level was more increased after 10 min up to 261 % and holding this level until the end of measurement. * = $p<0.05$, ** = $p<0.01$, *** = $p<0.001$; N=3.

4.3 Toxicity of ZnO NP

4.3.1 Cellular viability after ZnO NP treatment

The toxicity of different ZnO NP concentrations was analyzed by Alamar Blue® assay using a reagent containing resazurin. This non fluorescent dye is oxidized to the fluorescent product resorufin by viable cells. Color intensity was then referred to the number of viable cells measured by crystal violet staining of the cells and compared to the control set as 100 %. Figure 28 shows the cellular viability after treatment with both sizes of ZnO NP (A: 4-5 nm, B: 15-18 nm) of three different concentrations (0.1 µg/mL, 10 µg/mL, and 100 µg/mL) over the period in time. Figure 28A shows no reduction of cellular viability after treatment with 0.1 and 10 µg/mL of ZnO NP (4-5 nm). The exposure to 100 µg/mL resulted in a continuous decrease of viability to ~ 50 % after 4 h (Figure 28A). In contrast, the exposure to 0.1µg/mL ZnO NP (15-18 nm) resulted in an increase of cellular viability up to 137 % and this level remained until the end of measurement (4 h) (Figure 28B). The treatment with 10 µg/mL resulted in a similar increase. Exposure to 100 µg/mL ZnO NP (15-18 nm) resulted in a slight decrease ending in a maximal reduction of 17 % after 4 h (Figure 28B).

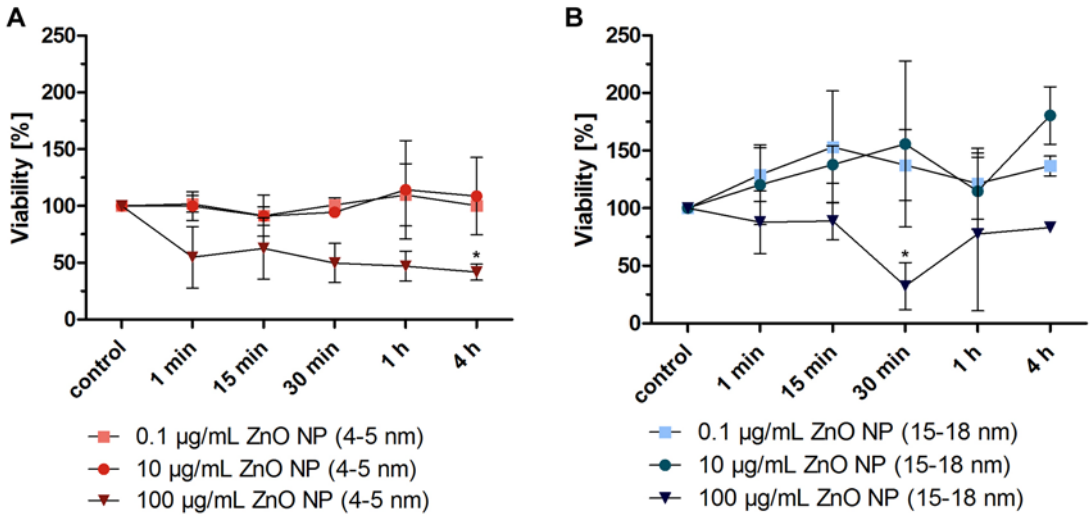

Figure 28: Cellular viability after ZnO NP treatment

The cellular viability of ZnO NP (4-5 nm and 15-18 nm) was measured using Alamar Blue®. Three different particle concentrations of 0.1, 10, and 100 µg/mL in A549 cells were applied. (A) 0.1 and 10 µg/mL of ZnO NP (4-5 nm) resulted in no reduction of cellular viability. Treatment with 100 µg/mL led to a continuous decrease of cellular viability. (B) The treatment with 0.1 µg/mL ZnO NP (15-18 nm) resulted in an initial increase until 15 min and keeping this level. Exposure to 10 µg/mL of ZnO NP (15-18 nm) led to a continuous increase until the end of measurement. The treatment with 100 µg/mL resulted in a slight reduction of cellular viability. Square = 0.1 µg/mL, dot = 10 µg/mL, and triangle = 100 µg/mL; * = $p<0.05$; N=3.

4.3.2 Stabilization of ZnO NP with BSA

Bovine serum albumin (BSA) was used to stabilize ZnO NP, preventing the particle dissociation to Zn^{2+}. The treatment with ZnO NP resulted in a strong reduction of cellular viability after 24 h. This effect became abolished by BSA stabilization of ZnO NP (Figure 29). The treatment with 100 µg/mL ZnO NP (4-5 nm) caused ~ 80 % decrease of viable cells. This toxic effect was reversed by BSA coating and resulted in increased cellular viability compared to untreated control (Figure 29A). This effect can be seen likewise after treatment with ZnO NP (15-18 nm) (Figure 29B).

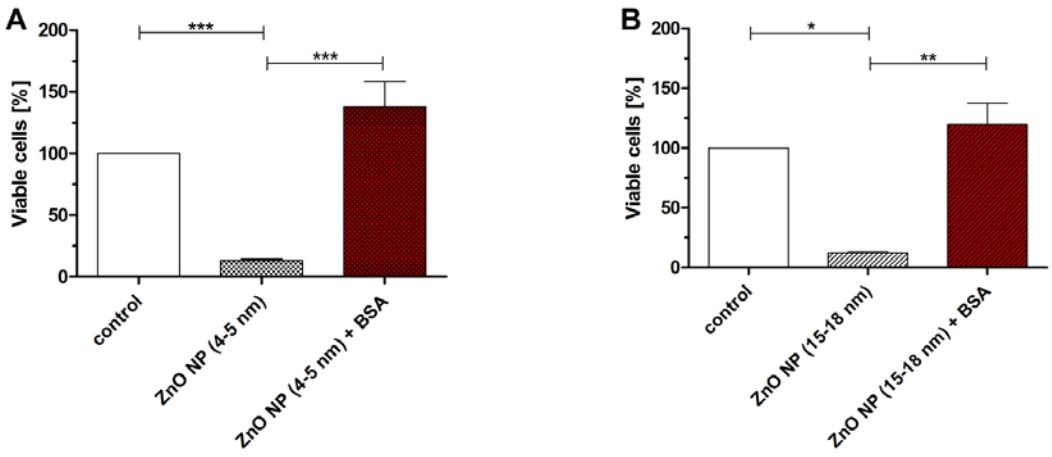

Figure 29: Analysis of viability after treatment with BSA coated ZnO NP

Cellular viability of A549 cells treated with ZnO NP and BSA stabilized ZnO NP after 24 h (100 µg/mL). (A) A549 cells treated with ZnO NP (4-5 nm). (B) A549 cells treated with ZnO NP (15-18 nm). BSA coating prevented cellular toxicity, while ZnO NP treatment caused ~ 80 % decrease of viable cells. * = $p<0.05$, ** = $p<0.01$, *** = $p<0.001$; N=3.

4.3.3 Measurement of intracellular reactive oxygen species

The generation of reactive oxygen species (ROS) may lead to DNA damages and is a discussed mechanism of nanoparticle induced toxicity. Intracellular ROS was analyzed after ZnO NP (4-5 nm, 15-18 nm) and $ZnCl_2$ treatment. ROS was determined using the compound H_2DCF-DA after exposure to ZnO NP, $ZnCl_2$, ZnO NP + BSA (particle stabilization), ZnO NP + DTPA (Zn^{2+} chelating) and ZnO NP + NAC (ROS scavenging). Hydrogen peroxide was used as positive control of ROS generation. Figure 30 shows the levels of ROS in untreated cells (light grey dots) and the H_2O_2 treated cells (grey quarters = 500 µM, black triangles = 1 mM) as positive controls. The untreated cells showed a maximal ROS-level with + 150 % after 6 h. Treatment with 500 µM H_2O_2 resulted in a continuous increase of ROS, reaching a stable level of about 450 %

after 2 h. A similar curve was found after treatment with 1 mM H_2O_2 reaching 630 % after 2 h.

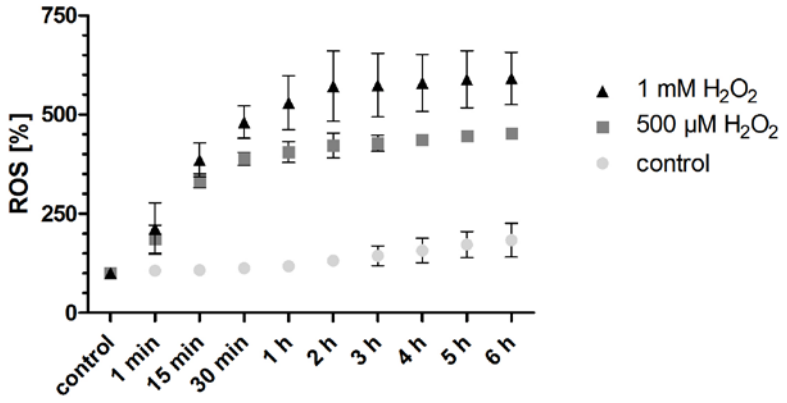

Figure 30: ROS-levels in untreated and H_2O_2 treated cells

Measurement of intracellular ROS-levels in A549 cells after treatment with 500 µM and 1 mM H_2O_2 as positive control for ROS. The control showed the level of ROS in untreated cells with a maximal increase of ROS up to ~ 150 % after 6 h. The treatment to the positive controls resulted in a continuous increase of intracellular ROS-levels reaching saturation after 1 h. The control showed a slight increase of ROS after 3 h. N=3.

In Figure 31A and B the ROS data of ZnO NP treated A549 cells are shown. Moreover, the controls including $ZnCl_2$, NAC, DTPA, and BSA coated ZnO NP are represented. The ROS-levels of each treatment were refered to the control of each point in time. All treatments except ZnO NP + NAC showed an approximately 25 % up-regulation of intracellular ROS until the first 30 min of exposure (Figure 31A and Figure 31B). The pretreatment with NAC was able to reduce the ROS-level strongly at all points in time to ~ 14 % compared to the untreated controls. Both sizes of BSA stabilized ZnO NP were able to reduce ROS generation after 30 min down to ~ 15 %. In spite of extracellular complexing of dissociated ZnO NP (4-5 nm) a 15 % up-regulation of ROS in the first 30 min followed by a down-regulation to basal levels was observed. The complexation of ZnO NP (15-18 nm) resulted in a generation of ROS up to 115 % in the first 30 min followed by a down-regulation to basal levels. Single treatment with ZnO NP (4-5 nm) resulted initially in increased ROS-levels (approx. + 25 %). In comparison to ZnO NP (4-5 nm), the exposure to ZnO NP (15-18 nm), reached an intracellular ROS-levels of 117 % after 1 min, 124 % after 15 min, and increased continuously to a maximum of 155 % after 6 h. $ZnCl_2$, as control for Zn^{2+}, led to increased intracellular ROS-levels comparable to ZnO NP treatment of both sizes until the first 30 min. After 30 min of $ZnCl_2$

exposure the ROS-levels increased further and achieved its maximum close to 200 % after 6 h.

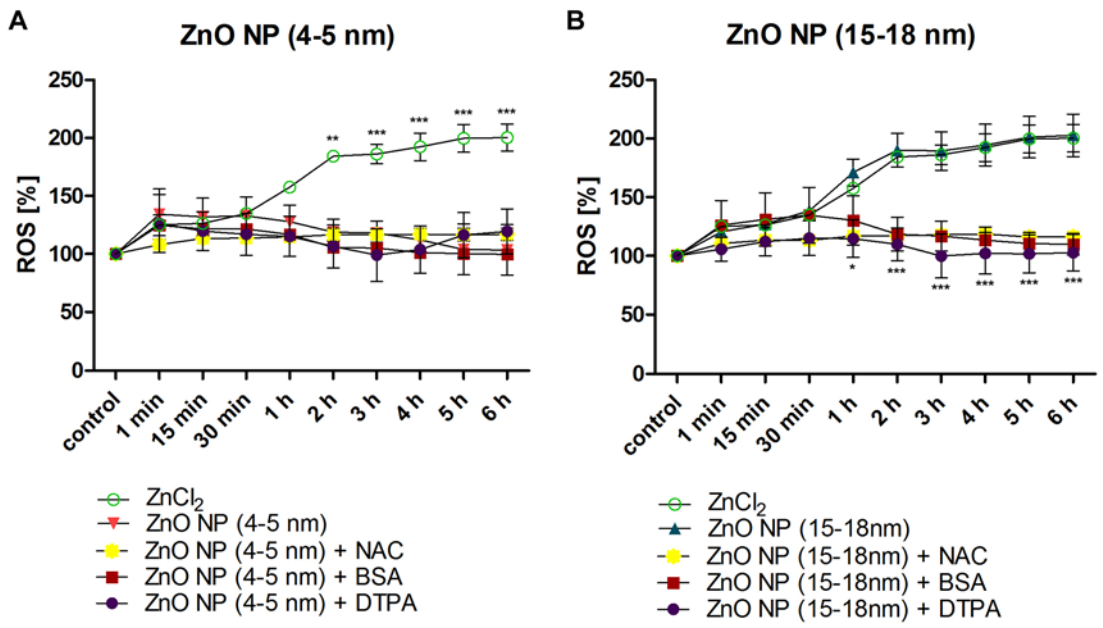

Figure 31: Measurement of intracellular ROS-levels

Measurement of intracellular ROS-levels in A549 cells after treatment with ZnO NP (4-5 nm, 15-18 nm), pretreatment with NAC, DTPA, stabilization of particles with BSA, and $ZnCl_2$ exposure. (A) Treatment with ZnO NP (4-5 nm, pink triangle) as well as all pretreatments led to slightly increased intracellular ROS-levels (~ 25 %) after the first 30 min. Then all treatments declined to basal levels. Exposure to $ZnCl_2$ resulted in continuously increased ROS-levels, reaching ~ 200 % (green circle). (B) Treatments with ZnO NP (15-18 nm) led to an up-regulation of ~ 25 % in the first 30 min returning to basal levels thereafter or reaching ~ 200 % in the case of $ZnCl_2$ (green circle). ZnO NP (15-18 nm) treatment resulted in further accumulation of ROS to levels reaching 150 % compared to the control (blue triangle). * = $p<0.05$, ** = $p<0.01$, *** = $p<0.001$ (all treatments are referred to ZnO NP single treatment), N=3.

4.3.4 Measurement of mitochondrial membrane potential

High levels of intracellular ROS are associated with the depolarization of mitochondrial membrane potential (ΔΨm) and released cytochrome c (cyt c) that further leads to apoptosis[129]. In order to investigate the mitochondrial response to ZnO NP and $ZnCl_2$, A549 cells were loaded with JC-1, a permeable, cationic, and mitochondrial specific fluorescent dye. JC-1 dye is subjected to form aggregates of multiple fluorophores in the highly electronegative environment of the mitochondrial matrix. The ΔΨm was measured after ZnO NP (4-5 nm, 15-18 nm) and $ZnCl_2$ treatment by fluorescence spectroscopy (Figure 32A). The acquired fluorescence images after treatment with ZnO NP (4-5 nm), ZnO NP (15-18 nm), and $ZnCl_2$ were visualized by fluorescence microscopy (Figure 32B). Figure 32A shows that ZnO NP (4-5 nm, pink triangle) as well as $ZnCl_2$ (green circle) treatment led to similar results and showed no depolarization of ΔΨm. In contrast

to these findings, the exposure to ZnO NP (15-18 nm, blue triangle) showed a continuous depolarization of ΔΨm with a maximum decrease to 25 % after 6 h. In Figure 32B the fluorescence images of A549 cells loaded with JC-1 dye before treatment and after 6 h of exposure to ZnO NP (4-5 nm, 15-18 nm) and $ZnCl_2$ comparable to the spectrofluorometric measurements are shown. In healthy cells, JC-1 forms J-aggregates with intense red fluorescence as seen in Figure 32B (control). However, in cells with depolarized ΔΨm the dye converted to monomers which exhibit green fluorescence (positive control, CCCP). Figure 32B shows the overlay images of red and green emission and demonstrates the ΔΨm in A549 cells after 6 h.

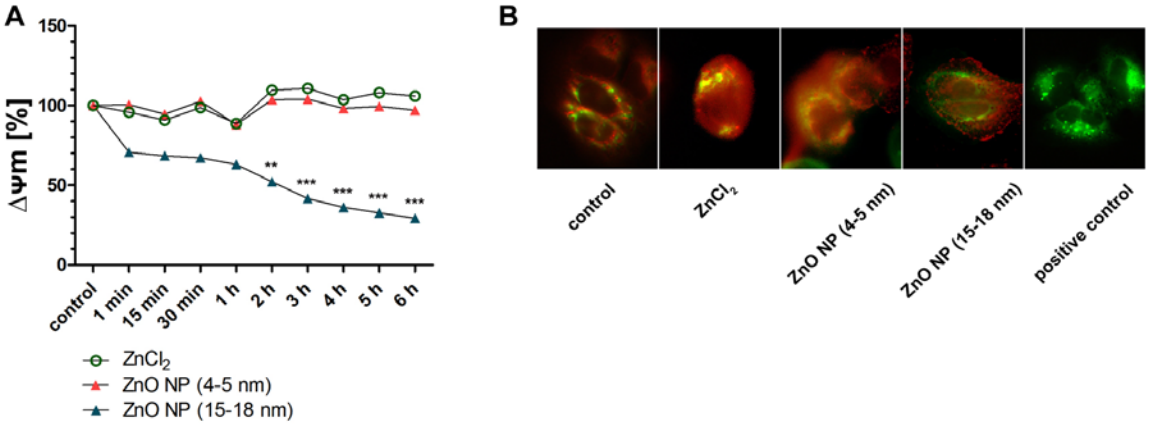

Figure 32: Analysis of ΔΨm after treatment with ZnO NP (4-5 nm), ZnO NP (15-18 nm), and $ZnCl_2$

(A) Spectrofluorimetric measurement of ΔΨm in A549 cells after treatment with ZnO NP (4-5 nm, 15-18 nm) and $ZnCl_2$. Mitochondrial membrane integrity was not reduced by ZnO NP (4-5 nm) and $ZnCl_2$ treatment. Treatment with ZnO NP (15-18 nm) showed a continuously decrease of ΔΨm to ~ 30 % after 6 h. (B) Corresponding fluorescence microscopy images of ΔΨm in untreated and treated cells after 6 h of ZnO NP (4-5 nm and 15-18 nm) and $ZnCl_2$ treatment. Red = polarized ΔΨm; green = depolarized ΔΨm. ** = $p<0.01$, *** = $p<0.001$ (all treatments are referred to ZnO NP (15-18 nm) treatment), N=3.

4.4 DNA damage analysis after ZnO NP exposure

γH2A.X immunofluorescence assay was performed to visualize and quantify DNA damages as well as the activation of DNA damage repair signaling after treatment with ZnO NP or $ZnCl_2$.

4.4.1 Concentration-dependent analysis of ZnO NP genotoxicity

Genotoxicity of ZnO NP has been analyzed in three different cell lines (A549, HNSCCUM-02T and NIH/3T3). The main uptake pathway of nanoparticles is by inhalation through the respiratory epithelia, therefore HNSCCUM-02T was used as a model for the primary upper contact area and A549 cells were used as model for the lower respiratory tract. NIH/3T3 cells served as fibroblast control. The cells were treated with 0.1, 10 and 100 µg/mL ZnO NP and the generation of DNA DSB was evaluated using γH2A.X immunofluorescence assay (see 3.2.7.6). The DNA damages after ZnO NP (4-5 nm) and ZnO NP (15-18 nm) treatments were investigated in three cell lines and the results are shown in Figure 33 and Figure 34.

4.4.1.1 Treatment of cell lines with ZnO NP (4-5 nm)

The treatment of all three cell lines with ZnO NP (4-5 nm) resulted in slight increase of DNA damages after 1 min (Figure 33A, B and C). A549 treatment with ZnO NP (4-5 nm) resulted in a concentration-dependent increase of DNA DSB after 15 min (Figure 33D), while the comparable treatments to HNSCCUM-02T- and NIH/3T3 cells showed no DNA damages (Figure 33E und F). The observed DNA damages in A549 cells after 15 min were not seen after 1 h presumably because of DNA damage repair activation (Figure 33G). NIH/3T3 cells reacted with a strong concentration-dependent phosphorylation of H2A.X to ZnO NP (4-5 nm) treatment (Figure 33I). Figure 33K showed a strong increase of DNA DSB in HNSCCUM-02T cells after 4 h of exposure (10 µg/mL ≙ + 1982 %, 100 µg/mL ≙ + 1992 %). Similar to HNSCCUM-02T cells, NIH/3T3 cells showed a strong phosphorylation of H2A.X after 4 h exposed to the highest ZnO NP concentration. After 24 h in all cell lines a dose-dependent increase of DNA DSB was observed and non remaining cells after treatment with the highest concentration were detected.

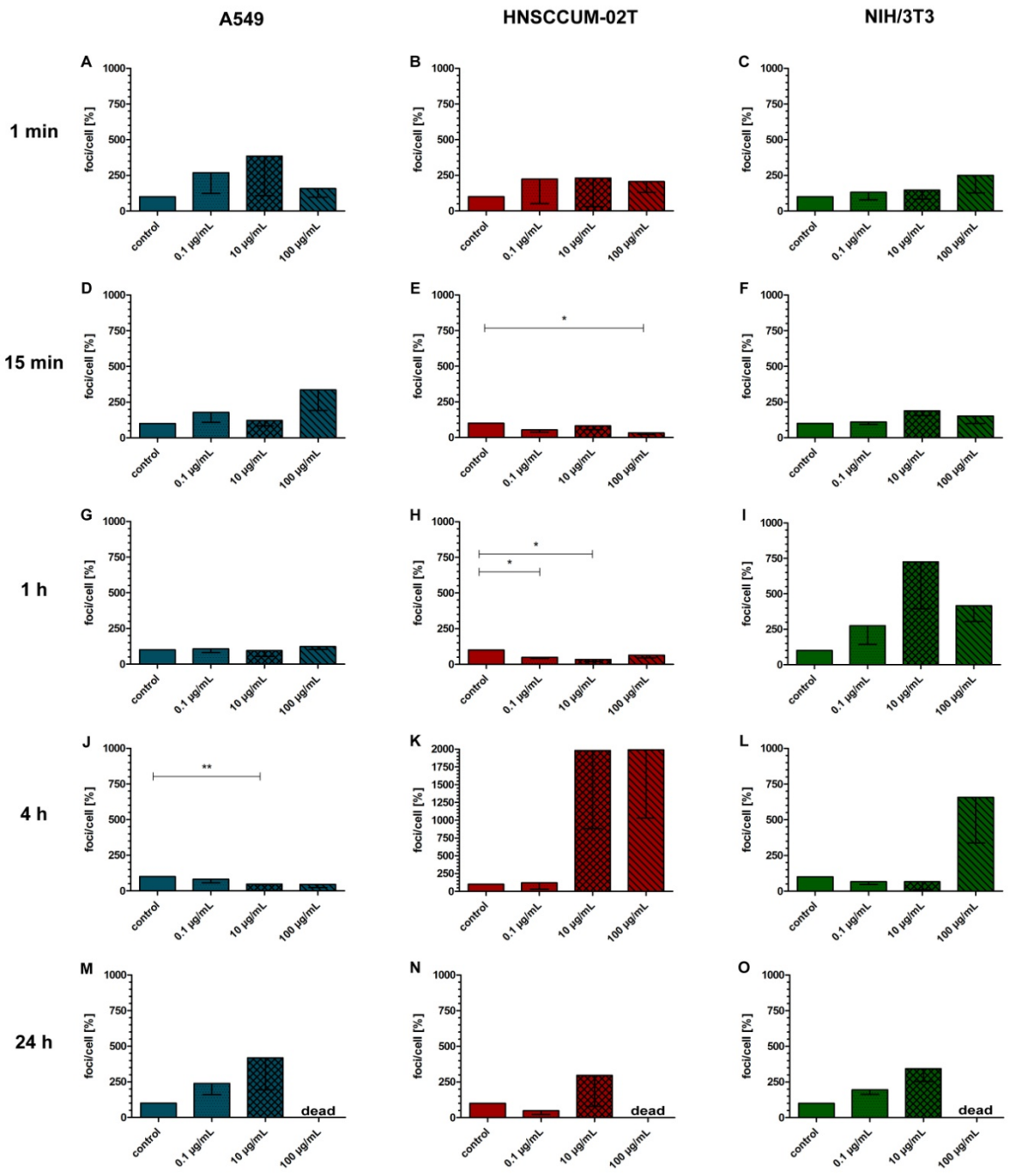

Figure 33: Concentration-dependent analysis of ZnO NP (4-5 nm) treated cells

A549, HNSCCUM-02T, and NIH/3T3 cells were exposed to ZnO NP (4-5 nm) with three different concentrations (0.1, 10, and 100 µg/mL) for the indicated points in time. DNA DSB were quantified by γH2A.X-foci analysis. Dead = no cells remaining. * = $p<0.05$, ** = $p<0.01$; N=3.

4.4.1.2 Treatment of cell lines with ZnO NP (15-18 nm)

ZnO NP (15-18 nm) treatment of HNSCCUM-02T cells with the highest concentration resulted in a strong generation of DNA DSB (+ 2924 %) after 1 min (Figure 34). In contrast, A549 and NIH/3T3 cells showed no or weak increase of DNA DSB. ZnO NP (15-18 nm) exposure to A549 cells with the highest concentration resulted in strongly increased DNA damages (+ 455 %) after 15 min (Figure 34D). The utilized treatments of HNSCCUM-02T cells resulted in the generation of DNA DSB applied to 0.1 and 10 µg/mL. DNA DSB in NIH/3T3 were observed in a dose-dependent increase after 15 min of ZnO NP exposure (Figure 34E und F). Treatment of NIH/3T3 resulted in no further DNA damages after particle exposure for 1 h, 4 h, and 24 h (Figure 34I, L, O). The exposure to the highest applied concentration resulted in increased DNA DSB in HNSCCUM-02T cells after 1 h and 4 h (Figure 34H und K). Treatments of A549 and NIH/3T3 cells led to no DNA damages after 1 h and 4 h of ZnO NP exposure (Figure 34G, I, J, and L). 24 h of particle exposure resulted in a dose-dependent increase of DNA DSB in A549 and HNSCCUM-02T cells as well as a weak increase in NIH/3T3 cells (Figure 34M, N, and O). After 24 h, no remaining cells were observed after treatment with highest concentration.

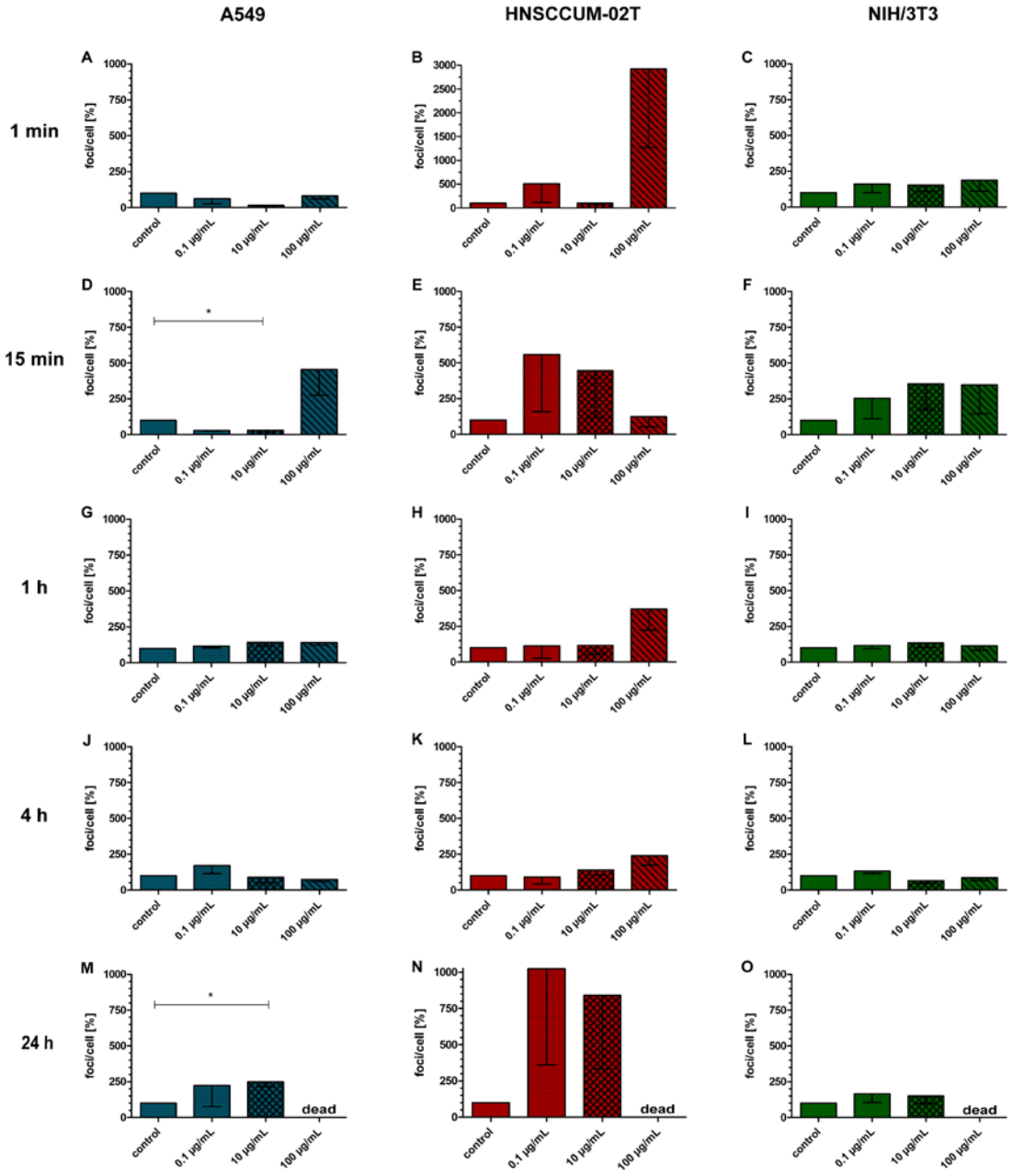

Figure 34: Concentration-dependent analysis of ZnO NP (15-18 nm) treated cells

A549, HNSCCUM-02T, and NIH/3T3 cells were exposed to ZnO NP (15-18 nm) with three different concentrations (0.1, 10, and 100 µg/mL) for the indicated points in time. DNA DSB were quantified by γH2A.X foci analysis. Dead = no cells remaining. * = $p<0.05$; N=3.

4.4.1.3 Analysis of $ZnCl_2$ genotoxicity in A549 cells

The genotoxicity of $ZnCl_2$ at comparable concentrations as used for ZnO NP treatments was analyzed in A549 cells. The treatment with $ZnCl_2$ showed early and strong increased DNA DSB after 1 min compared to 15 min observed for ZnO NP (15-18 nm). As seen after exposure to nanoparticles, foci counts per cell decreased in the following period in time. According to the observations made with the nanoparticles, the highest concentration of applied $ZnCl_2$ resulted in no detectable cells after 24 h, most likely because of cell death.

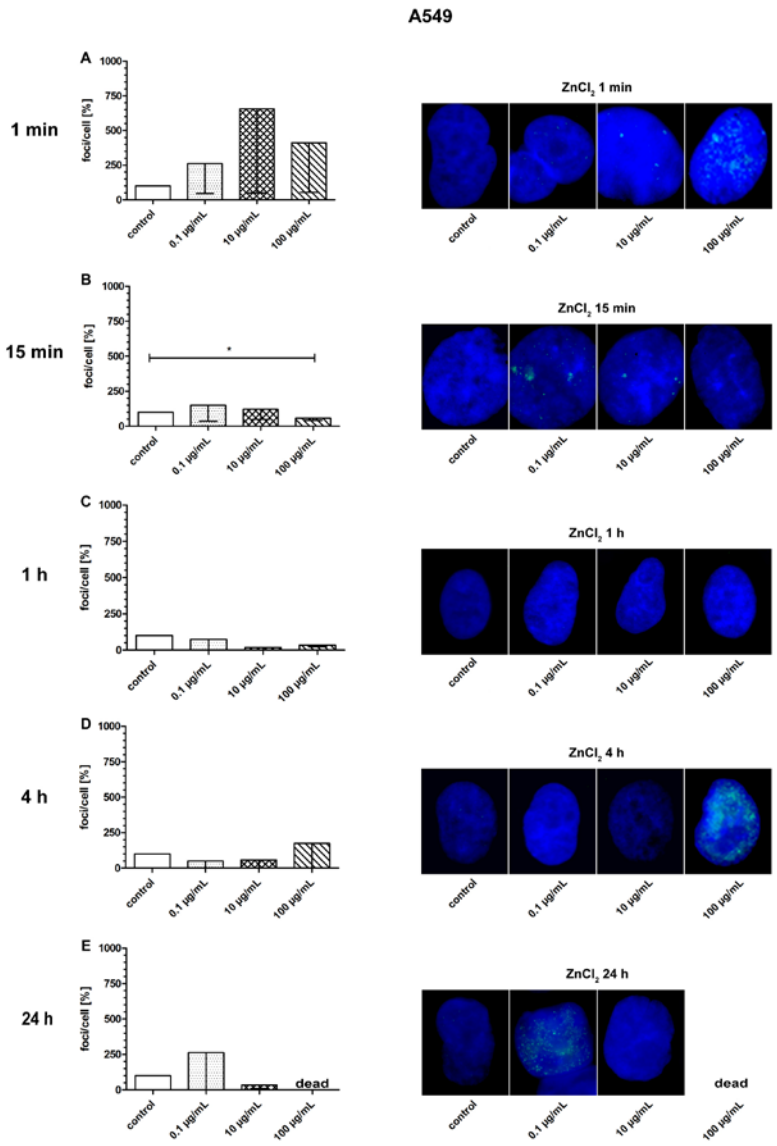

Figure 35: Analysis of DNA DSB after $ZnCl_2$ treatment of A549 cells

A549 cells were exposed to $ZnCl_2$ for the indicated points in time and concentrations. DNA DSB were quantified by γH2A.X foci analysis. DNA damages were strongly increased after 1 min of $ZnCl_2$ exposure. Treatment to the highest concentration resulted in no remaining cells after 24 h. * = $p<0.05$; N=3.

4.4.2 Time-dependent genotoxicity of ZnO NP, ZnO bulk and $ZnCl_2$

In order to investigate the time-dependent DNA damages after ZnO NP, ZnO bulk, and $ZnCl_2$ treatment, A549 cells were treated with the highest concentration of 100 µg/mL. Concerning the fast damaging effect of ZnO NP and $ZnCl_2$ as shown in 4.4.1.2 and 4.4.1.3 the measurement was made at several points in time until 4 h. The generation of DNA DSB was evaluated using γH2A.X immunofluorescence assay (see 3.2.7.6). Three different pretreatments with ZnO NP + DTPA (see 3.2.4.2), ZnO NP + NAC (see 3.2.4.3), and ZnO NP + BSA (see 3.2.4.4) were investigated. NP are supposed to have higher reactivity and therefore enhanced toxicity, because of their increased surface area to volume ratio. In addition to ZnO NP we used ZnO bulk material with reduced surface area to volume ratio to compare their genotoxic effects. $ZnCl_2$ was used as positive control for Zn^{2+}.

4.4.2.1 Treatment of A549 cells with ZnO NP (4-5 nm)

The treatment with ZnO NP (4-5 nm) resulted in fast generated DNA DSB (up to 336 %) after 15 min indicated by γH2A.X immunofluorescence staining (Figure 36A). This fast increase of DNA damages is followed by a quick dephosphorylation of H2A.X to basal levels. To differentiate between the generation of DNA DSB caused by ROS or dissociated ZnO NP, the cells were pretreated with NAC or DTPA. ROS scavenging by NAC prior to the treatment with ZnO NP showed reduced DNA DSB after 15 min, but still a slight increase of γH2A.X up to 150 % after 30 min (Figure 36B). The complexation of Zn^{2+} by DTPA resulted in a similar result as shown for ROS scavenging with ~ + 150 % after 30 min of treatment (Figure 36C).

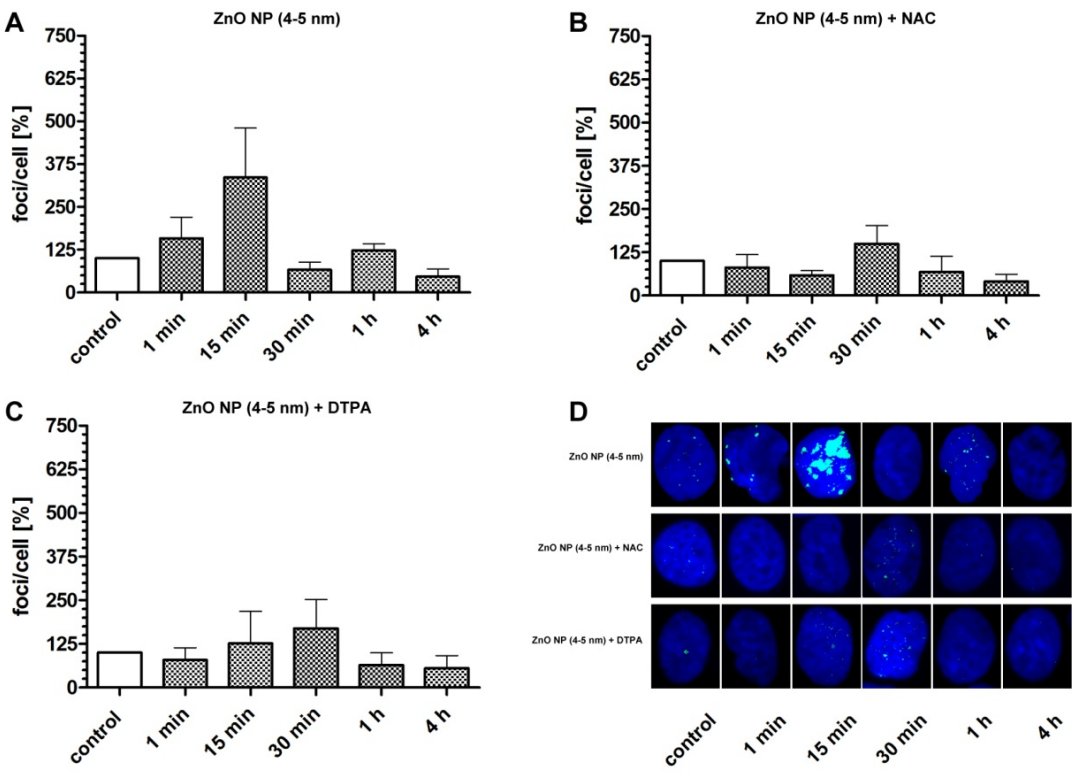

Figure 36: Quantification of DNA DSB after ZnO NP (4-5 nm) treatment

(A) Single treatment with ZnO NP (4-5 nm) resulted in increased DNA DSB up to 336 % after 15 min. This fast H2A.X phosphorylation is followed by recovery to basal levels until 4 h. (B) The particle treatment after ROS scavenging with NAC showed a slight increase of γH2A.X up to 150 % after 30 min followed by dephosphorylation to basal levels. (C) The complexation of Zn^{2+} by DTPA resulted in H2A.X phosphorylation up to 170 % after 30 min. (D) Representative images of foci suitable to graph A-C are shown. N=3.

4.4.2.2 Treatment of A549 cells with ZnO NP (15-18 nm)

Immunostaining of γH2A.X foci indicated a fast increase of DNA DSB after 15 min of ZnO NP (15-18 nm) treatment to 455 % of control (Figure 37A). This fast increase was followed by a fast desphosphorylation to basal levels prior to a second increase of foci counts after 1 h, keeping this level until the end of measurement. In Figure 37B the ROS-dependent generation of DNA DSB after ZnO NP (15-18 nm) + NAC treatment is shown. NAC was able to reduce γH2A.X strongly, but DNA DSB remained high after 15 min (+ 61 %). The extracellular chelation with DTPA prior to ZnO NP treatment impaired DNA DSB completely (Figure 37C). Figure 37D shows representative γH2A.X foci images.

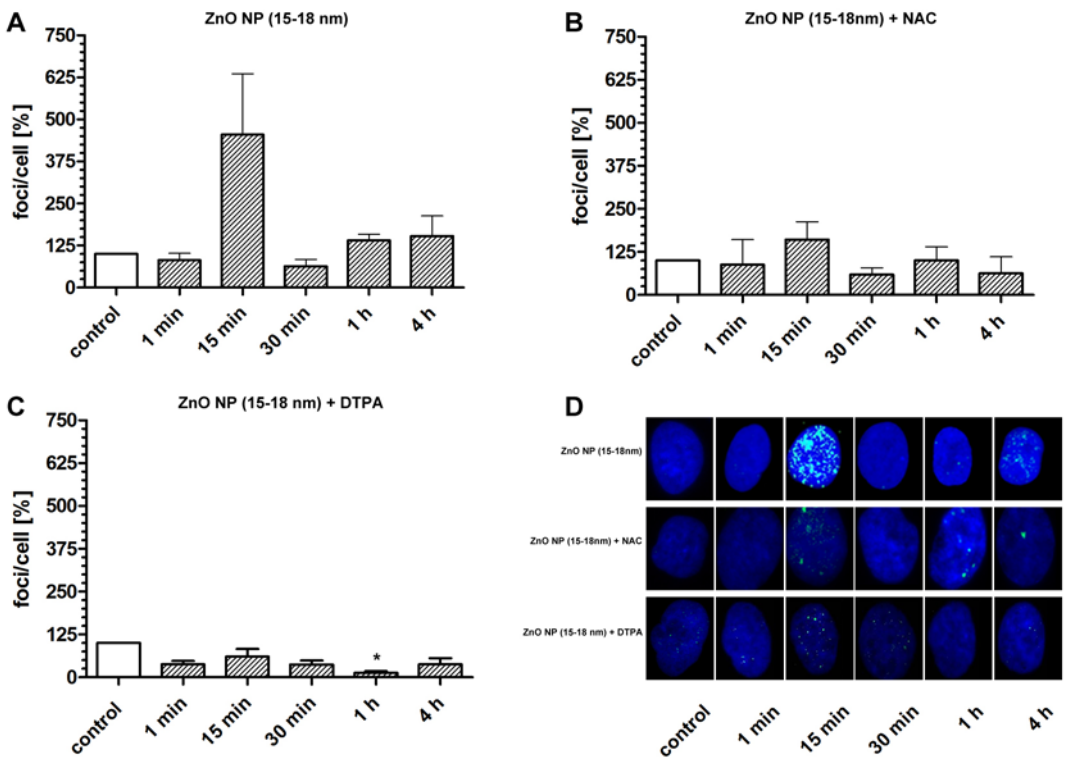

Figure 37: Quantification of DNA DSB after ZnO NP (15-18 nm) treatment

(A) The treatment with ZnO NP (15-18 nm) resulted in increased DNA DSB up to 455 % after 15 min. This fast increase after ZnO NP (15-18 nm) treatment is followed by fast dephosphorylation prior to a second, weaker, increase of foci numbers after 1 h until 4 h. (B) ROS scavenging by NAC was able to reduce the generation of foci after ZnO NP (15-18 nm) treatment, but the level of DNA DSB remain increased after 15 min (+ 61 %). (C) The extracellular complexation of Zn^{2+} by DTPA resulted in a complete inhibition of DNA DSB generation. (D) Representative images of γH2A.X foci suitable for graphic A-C. * = $p<0.05$; N=3.

4.4.2.3 Treatment of A549 cells with BSA stabilized ZnO NP

Bovine serum albumin (BSA) is able to stabilize ZnO NP (e.g., to reduce particle dissociation). The stabilization of ZnO NP (4-5 nm) using BSA resulted in DNA DSB up to ~ + 180 % (Figure 38A). DNA damages kept unchanged until 1 h and then were dephosphorylated to basal levels after 4 h (Figure 38A). BSA coated ZnO NP (15-18 nm) induced a weak phosphorylation of H2A.X up to 134 % after 30 min (Figure 38B).

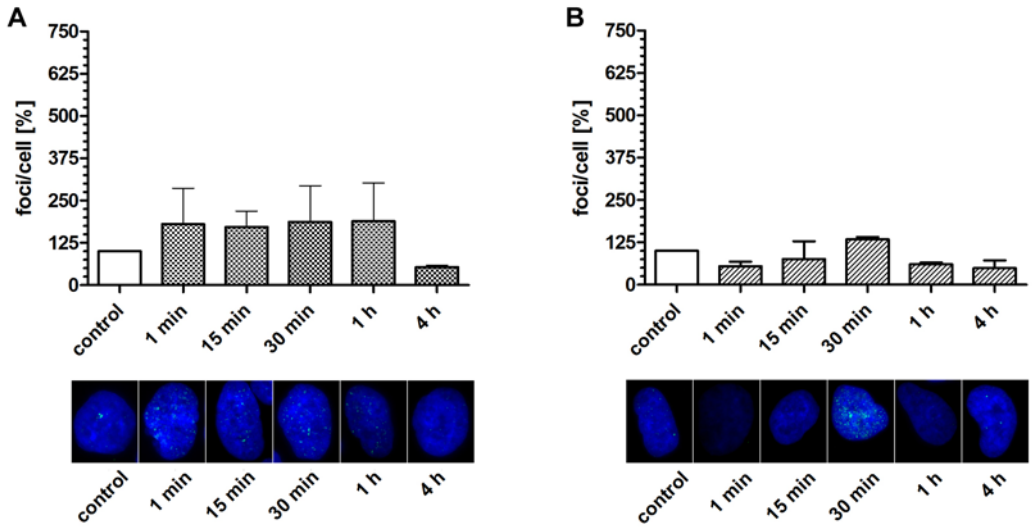

Figure 38: Quantification of DNA damages after exposure to BSA coated ZnO NP

(A) The exposure to BSA coated ZnO NP (4-5 nm) resulted in a fast phosphorylation of H2A.X up to 180 % after 1 min keeping this level for 1 h. (B) The treatment with BSA stabilized ZnO NP (15-18 nm) induced the phosphorylation of H2A.X up to 134 % after 30 min followed by dephosphorylation of H2A.X, indicating reduced DNA DSB. N=3.

4.4.2.4 Treatment of A549 cells with $ZnCl_2$ and ZnO bulk material

In Figure 39 the generation of DNA DSB after $ZnCl_2$ treatment is shown. $ZnCl_2$ induced a two phase generation of DNA DSB. The phosphorylation of H2A.X was observed quickly and strongly with an up-regulation to + 412 % after 1 min followed by recovery to basal levels. The second peak of foci formation was observed after 4 h with + 556 % (Figure 39). In order to investigate the genotoxic response of A549 cells to ZnO bulk material in contrast to nanoparticulated material, cells were treated with ZnO bulk in the highest concentration (100 µg/mL) and for the same points in time as mentioned for ZnO NP. Treatment to ZnO bulk showed a DNA damaging potential. Figure 40 shows a strong phosphorylation of H2A.X generated by ZnO bulk after 30 min of exposure. ZnO bulk phosphorylated H2A.X up to 334 % after 30 min followed by a continued dephosphorylation of γH2A.X until 4 h (Figure 40).

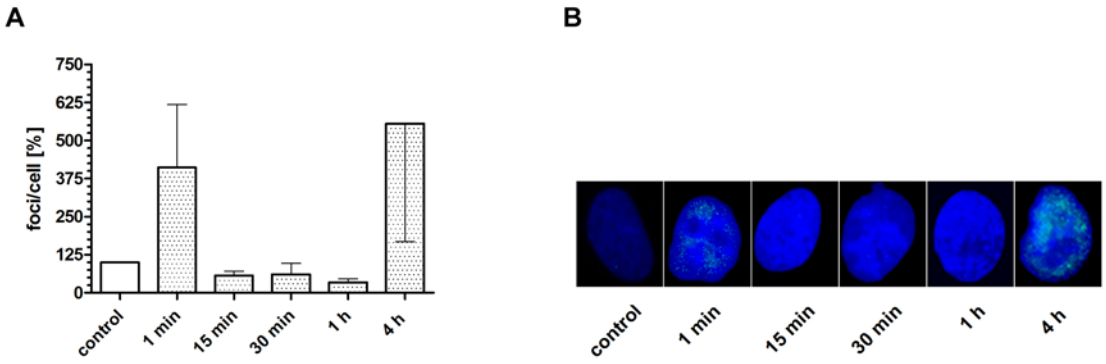

Figure 39: Quantification of DNA DSB after exposure to $ZnCl_2$

(A) The exposure to $ZnCl_2$ led to a similar biphasic generation of DNA damages in A549 cells as shown for ZnO NP (15-18 nm). The phosphorylation of γH2A.X showed two maxima after 1 min (+ 412 %) and 4 h (+ 556 %). (B) Corresponding representative γH2A.X images of A549 cells after treatment with $ZnCl_2$. N=3.

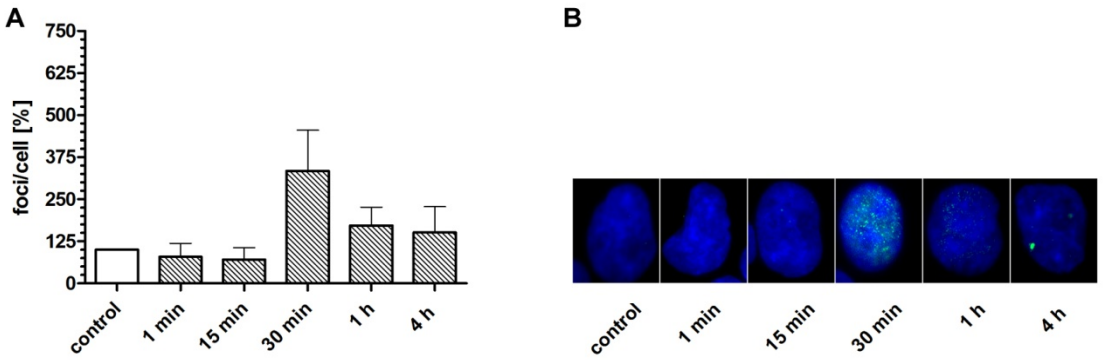

Figure 40: Quantification of DNA DSB after treatment with ZnO bulk material

(A) The exposure to ZnO bulk material showed a strong phosphorylation of H2A.X after 30 min. The ZnO bulk material activated H2A.X up to 334 % followed by a continued dephosphorylation of γH2A.X. (B) γH2A.X images of treated A549 cells with ZnO bulk material. N=3.

4.5 DNA damage response signaling

The cellular response to DNA damages is mainly mediated by the ATM or ATR kinases. ATM is mainly phosphorylated in the presence of DNA DSB, whereas ATR is activated in response to DNA SSB. These sensor proteins recognize the DNA damage and transfer the signal to effector proteins such as Chk1, Chk2, p53, and p21 promoting the DNA DDR. To investigate the impact of ZnO NP and $ZnCl_2$ on the activation of DDR, phosphorylated ATM was analyzed by ELISA (see 3.2.8.4). The proteins pChk2, p53, p21, ATR, and pChk1 were investigated by Western blotting (see 3.2.8.3.3). All presented data based on ZnO NP (15-18 nm) and $ZnCl_2$ treatments in a final concentration of 100 µg/mL. In the following section, ZnO NP (15-18 nm) are just named ZnO NP.

4.5.1 Analysis of ATR/Chk1 pathway

ATR is related to DNA single strand breaks (DNA SSB) as frequently observed after ROS induced DNA damages. Neither ATR nor Chk1 activation was observed after treatment with ZnO NP. In Figure 41A the level of ATR phosphorylation is shown. No activation of ATR after ZnO NP exposure was observed. Figure 41C shows a representative Western blot corresponding to Figure 41A. In fact, it was observed that the downstream kinase of ATR, pChk1 was dephosphorylated after ZnO NP treatment starting after 30 min and lasting until the end of measurement (see Figure 41 B/D).

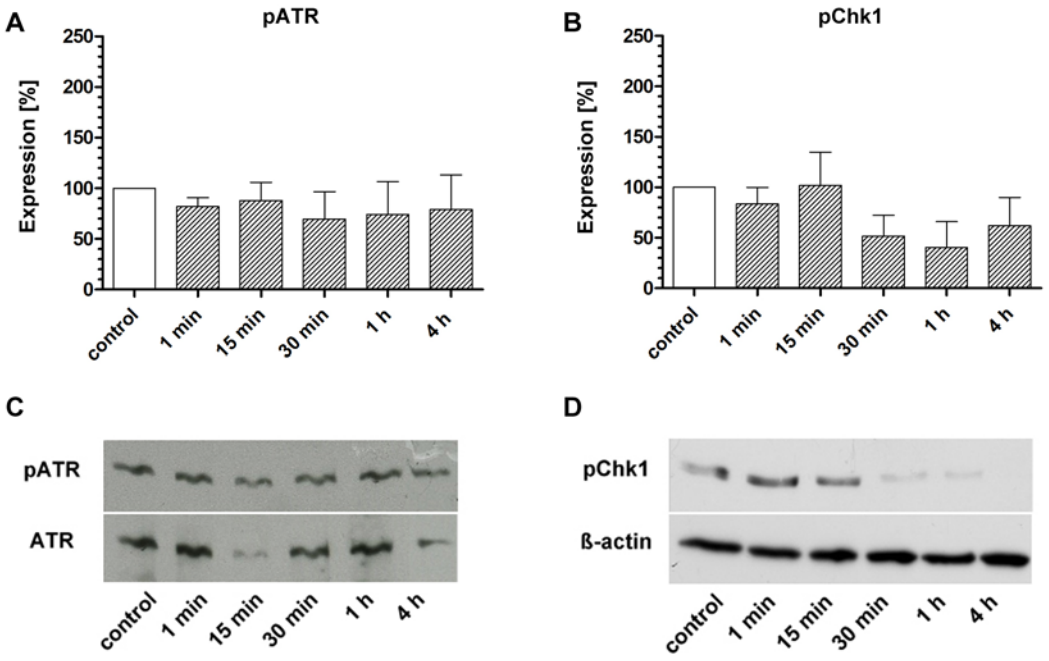

Figure 41: Western blot analysis of ATR/Chk1 pathway after ZnO NP treatment

(A) No phosphorylation of ATR was observed after ZnO NP treatment. (B) Reduced activation of Chk1 was observed after 30 min of ZnO NP exposure. (C) Representative Western blot of phosphorylated ATR referred to total ATR. (D) Representative Western blot of pChk1 referred to ß-actin. N=3.

4.5.2 Analysis of ATM/Chk2 signaling

ZnO NP and $ZnCl_2$ treatment resulted in H2A.X phosphorylation representing DNA DSB (see 4.4.2.2 and 4.4.2.4). DNA DSB resulted in activation of DDR, especially in activation of ATM/Chk2 pathway. The ATM phosphorylation status was investigated after ZnO NP and $ZnCl_2$ treatment. The results of pATM quantification in A549 cells is shown in Figure 42A and B. Accordingly, ATM as the major kinase, activated after induction of DNA DSB, was activated up to ~ 200 % after 30 min. This level was kept until the end of measurement (Figure 42A). $ZnCl_2$ treatment activated ATM similar to ZnO NP but faster, reaching the level of 200 % already after 15 min (Figure 42B).

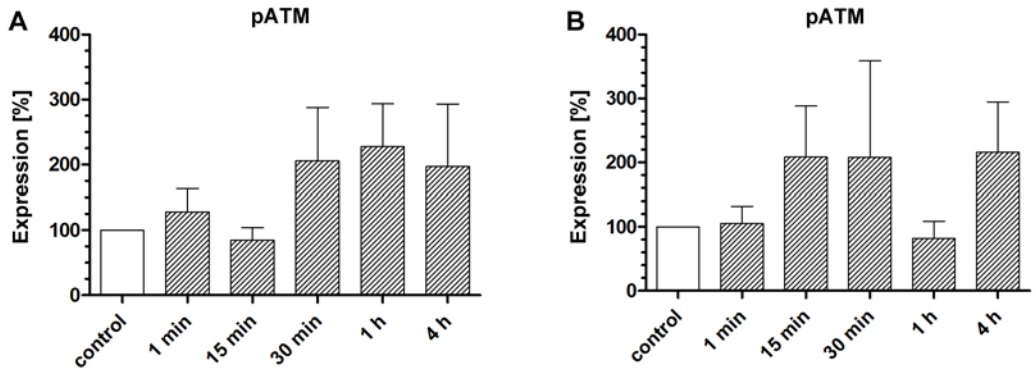

Figure 42: ELISA measurements of pATM after ZnO NP and $ZnCl_2$ treatment

A549 cells were exposed to 100 µg/mL of ZnO NP or $ZnCl_2$, respectively. (A) ZnO NP activated the ATM damage response pathway up to ~ 200 % after 30 min of exposure keeping this level until the end of measurement. (B) $ZnCl_2$ stimulated the phosphorylation of ATM more fastly after 15 min of exposure. ATM phosphorylation returned to basal level after 1 h. N=3.

4.5.2.1 Analysis of ATM downstream signaling

ZnO NP and $ZnCl_2$ induced DNA DSB as well as ATM activation, thus downstream signaling of ATM was evaluated. The activation of the effector proteins Chk2, p53, p21 after ZnO NP and $ZnCl_2$ treatment was observed. Chk2, p53, and p21 got activated during exposure to ZnO NP and $ZnCl_2$, respectively. In Figure 43A the phosphorylation of Chk2 is shown after ZnO NP treatment. Chk2 was increasingly activated starting 15 min after exposure until the end of measurement. The maximum pChk2 level during measurement was achieved with up to 174 % after 4 h (Figure 43A). Compatible with these data p53 was activated by ZnO NP only moderately and lately increased after 4 h to ~ 150 % (Figure 43B). In Figure 43E the slight activation of p21 after ZnO NP treatment is shown (+ 30 %). $ZnCl_2$ activated p21 up to 161 % after 4 h of exposure (Figure 43F). The exposure to $ZnCl_2$ led to a two phase phosphorylation of Chk2. In Figure 43B a slight activation of Chk2 after 15 min (+ 13 %) and a stronger phosphorylation after 4 h (+ 50 %) is shown. An equal level of pChk2 in ZnO NP and $ZnCl_2$ treated A549 cells was observed after 4 h (Figure 43A and B). P53 activation was also found after $ZnCl_2$ treatment. The activation of p53 up to 116 % was found after 4 h of $ZnCl_2$ treatment (Figure 43D). Figure 43G and H show the representative Western blots after ZnO NP and $ZnCl_2$ treatment.

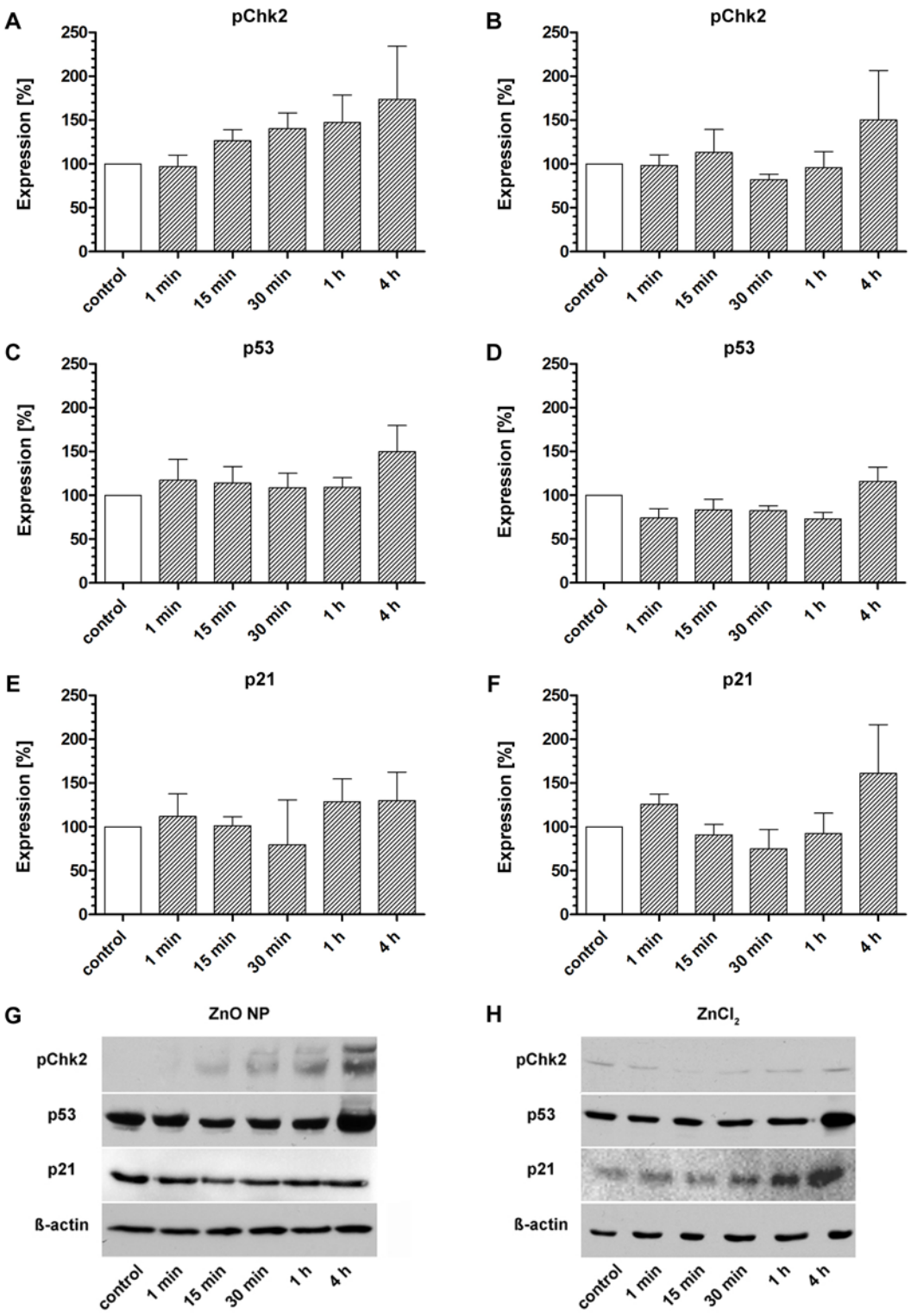

Figure 43: Western blot analysis of ATM downstream signaling after ZnO NP and $ZnCl_2$ exposure

Graph A, C, and E represent the results of ZnO NP treatment whereas B, D, and F represent the findings of $ZnCl_2$ treatment. (A) Chk2 phosphorylation increased continuously after 15 min until the end of exposure (4 h). (B) Slight phosphorylation of Chk2 after 15 min and stronger phosphorylation after 4 h of $ZnCl_2$ exposure. (C) Strong stabilization of p53, 4 h after ZnO NP exposure. (D) Stabilization of p53, 4 h after exposure to $ZnCl_2$. (E) Slight activation of p21 after ZnO NP treatment. (F) Stong activation of p21 by $ZnCl_2$ after 4 h. (G) and (H) showed the representative Western blots to graphic A-F. N=3.

4.5.2.2 Analysis of ATM downstream signaling after ROS scavenging and Zn^{2+} complexation

ATM/Chk2 signaling is activated by ZnO NP. To further evaluate the underlying mechanisms of Chk2/p53/p21 activation after ZnO NP exposure, we pretreated the cells with NAC and DTPA. Western blot analyses of pChk2, p53, and p21 were investigated after ROS scavenging and extracellular complexation of Zn^{2+}. In Figure 44A and B the activation of Chk2 is shown after ROS scavenging and ZnO NP treatment. In absence of ROS we observed persisting increased pChk2 up to ~ + 125 % and this level was kept until the end of measurement. Figure 44C shows a continuous up-regulation of p53 despite ROS scavenging. The p53-level was comparable to the single treatment of ZnO NP without any substitutes (cf. Figure 43C). Figure 44E shows the up-regulation of p21 after ZnO NP + NAC treatment. P21 reached a level of + 150 % after 4 h of treatment (Figure 44E).

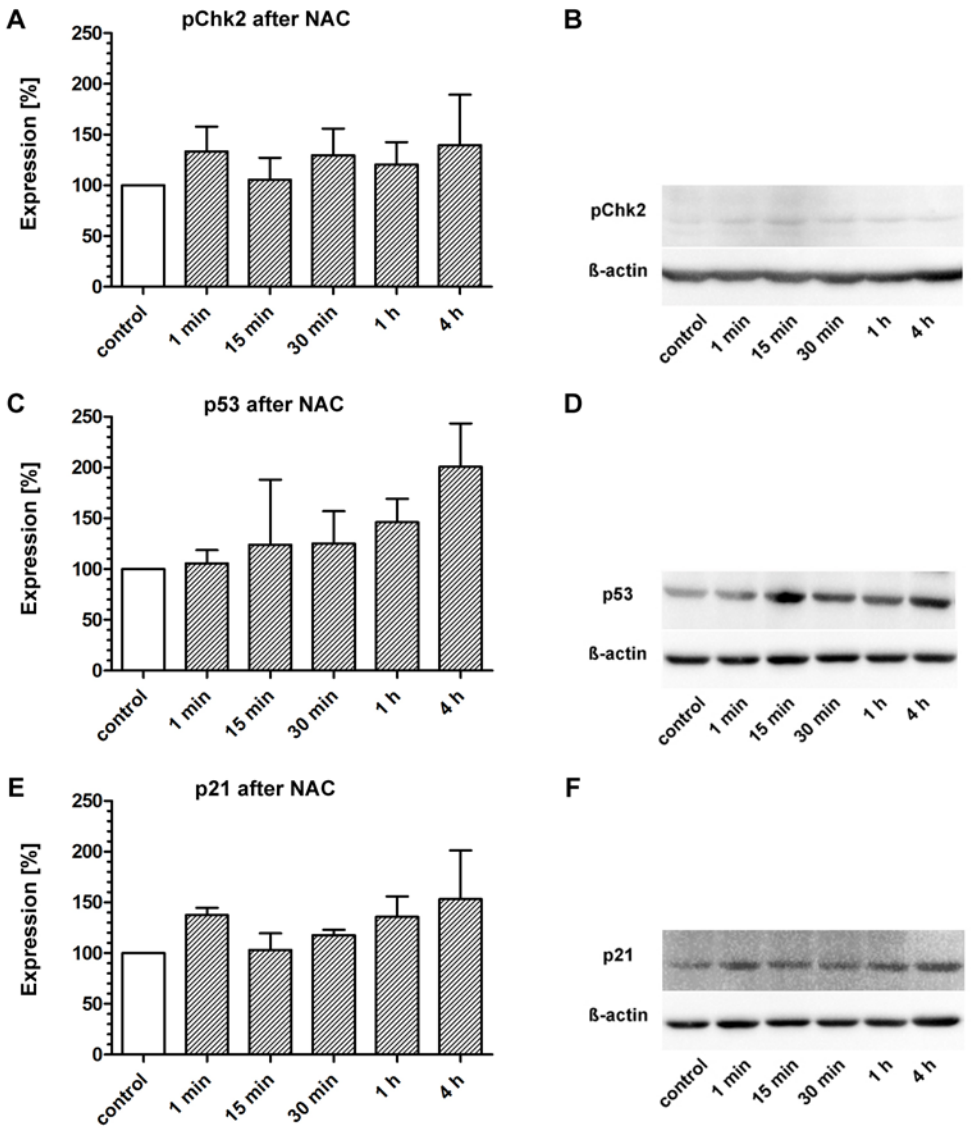

Figure 44: Western blot analysis of ATM/Chk2 pathway after ZnO NP + NAC treatment

(A) ROS scavenging by NAC led to fast but weak activation of Chk2. The level of approx. + 125 % of pChk2 after 1 min is remained unchanged over the period in time. (C) NAC and ZnO NP treatments led to continuous p53 activation with maximum of ~ + 200 % after 4 h. (E) P21 was up-regulated after treatment with ZnO NP + NAC reaching + 150 % after 4 h. (B), (D), and (F) show representative Western blots of graphic A, C, and E. N=3.

The extracellular chelator DTPA was used to complex dissociated ZnO NP. Neither Chk2 nor p53 were phosphorylated, i.e., not activated (Figure 45). The complexation of Zn^{2+} led to a dephosphorylation of pChk2 after 15 min of ZnO NP exposure (Figure 45A and B). In Figure 45C the stabilization of p53 after 30 min of DTPA + ZnO NP treatment is shown. DTPA treatment resulted in slightly reduced p21 levels with recovery after 1 h (Figure 45E). All these data taken together suggest that the ATM/Chk2 activation after

ZnO NP treatment relies on dissociated Zn^{2+} without ROS as an intermediate damaging the DNA.

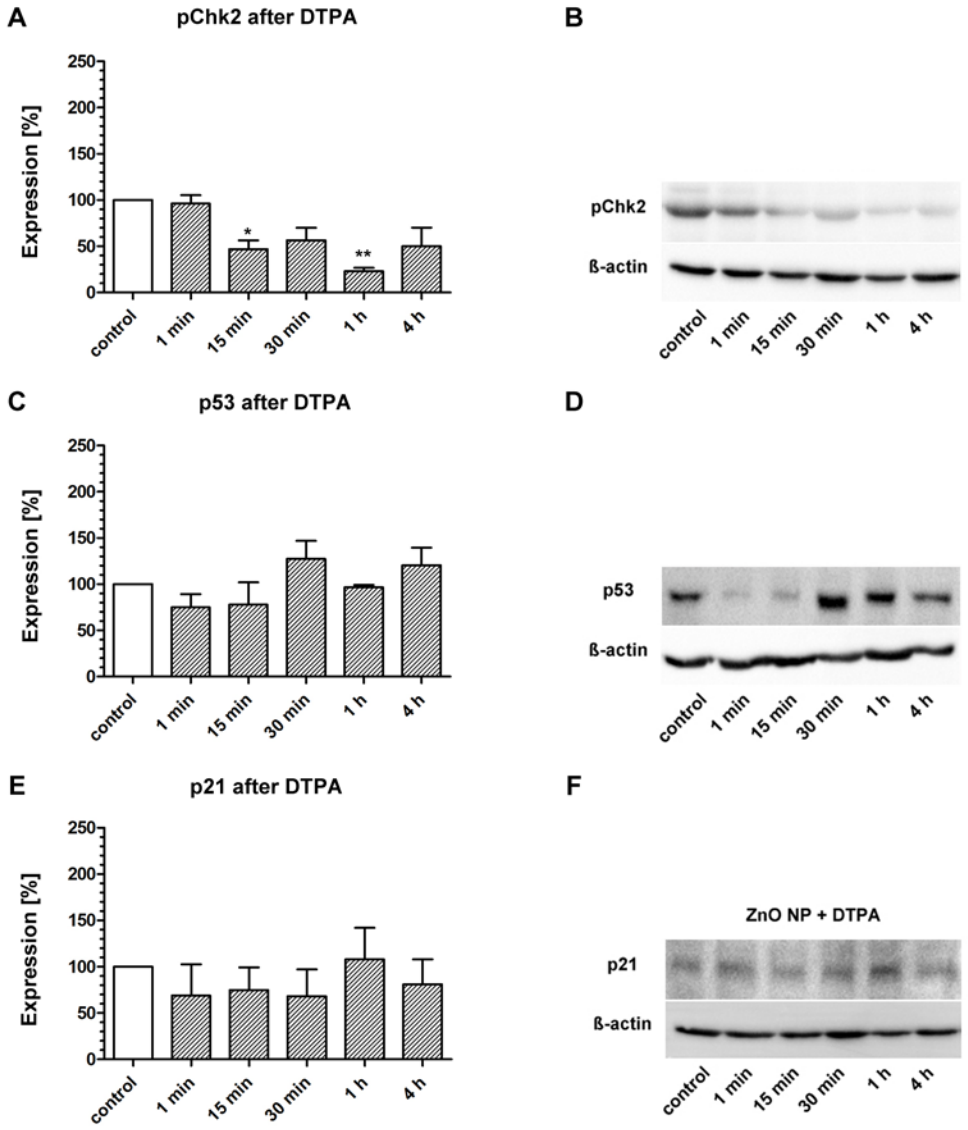

Figure 45: Western blot analysis of ATM/Chk2 pathway after ZnO NP + DTPA treatment

(A) The Chk2 kinase is deactivated after extracellular chelation of free Zn^{2+} after ZnO NP treatment. (C) P53 is slightly stabilized after 30 min. (E) P21 levels remained unchanged or were reduced in tendency until 30 min. (B), (D), and (F) show representative Western blots of graphic A, C, E. * = $p<0.05$, ** = $p<0.01$; N=3.

4.5.3 Apoptosis/necrosis after ZnO NP exposure

DNA damages and DDR activation may result in apoptosis as part of a cellular suicide mechanism. This event is accompanied by typical cellular changes that can be measured by flow cytometry. Cells were exposed to ZnO NP in a final concentration of 100 µg/mL and then stained with annexin V (AV) and propidium iodide (PI) (see 3.2.6.1). The cellular state was determined as live cell (PI -, AV -), early apoptosis (PI -, AV +), apoptosis (AV +, PI +) and necrosis (AV -, PI +) staining. After ZnO NP treatment of A549 cells, early apoptosis was induced (detected as PI-negative/AV-positive cells). Figure 46 shows the predominant cellular state after ZnO NP treatment as early apoptosis followed by apoptosis. ZnO NP led to early apoptosis + 150 % after 6 h in comparison to the untreated control (Figure 46, green). The apoptosis induced by ZnO NP is shown in Figure 46 (blue) with an up-regulation of 150 %. The necrosis (red) and cellular viability (yellow) decreased during the analyzed time (Figure 46).

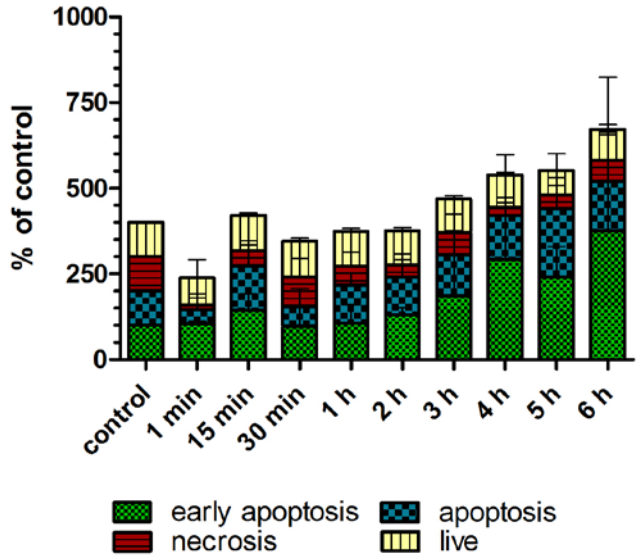

Figure 46: Flow cytometry analysis of apoptosis/necrosis after ZnO NP treatment

Cellular state of live, early apoptosis, apoptosis and necrosis were determined by AV/PI staining. ZnO NP exposure led to increased early apoptosis and slightly increases of apoptosis, while necrosis and viable cells are reduced in a time-dependent manner. N=3.

4.5.4 Activation of MAPK and PI3K pathways by ZnO NP

Nanoparticle toxicity is often associated with an activation of stress induced signaling. Here, two major pathways the MAPK/Erk and PI3K/Akt were investigated to get an overview of environmental stimuli triggered by ZnO NP or $ZnCl_2$. These activated signaling pathways lead to diverse cellular responses (e.g., proliferation, cell growth and apoptosis). In this study Erk1/2 and Akt were analyzed after ZnO NP and $ZnCl_2$ treatment. A549 cells were treated with 100 µg/mL ZnO NP or $ZnCl_2$ for 1 h and Western blot analyses were performed. EGF treatment was used as positive control for MAPK and PI3K pathway activation. The treatment with ZnO NP for 1 h caused an activation of both signaling pathways in terms of strong phosphorylation of Akt as well as Erk (Figure 47A, C and E). In Figure 47A the activation of Akt after ZnO NP treatment is demonstrated. It could be observed that the stimulation with EGF led to an activation of Akt up to 288 %. This activation of Akt was much higher after single treatment with ZnO NP resulting in an increase of phosphorylation up to + 1072 %. The combination of EGF stimulation and ZnO NP exposure did not cause an additive activation compared to the single exposure to ZnO NP (Figure 47A). In Figure 47B the activation of Akt is shown after $ZnCl_2$ treatment as positive control for dissociated ZnO NP. Akt was activated strongly and demonstrated a level of phosphorylation up to 3678 % compared to the untreated control. The combination with EGF led to an additional phosphorylation of + 722 %. The exposure to ZnO NP resulted in a phosphorylation of Erk up to 633 %. The combined treatment of ZnO NP with EGF caused a further phosphorylation to 786 % of Erk activation (Figure 47C). In Figure 47D the activation of Erk after $ZnCl_2$ treatment is demonstrated and shows a two times higher activation of Erk than observed after single treatment with ZnO NP. The high activation of Akt and Erk suggested that Zn^{2+} after dissociation of ZnO NP is the mediator in this cellular stress response. Figure 47E and F show exemplary Western blots adequate to Figure 47A, B, C and D.

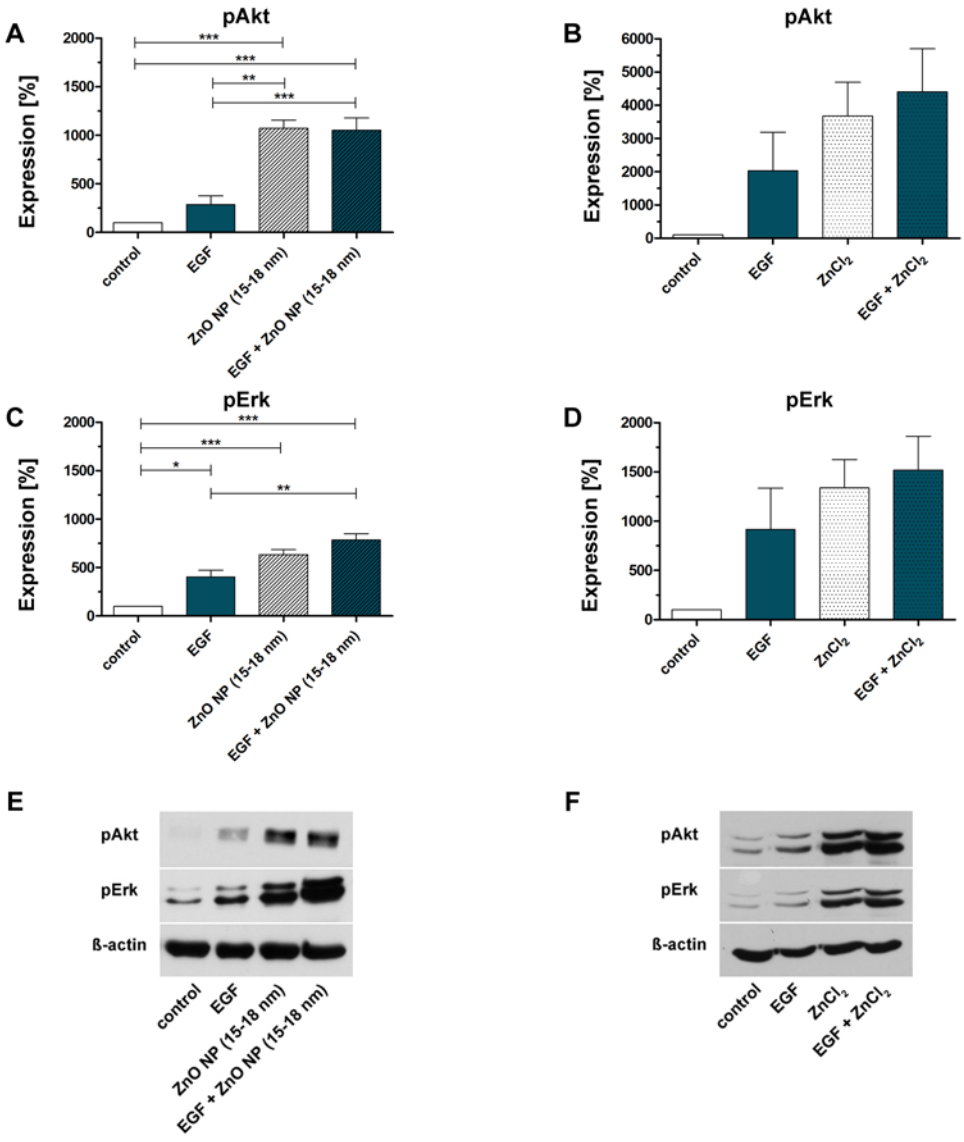

Figure 47: Activation of the MAPK/Erk- and PI3K/Akt-pathway after exposure to ZnO NP and $ZnCl_2$

The treatments with ZnO NP (15-18 nm) as well as with $ZnCl_2$ activate the MAPK/Erk- and PI3K/Akt-pathway. (A) and (C) The exposure to ZnO NP (15-18 nm) leads to a 6 times higher phosphorylation of Erk and a 10 times stronger phosphorylation of Akt compared to the controls. (B) and (D) This effect is multiply higher by the treatment with $ZnCl_2$. (E) and (F) Exemplary Western blots. (A, B) = pAkt, (C, D) = pErk. * = $p<0.05$, ** = $p<0.01$, *** = $p<0.001$; N=3.

4.6 Analysis of ZnO NP genotoxicity in primary cells of mucosa

In contrast to cell lines, primary cells are isolated from fresh tissue and used within the first passages. The cellular responses to ZnO NP exposure are assumed to be more similar to the *in vivo* situation than the results obtained from cell line experiments. To provide evidence of epithelial cells two different markers were used for primary cells of mucosa. Cytokeratin 13 was used as positive control for epithelial origin and FGFR4 as positive control for fibroblasts. Stainings confirm the epithelial origin of used primary cells (Figure 48).

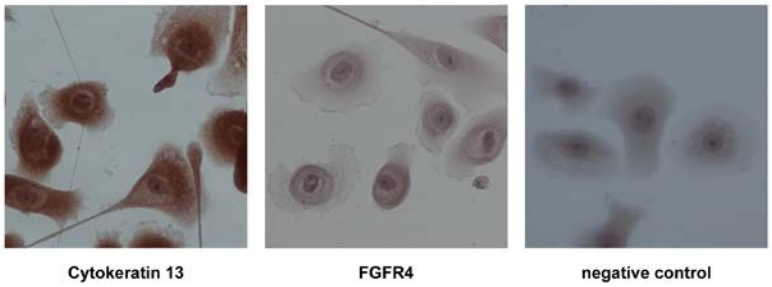

Figure 48: Confirmation of epithelial origin of primary cells of mucosa

The immunohistochemical analysis of primary cells of mucosa showed a cytokeratin 13 positive result indicated as an intensive brown staining. FGFR4 staining was negative, represent as a slight or no brown staining (cf. negative control). This result confirms that the primary cells were of epithelial origin. Magnification: 400x.

The primary cells were obtained and used from four different patients. The γH2A.X foci assays were realized comparable to the A549 cell line experiments in 3.2.4.1 and 3.2.7.6. Furthermore, the DNA damage response, downstream of ATM, was assessed after ZnO NP, ZnO NP + DTPA and ZnO NP + NAC treatment. The expression of the proteins Chk2, p53, and p21 was analyzed by Western bloting (see 3.2.8.3.3).

4.6.1 Analysis of DNA DSB after ZnO NP exposure

The influence of ZnO NP on primary cells of mucosal tissue (PMT) was evaluated by γH2A.X immunofluorescence staining. Samples (PMT1-4) were treated as mentioned before (see 3.2.4.1 and 3.2.4). Treatment with ZnO NP resulted in PMT1 in fast and continuous increase of DNA DSB up to 944 % after 15 min of exposure (Figure 49A) followed by dephosphorylation of H2A.X to basal levels of untreated control. PMT1 reacted closely to the outcomes of A549 experiments (cf. Figure 37A). In Figure 49B the DNA damages in PMT2 after ZnO NP treatment is shown and demonstrated a fast increase of DNA DSB up to 580 % after 1 min of exposure. The strong phosphorylation was reduced to 153 % after 15 min and down to basal level after 30 min. Treatment of PMT2 showed a renewed phosphorylation after 1 h followed by dephosphorylation to basal level of untreated control (Figure 49B). Exposure of PMT3 with ZnO NP showed a slight but continuous increase of DNA DSB resulting in + 324 % after 4 h (Figure 49C). The result of PMT4 showed as well a fast increase of DNA DSB after ZnO NP treatment. H2A.X phosphorylation was up to + 602 % after 1 min keeping this level until 15 min of ZnO NP exposure. Afterwards the DNA damages were reduced to ~ 280 % until the end of measurement (Figure 49D).

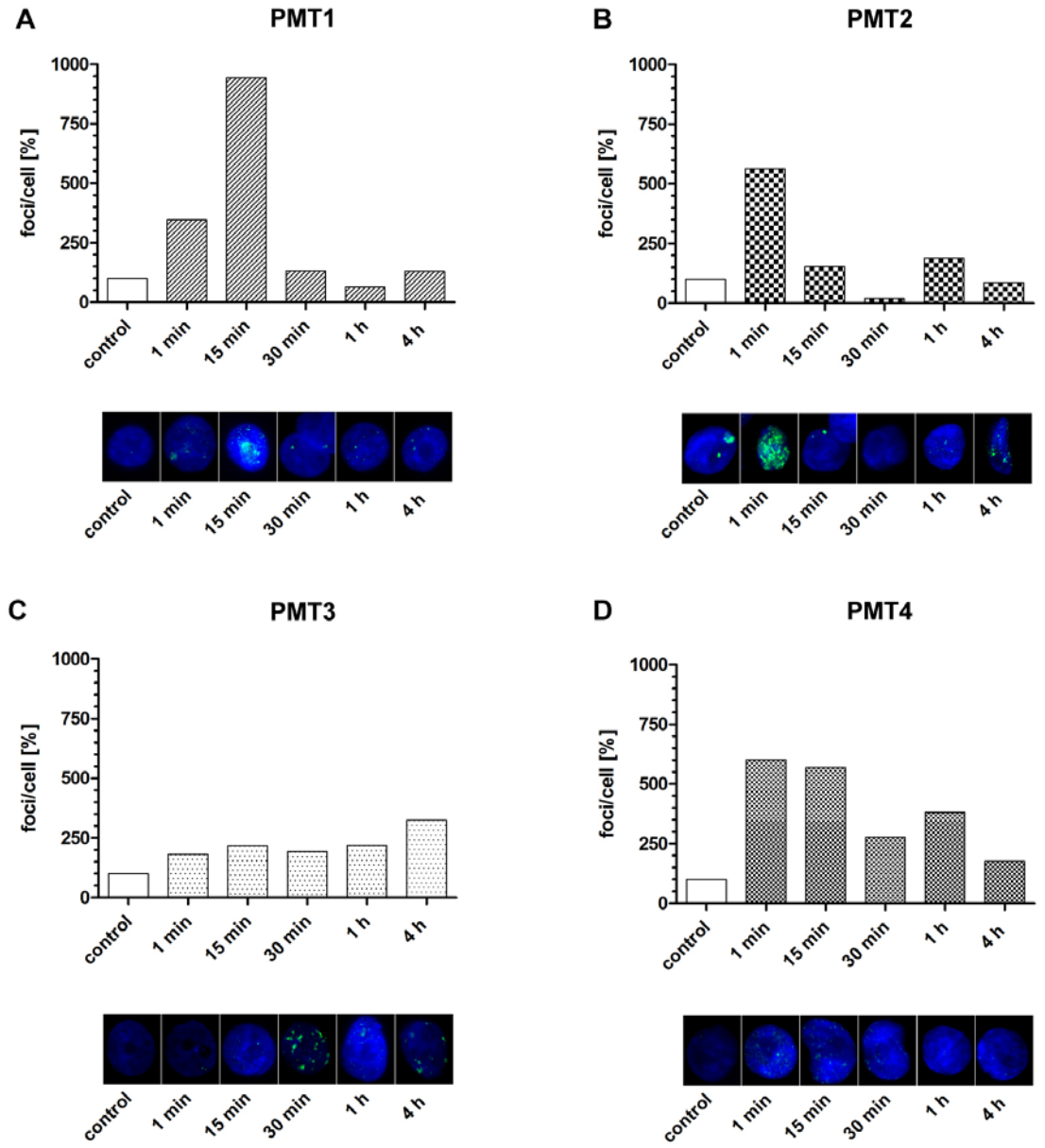

Figure 49: Quantification of DNA DSB in primary mucosal cells after ZnO NP treatment

(A) PMT1 showed a fast and continuous up-regulation to 944 % of γH2A.X after 15 min of exposure followed by dephosphorylation to basal level. (B) PMT2 demonstrated a fast increase of DNA DSB after 1 min of exposure ensued by reduction to 153 % after 15 min and a further activation of H2A.X after 1 h. (C) Treatment of PMT3 resulted in a slight but continuous increase of DNA damages of + 324 % after 4 h. (D) In PMT4, H2A.X is phosphorylated up to + 602 % after 1 min keeping this level until 15 min, then the DNA DSB are down-regulated to 278 %. N=4. PMT = primary cells of mucosal tissue, 1-4 represent patient, repsectively.

4.6.2 Analysis of ATM downstream signaling in primary cells of mucosa

The analysis of ATM downstream signaling in A549 cells showed a strong activation of pChk2, p53, and p21 after 4 h of ZnO NP exposure (cf. Figure 43). The mucosal cells were treated with ZnO NP and ATM downstream signaling was analyzed using Western blotting. The signaling activation in primary cells of mucosa was analyzed in dependence of Zn^{2+} and ROS. After 4 h of ZnO NP exposure pChk2 was strongly activated and showed a phosphorylation-level up to 1200 % compared to the untreated control. This Chk2 activation was six times higher than the activation of pChk2 in A549 cells after 4 h. Zn^{2+} complexation resulted in a slight activation of pChk2 up to 200 % after 4 h. All treatments showed an increase of p53 of approx. ~ + 200 % compared to each control (Figure 50B). The treatment with ZnO NP resulted in an up-regulation of p21 after 4 h. In case of pretreatment with NAC or DTPA no activation of p21 was found (Figure 50C). Figure 50D shows the representative Western blots corresponding to Figure 50A, B and C. Cell lysates were corresponding to the patients of Figure 49 without PMT 3, because of weak cell amounts that were available for both experiments.

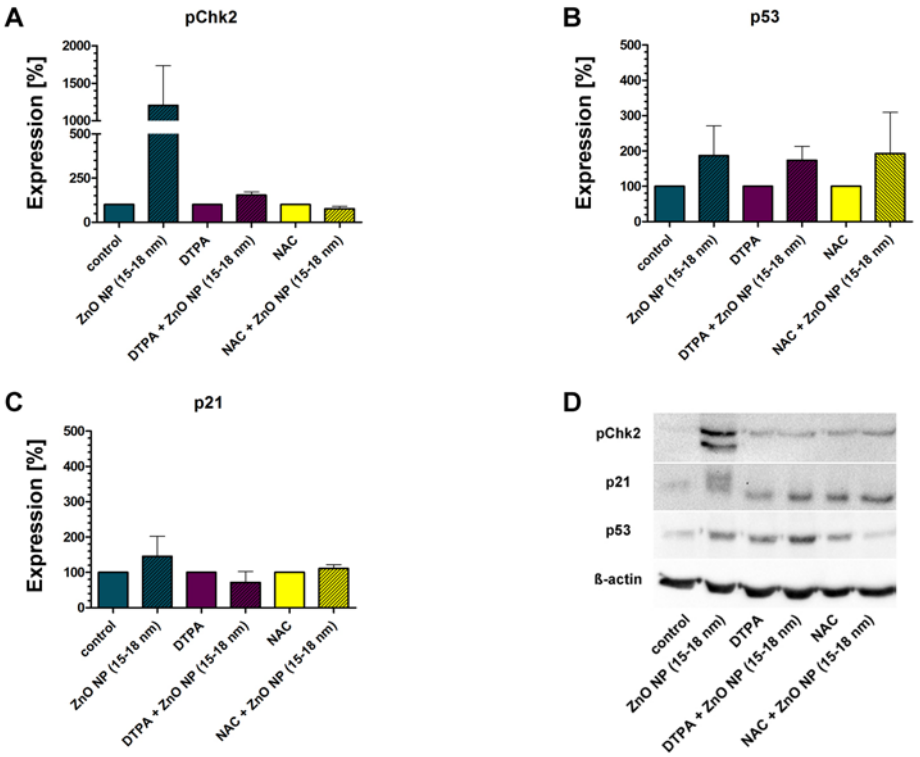

Figure 50: Analysis of ATM downstream signaling in primary cells of mucosa

(A) Chk2 was activated strongly after ZnO NP, slightly after ZnO NP + DTPA but not after ZnO NP + NAC treatment. (B) P53 after ZnO NP, ZnO NP + NAC, and ZnO NP + DTPA exposure resulted in an up-regulation to + 180 %. (C) The treatment with ZnO NP resulted in an up-regulation of p21 after 4 h. In case of pretreatment with NAC or DTPA no activation of p21 was observed. N=3.

5 Discussion

5.1 Toxicity of ZnO

The enormous increase of industrial applied ZnO NP, and the use of daily products containing ZnO NP, is attended with boosted environmental release and may result in health hazards. Therefore, the investigations on possible risk assessment of synthesized ZnO NP are inevitable. The primary contact organ for inhaled aerosols is the respiratory epithelia. For this reason the effect of ZnO NP on the respiratory epithelia, especially their possible toxicity, has to be analyzed.

5.1.1 ZnO NP impair the cellular viability of A549 cells

Both sizes of ZnO NP lead to a concentration-dependent toxicity (see Figure 28). The treatment of A549 cells with the highest concentration (100 µg/mL) results in a continuous decrease of cellular viability. The exposure to lower concentrations (0.1 µg/mL and 10 µg/mL) leads in case of ZnO NP (15-18 nm) to an increased viability respectively to no changes after treatment with ZnO NP (4-5 nm). The proved impairment of cellular viability of alveolar epithelial cells after ZnO NP exposure conforms to different studies in many types of cells[228–233]. The ZnO NP (15-18 nm) showed an improved toxicity in comparison to the ZnO NP (4-5 nm). These outcomes were surprising, because different working groups described that smaller particles are more reactive and further toxic, because of their larger surface to volume ratio, compared to larger particles[23]. *Adamson et al. (2000)* determined ZnO NP as a component of atmospheric dust and to be a toxic factor, which is responsible for pulmonary reactivity after instillation to mouse lung[234]. Furthermore, the toxicity of ZnO NP was observed in bronchial cells of rats as well as human alveolar epithelial cells[117,235,236]. This observed toxicity of ZnO NP could be caused by different damaging mechanisms. *George et al. (2009)* showed a reduced mitochondrial membrane potential as well as a loss of membrane integrity after treatment with ZnO NP in murine macrophages and BEAS-2B cells[237]. These outcomes confirm our results of reduced ΔΨm after treatment with ZnO NP (15-18 nm). Some authors showed that ZnO NP damage cell membranes and lead to lowered mitochondrial activity in A549 cells[238,239]. In addition, the increased production of inflammatory mediators such as IL-8, the generation of intracellular ROS, and the induction of apoptotic pathways are already described as toxic mechanisms of ZnO NP[226,239,240,241]. *Hsiao et al. (2011)* also demonstrated decreased viability after treatment with smaller particles, while larger particles were less toxic[239]. Different parameters like size, surface charge and

agglomeration behavior of particles have an influence on dissociation and cellular uptake. The used particles have different ζ-potentials (see 4.1.1), which may explain the stronger toxicity of the larger particles. *Fröhlich (2012)* reviewed that positively charged particles cause more disruptions of plasma membrane integrity and mitochondrial damages than negatively charged particles[242]. Alternatively, a connection between the ζ-potential and agglomeration behavior was observed by *Cho et al. (2012)*. They further described that the surface charge influences the inflammatory potential in rats[243]. Furthermore, *Bian et al. (2011)* observed that smaller particles often dissociate faster than larger particles[244]. In contrast, we found a faster dissociation and cellular uptake of the larger particles. Zn^{2+} dissociated from ZnO NP are often hypothesized as the main toxic mechanism[245,246]. Therefore, we observed that the prevention of ZnO NP dissociation, using BSA coating, results in a complete inhibition of toxicity after exposure to ZnO NP (see Figure 29). This inhibition of toxicity by particle stabilization could also be observed in *in vivo* studies of rodent lung and zebrafish embryos exposed to iron doped ZnO NP[186]. Dissociated particles in the supernatants of cell culture medium indicated a similar damaging potential as shown for ZnO NP in previous results of our working group[247,248]. Analysis of alveolar epithelial cells cultivated in the air-liquid interface suppose the direct interaction of cellular structures with particles or by a local release of Zn^{2+} at the contact side of particles with the cells as underlying toxic mechanism[223,236,237,249]. Furthermore, it is a matter of debate if Zn^{2+}, dissociated from particles, cause different cellular reactions than ZnO NP after local enrichment and both possibly act in synergistic way[223,236,237,249].

5.1.2 Toxicity through intracellular generation of ROS induced by ZnO NP

Another popular concept of nanoparticle toxicity is the intracellular release of ROS[250]. Under normal physiological conditions, the detoxification system and generation of ROS should be balanced in organisms. Based on the intracellular ROS-level, ROS serves as signaling molecule or could cause oxidative damages. The treatment of alveolar epithelial cells with ZnO NP (4-5 nm) results in slightly increased intracellular ROS-levels. Low ROS-levels are known to serve as signaling molecules and act as important physiological regulators of intracellular signaling pathways[251]. The exposure to ZnO NP (15-18 nm) leads to reinforced generation of ROS (see Figure 31). Remarkably, the results in Figure 28 demonstrate increased counts of viable cells at low concentrations of ZnO NP (15-18 nm). This unexpected result might be explained by the observed slightly increase of ROS after ZnO NP (15-18 nm) treatment. The current study has also investigated MAPK/Erk- and PI3K/Akt signaling and we found activation, in the

case of ZnO NP as well as $ZnCl_2$ treatment. Zinc is a regulator of cell proliferation and *Huang et al. (2000)* postulated that Zn^{2+} and Ca^{2+} have synergistically effects on DNA synthesis and mitogenic signaling in fibroblasts[252]. It is already described in literature, that generation of ROS is enhanced by intracellular Zn^{2+} and has the potential to stimulate growth promoting pathways[253,254,255]. These suggestions correspond with the results in Figure 47 demonstrating the strong activation of Erk and Akt after nanoparticle treatment. Furthermore, the treatment with $ZnCl_2$ leads to stronger ROS-levels as well as an intensified Erk and Akt activation in contrast to ZnO NP (15-18 nm). *Seo et al. (2001)* demonstrated that the intracellular accumulation of Zn^{2+} resulted in the generation of ROS activating the MAPK/Erk pathway that further contributes to Zn^{2+} induced cell death[255]. These results are in line with the outcomes of the ZnO NP (15-18 nm) induced analysis of apoptosis (see Figure 46). Zn^{2+} is an essential cofactor for the activity of proteins involving in the reduction of oxidative stress (e.g., SOD and MT)[256]. The stress-related protein MT has antioxidant properties and protects cells against over production of ROS[257]. MT are cysteine-rich proteins with a low molecular weight. The protein has a high and specific affinity, mediated by their thiol groups of its cysteine residues, to bind biologic essential metals such as Zn[256,257,258]. Increasing ROS-levels after ZnO NP treatment, as shown after 30 min of exposure, may lead to oxidation of the zinc binding thiol groups of MT, which further reduces the puffer capacity enhancing the damaging potential of additional Zn^{2+} [259]. Additionally, in the present study, it could be observed that the complexation of Zn^{2+} by DTPA resulted in a complete inhibition of ROS. The release of Zn^{2+} is triggered by ROS and therefore oxidative distress seems to be a common constituent of different toxic signaling pathways in neurons[260]. This intracellular Zn^{2+} accumulation promotes the activation of harmful signaling processes such as the production of superoxide from 12-LOX that leads to further ROS production, initiating a positive feedback loop[246,260,261].

5.1.3 Toxicity through ZnO NP dissociation into Zn^{2+}

In this study we observed a fast cellular intake of Zn^{2+} as well as a reduced viability. The pretreatment with DTPA resulted in initially reduced viability but recovered and is later completely abolished, proposing Zn^{2+} as main mediator of ZnO NP toxicity. The dissociation of Zn^{2+} from ZnO NP is discussed as possible mechanism of toxicity[249,262]. Furthermore, we observed no reduction of viability after BSA stabilization, suggesting again Zn^{2+} as mediator of toxicity. *Xia et al. (2011)* also observed a reduced toxicity after doping ZnO NP with iron similar to the effects after the use of chelators[186]. Previous results of our working group showed that Zn^{2+} ions released from ZnO NP in the

supernatant of the cell culture medium have similar toxic potential comparable to the exposition with ZnO NP[233,247,262]. Air-liquid-interface models show no complete dissociation of ZnO NP and therefore the authors discussed their observed toxicity as effect of direct particle interactions with cellular structures and a high local release of Zn^{2+} at the particle-cell interaction side[236]. They suggested a different toxic mechanism based on ZnO NP and dissociated ions and discussed a possible synergistic cellular damage[116,117,236,249]. We showed a fast decrease of cellular viability of ZnO NP exposed cells, while previous data of our working group represented a reduced cellular viability of $ZnCl_2$ treated cells just after 48 h compared to single particle treatment[247]. The treatment with $ZnCl_2$ resulted in an earlier generation of DNA DSB in comparison to the treatment with ZnO NP, suggesting possibly two different damaging mechanisms of mediated by released ions dissociated from particles in contrast to treatment with $ZnCl_2$. The zinc homeostasis is highly controlled by different zinc transporters and divalent cation transporters (DMT1) which regulate the zinc influx and efflux, leading possibly to retarded nanotoxicity. These results are confirmed by *Zhang et al. (2012)* in comparative experiments investigating the effects of intra- and extracellular Zn^{2+} on toxicity by exposing cells with ZnO NP and $ZnCl_2$[233]. Another possibility how Zn^{2+} may lead to cellular damages is by blocking the four complexes of mitochondrial respiration with different affinity as observed by other authors[70,79,80,129]. *Fukui et al. (2012)* described a significant correlation between high intracellular Zn^{2+} levels and the generation of ROS[240]. We observed a fast intake of Zn^{2+}, increased ROS-levels, continuously decreased ΔΨm, and induction of early apoptosis. ROS may react in a damaging way to mitochondria and DNA leading to apoptosis. Furthermore, an increased intracellular Zn^{2+} level leads to a destabilization of mitochondria mediated by the release of Ca^{2+} [263]. This could be confirmed by *Kao et al. (2012)* who observed a strong increase of cytosolic and mitochondrial Zn^{2+} levels after ZnO NP treatment. These high levels of mitochondrial Zn^{2+} resulted in the depolarization of ΔΨm and increased permeability which further leads to the activation of the intrinsic apoptosis pathway, confiming our outcomes[72]. These findings are a further proof of ZnO NP toxicity mediated by dissociated ions.

5.2 Solubility of ZnO NP

We hypothesized that the ZnO NP are quickly dissociated outside the cell and are internalised as Zn^{2+} or, in case of endocytic uptake, dissociate in the acidic endosomal environment[21]. We analyzed the ZnO NP solubility in high purity H_2O (pH 5.8) and cell culture medium (pH 7.4). Both sizes of ZnO NP showed a strong time-dependent dissociation in high purity H_2O and cell culture medium. ZnO is often classified in material safety data sheets as insoluble in H_2O, while others reported a highly pH-dependent solubility of ZnO[188,189]. The existent pH in the solutions and the availability of ions might influence the surface charge of the particles and further the grade of agglomeration[188]. *Illés et al. (2006)* postulated increased aggregation behavior of particles at any pH if electrolyte concentration is raising[264]. This possibly explains the reduced dissociation in cell culture medium in contrast to high purity H_2O because of the electrolytical components needed for cell survival in the medium. We further suggest that our observed time-dependent ZnO solubility is linked to the *Ostwald ripening phenomena*. This phenomenon describes that unstable surface ions usually disolve diminishing the particles over the period in time, while the number of free ions in solution is increasing. If the solution is saturated with the free ions, those will redeposit on the surface of larger particles. This means, that smaller particles may dissociate, while larger particles grow and dissociate slowly in contrast to the smaller particles[265–267]. *Borm et al. (2006)* postulated that the rate of dissolution is proportional to particle surface area meaning that smaller particles, with an increased surface area, dissolve faster than larger particles for the same mass[266]. This possibly explains the faster dissolution of ZnO NP (4-5 nm) in comparison to ZnO NP (15-18 nm) observed in this study.

5.3 ZnO NP uptake

5.3.1 Size and charge dependent uptake of ZnO NP

The TEM-data of this study showed only very minor amounts of ZnO NP inside the cell. ZnO NP of both sizes were only detectable after 1 h of treatment. ZnO NP (4-5 nm) are rarely located in the cytoplasm, while ZnO NP (15-18 nm) are additionally infrequently localized in the mitochondria, nuclear envelope, and nucleus (see Figure 14 and Figure 15). Usually, the cellular uptake of nanoparticles takes place by endocytosis and is dependent on different factors such as size, form, and ζ-potential of the particles. The physico-chemical properties of the particle surface influence the interaction with cellular membranes. The negatively charged smaller particles are less detectable intracellularly in contrast to the positively charged larger particles using TEM measurement. Different

studies have shown that positively and negatively charged particles are taken up easier than neutral particles[242]. The unspecific interactions of negatively charged particles with membrane receptors have been demonstrated, leading to enhanced cellular particle uptake[242]. Nevertheless, it is no explanation of the less intracellular accumulation of both particle sizes in general. The infrequent detection of particles inside the cells using TEM and the observed fast dissociation in cell culture medium and high purity H_2O suppose a fast dissociation of ZnO NP. Therefore, two probably consecutive mechanisms of ZnO NP intake are suggested: first, the fast internalization of extracellular dissociated ZnO NP and second the endocytic uptake of solid particles and their subsequent intracellular dissociation into Zn^{2+} at low pH.

5.3.2 Intracellular accumulation of Zn^{2+}

We measured the dissociation of ZnO NP by spectrofluorimetry and cLSM using FluoZin^{TM}-3. Cellular treatment with ZnO NP (4-5 nm) resulted in a slight but continuously increased intracellular Zn^{2+} concentration, while the exposure to ZnO NP (15-18 nm) showed a fast and strong intracellular ion accumulation. To prove the concept of extracellular dissociation of ZnO NP, the cells were pretreated with the extracellular Zn^{2+} chelator DTPA prior to particle treatment. In both cases, pretreatment with DTPA resulted in no intracellular Zn^{2+} increase, confirming the assumed hypothesis of fast extracellular particle dissociation and uptake of Zn^{2+}. An endosomal ZnO NP uptake was not detectable by TEM measurements. The dissociation of affiliated particles in the acidic environment of early endosomes was proven by cLSM measurements using FluoZin^{TM}-3 detecting free Zn^{2+} in labeled endosomes (see 4.2.3.1, 4.2.3.2, 4.2.3.3). The treatments with ZnO NP of both sizes resulted in no endosomal uptake of ZnO NP and accumulation of Zn^{2+} in early endosomes. One might prompt that we found an endosomal independent mechanism of intracellular Zn^{2+} accumulation of dissociated ZnO NP. These findings disprove the popular hypothesis suggesting an endocytic ZnO NP uptake and dissociation in early endosomes at pH 5-6 as reported by *Kao et al. (2012)*[72]. *Xia et al. (2008)* showed an endosomal accumulation of FITC labeled and stabilized ZnO NP[263]. *Hackenberg et al. (2011)* also demonstrated the cellular uptake of ZnO NP coated with BSA[71]. However, these authors used stabilized ZnO NP; these particles are expected to dissociate slowly, enabling endocytic uptake of NP, which is different compared to our experiments, using unmodified ZnO NP. Accordingly to our data, *Valdiglesias et al. (2013)* observed in neuronal cells that none-stabilized ZnO NP are not incorporated[268]. Furthermore, it is important to emphasize that granular structures were observed before exposure to the cells. However, these structures were monitored

at basal levels and became intensified in any case of exposure, i.e., with ZnO NP as well as $ZnCl_2$. Some studies reported that extracellular Zn^{2+} ions were absorbed by the cells and captured in specialized vesicles named zincosomes[238,252,269,253]. The nature of these vesicles is still unknown but they have been detected in several cell types[269,270]. These granular structures were discussed to have an endosomal origin[271]. *Gojova et al. (2007)* found ZnO NP within vesicles in the cytoplasm. We observed as well vesicular structures, which possibly are zincosomes, in the cytoplasm but they contained Zn^{2+} that is dissociated extracellularly from ZnO NP[272]. Further, *Gojova et al. (2007)* observed less vesicular embedding for ZnO NP in contrast to other metal oxide nanoparticles as well as impairments of the membrane through intercalated particles[272]. In summary, the co-localization of Zn^{2+} in early endosomes after ZnO NP treatment was not detected. This data again support the hypothesis of cellular Zn^{2+} intake without the use of the endocytosis machinery. The cellular uptake of Zn^{2+}, and the transport into and out of organelles, requires specific transport proteins spanning these membranes[270]. Two main families of eukaryotic zinc transporters, named ZIP and ZnT proteins, are known[273,274]. The ZIP proteins transport Zn^{2+} from the extracellular space or organelle lumen, into the cytoplasm[270,275]. The corresponding antagonists of the ZIPs are the ZnTs which are responsible for the Zn^{2+} transportation from the cytoplasm to organelles or outside the cell[270,275]. *Gunshin et al. (1997)* described a cationic transporter known as divalent cation transporter 1 (DCT1) which binds a variety of divalent metals such as Zn^{2+} [276]. The intracellular Zn^{2+} level is distributed to cytoplasm (50 %), nucleus (20-30 %), and are membrane associated (10-20 %). However, 90 % of total intracellular Zn^{2+} amount is bound to proteins[194]. Our data showed a continous increase of intracellular free Zn^{2+} concentration with + 35 nM after 1 h of treatment with ZnO NP (15-18 nm). Several studies analyzing different cell types report a total intracellular Zn^{2+} concentration in a range of <0.1 nM to 0.5 mM depending on the used methods[270,277–279]. Low levels of Zn^{2+} are required for cellular Zn^{2+} homeostasis but in case of ZnO NP exposure a plus of 35 nM after 4 h possibly is enough for cellular imbalance. In this case the normal Zn^{2+} level is raised and efflux mechanisms mediated by ZnTs are necessary to prevent the cell of over accumulation and subsequently toxic consequences[224,280,281]. The amount of released Zn^{2+} from ZnO NP is dependent on several factors e.g., pH, agglomeration behavior, cell culture medium as well as the experimental set-up[245,282]. This fast Zn^{2+} dissociation and intake could play an essential role in ZnO NP toxicity.

5.3.3 Co-localization of Zn^{2+} with cellular organelles

The biological roles of zinc are mainly of structural, catalytical and regulatory functions. Zinc is essential as a structural element in protein folding as well as in macromolecular and enzyme stabilization (e.g., superoxide dismutase)[269,283]. *Vallee and Falchuk (1993)* showed that zinc is a component of the catalytic site of many metalloenzymes[194]. Furthermore, zinc is a regulator of different biological processes (e.g., gene regulation)[269,280,284]. We observed that the Zn^{2+} after cellular intake shifted subsequently into mitochondria and nucleus but not in the ER.

5.3.3.1 Mitochondrial accumulation of Zn^{2+}

Using TEM we rarely illustrated ZnO NP in mitochondria. Furthermore, we observed free Zn^{2+} in mitochondria after treatment with ZnO NP. The mechanism of mitochondrial Zn^{2+} uptake and function is not fully understood yet. Different metalloenzymes, such as Zim17, are localized in the matrix of mitochondria requiring Zn^{2+} as co-factor for their functions[285,194]. *Maret et al. (2000)* and *Ye et al. (2001)* observed metallothionein (MT) in the intermembrane space of mitochondria and pointed out that MT may serve as source of increased Zn^{2+} concentrations within the matrix[286]. MT are able to detoxify ROS to maintain homeostasis. ROS is known to oxidize thiol groups of MT during respiration leading to release of Zn^{2+} [198]. We observed increased ROS-levels after 30 min of ZnO NP as well as $ZnCl_2$ treatment and in both treatments an increase of intracellular Zn^{2+}-levels, assuming a release of Zn^{2+} from MT through oxidization by ROS. The released Zn^{2+} accumulates in the nucleus and activates the metal regulatory transcription factor 1 (MTF-1), the known activator of MT genes. MTF-1 binds with its four zinc finger domains to the promoters containing a metal-response element (MRE) of the MT gene, leading to MT transcription[198]. We suppose that a physiological level of Zn^{2+} is important for mitochondrial homeostasis, because Zn^{2+} is necessary for ROS detoxification after binding to MT. We observed a depolarization of $\Delta\Psi m$ after treatment with ZnO NP (15-18 nm), as well as the starting of early apoptosis events (discussed later). The $\Delta\Psi m$ depolarize after Zn^{2+} overload, resulting in Zn^{2+} and cytochrome c (cyt c) release into the cytoplasm. Cyt c forms an apoptosom initiating the activation of several caspases leading to apoptosis[254]. *Sensi et al. (2003)* reported that the depolarization of $\Delta\Psi m$ leads to an accumulation of Zn^{2+} in the cytosol released from mitochondria[254]. This effect was observed in neurons and is associated with cell death in diseases such as ischemia and epilepsy[288]. Many years ago it was postulated that Zn^{2+} is able to inhibit oxidative phosphorylation as well as all complexes of the respiratory chain, with dramatically outcomes for cell fate[289,290]. *Medvedeva et al. (2014)* suggest, that the Zn^{2+} entry into

mitochondria led to ROS generation and resulted in mitochondrial dysfunction and played a role in the deregulation of Ca^{2+} [291]. They further blocked the Ca^{2+} uniporter by ruthenium red and showed a reduced mitochondrial Zn^{2+} uptake but no totally inhibition[291]. We suppose that Zn^{2+} partially enters mitochondria by a pathway that naturally transports Ca^{2+} and the accumulation over the physiological level leads to toxicological effects in form of increased ROS-levels, reduced ΔΨm and the initiation of the intrinsic apoptosis pathway.

5.3.3.2 Endoplasmatic accumulation of Zn^{2+}

Early data of our working group reported an ER swelling in form of homogenous perinuclear clouds after ZnO NP treatment[247], that was also observed by *Chen et al. (2014)*[292]*.* Due to this reported ER swelling we observed no Zn^{2+} inside the ER. *Chen et al. (2014)* postulated the presence of ER stress after ZnO NP treatment as cellular imbalance and initiator of apoptosis by activation of caspase-12, which is localized inside the ER[292]. They analyzed the ER stress level using quantitative real-time PCR and found significant increased levels of *xbp-1s* mRNA (activator of UPR pathway)[292]. *Chen et al. (2014)* proposed that ER stress is mainly associated with generated ROS mediated by ZnO NP or released Zn^{2+}. Subsequently the increased ROS-level could activate apoptosis and necrosis mediated by early signals of ER stress response [292]. The lumen of the ER is the site for synthesis, folding, and assembling of proteins and many of these processes are Zn^{2+}-dependent[256,270,292,270,293]. We observed no Zn^{2+} accumulation in the ER after treatment with ZnO NP but with this observation we can not confirm if ER stress is still present. We suggest that the observed ER swelling in earlier results of our working group is an indicator for ER stress but not directly mediated by ZnO NP and Zn^{2+} but rather indirectly by ROS.

5.3.3.3 Nuclear accumulation of Zn^{2+}

Interestingly, the TEM-data of A549 cells showed nanoparticles in the nuclear envelope as well as inside the nucleus (see Figure 15). Published data of our working group indicated a strong increase of nuclear Zn^{2+} after treatment with ZnO NP measured by AAS [248]. This data could be confirmed by cLSM measurement of A549 cells in the current study (see Figure 27). Treatment with both particle sizes resulted in a fast and strong accumulation of Zn^{2+} in the nucleus. Zn^{2+} is a possible second messenger and an integral part of the active center of multiple enzymes (e.g., carboanhydrase) and nuclear proteins (e.g., zinc finger transcription factors and zinc finger nucleases). Our group

measured higher levels of Zn^{2+} in the nuclear than the cytoplasmic fraction, considering the smaller volume of the nucleus showing a strong accumulation of Zn^{2+} in the nucleus[248]. These data suggested an active transport into this cellular compartment. The data fit to our hypothesis of a direct Zn^{2+} activity in the nucleus very well. *Weser et al. (1973)* showed a strong increase of nuclear Zn^{2+} in liver cells of rat and chicken, after *in vitro* and *in vivo* administration of $ZnCl_2$[294]. The nuclear uptake of Zn^{2+} is discussed as ATP dependent translocation of MT, in absence Zn^{2+} transporters in the nucleus[295,296]. Zn^{2+} contributes in many important processes like gene expression at the site of nucleus. The generation of ROS resulted in oxidation of thiol groups, leading to release of Zn^{2+} storing proteins, such as MT and other proteins complexing Zn^{2+} by cysteine thiols. *Spahl (2007)* observed that exogenously applied nitrosative stress increases MT mRNA expression in a Zn^{2+} dependent manner released from MT[297].The high level of Zn^{2+} inside the nucleus may interact directly to DNA through unknown mechanisms. Zn^{2+} might interact with negatively charged residues of DNA (e.g., the phosphates of the DNA backbone)[298,299]. As mentioned before, high amounts of Zn^{2+} inside the nucleus may lead to toxicity especially genotoxicity in form of direct interactions with DNA to induce DNA damages.

5.4 Genotoxicity of ZnO NP

The permanent exposure of cells to ZnO NP may lead to DNA damages and might bear a possible mutagenic potential. For this reason, a possible DNA damaging potential, as well as DDR regulatory abilities were analyzed. In the following section the *in vitro* genotoxicity of ZnO NP (15-18 nm), and $ZnCl_2$ in A549 cells and primary mucosal cells will be discussed.

5.4.1 ZnO NP induce DNA double strand breaks

The *in vitro* genotoxicity of two different sizes of ZnO NP (4-5 nm, 15-18 nm), ZnO bulk as well as $ZnCl_2$ was investigated. The cells were also pretreated with NAC scavenging ROS, DTPA complexing dissociated Zn^{2+}, and particle coating with BSA reducing dissociation. The treatment with ZnO NP (15-18 nm) resulted in a strong DNA damaging of A549 cells within 15 min of exposure, while strong intracellular increased Zn^{2+} and marginal ROS-levels were observed, suggesting that ZnO NP could trigger DNA damages. Furthermore we observed as well DNA DSB in primary cells of mucosa after treatment with ZnO NP (15-18 nm). The treatment with ZnO NP (4-5 nm) also leads to strong increased DNA damages in A549 cells within 15 min, while lesser intracellular Zn^{2+}-levels and slight ROS-levels were detected. Comparable to our results of treatment with ZnO NP (15-18 nm), several investigations showed a concentration-dependent enhanced generation of ROS and DNA damages in different cell lines after ZnO NP treatment using 60-70 µg/mL as highest concentration in contrast to our final concentration of 100 µg/mL[136,152,240,268]. Moreover, DNA damages have been shown to occur after repetitive exposure to low concentrations of ZnO NP[300]. Generation of ROS is often used to explain toxic and especially genotoxic responses to ZnO NP, after overwhelming intracellular ROS detoxification pathways[172,187,301,187,302–304]. *Karlsson et al. (2014)* observed oxidative distress as the main genotoxic product in A549 cells, after exposure to ZnO NP for 4 h[305]. In our study the scavenging of ROS by NAC resulted in an inclomplete inhibition of DNA DSB after treatment with ZnO NP of both sizes. *Karlsson et al. (2014)* observed DNA DSB after 4 h of treatment with 20 µg/mL ZnO NP in contrast to our observed early generation of DNA DSB after treatment with 100 µg/mL[305]. Furthermore, we observed ROS, in case of ZnO NP (15-18 nm) after 30 min and just a slight increase after ZnO NP (4-5 nm) exposure, suggesting ROS as minor harmful factor in the early event of DNA damage. Furthermore we found DNA damages after treatment with ZnO bulk material. Bulk material is in the size of micrometer. Usually, the toxicity of nanoparticles is associated with their enhanced

reactivity due to their increased surface area to volume ratio. It is larger and thus has a reduced reactivity compared to nanoparticles. Nevertheless, we observed DNA DSB induced by ZnO bulk material. This genotoxic potential of ZnO bulk material could also be an effect of Zn^{2+} dissociation from the material. To analyze if Zn^{2+} is the more decisive damaging mechanism we pretreated the cells with DTPA. Complexation of Zn^{2+} by DTPA resulted in a complete inhibition of DNA DSB in case of ZnO NP (15-18 nm) treatment. We therefore recommend that the DNA damages are directly attributed to Zn^{2+}, by an unknown mechanism of Zn^{2+}-DNA-interaction. We found a strong accumulation of Zn^{2+} in the nucleus, after ZnO NP and $ZnCl_2$ treatment (see Figure 27). The Zn^{2+} ions possibly interact directly with negatively charged phosphates of the DNA backbone. However, the early peak of DNA damage (1 min after $ZnCl_2$ and 15 min after ZnO NP treatment) could be explained by dissociated particles. Generally under physiological conditions, most of Zn^{2+} is bound to proteins, such as MT. Enhanced levels of ROS may oxidize the zinc binding thiol groups of MT, which lead to the release of MT-bound Zn^{2+} reducing the puffer capacity and in turn reinforcing the DNA damaging capability of free Zn^{2+} [306]. Especially the second peak of DNA DSB could be attributed to increased ROS-levels, measured after 30 min and thereafter increased Zn^{2+} concentrations. Looking at all observations together, we suggest that DNA damages are related to two different mechanisms. The first peak is directly related to the internalized Zn^{2+}, taking place in the first minutes after ZnO NP exposure and minor to the involvement of generated ROS. The second peak is related to the induced ROS and thereafter increased Zn^{2+} concentrations. The nuclear Zn^{2+} could interact with the DNA by intercalation in the helix, or as already mentioned before, react with the phosphates in the DNA backbone.

5.4.2 Activation of DNA damage response

In this study, we observed an early and late induction of DNA DSB, after ZnO NP and $ZnCl_2$ exposure. The fast generation of DNA DSB, as well as the fast intracellular uptake of Zn^{2+}, in comparison to later generation of ROS, suggests Zn^{2+} as main mechanism behind ZnO NP genotoxicity. Therefore, we analyzed the DNA damage response activation of two well known pathways after ZnO NP treatment: ATM/Chk2- and ATR/Chk1 signaling. The ATM/Chk2 signaling was activated following cell exposure to ZnO NP as well as $ZnCl_2$. Regardless, no activation of ATR/Chk1 signaling was observed. These data show that the ZnO NP induced DNA DSB activated the DDR by ATM/Chk2- and not by ATM/Chk1 signaling. *Setyawati et al. (2015)* observed ATM, ATR and Chk1 activation leading to cell cycle arrest or apoptosis in presence of ZnO NP. They discussed their outcomes as mainly mediated by ROS, but they implicated Zn^{2+} as

an alternative regulator[307]. The autophosphorylation of ATM at Ser1981 is still known as sensitive marker for DNA DSB and a key process representing cellular responses to DNA damages[308,309], while ATR is mainly activated in presence of DNA SSB. Therefore, we suggested that the activation of ATM/Chk2 pathway is mediated by the generated DNA DSB which are observed in this study. After ATM phosphorylation we observed increased phosphorylation levels of the downstream effector proteins, Chk2, p53 and p21 after treatment with ZnO NP and $ZnCl_2$. Previously, we showed that ZnO NP, as well as $ZnCl_2$, induce DNA DSB in a biphasic way. We further investigated whether ZnO NP induce ATM/Chk2 activation through Zn^{2+} or ROS. The extracellular complexation of Zn^{2+} by DTPA resulted in a total inhibition of DNA DSB and an inactivation of ATM/Chk2 signaling. In contrast, scavenging of ROS led to no complete inhibition of DNA DSB and the ATM/Chk2 signaling is activated. We suggested that these outcomes further confirmed Zn^{2+} as the basic mechanism of ZnO NP genotoxicity. Chk2 is located downstream of ATM and is activated in an ATM-dependent manner after DNA damages. Chk2 is activated in response to ZnO NP, while DTPA pretreatment resulted in a Chk2 inhibition and NAC treatment in no inhibition, confirming again the activation of ATM/Chk2 signaling mediated by dissociated Zn^{2+}. P53 is stabilized by a variety of stress related signals. Subsequently, the tumorsuppressor p53 accumulates in the nucleus, binds in a specific way to DNA and regulates the transcription of several downstream effector genes[310]. In case of DNA damage, ATM induces different p53 modifications, resulting in two well investigated main consequences: the cell cycle arrest with induction of DNA repair or apoptosis. We observed a strong stabilization of p53 in presence of ZnO NP and $ZnCl_2$, as consequence of DNA damage, after 4 h. This strong p53 stabilization was reported before by *Meyer et al. (2011)* in human fibroblasts using same exposure time and concentration[311]. *Hainout et al. (2001)* described two ways of p53 activation in presence of ROS. P53 is activated after ROS induced DNA damages through AMT/Chk2 signaling or hypoxia[310]. The second possibility requires an interaction of hypoxia inducible factor (HIF-1α) and p53 but the detailed mechanism is still less understood[310]. *Chandel et al. (2000)* postulated that the mitochondrial generation of ROS regulates the redox state of cytoplasm and is responsible for p53 stabilization in presence of hypoxia[312]. In case of ZnO NP (15-18 nm), we observed a time-dependent increase of ROS while $\Delta\Psi m$ depolarized, but no ROS-dependent activation of p53 was observed. These findings suggested that the activation of p53 after particle treatment is independent of ROS. Furthermore, the p53 protein contains cysteins localized within the DNA binding domain. Three of these cysteins and a histidin are needed to coordinate the zinc building a protein structure that interacts directly to DNA[310,311,313,314]. Metal chelation experiments from *Méplan et al. (2000)* reported, that p53 is dependent on Zn^{2+}

coordination to bind specifically to DNA, as well as for a correct protein folding[310,314]. *Hainaut et al. (2001)* reported that the p53 zinc-binding activity is regulated by MT. High levels of MT operate as chelator for Zn^{2+} resulting in the prevention of p53 folding to an active form[310]. Interestingly, beside the p53 activation by ZnO NP and $ZnCl_2$ treatment we found a total inhibition of p53 after complexing Zn^{2+} by DTPA, suggesting Zn^{2+} as mediator of p53 stabilization in presence of DNA DSB. P53 activates the p21 gene, which suppresses the cell cycle phase. Another possibility for p21 activation is the accumulation of p16 in presence of DNA damages. P21 is a cyclin-dependent kinase inhibitor and known as a transcriptional target of p53. It triggers the degradation of cyclin B1 mediating the G2/M cell-cycle arrest[315,316]. We found that p21 was highly activated in ZnO NP treated cells after 4 h, suggesting that p21 activation has been triggered by the approved p53 signaling pathway. *Setyawati et al. (2015)* showed a p53 independent activation of p21 in carcinogenic epithelial cells, while p21 activation is triggered by p53 after ZnO NP treatment of normal epithelial cells[307]. They further hypothesized p21 activation as consequence of Erk-mediated pathway activation. They based their hypothesis on zinc ions released from ZnO NP, because Zn^{2+} is known as transducer of EGFR-signaling[293,308,317,307]. Interestingly, we found an activation of Erk and p21 after treatment with ZnO NP and $ZnCl_2$ in a Zn^{2+} dependent manner. Data reported by *Setywatis et al. (2015)* support our findings by observing a Zn^{2+} mediated activation of Erk and p21[307]. They suggested p21 as a second possible mediator besides p53. Concluding, we suggested an activation of ATM/Chk2 activation in a Zn^{2+} dependent manner after dissociation from the particles.

6 Conclusion and Outlook

The combination of physico-chemical characteristics, as found in ZnO nanoparticles, allows interactions with cells and opens up new research directions for medicine, industrial product design, and environmental remediation. Besides these excellent properties for future industrial applications the risk of possible harmful side effects is important to investigate. In this context we showed that ZnO NP exposure to cells results in toxic effects with reduced viability, decreased ΔΨm, released ROS, initiation of apoptosis and considerably increased DNA damages in form of DNA DSB. We observed increased Zn^{2+} levels in cytoplasm, nucleus and mitochondria but rarely detectable ZnO NP. We found evidence for the assumption that Zn^{2+} intake is the initial step of ZnO NP intoxication rather than uptake of ZnO NP. We found increased ROS-levels after ZnO NP exposure, but strongly reduced ROS-levels after NAC treatment were not reflected in equivalently decreased levels of DNA DSB. This concept of Zn^{2+} rather than ROS mediated DNA damages are supported by our DNA damage response pathway analysis. We found ATM/Chk2, but no ATR/Chk1 pathway activation after ZnO NP exposure. This is indicative for DNA DSB recognition, but not DNA SSB frequently induced by ROS. Complexing of free Zn^{2+} resulted consequently in inhibited ATM/Chk2 activation, but NAC treatment resulted in no change of activation level. Taken together we suggest that the two phases of DNA damages are related to two different mechanisms: the first peak is related to the internalized Zn^{2+} taking place in the first minutes after the ZnO NP exposure and the second peak is related to the release of endogenous Zn^{2+} by increasing ROS-levels. Our data suggest a direct DNA damaging potential of Zn^{2+} by an unknown mechanism and ROS as a trigger of endogenous zinc release.

For this reasons further studies are now mandatory to decipher the mechanisms resulting in DNA damages. Especially the direct interactions of Zn^{2+} with DNA structure as well as the ROS triggered release of Zn^{2+} from intracellular proteins have to be investigated. The DNA damaging mechanism and possible mutagenic potential of ZnO NP have to be evaluated more detailed to reduce their hazardous health effects and optimize their physico-chemical characteristics for industrial application.

7 References

1. Krug HF and Wick P. Nanotoxicology: an interdisciplinary challenge. *Angewandte Chemie (International ed. in English)* 2011; 50: 1260–1278.
2. Bund für Umwelt und Naturschutz Deutschland e.V. (BUND). Nanotechnologie: Nanomaterialien, http://www.bund.net/themen_und_projekte/nanotechnologie/nanomaterialien/ (2015, accessed 24 June 2015).
3. Office of the Director and Office of Communication and Public Liaison. Nanotechnology at the National Institutes of Health, http://www.nih.gov/science/nanotechnology/sci_NANO_brochure.pdf (2007, accessed 24 May 2015).
4. Burleson DJ, Driessen MD and Penn RL. On the characterization of environmental nanoparticles. *Journal of environmental science and health. Part A, Toxic/hazardous substances & environmental engineering* 2004; 39: 2707–2753.
5. Nel A, Xia T, Madler L and Li N. Toxic potential of materials at the nanolevel. *Science (New York, N.Y.)* 2006; 311: 622–627.
6. Tiede K, Hassellov M, Breitbarth E, Chaudhry Q and Boxall, Alistair B A. Considerations for environmental fate and ecotoxicity testing to support environmental risk assessments for engineered nanoparticles. *J Chromatogr A (Journal of chromatography A)* 2009; 1216: 503–509.
7. Xia T, Li N and Nel AE. Potential health impact of nanoparticles. *Annual review of public health* 2009; 30: 137–150.
8. Jones CF and Grainger DW. In vitro assessments of nanomaterial toxicity. *Advanced drug delivery reviews* 2009; 61: 438–456.
9. U.S. EPA. Types of Nanomaterials Under Investigation by EPA, epa.gov., http://www.epa.gov/nanoscience/quickfinder/nanomaterials.htm (2012, accessed 24 May 2015).
10. Gottschalk F, Sonderer T, Scholz RW and Nowack B. Modeled environmental concentrations of engineered nanomaterials (TiO(2), ZnO, Ag, CNT, Fullerenes) for different regions. *Environmental science & technology* 2009; 43: 9216–9222.
11. Horikoshi S and Serpone N. *Microwaves in nanoparticle synthesis: Fundamentals and applications*. Weinheim: Wiley-VCH, 2013.
12. Mody V, Siwale R, Singh A and Mody H. Introduction to metallic nanoparticles. *J Pharm Bioall Sci* 2010; 2: 282–289.
13. Haas, K. H., Hutter, F. Produktion von Nanomaterialien: Schlussbericht zum BMBF-Projekt (FKZ 02PH 2107) 2003, http://www.produktionsforschung.de/ucm/groups/contribution/@pft/documents/native/ucm01_000317.pdf (2003, accessed 15 August 2015).
14. Freudenreich DJ. Die Herstellung von Nanopartikeln: Erfinderaktivitäten 2010 2010, http://www.dpma.de/docs/service/veroeffentlichungen/erfinderaktivitaeten/ea_2010.pdf (2010, accessed 15 August 2015).
15. Future Markets Inc. (2013). The Global Market for Metal Oxide Nanoparticles to 2020, http://www.researchandmarkets.com/research/jkjd5k/the_global_market (2013, accessed 20 August 2015).
16. Piccinno F, Gottschalk F, Seeger S and Nowack B. Industrial production quantities and uses of ten engineered nanomaterials in Europe and the world. *Journal of Nanoparticle Research* 2012; 14: 1109–1120.
17. Ivask A, Titma T, Visnapuu M, et al. Toxicity of 11 Metal Oxide Nanoparticles to Three Mammalian Cell Types In Vitro. *Current topics in medicinal chemistry* 2015; 15: 1914–1929.

18. Brunner TJ, Wick P, Manser P, et al. In vitro cytotoxicity of oxide nanoparticles: comparison to asbestos, silica, and the effect of particle solubility. *Environmental science & technology* 2006; 40: 4374–4381.
19. Kołodziejczak-Radzimska A and Jesionowski T. Zinc Oxide—From Synthesis to Application: A Review. *Materials* 2014; 7: 2833–2881.
20. International Zinc Association. Zinc oxide applications, http://www.zinc.org.in/zinc-oxide-applications/ (2015, accessed 25 June 2015).
21. Bondarenko O, Juganson K, Ivask A, Kasemets K, Mortimer M and Kahru A. Toxicity of Ag, CuO and ZnO nanoparticles to selected environmentally relevant test organisms and mammalian cells in vitro: a critical review. *Archives of toxicology* 2013; 87: 1181–1200.
22. Hernández Battez A, González R, Viesca JL, et al. CuO, ZrO_2 and ZnO nanoparticles as antiwear additive in oil lubricants. *Wear* 2008; 265: 422–428.
23. Oberdörster G, Oberdörster E and Oberdörster J. Nanotoxicology: An Emerging Discipline Evolving from Studies of Ultrafine Particles. *Environmental Health Perspectives* 2005; 113: 823–839.
24. DeLouise LA. Applications of Nanotechnology in Dermatology. *Journal of Investigative Dermatology* 2012; 132: 964–975.
25. Endo M, Hayashi T, Kim YA, Terrones M and Dresselhaus MS. Applications of carbon nanotubes in the twenty-first century. *Philosophical transactions. Series A, Mathematical, physical, and engineering sciences* 2004; 362: 2223–2238.
26. Nohynek GJ and Dufour EK. Nano-sized cosmetic formulations or solid nanoparticles in sunscreens: a risk to human health? *Archives of toxicology* 2012; 86: 1063–1075.
27. Kocbek P, Teskac K, Kreft ME and Kristl J. Toxicological aspects of long-term treatment of keratinocytes with ZnO and TiO_2 nanoparticles. *Small (Weinheim an der Bergstrasse, Germany)* 2010; 6: 1908–1917.
28. Hackenberg S and Kleinsasser N. Dermal toxicity of ZnO nanoparticles: a worrying feature of sunscreen? *Nanomedicine (London, England)* 2012; 7: 461–463.
29. Rouse JG, Yang J, Ryman-Rasmussen JP, Barron AR and Monteiro-Riviere NA. Effects of mechanical flexion on the penetration of fullerene amino acid-derivatized peptide nanoparticles through skin. *Nano letters* 2007; 7: 155–160.
30. Schneider M, Stracke F, Hansen S and Schaefer UF. Nanoparticles and their interactions with the dermal barrier. *Dermato-endocrinology* 2009; 1: 197–206.
31. Hillyer JF and Albrecht RM. Gastrointestinal persorption and tissue distribution of differently sized colloidal gold nanoparticles. *Journal of pharmaceutical sciences* 2001; 90: 1927–1936.
32. Florence AT. The oral absorption of micro- and nanoparticulates: neither exceptional nor unusual. *Pharmaceutical research* 1997; 14: 259–266.
33. Florence AT and Hussain N. Transcytosis of nanoparticle and dendrimer delivery systems: evolving vistas. *Advanced drug delivery reviews* 2001; 50 Suppl 1: S69-89.
34. Hussain N, Jaitley V and Florence AT. Recent advances in the understanding of uptake of microparticulates across the gastrointestinal lymphatics. *Advanced drug delivery reviews* 2001; 50: 107–142.
35. Szentkuti L and Enss ML. Comparative lectin-histochemistry on the pre-epithelial mucus layer in the distal colon of conventional and germ-free rats. *Comparative biochemistry and physiology. Part A, Molecular & integrative physiology* 1998; 119: 379–386.
36. Suran M. A little hard to swallow? *EMBO Reports* 2014; 15: 638–641.
37. Bacchetta R, Moschini E, Santo N, et al. Evidence and uptake routes for Zinc oxide nanoparticles through the gastrointestinal barrier in Xenopus laevis. *Nanotoxicology* 2014; 8: 728–744.

38. Bruinink A, Wang J and Wick P. Effect of particle agglomeration in nanotoxicology: Archives of Toxicology. *Arch Toxicol* 2015; 89: 659–675.
39. Hoet PH, Bruske-Hohlfeld I and Salata OV. Nanoparticles - known and unknown health risks. *Journal of nanobiotechnology* 2004; 2: 12.
40. Marieb EN and Hoehn K. *Human anatomy & physiology*: Pearson Education, 2007.
41. Human respiratory tract model for radiological protection. A report of a Task Group of the International Commission on Radiological Protection. *Annals of the ICRP* 1994; 24: 1–482.
42. Bowden DH. The alveolar macrophage. *Environmental Health Perspectives* 1984; 55: 327–341.
43. Bowden DH and Adamson IY. Pathways of cellular efflux and particulate clearance after carbon instillation to the lung. *The Journal of pathology* 1984; 143: 117–125.
44. Bowden DH and Adamson IY. Response of pulmonary macrophages to unilateral instillation of carbon. *The American journal of pathology* 1984; 115: 151–155.
45. Katsnelson BA and Privalova LI. Recruitment of phagocytizing cells into the respiratory tract as a response to the cytotoxic action of deposited particles. *Environmental Health Perspectives* 1984; 55: 313–325.
46. Lippmann M, Yeates DB and Albert RE. Deposition, retention, and clearance of inhaled particles. *British journal of industrial medicine* 1980; 37: 337–362.
47. Gil H, Oh M, Woo K, Lee E, Oh M and Hong S. Relationship between pulmonary surfactant protein and lipid peroxidation in lung injury due to paraquat intoxication in rats. *The Korean journal of internal medicine* 2007; 22: 67–72.
48. Jachak A, Lai SK, Hida K, et al. Transport of metal oxide nanoparticles and single-walled carbon nanotubes in human mucus. *Nanotoxicology* 2012; 6: 614–622.
49. Cho W, Duffin R, Howie, Sarah E M, et al. Progressive severe lung injury by zinc oxide nanoparticles; the role of Zn^{2+} dissolution inside lysosomes. *Particle and fibre toxicology* 2011; 8: 27.
50. Blanc PD, Boushey HA, Wong H, Wintermeyer SF and Bernstein MS. Cytokines in metal fume fever. *The American review of respiratory disease* 1993; 147: 134–138.
51. Kaye P, Young H and O'Sullivan I. Metal fume fever: a case report and review of the literature. *Emergency medicine journal EMJ* 2002; 19: 268–269.
52. Lindahl M, Leanderson P and Tagesson C. Novel aspect on metal fume fever: zinc stimulates oxygen radical formation in human neutrophils. *Human & experimental toxicology* 1998; 17: 105–110.
53. Vandebriel RJ and De Jong, Wim H. A review of mammalian toxicity of ZnO nanoparticles. *Nanotechnology, science and applications* 2012; 5: 61–71.
54. Iversen T, Skotland T and Sandvig K. Endocytosis and intracellular transport of nanoparticles: Present knowledge and need for future studies. *Nano Today* 2011; 6: 176–185.
55. Oh N and Park J. Endocytosis and exocytosis of nanoparticles in mammalian cells. *International journal of nanomedicine* 2014; 9 Suppl 1: 51–63.
56. Pelkmans L, Kartenbeck J and Helenius A. Caveolar endocytosis of simian virus 40 reveals a new two-step vesicular-transport pathway to the ER. *Nature cell biology* 2001; 3: 473–483.
57. Tomatis M, Turci F, Ceschino R, et al. High aspect ratio materials: role of surface chemistry vs. length in the historical "long and short amosite asbestos fibers". *Inhalation toxicology* 2010; 22: 984–998.

58. Wang Z, Tiruppathi C, Minshall RD and Malik AB. Size and dynamics of caveolae studied using nanoparticles in living endothelial cells. *ACS nano* 2009; 3: 4110–4116.
59. Lu F, Wu S, Hung Y and Mou C. Size effect on cell uptake in well-suspended, uniform mesoporous silica nanoparticles. *Small (Weinheim an der Bergstrasse, Germany)* 2009; 5: 1408–1413.
60. Young KD. The selective value of bacterial shape. *Microbiology and molecular biology reviews MMBR* 2006; 70: 660–703.
61. Geiser M. Update on macrophage clearance of inhaled micro- and nanoparticles. *Journal of aerosol medicine and pulmonary drug delivery* 2010; 23: 207–217.
62. Jovic M, Sharma M, Rahajeng J and Caplan S. The early endosome: a busy sorting station for proteins at the crossroads. *Histology and histopathology* 2010; 25: 99–112.
63. Stoorvogel W, Strous GJ, Geuze HJ, Oorschot V and Schwartz AL. Late endosomes derive from early endosomes by maturation. *Cell* 1991; 65: 417–427.
64. Appelqvist H, Waster P, Kagedal K and Ollinger K. The lysosome: from waste bag to potential therapeutic target. *Journal of molecular cell biology* 2013; 5: 214–226.
65. Knight DE, Grafenstein H von and Athayde CM. Calcium-dependent and calcium-independent exocytosis. *Trends in neurosciences* 1989; 12: 451–458.
66. Burgoyne RD and Morgan A. Ca^{2+} and secretory-vesicle dynamics. *Trends in neurosciences* 1995; 18: 191–196.
67. Manjithaya R and Subramani S. Autophagy: a broad role in unconventional protein secretion? *Trends in cell biology* 2011; 21: 67–73.
68. Morgan A. Exocytosis. *Essays in biochemistry* 1995; 30: 77–95.
69. Nickel W and Seedorf M. Unconventional mechanisms of protein transport to the cell surface of eukaryotic cells. *Annual review of cell and developmental biology* 2008; 24: 287–308.
70. Hsiao I and Huang Y. Effects of serum on cytotoxicity of nano- and micro-sized ZnO particles. *Journal of nanoparticle research an interdisciplinary forum for nanoscale science and technology* 2013; 15: 1829.
71. Hackenberg S, Zimmermann F, Scherzed A, et al. Repetitive exposure to zinc oxide nanoparticles induces dna damage in human nasal mucosa mini organ cultures. *Environmental and molecular mutagenesis* 2011; 52: 582–589.
72. Kao Y, Chen Y, Cheng T, Chiung Y and Liu P. Zinc oxide nanoparticles interfere with zinc ion homeostasis to cause cytotoxicity. *Toxicological sciences an official journal of the Society of Toxicology* 2012; 125: 462–472.
73. Dockery DW, Pope CA, Xu X, et al. An association between air pollution and mortality in six U.S. cities. *The New England journal of medicine* 1993; 329: 1753–1759.
74. Hsiao I and Huang Y. Effects of various physicochemical characteristics on the toxicities of ZnO and TiO_2 nanoparticles toward human lung epithelial cells. *The Science of the total environment* 2011; 409: 1219–1228.
75. HEI Health Review Committee and Scientific Staff. HEI Perspectives 2002; 2002.
76. Fine JM, Gordon T, Chen LC, Kinney P, Falcone G and Beckett WS. Metal fume fever: characterization of clinical and plasma IL-6 responses in controlled human exposures to zinc oxide fume at and below the threshold limit value. *Journal of occupational and environmental medicine / American College of Occupational and Environmental Medicine* 1997; 39: 722–726.
77. Kelley J, Shull S, Walsh JJ, Cutroneo KR and Absher M. Auto-induction of transforming growth factor-beta in human lung fibroblasts. *American journal of respiratory cell and molecular biology* 1993; 8: 417–424.

78. Nelson S and Mason CM. The inflammatory response in chronic bronchitis. *Seminars in respiratory and critical care medicine* 2000; 21: 79–86.
79. Veranth JM, Kaser EG, Veranth MM, Koch M and Yost GS. Cytokine responses of human lung cells (BEAS-2B) treated with micron-sized and nanoparticles of metal oxides compared to soil dusts. *Particle and fibre toxicology* 2007; 4: 2.
80. McCreanor J, Cullinan P, Nieuwenhuijsen MJ, et al. Respiratory effects of exposure to diesel traffic in persons with asthma. *The New England journal of medicine* 2007; 357: 2348–2358.
81. Gojova A, Guo B, Kota RS, Rutledge JC, Kennedy IM and Barakat AI. Induction of inflammation in vascular endothelial cells by metal oxide nanoparticles: effect of particle composition. *Environmental Health Perspectives* 2007; 115: 403–409.
82. Circu ML and Aw TY. Reactive oxygen species, cellular redox systems, and apoptosis. *Free radical biology & medicine* 2010; 48: 749–762.
83. Halliwell B. Free radicals, antioxidants, and human disease: curiosity, cause, or consequence? *Lancet* 1994; 344: 721–724.
84. Halliwell B. Free radicals and antioxidants: a personal view. *Nutrition reviews* 1994; 52: 253–265.
85. Schieber M and Chandel NS. ROS function in redox signaling and oxidative stress. *Current biology CB* 2014; 24: R453-62.
86. Cross CE, Halliwell B, Borish ET, et al. Oxygen radicals and human disease. *Annals of internal medicine* 1987; 107: 526–545.
87. Finkel T. Signal transduction by reactive oxygen species. *The Journal of cell biology* 2011; 194: 7–15.
88. Brieger K, Schiavone S, Miller, F J Jr and Krause K. Reactive oxygen species: from health to disease. *Swiss medical weekly* 2012; 142: w13659.
89. Nel A. Toxic Potential of Materials at the Nanolevel. *Science* 2006; 311: 622–627.
90. Provinciali M, Donnini A, Argentati K, Di Stasio G, Bartozzi B and Bernardini G. Reactive oxygen species modulate Zn(2+)-induced apoptosis in cancer cells. *Free radical biology & medicine* 2002; 32: 431–445.
91. Bishop GM, Dringen R and Robinson SR. Zinc stimulates the production of toxic reactive oxygen species (ROS) and inhibits glutathione reductase in astrocytes. *Free radical biology & medicine* 2007; 42: 1222–1230.
92. Walther UI, Wilhelm B, Walther S, Muckter H and Fichtl B. Zinc toxicity in various lung cell lines is mediated by glutathione and GSSG reductase activity. *Biological trace element research* 2000; 78: 163–177.
93. Xia T, Kovochich M, Brant J, et al. Comparison of the abilities of ambient and manufactured nanoparticles to induce cellular toxicity according to an oxidative stress paradigm. *Nano letters* 2006; 6: 1794–1807.
94. Harrison DG and Ohara Y. Physiologic consequences of increased vascular oxidant stresses in hypercholesterolemia and atherosclerosis: implications for impaired vasomotion. *The American journal of cardiology* 1995; 75: 75B-81B.
95. Kamata H, Honda S, Maeda S, Chang L, Hirata H and Karin M. Reactive oxygen species promote TNFalpha-induced death and sustained JNK activation by inhibiting MAP kinase phosphatases. *Cell* 2005; 120: 649–661.
96. Rahman I and MacNee W. Oxidant/antioxidant imbalance in smokers and chronic obstructive pulmonary disease. *Thorax* 1996; 51: 348–350.
97. Valko M, Leibfritz D, Moncol J, Cronin MT, Mazur M and Telser J. Free radicals and antioxidants in normal physiological functions and human disease. *The International Journal of Biochemistry & Cell Biology* 2007; 39: 44–84.
98. Moschini E, Gualtieri M, Colombo M, Fascio U, Camatini M and Mantecca P. The modality of cell-particle interactions drives the toxicity of nanosized CuO and TiO(2) in human alveolar epithelial cells. *Toxicology letters* 2013; 222: 102–116.

99. Kroemer G and Reed JC. Mitochondrial control of cell death. *Nature medicine* 2000; 6: 513–519.
100. Kuznetsov AV, Kehrer I, Kozlov AV, et al. Mitochondrial ROS production under cellular stress: comparison of different detection methods. *Analytical and bioanalytical chemistry* 2011; 400: 2383–2390.
101. Newmeyer DD and Ferguson-Miller S. Mitochondria: releasing power for life and unleashing the machineries of death. *Cell* 2003; 112: 481–490.
102. Moschini E, Gualtieri M, Colombo M, Fascio U, Camatini M and Mantecca P. The modality of cell-particle interactions drives the toxicity of nanosized CuO and TiO(2) in human alveolar epithelial cells. *Toxicology letters* 2013; 222: 102–116.
103. Savic R, Luo L, Eisenberg A and Maysinger D. Micellar nanocontainers distribute to defined cytoplasmic organelles. *Science (New York, N.Y.)* 2003; 300: 615–618.
104. Tang Y, Wang F, Jin C, Liang H, Zhong X and Yang Y. Mitochondrial injury induced by nanosized titanium dioxide in A549 cells and rats. *Environmental toxicology and pharmacology* 2013; 36: 66–72.
105. Unfried K, Sydlik U, Bierhals K, Weissenberg A and Abel J. Carbon nanoparticle-induced lung epithelial cell proliferation is mediated by receptor-dependent Akt activation. *American journal of physiology. Lung cellular and molecular physiology* 2008; 294: L358-67.
106. Zhu M, Wang B, Wang Y, et al. Endothelial dysfunction and inflammation induced by iron oxide nanoparticle exposure: Risk factors for early atherosclerosis. *Toxicology letters* 2011; 203: 162–171.
107. Salnikov V, Lukyanenko YO, Frederick CA, Lederer WJ and Lukyanenko V. Probing the outer mitochondrial membrane in cardiac mitochondria with nanoparticles. *Biophysical journal* 2007; 92: 1058–1071.
108. Qi L, Xu Z, Li Y, Jiang X and Han X. In vitro effects of chitosan nanoparticles on proliferation of human gastric carcinoma cell line MGC803 cells. *World journal of gastroenterology WJG* 2005; 11: 5136–5141.
109. Fulda S and Debatin K. Extrinsic versus intrinsic apoptosis pathways in anticancer chemotherapy. *Oncogene* 2006; 25: 4798–4811.
110. Cho W, Duffin R, Howie SEM, et al. Progressive severe lung injury by zinc oxide nanoparticles; the role of Zn^{2+} dissolution inside lysosomes. *Particle and fibre toxicology* 2011; 8: 27.
111. Stern ST, Adiseshaiah PP and Crist RM. Autophagy and lysosomal dysfunction as emerging mechanisms of nanomaterial toxicity. *Particle and fibre toxicology* 2012; 9: 20.
112. Muller KH, Kulkarni J, Motskin M, et al. pH-dependent toxicity of high aspect ratio ZnO nanowires in macrophages due to intracellular dissolution. *Acs Nano* 2010; 4: 6767–6779.
113. Aits S and Jaattela M. Lysosomal cell death at a glance. *Journal of cell science* 2013; 126: 1905–1912.
114. Yuan X, Li W, Dalen H, et al. Lysosomal destabilization in p53-induced apoptosis. *Proceedings of the National Academy of Sciences of the United States of America* 2002; 99: 6286–6291.
115. Cho W, Duffin R, Howie SEM, et al. Progressive severe lung injury by zinc oxide nanoparticles; the role of Zn^{2+} dissolution inside lysosomes. *Particle and fibre toxicology* 2011; 8: 27.
116. Kirsten Gerloff, Catrin Albrecht, Agnes W. Boots, Irmgard Förster and Roel P. F. Schins. Cytotoxicity and oxidative DNA damage by nanoparticles in human intestinal Caco-2 cells. *Nanotoxicology* 2009; 3: 355–364.
117. Kim YH, Fazlollahi F, Kennedy IM, et al. Alveolar epithelial cell injury due to zinc oxide nanoparticle exposure. *American journal of respiratory and critical care medicine* 2010; 182: 1398–1409.

118. Ahlinder L, Ekstrand-Hammarstrom B, Geladi P and Osterlund L. Large uptake of titania and iron oxide nanoparticles in the nucleus of lung epithelial cells as measured by Raman imaging and multivariate classification. *Biophysical journal* 2013; 105: 310–319.
119. Pante N and Kann M. Nuclear pore complex is able to transport macromolecules with diameters of about 39 nm. *Molecular biology of the cell* 2002; 13: 425–434.
120. Terry LJ, Shows EB and Wente SR. Crossing the nuclear envelope: hierarchical regulation of nucleocytoplasmic transport. *Science (New York, N.Y.)* 2007; 318: 1412–1416.
121. Lopez-Contreras AJ, Gutierrez-Martinez P, Specks J, Rodrigo-Perez S and Fernandez-Capetillo O. An extra allele of Chk1 limits oncogene-induced replicative stress and promotes transformation. *The Journal of experimental medicine* 2012; 209: 455–461.
122. Fridman JS and Lowe SW. Control of apoptosis by p53. *Oncogene* 2003; 22: 9030–9040.
123. Peter ME and Krammer PH. The CD95(APO-1/Fas) DISC and beyond. *Cell death and differentiation* 2003; 10: 26–35.
124. Kroemer G and Reed JC. Mitochondrial control of cell death. *Nature medicine* 2000; 6: 513–519.
125. Nakano K and Vousden KH. PUMA, a novel proapoptotic gene, is induced by p53. *Molecular cell* 2001; 7: 683–694.
126. Martinou JC and Green DR. Breaking the mitochondrial barrier. *Nature reviews. Molecular cell biology* 2001; 2: 63–67.
127. Jiang X and Wang X. Cytochrome C-mediated apoptosis. *Annual review of biochemistry* 2004; 73: 87–106.
128. Wang C and Youle RJ. The role of mitochondria in apoptosis*. *Annual review of genetics* 2009; 43: 95–118.
129. Ferri KF and Kroemer G. Mitochondria--the suicide organelles. *BioEssays news and reviews in molecular, cellular and developmental biology* 2001; 23: 111–115.
130. Shrivastava P, Pantano C, Watkin R, et al. Reactive nitrogen species-induced cell death requires Fas-dependent activation of c-Jun N-terminal kinase. *Molecular and cellular biology* 2004; 24: 6763–6772.
131. Akhtar MJ, Ahamed M, Kumar S, Khan MM, Ahmad J and Alrokayan SA. Zinc oxide nanoparticles selectively induce apoptosis in human cancer cells through reactive oxygen species. *International journal of nanomedicine* 2012; 7: 845–857.
132. Jeong SH, Kim HJ, Ryu HJ, et al. ZnO nanoparticles induce TNF-alpha expression via ROS-ERK-Egr-1 pathway in human keratinocytes. *Journal of dermatological science* 2013; 72: 263–273.
133. McCubrey JA, Steelman LS, Franklin RA, et al. Targeting the RAF/MEK/ERK, PI3K/AKT and p53 pathways in hematopoietic drug resistance. *Advances in enzyme regulation* 2007; 47: 64–103.
134. ang L and Karin M. Mammalian MAP kinase signalling cascades. *Nature* 2001; 410: 37–40.
135. Persons DL, Yazlovitskaya EM and Pelling JC. Effect of extracellular signal-regulated kinase on p53 accumulation in response to cisplatin. *The Journal of biological chemistry* 2000; 275: 35778–35785.
136. Tang D, Wu D, Hirao A, et al. ERK activation mediates cell cycle arrest and apoptosis after DNA damage independently of p53. *The Journal of biological chemistry* 2002; 277: 12710–12717.
137. Meyer K, Rajanahalli P, Ahamed M, Rowe JJ and Hong Y. ZnO nanoparticles induce apoptosis in human dermal fibroblasts via p53 and p38 pathways.

Toxicology in vitro an international journal published in association with BIBRA 2011; 25: 1721–1726.

138. Wilhelmi V, Fischer U, Weighardt H, et al. Zinc oxide nanoparticles induce necrosis and apoptosis in macrophages in a p47phox- and Nrf2-independent manner. *PloS one* 2013; 8: e65704.
139. Ciccia A and Elledge SJ. The DNA damage response: making it safe to play with knives. *Molecular cell* 2010; 40: 179–204.
140. Friedberg EC, Walker GC, Siede W and Wood RD. *DNA repair and mutagenesis.* 2nd ed. Washington: American Society for Microbiology Press, 2006.
141. Houtgraaf JH, Versmissen J and van der Giessen, Wim J. A concise review of DNA damage checkpoints and repair in mammalian cells. *Cardiovascular revascularization medicine including molecular interventions* 2006; 7: 165–172.
142. Jackson SP and Bartek J. The DNA-damage response in human biology and disease. *Nature* 2009; 461: 1071–1078.
143. Risom L, Moller P and Loft S. Oxidative stress-induced DNA damage by particulate air pollution. *Mutation research* 2005; 592: 119–137.
144. Shukla RK, Sharma V, Pandey AK, Singh S, Sultana S and Dhawan A. ROS-mediated genotoxicity induced by titanium dioxide nanoparticles in human epidermal cells. *Toxicology in vitro an international journal published in association with BIBRA* 2011; 25: 231–241.
145. Valko M, Rhodes CJ, Moncol J, Izakovic M and Mazur M. Free radicals, metals and antioxidants in oxidative stress-induced cancer. *Chemico-biological interactions* 2006; 160: 1–40.
146. Valko M, Leibfritz D, Moncol J, Cronin MTD, Mazur M and Telser J. Free radicals and antioxidants in normal physiological functions and human disease. *The international journal of biochemistry & cell biology* 2007; 39: 44–84.
147. Marnett LJ. Oxy radicals, lipid peroxidation and DNA damage. *Toxicology* 2002; 181-182: 219–222.
148. Hong SC, Lee JH, Lee J, et al. Subtle cytotoxicity and genotoxicity differences in superparamagnetic iron oxide nanoparticles coated with various functional groups. *International journal of nanomedicine* 2011; 6: 3219–3231.
149. Misra SK, Dybowska A, Berhanu D, Luoma SN and Valsami-Jones E. The complexity of nanoparticle dissolution and its importance in nanotoxicological studies. *The Science of the total environment* 2012; 438: 225–232.
150. Langerak P and Russell P. Regulatory networks integrating cell cycle control with DNA damage checkpoints and double-strand break repair. *Philosophical transactions of the Royal Society of London. Series B, Biological sciences* 2011; 366: 3562–3571.
151. Khanna KK and Jackson SP. DNA double-strand breaks: signaling, repair and the cancer connection. *Nature genetics* 2001; 27: 247–254.
152. Khanna KK, Lavin MF, Jackson SP and Mulhern TD. ATM, a central controller of cellular responses to DNA damage. *Cell death and differentiation* 2001; 8: 1052–1065.
153. Li JJ, Hartono D, Ong C, Bay B and Yung LL. Autophagy and oxidative stress associated with gold nanoparticles. *Biomaterials* 2010; 31: 5996–6003.
154. Singh N, Manshian B, Jenkins GJS, et al. NanoGenotoxicology: the DNA damaging potential of engineered nanomaterials. *Biomaterials* 2009; 30: 3891–3914.
155. Rogakou EP, Pilch DR, Orr AH, Ivanova VS and Bonner WM. DNA double-stranded breaks induce histone H2AX phosphorylation on serine 139. *The Journal of biological chemistry* 1998; 273: 5858–5868.
156. Rogakou EP and Sekeri-Pataryas KE. Histone variants of H2A and H3 families are regulated during in vitro aging in the same manner as during differentiation. *Experimental gerontology* 1999; 34: 741–754.

157. Paull TT, Rogakou EP, Yamazaki V, Kirchgessner CU, Gellert M and Bonner WM. A critical role for histone H2AX in recruitment of repair factors to nuclear foci after DNA damage. *Current biology CB* 2000; 10: 886–895.
158. Rogakou EP, Nieves-Neira W, Boon C, Pommier Y and Bonner WM. Initiation of DNA fragmentation during apoptosis induces phosphorylation of H2AX histone at serine 139. *The Journal of biological chemistry* 2000; 275: 9390–9395.
159. Sedelnikova OA, Rogakou EP, Panyutin IG and Bonner WM. Quantitative detection of (125)IdU-induced DNA double-strand breaks with gamma-H2AX antibody. *Radiation research* 2002; 158: 486–492.
160. Chowdhury D, Keogh M, Ishii H, Peterson CL, Buratowski S and Lieberman J. gamma-H2AX dephosphorylation by protein phosphatase 2A facilitates DNA double-strand break repair. *Molecular cell* 2005; 20: 801–809.
161. Bartek J and Lukas J. DNA damage checkpoints: from initiation to recovery or adaptation. *Current opinion in cell biology* 2007; 19: 238–245.
162. Cimprich KA and Cortez D. ATR: an essential regulator of genome integrity. *Nature reviews. Molecular cell biology* 2008; 9: 616–627.
163. Shiloh Y. ATM and related protein kinases: safeguarding genome integrity. *Nature reviews. Cancer* 2003; 3: 155–168.
164. Roos WP and Kaina B. DNA damage-induced cell death: from specific DNA lesions to the DNA damage response and apoptosis. *Cancer letters* 2013; 332: 237–248.
165. Guo Z, Deshpande R and Paull TT. ATM activation in the presence of oxidative stress. *Cell Cycle* 2010; 9: 4805–4811.
166. Matsuoka S, Rotman G, Ogawa A, Shiloh Y, Tamai K and Elledge SJ. Ataxia telangiectasia-mutated phosphorylates Chk2 in vivo and in vitro. *Proceedings of the National Academy of Sciences of the United States of America* 2000; 97: 10389–10394.
167. Lankenau DH (ed). *Genome Integrity: Facets and Perspectives*. Heidelberg: Springer, 2007.
168. Chehab NH, Malikzay A, Appel M and Halazonetis TD. Chk2/hCds1 functions as a DNA damage checkpoint in G(1) by stabilizing p53. *Genes & development* 2000; 14: 278–288.
169. Christmann M, Fritz G and Kaina B. Induction of DNA repair genes in mammalian cells in response to genotoxic stress. In: Lankenau DH (ed.) *Genome Integrity: Facets and Perspectives*. Heidelberg: Springer, 2007, pp. 383–398.
170. Sirbu BM and Cortez D. DNA damage response: three levels of DNA repair regulation. *Cold Spring Harbor perspectives in biology* 2013; 5: a012724.
171. Meek DW. Tumour suppression by p53: a role for the DNA damage response? *Nature reviews. Cancer* 2009; 9: 714–723.
172. Lakin ND and Jackson SP. Regulation of p53 in response to DNA damage. *Oncogene* 1999; 18: 7644–7655.
173. Mandinova A and Lee SW. The p53 pathway as a target in cancer therapeutics: obstacles and promise. *Science translational medicine* 2011; 3: 64rv1.
174. Toledo F and Wahl GM. Regulating the p53 pathway: in vitro hypotheses, in vivo veritas. *Nature reviews. Cancer* 2006; 6: 909–923.
175. Vousden KH and Lane DP. p53 in health and disease. *Nature reviews. Molecular cell biology* 2007; 8: 275–283.
176. Bellamy CO. p53 and apoptosis. *British medical bulletin* 1997; 53: 522–538.
177. Toledo LI, Murga M, Gutierrez-Martinez P, Soria R and Fernandez-Capetillo O. ATR signaling can drive cells into senescence in the absence of DNA breaks. *Genes & development* 2008; 22: 297–302.
178. Tang J, Qu L, Zhang J, et al. Critical role for Daxx in regulating Mdm2. *Nature cell biology* 2006; 8: 855–862.

179. Langerak P, Mejia-Ramirez E, Limbo O and Russell P. Release of Ku and MRN from DNA ends by Mre11 nuclease activity and Ctp1 is required for homologous recombination repair of double-strand breaks. *PLoS genetics* 2011; 7: e1002271.
180. Langerak P and Russell P. Regulatory networks integrating cell cycle control with DNA damage checkpoints and double-strand break repair. *Philosophical transactions of the Royal Society of London. Series B, Biological sciences* 2011; 366: 3562–3571.
181. Lieber MR. The mechanism of human nonhomologous DNA end joining. *The Journal of biological chemistry* 2008; 283: 1–5.
182. Moore JK and Haber JE. Cell cycle and genetic requirements of two pathways of nonhomologous end-joining repair of double-strand breaks in Saccharomyces cerevisiae. *Molecular and cellular biology* 1996; 16: 2164–2173.
183. Branzei D and Foiani M. Regulation of DNA repair throughout the cell cycle. *Nature reviews. Molecular cell biology* 2008; 9: 297–308.
184. Kadyk LC and Hartwell LH. Sister chromatids are preferred over homologs as substrates for recombinational repair in Saccharomyces cerevisiae. *Genetics* 1992; 132: 387–402.
185. Horie M, Kato H, Fujita K, Endoh S and Iwahashi H. In vitro evaluation of cellular response induced by manufactured nanoparticles. *Chemical research in toxicology* 2012; 25: 605–619.
186. Xia T, Zhao Y, Sager T, et al. Decreased dissolution of ZnO by iron doping yields nanoparticles with reduced toxicity in the rodent lung and zebrafish embryos. *ACS nano* 2011; 5: 1223–1235.
187. Hsiao I and Huang Y. Titanium oxide shell coatings decrease the cytotoxicity of ZnO nanoparticles. *Chemical research in toxicology* 2011; 24: 303–313.
188. Franklin NM, Rogers NJ, Apte SC, Batley GE, Gadd GE and Casey PS. Comparative toxicity of nanoparticulate ZnO, bulk ZnO, and $ZnCl_2$ to a freshwater microalga (Pseudokirchneriella subcapitata): the importance of particle solubility. *Environmental science & technology* 2007; 41: 8484–8490.
189. Haynes WM. *CRC handbook of chemistry and physics: A ready-reference book of chemical and physical data.* 95th ed. Boca Raton: CRC Press, 2014.
190. Colvin RA, Holmes WR, Fontaine CP and Maret W. Cytosolic zinc buffering and muffling: their role in intracellular zinc homeostasis. *Metallomics integrated biometal science* 2010; 2: 306–317.
191. IRVING H and WILLIAMS RJP. Order of Stability of Metal Complexes. *Nature* 1948; 162: 746–747.
192. Peck EJ JR and Ray WJ JR. Metal complexes of phosphoglucomutase in vivo. Alterations induced by insulin. *The Journal of biological chemistry* 1971; 246: 1160–1167.
193. Mocchegiani E, Giacconi R and Malavolta M. Zinc signalling and subcellular distribution: emerging targets in type 2 diabetes. *Trends in molecular medicine* 2008; 14: 419–428.
194. Vallee BL and Falchuk KH. The biochemical basis of zinc physiology. *Physiological reviews* 1993; 73: 79–118.
195. Maret W. Zinc biochemistry: from a single zinc enzyme to a key element of life. *Advances in nutrition (Bethesda, Md.)* 2013; 4: 82–91.
196. Tapiero H and Tew KD. Trace elements in human physiology and pathology: zinc and metallothioneins. *Biomedicine & pharmacotherapy = Biomedecine & pharmacotherapie* 2003; 57: 399–411.
197. Villar-Garea A and Esteller M. Histone deacetylase inhibitors: understanding a new wave of anticancer agents. *International journal of cancer. Journal international du cancer* 2004; 112: 171–178.

198. Hartwig A (ed). *Nutzen-Risiko-Bewertung von Mineralstoffen und Spurenelementen: Biochemische, physiologische und toxikologische Aspekte*. Karlsruhe: KIT Scientific Publishing, 2013.
199. Zharkov DO and Rosenquist TA. Inactivation of mammalian 8-oxoguanine-DNA glycosylase by cadmium(II): implications for cadmium genotoxicity. *DNA repair* 2002; 1: 661–670.
200. Kosinski J, Plotz G, Guarne A, Bujnicki JM and Friedhoff P. The PMS2 subunit of human MutLalpha contains a metal ion binding domain of the iron-dependent repressor protein family. *Journal of molecular biology* 2008; 382: 610–627.
201. Fukada T, Yamasaki S, Nishida K, Murakami M and Hirano T. Zinc homeostasis and signaling in health and diseases: Zinc signaling. *Journal of biological inorganic chemistry JBIC a publication of the Society of Biological Inorganic Chemistry* 2011; 16: 1123–1134.
202. Hirano T, Murakami M, Fukada T, Nishida K, Yamasaki S and Suzuki T. Roles of zinc and zinc signaling in immunity: zinc as an intracellular signaling molecule. *Advances in immunology* 2008; 97: 149–176.
203. Yamashita S, Miyagi C, Fukada T, Kagara N, Che Y and Hirano T. Zinc transporter LIVI controls epithelial-mesenchymal transition in zebrafish gastrula organizer. *Nature* 2004; 429: 298–302.
204. Andreeva A and Tidow H. A novel CHHC Zn-finger domain found in spliceosomal proteins and tRNA modifying enzymes. *Bioinformatics (Oxford, England)* 2008; 24: 2277–2280.
205. Butcher SE. The spliceosome and its metal ions. *Metal ions in life sciences* 2011; 9: 235–251.
206. Cheng B, Shi, Russell-Tanner JM, Zhang L and Samulski ET. Synthesis of Variable-Aspect-Ratio, Single-Crystalline ZnO Nanostructures. *Inorganic Chemistry* 2006; 45: 1208–1214.
207. Tahir MN, Yella A, Therese HA, et al. Synthesis of Hierarchically Grown ZnO@NT-WS 2 Nanocomposites. *Chemistry of Materials* 2009; 21: 5382–5387.
208. Welkoborsky H, Jacob R, Riazimand SH, Bernauer HS and Mann WJ. Molecular biologic characteristics of seven new cell lines of squamous cell carcinomas of the head and neck and comparison to fresh tumor tissue. *Oncology* 2003; 65: 60–71.
209. Lewicka ZA, Benedetto AF, Benoit DN, Yu WW, Fortner JD and Colvin VL. The structure, composition, and dimensions of TiO_2 and ZnO nanomaterials in commercial sunscreens. *Journal of Nanoparticle Research* 2011; 13: 3607–3617.
210. Klümper TH and Waider D. *Wasserverwendung - Trinkwasser-Installation*. München: Oldenbourg Wissenschaftsverlag, 2000.
211. Amos WB and White JG. How the confocal laser scanning microscope entered biological research. *Biology of the cell / under the auspices of the European Cell Biology Organization* 2003; 95: 335–342.
212. Conchello J and Lichtman JW. Optical sectioning microscopy. *Nature methods* 2005; 2: 920–931.
213. Brown M and Wittwer C. Flow cytometry: principles and clinical applications in hematology. *Clinical chemistry* 2000; 46: 1221–1229.
214. Givan AL. *Flow cytometry: first principles.* 2nd ed. Hoboken: John Wiley & Sons, 2013.
215. Gabriel Horton. Flow Cytometry, http://www.biotech.uiuc.edu/flowcytometry/ (2015, accessed 10 July 2015).
216. Martin SJ, Reutelingsperger CP, McGahon AJ, et al. Early redistribution of plasma membrane phosphatidylserine is a general feature of apoptosis regardless of the initiating stimulus: inhibition by overexpression of Bcl-2 and Abl. *The Journal of experimental medicine* 1995; 182: 1545–1556.

217. Marcus Eich (ed). *Untersuchungen zum Einfluss von NBN, ATM und ATR auf die Alkylanzien-induzierte Toxizität*. Dissertation Johannes Gutenberg-Universität. Mainz, 2011.
218. Junker M and Creutz CE. Ca(2+)-dependent binding of endonexin (annexin IV) to membranes: analysis of the effects of membrane lipid composition and development of a predictive model for the binding interaction. *Biochemistry* 1994; 33: 8930–8940.
219. BD Biosciences, Becton, Dickinson and Company: Annexin V Assay, http://www.bdbiosciences.com/sg/instruments/accuri/articles/archive/2015_02/index.jsp (2015, accessed 10 July 2015).
220. Wan CP, Myung E and Lau BH. An automated micro-fluorometric assay for monitoring oxidative burst activity of phagocytes. *Journal of immunological methods* 1993; 159: 131–138.
221. O'Brien J, Wilson I, Orton T and Pognan F. Investigation of the Alamar Blue (resazurin) fluorescent dye for the assessment of mammalian cell cytotoxicity. *European journal of biochemistry / FEBS* 2000; 267: 5421–5426.
222. Jakob B, Splinter J, Conrad S, et al. DNA double-strand breaks in heterochromatin elicit fast repair protein recruitment, histone H2AX phosphorylation and relocation to euchromatin. *Nucleic acids research* 2011; 39: 6489–6499.
223. Olga A. Sedelnikova, Emmy P. Rogakou, Igor G. Panyutin and William M. Bonner. Quantitative Detection of 125IdU-Induced DNA Double-Strand Breaks with γ-H2AX Antibody. *Radiation Research* 2002; 158: 486–492.
224. Nikolova T, Dvorak M, Jung F, et al. The gammaH2AX assay for genotoxic and nongenotoxic agents: comparison of H2AX phosphorylation with cell death response. *Toxicological sciences an official journal of the Society of Toxicology* 2014; 140: 103–117.
225. Lowry OH, Rosebrough NJ, Farr AL and Randall RJ. Protein measurement with the Folin phenol reagent. *The Journal of biological chemistry* 1951; 193(1): 265–275.
226. Renart J, Reiser J and Stark GR. Transfer of proteins from gels to diazobenzyloxymethyl-paper and detection with antisera: a method for studying antibody specificity and antigen structure. *Proceedings of the National Academy of Sciences* 1979; 76: 3116–3120.
227. Leinco Technologies. Western Blot protocol, http://www.leinco.com/general_wb (2015, accessed 10 July 2015).
228. Hanley C, Layne J, Punnoose A, et al. Preferential killing of cancer cells and activated human T cells using ZnO nanoparticles. *Nanotechnology* 2008; 19: 295103.
229. Huang C, Aronstam RS, Chen D and Huang Y. Oxidative stress, calcium homeostasis, and altered gene expression in human lung epithelial cells exposed to ZnO nanoparticles. *Toxicology in vitro an international journal published in association with BIBRA* 2010; 24: 45–55.
230. Lin W, Xu Y, Huang C, et al. Toxicity of nano- and micro-sized ZnO particles in human lung epithelial cells. *Journal of Nanoparticle Research* 2009; 11: 25–39.
231. Reddy KM, Feris K, Bell J, Wingett DG, Hanley C and Punnoose A. Selective toxicity of zinc oxide nanoparticles to prokaryotic and eukaryotic systems. *Applied physics letters* 2007; 90: 213902-1-213902-3.
232. Yuan J, Chen Y, Zha H, et al. Determination, characterization and cytotoxicity on HELF cells of ZnO nanoparticles. *Colloids and surfaces. B, Biointerfaces* 2010; 76: 145–150.
233. Zhang J, Song W, Guo J, et al. Toxic effect of different ZnO particles on mouse alveolar macrophages. *Journal of hazardous materials* 2012; 219-220: 148–155.

234. Adamson IY, Prieditis H, Hedgecock C and Vincent R. Zinc is the toxic factor in the lung response to an atmospheric particulate sample. *Toxicology and applied pharmacology* 2000; 166: 111–119.
235. Vandebriel RJ and Jong WH de. A review of mammalian toxicity of ZnO nanoparticles. *Nanotechnology, science and applications* 2012; 5: 61–71.
236. Xie Y, Williams NG, Tolic A, et al. Aerosolized ZnO nanoparticles induce toxicity in alveolar type II epithelial cells at the air-liquid interface. *Toxicological sciences an official journal of the Society of Toxicology* 2012; 125: 450–461.
237. George S, Pokhrel S, Xia T, et al. Use of a rapid cytotoxicity screening approach to engineer a safer zinc oxide nanoparticle through iron doping. *Acs Nano* 2009; 4: 15–29.
238. Chiang H, Xia Q, Zou X, et al. Nanoscale ZnO induces cytotoxicity and DNA damage in human cell lines and rat primary neuronal cells. *Journal of nanoscience and nanotechnology* 2012; 12: 2126–2135.
239. Hsiao I and Huang Y. Titanium oxide shell coatings decrease the cytotoxicity of ZnO nanoparticles. *Chemical research in toxicology* 2011; 24: 303–313.
240. Fukui H, Horie M, Endoh S, et al. Association of zinc ion release and oxidative stress induced by intratracheal instillation of ZnO nanoparticles to rat lung. *Chemico-biological interactions* 2012; 198: 29–37.
241. Lenz A, Karg E, Brendel E, et al. Inflammatory and oxidative stress responses of an alveolar epithelial cell line to airborne zinc oxide nanoparticles at the air-liquid interface: a comparison with conventional, submerged cell-culture conditions. *BioMed research international* 2013; 652632: 1–12.
242. Frohlich E. The role of surface charge in cellular uptake and cytotoxicity of medical nanoparticles. *International journal of nanomedicine* 2012; 7: 5577–5591.
243. Cho W, Duffin R, Thielbeer F, et al. Zeta potential and solubility to toxic ions as mechanisms of lung inflammation caused by metal/metal oxide nanoparticles. *Toxicological sciences an official journal of the Society of Toxicology* 2012; 126: 469–477.
244. Bian S, Mudunkotuwa IA, Rupasinghe T and Grassian VH. Aggregation and dissolution of 4 nm ZnO nanoparticles in aqueous environments: influence of pH, ionic strength, size, and adsorption of humic acid. *Langmuir the ACS journal of surfaces and colloids* 2011; 27: 6059–6068.
245. Ma H, Williams PL and Diamond SA. Ecotoxicity of manufactured ZnO nanoparticles--a review. *Environmental pollution (Barking, Essex 1987)* 2013; 172: 76–85.
246. Mihai C, Chrisler WB, Xie Y, et al. Intracellular accumulation dynamics and fate of zinc ions in alveolar epithelial cells exposed to airborne ZnO nanoparticles at the air-liquid interface. *Nanotoxicology* 2015; 9: 9–22.
247. Felder Eva Friederike (ed). *Analyse von Toxizitätsmechanismen metallischer Nanopartikel im respiratorischen Epithel*. Dissertation Johannes Gutenberg-Universität. Mainz, 2015.
248. Heim J, Felder E, Tahir MN, et al. Genotoxic effects of zinc oxide nanoparticles. *Nanoscale* 2015; 7: 8931–8938.
249. Mihai C, Chrisler WB, Xie Y, et al. Intracellular accumulation dynamics and fate of zinc ions in alveolar epithelial cells exposed to airborne ZnO nanoparticles at the air-liquid interface. *Nanotoxicology* 2015; 9: 9–22.
250. Sabella S, Carney RP, Brunetti V, et al. A general mechanism for intracellular toxicity of metal-containing nanoparticles. *Nanoscale* 2014; 6: 7052–7061.
251. Finkel T. Signal transduction by mitochondrial oxidants. *The Journal of biological chemistry* 2012; 287: 4434–4440.
252. Huang JS, She QB, Crilly KS and Kiss Z. Ethanol, Zn^{2+} and insulin interact as progression factors to enhance DNA synthesis synergistically in the presence of

Ca^{2+} and other cell cycle initiators in fibroblasts. *Biochemical Journal* 2000; 346: 241–247.
253. Beyersmann D and Haase H. Functions of zinc in signaling, proliferation and differentiation of mammalian cells. *Biometals an international journal on the role of metal ions in biology, biochemistry, and medicine* 2001; 14: 331–341.
254. Sensi SL, Ton-That D, Weiss JH, Rothe A and Gee KR. A new mitochondrial fluorescent zinc sensor. *Cell calcium* 2003; 34: 281–284.
255. Seo SR, Chong SA, Lee S, et al. Zn2+-induced ERK activation mediated by reactive oxygen species causes cell death in differentiated PC12 cells. *Journal of Neurochemistry* 2001; 78: 600–610.
256. Alam S and Kelleher SL. Cellular mechanisms of zinc dysregulation: a perspective on zinc homeostasis as an etiological factor in the development and progression of breast cancer. *Nutrients* 2012; 4: 875–903.
257. Theocharis SE, Margeli AP, Klijanienko JT and Kouraklis GP. Metallothionein expression in human neoplasia. *Histopathology* 2004; 45: 103–118.
258. Nordberg M, Schaffner W, Blindauer CA, et al. *Metal ions in life sciences: Metallothioneins: historical development and overview.* 5th ed. Cambridge: The Royal Society of Chemistry, 2009.
259. Krezel A, Hao Q and Maret W. The zinc/thiolate redox biochemistry of metallothionein and the control of zinc ion fluctuations in cell signaling. *Archives of biochemistry and biophysics* 2007; 463: 188–200.
260. McCord MC and Aizenman E. The role of intracellular zinc release in aging, oxidative stress, and Alzheimer's disease. *Frontiers in Aging Neuroscience* 2014; 6: 77.
261. Aizenman E, Stout AK, Hartnett KA, Dineley KE, McLaughlin B and Reynolds IJ. Induction of neuronal apoptosis by thiol oxidation: putative role of intracellular zinc release. *Journal of Neurochemistry* 2000; 75: 1878–1888.
262. Ma H, Williams PL and Diamond SA. Ecotoxicity of manufactured ZnO nanoparticles--a review. *Environmental pollution (Barking, Essex 1987)* 2013; 172: 76–85.
263. Xia T, Kovochich M, Liong M, et al. Comparison of the mechanism of toxicity of zinc oxide and cerium oxide nanoparticles based on dissolution and oxidative stress properties. *Acs Nano* 2008; 2: 2121–2134.
264. Illés E and Tombácz E. The effect of humic acid adsorption on pH-dependent surface charging and aggregation of magnetite nanoparticles. *Journal of colloid and interface science* 2006; 295: 115–123.
265. Rickard D, Morse JW and Luther GW. *Cluster, nanoparticles and the solubility constant.* Presentation. Copenhagen, Denmark, 2004.
266. Borm P, Klaessig FC, Landry TD, et al. Research strategies for safety evaluation of nanomaterials, part V: role of dissolution in biological fate and effects of nanoscale particles. *Toxicological sciences an official journal of the Society of Toxicology* 2006; 90: 23–32.
267. Liu B and Zeng HC. Symmetric and asymmetric Ostwald ripening in the fabrication of homogeneous core-shell semiconductors. *Small (Weinheim an der Bergstrasse, Germany)* 2005; 1: 566–571.
268. Valdiglesias V, Costa C, Kilic G, et al. Neuronal cytotoxicity and genotoxicity induced by zinc oxide nanoparticles. *Environment international* 2013; 55: 92–100.
269. Ballestin R, Molowny A, Marin MP, et al. Ethanol reduces zincosome formation in cultured astrocytes. *Alcohol and alcoholism (Oxford, Oxfordshire)* 2011; 46: 17–25.
270. Eide DJ. Zinc transporters and the cellular trafficking of zinc. *Biochimica et biophysica acta* 2006; 1763: 711–722.
271. Varea E, Alonso-Llosa G, Molowny A, Lopez-Garcia C and Ponsoda X. Capture of extracellular zinc ions by astrocytes. *Glia* 2006; 54: 304–315.

272. Gojova A, Guo B, Kota RS, Rutledge JC, Kennedy IM and Barakat AI. Induction of inflammation in vascular endothelial cells by metal oxide nanoparticles: effect of particle composition. *Environmental health perspectives* 2007; 115: 403–409.
273. Gaither LA and Eide DJ. Eukaryotic zinc transporters and their regulation. *Biometals an international journal on the role of metal ions in biology, biochemistry, and medicine* 2001; 14: 251–270.
274. Liuzzi JP and Cousins RJ. Mammalian zinc transporters. *Annual review of nutrition* 2004; 24: 151–172.
275. Kambe T, Hashimoto A and Fujimoto S. Current understanding of ZIP and ZnT zinc transporters in human health and diseases. *Cellular and molecular life sciences CMLS* 2014; 71: 3281–3295.
276. Gunshin H, Mackenzie B, Berger UV, et al. Cloning and characterization of a mammalian proton-coupled metal-ion transporter. *Nature* 1997; 388: 482–488.
277. MacDiarmid CW, Gaither LA and Eide D. Zinc transporters that regulate vacuolar zinc storage in Saccharomyces cerevisiae. *The EMBO journal* 2000; 19: 2845–2855.
278. Suhy DA, Simon KD, Linzer DI and O'Halloran TV. Metallothionein is part of a zinc-scavenging mechanism for cell survival under conditions of extreme zinc deprivation. *The Journal of biological chemistry* 1999; 274: 9183–9192.
279. Atar D, Backx PH, Appel MM, Gao WD and Marban E. Excitation-transcription coupling mediated by zinc influx through voltage-dependent calcium channels. *The Journal of biological chemistry* 1995; 270: 2473–2477.
280. Cousins RJ. Metal elements and gene expression. *Annual review of nutrition* 1994; 14: 449–469.
281. Palmiter RD and Huang L. Efflux and compartmentalization of zinc by members of the SLC30 family of solute carriers. *Pflugers Archiv European journal of physiology* 2004; 447: 744–751.
282. Mudunkotuwa IA, Rupasinghe T, Wu C and Grassian VH. Dissolution of ZnO nanoparticles at circumneutral pH: a study of size effects in the presence and absence of citric acid. *Langmuir the ACS journal of surfaces and colloids* 2012; 28: 396–403.
283. Roberts BR, Tainer JA, Getzoff ED, et al. Structural characterization of zinc-deficient human superoxide dismutase and implications for ALS. *Journal of molecular biology* 2007; 373: 877–890.
284. Dalton T, Paria BC, Fernando LP, Huet-Hudson YM, Dey SK and Andrews GK. Activation of the chicken metallothionein promoter by metals and oxidative stress in cultured cells and transgenic mice. *Comparative biochemistry and physiology. Part B, Biochemistry & molecular biology* 1997; 116: 75–86.
285. Burri L, Vascotto K, Fredersdorf S, Tiedt R, Hall MN and Lithgow T. Zim17, a novel zinc finger protein essential for protein import into mitochondria. *The Journal of biological chemistry* 2004; 279: 50243–50249.
286. Maret W. The function of zinc metallothionein: a link between cellular zinc and redox state. *The Journal of nutrition* 2000; 130: 1455S-8S.
287. Ye B, Maret W and Vallee BL. Zinc metallothionein imported into liver mitochondria modulates respiration. *Proceedings of the National Academy of Sciences of the United States of America* 2001; 98: 2317–2322.
288. Sensi SL, Ton-That D, Sullivan PG, et al. Modulation of mitochondrial function by endogenous Zn2+ pools. *Proceedings of the National Academy of Sciences of the United States of America* 2003; 100: 6157–6162.
289. HUNTER FE JR and FORD L. Inactivation of oxidative and phosphorylative systems in mitochondria by preincubation with phosphate and other ions. *The Journal of biological chemistry* 1955; 216: 357–369.
290. Skulachev VP, Chistyakov VV, Jasaitis AA and Smirnova EG. Inhibition of the respiratory chain by zinc ions. *Biochemical and biophysical research communications* 1967; 26: 1–6.

291. Medvedeva YV and Weiss JH. Intramitochondrial Zn^{2+} accumulation via the Ca^{2+} uniporter contributes to acute ischemic neurodegeneration. *Neurobiology of disease* 2014; 68: 137–144.
292. Chen R, Huo L, Shi X, et al. Endoplasmic Reticulum Stress Induced by Zinc Oxide Nanoparticles Is an Earlier Biomarker for Nanotoxicological Evaluation: ACS Nano. *Acs Nano* 2014; 8: 2562–2574.
293. Roussel BD, Kruppa AJ, Miranda E, Crowther DC, Lomas DA and Marciniak SJ. Endoplasmic reticulum dysfunction in neurological disease. *The Lancet. Neurology* 2013; 12: 105–118.
294. Weser U, Rupp H, Donay F, et al. Characterization of Cd, Zn-thionein (metallothionein) isolated from rat and chicken liver. *European journal of biochemistry / FEBS* 1973; 39: 127–140.
295. Nagano T, Itoh N, Ebisutani C, et al. The transport mechanism of metallothionein is different from that of classical NLS-bearing protein. *Journal of Cellular Physiology* 2000; 185: 440–446.
296. Spahl DU, Berendji-Grün D, Suschek CV, Kolb-Bachofen V and Kröncke K. Regulation of zinc homeostasis by inducible NO synthase-derived NO: Nuclear metallothionein translocation and intranuclear Zn^{2+} release. *Proceedings of the National Academy of Sciences* 2003; 100: 13952–13957.
297. Spahl Daniela Ursula. *Regulation der intrazellulären Zink-Homöostase durch iNOS-Aktivität: Translokation von Metallothionein in den Zellkern und nachfolgende nukleäre Zink-Freisetzung*. Habilitation Heinrich Heine Universität. Düsseldorf, 2004.
298. Anastassopoulou J. Metal–DNA interactions. *Journal of Molecular Structure* 2003; 651-653: 19–26.
299. Muntean CM, Nalpantidis K, Feldmann I and Deckert V. Zn< sup> 2. *Journal of Spectroscopy* 2009; 23: 155–163.
300. Hackenberg S, Zimmermann F, Scherzed A, et al. Repetitive exposure to zinc oxide nanoparticles induces dna damage in human nasal mucosa mini organ cultures. *Environmental and molecular mutagenesis* 2011; 52: 582–589.
301. Adams LK, Lyon DY and Alvarez PJJ. Comparative eco-toxicity of nanoscale TiO_2, SiO_2, and ZnO water suspensions. *Water research* 2006; 40: 3527–3532.
302. Lin D and Xing B. Phytotoxicity of nanoparticles: inhibition of seed germination and root growth. *Environmental pollution (Barking, Essex 1987)* 2007; 150: 243–250.
303. Wong SWY, Leung PTY, Djurisic AB and Leung KMY. Toxicities of nano zinc oxide to five marine organisms: influences of aggregate size and ion solubility. *Analytical and bioanalytical chemistry* 2010; 396: 609–618.
304. Xiong D, Fang T, Yu L, Sima X and Zhu W. Effects of nano-scale TiO_2, ZnO and their bulk counterparts on zebrafish: acute toxicity, oxidative stress and oxidative damage. *The Science of the total environment* 2011; 409: 1444–1452.
305. Karlsson HL, Gliga AR, Calleja, Fabienne M G R, et al. Mechanism-based genotoxicity screening of metal oxide nanoparticles using the ToxTracker panel of reporter cell lines. *Particle and fibre toxicology* 2014; 11: 41.
306. Krezel A and Maret W. Zinc-buffering capacity of a eukaryotic cell at physiological pZn. *Journal of biological inorganic chemistry JBIC a publication of the Society of Biological Inorganic Chemistry* 2006; 11: 1049–1062.
307. Setyawati MI, Tay CY and Leong DT. Nanotoxicity: Mechanistic Investigation of the Biological Effects of SiO_2 TiO_2 and ZnO Nanoparticles on Intestinal Cells (Small 28/2015). *Small (Weinheim an der Bergstrasse, Germany)* 2015; 11: 3390.
308. Ismail IH, Nystrom S, Nygren J and Hammarsten O. Activation of ataxia telangiectasia mutated by DNA strand break-inducing agents correlates closely with the number of DNA double strand breaks. *The Journal of biological chemistry* 2005; 280: 4649–4655.

309. Xie H, Wise SS, Holmes AL, et al. Carcinogenic lead chromate induces DNA double-strand breaks in human lung cells. *Mutation research* 2005; 586: 160–172.
310. Hainaut P and Mann K. Zinc binding and redox control of p53 structure and function. *Antioxidants & redox signaling* 2001; 3: 611–623.
311. Meyer K, Rajanahalli P, Ahamed M, Rowe JJ and Hong Y. ZnO nanoparticles induce apoptosis in human dermal fibroblasts via p53 and p38 pathways. *Toxicology in vitro an international journal published in association with BIBRA* 2011; 25: 1721–1726.
312. Chandel NS, Vander Heiden MG, Thompson CB and Schumacker PT. Redox regulation of p53 during hypoxia. *Oncogene* 2000; 19: 3840–3848.
313. Cho Y, Gorina S, Jeffrey PD and Pavletich NP. Crystal structure of a p53 tumor suppressor-DNA complex: understanding tumorigenic mutations. *Science (New York, N.Y.)* 1994; 265: 346–355.
314. Meplan C, Richard MJ and Hainaut P. Redox signalling and transition metals in the control of the p53 pathway. *Biochemical pharmacology* 2000; 59: 25–33.
315. Gartel AL. The conflicting roles of the cdk inhibitor p21(CIP1/WAF1) in apoptosis. *Leukemia research* 2005; 29: 1237–1238.
316. Gartel AL and Radhakrishnan SK. Lost in transcription: p21 repression, mechanisms, and consequences. *Cancer research* 2005; 65: 3980–3985.
317. Wu W, Jaspers I, Zhang W, Graves LM and Samet JM. Role of Ras in metal-induced EGF receptor signaling and NF-kappaB activation in human airway epithelial cells. *American journal of physiology. Lung cellular and molecular physiology* 2002; 282: L1040-8.

8 Appendix

8.1 Solubility of ZnO NP

Table 14: AAS measurement of ZnO NP solubility

	ZnO NP (4-5 nm)		ZnO NP (15-18 nm)	
	Zn (mg/L)		Zn (mg/L)	
	High purity H_2O	Cell culture medium	High purity H_2O	Cell culture medium
1 min	16.88	12.56	3.70	9.52
5 min	19.17	12.28	5.92	6.34
15 min	15.96	7.71	4.14	5.80
30 min	15.73	6.85	5.15	5.42
1 h	16.69	6.16	4.07	5.26
4 h	14.83	5.51	4.63	4.79

8.2 Stabilization of ZnO NP with BSA

Stabilization experiments are based on 3 independent experiments. For the statistical analysis the one-way analysis of variance (ANOVA) with Bonferroni´s multiple comparison test was carried out to compare the group of control with ZnO NP, control with ZnO NP + BSA, ZnO NP with ZnO NP + BSA (* for $p<0.05$ is significant, ** for $p<0.01$ is highly significant, *** for $p<0.001$ is extremely significant).

8.2.1 ZnO NP (4-5 nm)

Table 15: ZnO NP (4-5 nm) stabilization with BSA in A549 cells after 24 h.

	A549 cells		
	viable cells [%]		
		100 µg/mL	
	control	ZnO NP (4-5 nm)	ZnO NP (4-5 nm) + BSA
N=1	100.00	15.87	178.64
N=2	100.00	13.07	112.41
N=3	100.00	9.62	122.16
mean	100.00	12.85	137.74
SD	0.00	3.13	35.76

Table 16: Statistical analysis of A549 cells treated with BSA stabilized ZnO NP (4-5 nm) after 24 h

	A549 cells				
	100 µg/mL ZnO NP (4-5 nm)				
Table Analyzed	24 h				
One-way analysis of variance					
P value	< 0,0001				
P value summary	***				
Are means signif. different? (P < 0.05)	Yes				
Number of groups	3				
F	45.69				
R square	0.9195				
ANOVA Table	SS	df	MS		
Treatment (between columns)	29447	2	14724		
Residual (within columns)	2578	8	322.2		
Total	32025	10			
Bonferroni's Multiple Comparison Test	Mean Diff,	t	Significant? P < 0,05?	Summary	95% CI of diff
control vs ZnO NP (4-5 nm)	86.83	6.841	Yes	***	48,55 to 125,1
control vs ZnO NP (4-5 nm) + BSA	-37.74	2.752	No	ns	-79,08 to 3,611

ZnO NP (4-5 nm) vs ZnO NP (4-5 nm) + BSA	-124.6	9.086	Yes	***	-165,9 to -83,22

8.2.2 ZnO NP (15-18 nm)

Table 17: ZnO NP (15-18 nm) stabilization with BSA in A549 cells after 24 h.

	A549 cells		
	viable cells [%]		
	control	ZnO NP (15-18 nm)	ZnO NP (15-18 nm) + BSA
N=1	100.00	12.40	93.34
N=2	100.00	13.66	112.41
N=3	100.00	10.46	153.38
mean	100.00	12.17	119.71
SD	0.00	1.61	30.68

Table 18: Statistical analysis of A549 cells treated with BSA stabilized ZnO NP (15-18 nm) after 24 h

	A549 cells				
	100 µg/mL ZnO NP (15-18 nm)				
Table Analyzed	24 h				
Repeated Measures ANOVA					
P value	0.0039				
P value summary	**				
Are means signif. different? (P < 0.05)	Yes				
Number of groups	3				
F	30.07				
R square	0.9376				
ANOVA Table	SS	df	MS		
Treatment (between columns)	19666	2	9833		
Individual (between rows)	579.5	2	289.7		
Residual (random)	1308	4	327		
Total	21554	8			
Bonferroni's Multiple Comparison Test	Mean Diff,	t	Significant? P < 0,05?	Summary	95% CI of diff

control vs ZnO NP (15-18 nm)	87.83	5.948	Yes	*	29,35 to 146,3
control vs ZnO NP (15-18 nm) + BSA	-19.71	1.335	No	ns	-78,19 to 38,77
ZnO NP (15-18 nm) vs ZnO NP (15-18 nm) + BSA	-107.5	7.283	Yes	**	-166,0 to -49,06

8.3 Intracellular Zn^{2+} distribution after ZnO NP treatment

Spectrofluorimetric experiments of intracellular Zn^{2+} distribution are based on at least 3 independent experiments. For the statistical analysis the one-way analysis of variance (ANOVA) with Bonferroni´s multiple comparison test was carried out to compare the group of ZnO NP with ZnO NP + BSA and ZnO NP + DTPA (* for $p<0.05$ is significant, ** for $p<0.01$ is highly significant, *** for $p<0.001$ is extremely significant).

8.3.1 ZnO NP (4-5 nm)

Table 19: Intracellular distribution of Zn^{2+} after treatment with ZnO NP (4-5 nm)

	A549 cells				
	100 µg/mL ZnO NP (4-5 nm)				
	Zn^{2+} [nM]				
	N=1	N=2	N=3	mean	SD
control	0.17	0.07	0.16	0.13	0.06
6 sec	1.69	0.77	0.65	1.04	0.57
18 sec	1.96	0.81	0.68	1.15	0.71
30 sec	1.89	0.87	0.74	1.17	0.63
42 sec	1.87	0.88	0.74	1.16	0.62
54 sec	2.21	0.92	0.75	1.29	0.80
2 min	2.18	0.88	0.83	1.30	0.76
4 min	2.36	0.94	0.80	1.37	0.87
10 min	2.43	1.09	1.03	1.52	0.79
20 min	2.71	1.18	1.15	1.68	0.89
30 min	3.20	1.18	1.37	1.92	1.12
40 min	3.13	1.23	1.47	1.95	1.04
50 min	3.43	1.35	1.43	2.07	1.18

60 min	3.39	1.51	1.52	2.14	1.08

Table 20: Intracellular distribution of Zn^{2+} after treatment with ZnO NP (4-5 nm) + DTPA

	A549 cells				
	100 µg/mL ZnO NP (4-5 nm) + 0.06 mM DTPA				
	Zn^{2+} [nM]				
	N=1	N=2	N=3	mean	SD
control	0.00	0.20	0.17	0.12	0.11
6 sec	0.00	0.48	0.46	0.31	0.27
18 sec	0.05	0.54	0.47	0.35	0.26
30 sec	0.06	0.51	0.49	0.36	0.25
42 sec	0.06	0.50	0.52	0.36	0.26
54 sec	0.12	0.52	0.57	0.40	0.24
2 min	0.08	0.54	0.49	0.37	0.25
4 min	0.11	0.66	0.70	0.49	0.33
10 min	0.09	0.73	0.95	0.59	0.44
20 min	0.20	0.99	1.04	0.74	0.47
30 min	0.15	1.08	1.09	0.77	0.54
40 min	0.20	1.06	1.04	0.77	0.49
50 min	0.14	1.03	0.91	0.69	0.48
60 min	0.19	1.11	0.93	0.74	0.49

Table 21: Intracellular distribution of Zn^{2+} after treatment with ZnO NP (4-5 nm) + BSA

	A549 cells				
	100 µg/mL ZnO NP (4-5 nm) + BSA				
	Zn^{2+} [nM]				
	N=1	N=2	N=3	mean	SD
control	0.00	0.12	0.23	0.12	0.12
6 sec	0.53	1.50	0.47	0.83	0.58
18 sec	0.58	1.64	0.56	0.93	0.62
30 sec	0.49	1.76	0.45	0.90	0.74
42 sec	0.50	1.78	0.52	0.94	0.73

54 sec	0.49	1.78	0.53	0.93	0.73
2 min	0.57	1.98	0.59	1.05	0.81
4 min	0.49	2.25	0.63	1.12	0.98
10 min	0.60	2.42	0.75	1.25	1.01
20 min	0.63	2.93	0.85	1.47	1.27
30 min	0.66	3.38	1.15	1.73	1.45
40 min	0.70	3.58	1.18	1.82	1.54
50 min	0.68	4.13	1.22	2.01	1.85
60 min	0.73	4.18	1.35	2.09	1.84

8.3.2 ZnO NP (15-18 nm)

Table 22: Intracellular distribution of Zn^{2+} after treatment with ZnO NP (15-18 nm)

	A549 cells					
	100 µg/mL ZnO NP (15-18 nm)					
	Zn^{2+} [nM]					
	N=1	N=2	N=3	N=4	mean	SD
control	0.02	0.23	0.03	0.16	0.11	0.10
6 sec	25.81	1.65	7.57	10.69	11.43	10.29
18 sec	23.39	1.48	7.93	11.99	11.20	9.21
30 sec	24.06	1.67	8.60	11.74	11.52	9.36
42 sec	23.06	1.50	8.67	13.80	11.76	9.06
54 sec	28.70	1.61	8.90	14.71	13.48	11.47
2 min	30.42	1.48	10.23	12.35	13.62	12.15
4 min	26.84	1.54	11.10	20.20	14.92	11.01
10 min	24.47	1.61	12.55	28.24	16.72	12.09
20 min	29.51	1.66	15.52	29.12	18.95	13.24
30 min	38.48	1.84	15.89	30.18	21.60	16.14
40 min	37.95	1.90	19.79	31.02	22.66	15.74
50 min	58.70	2.10	20.56	36.51	29.47	24.03
60 min	59.11	2.15	45.15	32.31	34.68	24.29

Table 23: Intracellular distribution of Zn^{2+} after treatment with ZnO NP (15-18 nm) + DTPA

	A549 cells				
	100 µg/mL ZnO NP (15-18 nm) + 0.06 mM DTPA				
	Zn^{2+} [nM]				
	N=1	N=2	N=3	mean	SD
control	0.02	0.27	0.09	0.13	0.13
6 sec	1.93	4.57	2.50	3.00	1.39
18 sec	2.02	4.23	2.75	3.00	1.13
30 sec	2.22	4.51	2.62	3.12	1.22
42 sec	1.94	4.47	2.45	2.95	1.34
54 sec	1.92	4.78	2.49	3.06	1.51
2 min	2.04	4.20	2.47	2.90	1.14
4 min	2.15	3.96	2.15	2.75	1.05
10 min	2.10	3.93	2.09	2.71	1.06
20 min	2.67	3.78	1.92	2.79	0.93
30 min	2.63	3.66	1.91	2.73	0.88
40 min	2.84	3.52	1.78	2.71	0.88
50 min	2.96	4.32	1.79	3.02	1.27
60 min	3.10	3.92	1.99	3.00	0.97

Table 24: Intracellular distribution of Zn^{2+} after treatment with ZnO NP (15-18 nm) + BSA

	A549 cells				
	100 µg/mL ZnO NP (15-18 nm) + BSA				
	Zn^{2+} [nM]				
	N=1	N=2	N=3	mean	SD
control	0.02	0.01	0.82	0.28	0.46
6 sec	0.37	0.67	1.38	0.80	0.52
18 sec	0.32	0.62	0.12	0.36	0.25
30 sec	0.23	0.58	-0.04	0.26	0.31
42 sec	0.22	0.59	-0.12	0.23	0.35
54 sec	0.19	0.56	-0.08	0.23	0.32
2 min	0.12	0.64	0.01	0.26	0.34

4 min	0.11	0.72	0.02	0.28	0.38
10 min	0.91	0.76	0.23	0.63	0.36
20 min	1.06	1.07	0.41	0.85	0.38
30 min	1.16	0.80	0.47	0.81	0.34
40 min	1.13	1.00	0.40	0.84	0.39
50 min	1.39	1.01	0.61	1.01	0.39
60 min	1.30	1.06	0.64	1.00	0.34

Table 25: Statistical analysis of intracellular Zn^{2+} accumulation after ZnO NP (15-18 nm) treatment

	A549 cells			
	100 µg/mL ZnO NP (4-5 nm)			
Table Analyzed				
Two-way ANOVA				
Source of Variation	% of total variation	P value		
Interaction	9,64	0,8134		
Column Factor	39,68	< 0,0001		
Row Factor	5,19	0,6469		
Source of Variation	P value summary	Significant?		
Interaction	ns	No		
Column Factor	***	Yes		
Row Factor	ns	No		
Source of Variation	Df	Sum-of-squares	Mean square	F
Interaction	52	3562	68,50	0,8095
Column Factor	2	14664	7332	86,65
Row Factor	26	1919	73,82	0,8724
Residual	189	15992	84,61	
Number of missing values	54			
Bonferroni posttests				
	ZnO NP (15-18 nm) vs ZnO NP (15-18 nm) + BSA			
Row Factor	ZnO NP (15-18 nm)	ZnO NP (15-18 nm) + BSA	Difference	95% CI of diff,
Row Factor	Difference	t	P value	Summary
control	-0,04497	0,006401	P > 0,05	ns

1 sec	-6,700	0,9537	P > 0,05	ns
6 sec	-8,426	1,199	P > 0,05	ns
12 sec	-7,636	1,087	P > 0,05	ns
18 sec	-8,197	1,167	P > 0,05	ns
24 sec	-8,130	1,157	P > 0,05	ns
30 sec	-8,403	1,196	P > 0,05	ns
36 sec	-9,629	1,371	P > 0,05	ns
42 sec	-8,804	1,253	P > 0,05	ns
48 sec	-9,314	1,326	P > 0,05	ns
54 sec	-10,42	1,483	P > 0,05	ns
1 min	-9,402	1,338	P > 0,05	ns
2 min	-10,72	1,526	P > 0,05	ns
3 min	-9,108	1,296	P > 0,05	ns
4 min	-12,17	1,732	P > 0,05	ns
5 min	-11,78	1,677	P > 0,05	ns
10 min	-14,01	1,994	P > 0,05	ns
15 min	-15,17	2,159	P > 0,05	ns
20 min	-16,16	2,300	P > 0,05	ns
25 min	-16,62	2,365	P > 0,05	ns
30 min	-18,87	2,685	P > 0,05	ns
35 min	-21,81	3,104	P > 0,05	ns
40 min	-19,95	2,840	P > 0,05	ns
45 min	-26,11	3,717	P<0,01	**
50 min	-26,44	3,764	P<0,01	**
55 min	-27,29	3,884	P<0,01	**
60 min	-31,67	4,508	P<0,001	***
	ZnO NP (15-18 nm) vs ZnO NP (15-18 nm) + DTPA			
Row Factor	ZnO NP (15-18 nm)	ZnO NP (15-18 nm) + DTPA	Difference	95% CI of diff,
Row Factor	Difference	t	P value	Summary
control	0,2907	0,04138	P > 0,05	ns
1 sec	-8,996	1,280	P > 0,05	ns
6 sec	-10,62	1,512	P > 0,05	ns

12 sec	-10,22	1,455	P > 0,05	ns
18 sec	-10,84	1,543	P > 0,05	ns
24 sec	-10,82	1,541	P > 0,05	ns
30 sec	-11,26	1,603	P > 0,05	ns
36 sec	-12,39	1,764	P > 0,05	ns
42 sec	-11,53	1,640	P > 0,05	ns
48 sec	-12,06	1,716	P > 0,05	ns
54 sec	-13,26	1,887	P > 0,05	ns
1 min	-12,15	1,729	P > 0,05	ns
2 min	-13,36	1,902	P > 0,05	ns
3 min	-11,73	1,669	P > 0,05	ns
4 min	-14,64	2,083	P > 0,05	ns
5 min	-14,23	2,025	P > 0,05	ns
10 min	-16,08	2,289	P > 0,05	ns
15 min	-17,13	2,438	P > 0,05	ns
20 min	-18,10	2,577	P > 0,05	ns
25 min	-18,67	2,657	P > 0,05	ns
30 min	-20,79	2,959	P > 0,05	ns
35 min	-23,68	3,371	P < 0,05	*
40 min	-21,82	3,106	P > 0,05	ns
45 min	-28,03	3,989	P<0,01	**
50 min	-28,46	4,051	P<0,01	**
55 min	-29,40	4,185	P<0,01	**
60 min	-33,68	4,793	P<0,001	***

8.4 Nuclear Zn^{2+} accumulation

cLSM measurements of nuclear Zn^{2+} distribution are based on at least 3 independent experiments. The FluoZin™-3 intensity of at least, 2 cells per image was calculated by the use of Image J 1.47f. For the statistical analysis of nuclear Zn^{2+} accumulation after ZnO NP (4-5 nm), ZnO NP (15-18 nm), and $ZnCl_2$ treatment the one-way analysis of variance (ANOVA) with Bonferroni´s multiple comparison test was carried out to compare the time points in each groups to the untreated control (* for $p<0.05$ is significant, ** for $p<0.01$ is highly significant, *** for $p<0.001$ is extremely significant).

Table 26: Measurement of nuclear Zn^{2+} accumulation after ZnO NP (4-5 nm) treatment

		A549 cells							
		Zn^{2+} [%] of control							
		100 µg/mL ZnO NP (4-5 nm)							
		control	1 min	10 min	20 min	30 min	40 min	50 min	60 min
N=1	cell 1	100.00	222.94	2122.25	3576.14	3188.22	1956.20	3145.96	1440.57
	cell 2	100.00	284.50	3599.23	6626.16	6655.81	2825.39	6414.15	5213.37
	cell 3	100.00	282.72	3713.06	6038.37	2641.50	3560.68	1349.52	1507.62
	cell 4	100.00	353.91	4260.87	6211.13	4747.65	6596.17	2303.13	1788.00
	cell 5	100.00	223.71	2460.72	4238.68	3774.85	4595.09	2818.92	2044.79
	cell 6	100.00	81.24	67.00	83.22	203.39	413.82	686.32	1183.08
	cell 7	100.00	78.76	49.64	56.01	77.57	154.97	235.32	361.81
N=2	cell 1	100.00	89.37	71.44	81.20	107.56	164.85	242.97	365.55
	cell 2	100.00	59.52	34.98	45.60	91.76	243.96	404.95	666.30
	cell 3	100.00	64.63	47.76	52.85	104.07	264.43	803.25	1154.68
	cell 4	100.00	103.52	94.53	99.02	113.90	119.95	136.55	227.51
	cell 5	100.00	99.48	98.79	70.48	52.51	66.67	68.74	88.74
N=3	cell 1	100.00	112.95	112.35	152.28	188.31	213.25	274.10	422.18
	cell 2	100.00	91.58	109.01	138.92	156.72	134.12	217.65	412.63
	cell 3	100.00	65.56	55.75	52.15	55.58	61.99	127.72	244.68
	cell 4	100.00	96.12	88.95	134.09	124.57	117.55	140.79	191.69

Table 27: Measurement of nuclear Zn^{2+} accumulation after ZnO NP (15-18 nm) treatment

		A549 cells							
		Zn^{2+} [%] of control							
		100 µg/mL ZnO NP (15-18 nm)							
		control	1 min	10 min	20 min	30 min	40 min	50 min	60 min
N=1	cell 1	100.00	113.58	241.72	314.47	382.65	430.71	N/A	N/A
	cell 2	100.00	161.60	587.50	687.32	681.05	639.21	N/A	N/A
	cell 3	100.00	171.25	1017.38	1451.63	1529.00	1559.53	N/A	N/A
	cell 4	100.00	152.52	554.06	755.38	873.64	919.88	N/A	N/A
	cell 5	100.00	127.56	344.48	469.68	527.28	554.20	N/A	N/A

	cell 6	100.00	161.33	373.25	493.21	575.82	616.86	N/A	N/A
	cell 7	100.00	134.13	431.21	623.23	723.64	766.36	N/A	N/A
	cell 8	100.00	156.79	465.32	547.55	577.87	580.40	N/A	N/A
	cell 9	100.00	161.41	442.81	548.56	589.08	587.93	N/A	N/A
	cell 10	100.00	171.41	432.22	486.90	503.02	502.99	N/A	N/A
N=2	cell 1	100.00	110.49	111.11	296.30	549.38	800.62	843.83	530.86
	cell 2	100.00	107.94	222.22	246.03	460.32	749.21	820.63	503.97
N=3	cell 1	100.00	101.16	81.76	154.09	462.26	427.67	695.60	484.59
	cell 2	100.00	105.92	184.21	315.79	618.42	1367.11	936.84	700.00
	cell 3	100.00	138.36	392.09	527.87	646.67	750.19	824.23	554.86
	cell 4	100.00	103.97	130.19	40.90	65.69	101.84	159.23	163.19
	cell 5	100.00	102.50	162.33	38.00	74.31	169.98	280.79	217.28
	cell 6	100.00	93.49	85.99	34.49	32.99	38.03	36.78	44.50
	cell 7	100.00	123.46	131.43	30.44	38.89	43.55	28.34	36.87

Table 28: Statistical analysis of nuclear Zn^{2+} accumulation after ZnO NP (15-18 nm) treatment

	A549 cells			
	100 µg/mL ZnO NP (15-18 nm)			
Table Analyzed				
One-way analysis of variance				
P value	< 0,0001			
P value summary	***			
Are means signif. different? (P < 0.05)	Yes			
Number of groups	8			
F	7.803			
R square	0.3058			
P value summary	ns			
Do the variances differ signif. (P < 0.05)	No			
ANOVA Table	SS	df	MS	
Treatment (between columns)	4267000	7	609636	
Residual (within columns)	9688000	124	78128	

Total	13960000	131			
Bonferroni's Multiple Comparison Test	Mean Diff,	t	Significant? P < 0,05?	Summary	95% CI of diff
control vs 1 min	-31.52	0.3476	No	ns	-321,1 to 258,0
control vs 10 min	-236.4	2.607	No	ns	-525,9 to 53,16
control vs 20 min	-324.3	3.576	Yes	*	-613,9 to -34,76
control vs 30 min	-421.7	4.65	Yes	***	-711,2 to -132,1
control vs 40 min	-510.9	5.633	Yes	***	-800,4 to -221,3
control vs 50 min	-414	3.661	Yes	*	-775,2 to -52,90
control vs 60 min	-259.6	2.295	No	ns	-620,7 to 101,6

Table 29: Measurement of nuclear Zn^{2+} accumulation after $ZnCl_2$ treatment

		A549 cells							
		Zn^{2+} [%] of control							
		100 µg/mL $ZnCl_2$							
		control	1 min	10 min	20 min	30 min	40 min	50 min	60 min
N=1	cell 1	100.00	258.35	444.74	487.24	513.21	535.66	452.55	411.26
	cell 2	100.00	299.26	462.15	480.05	486.13	492.01	448.89	391.50
	cell 3	100.00	202.08	271.52	301.78	331.58	353.92	334.93	325.92
N=2	cell 1	100.00	312.66	501.19	504.10	503.25	505.92	438.19	288.18
	cell 2	100.00	216.31	262.45	255.59	257.49	269.83	338.70	299.02
	cell 3	100.00	319.39	491.50	490.62	489.32	491.25	455.74	214.65
	cell 4	100.00	319.54	452.79	453.07	453.23	453.32	302.96	67.84
	cell 5	100.00	152.84	161.81	156.38	144.38	91.63	135.42	132.41
	cell 6	100.00	131.80	145.02	148.87	147.00	87.72	134.32	131.85
	cell 7	100.00	142.98	143.75	134.94	122.87	71.65	112.60	108.05
N=3	cell 1	100.00	83.97	76.42	83.26	104.36	171.75	210.17	211.80
	cell 2	100.00	90.35	107.42	123.74	142.82	191.92	239.55	264.32

	cell 3	100.00	156.98	148.04	154.19	188.18	303.26	468.53	168.96
	cell 4	100.00	126.64	178.83	208.63	258.03	262.20	296.64	323.49
	cell 5	100.00	110.90	156.00	199.27	220.42	259.62	328.78	430.39
	cell 6	100.00	126.80	178.71	212.52	263.08	326.39	427.03	569.14

Table 30: Statistical analysis of nuclear Zn^{2+} accumulation after $ZnCl_2$ treatment

	A549 cells				
	100 µg/mL $ZnCl_2$ [%]				
Table Analyzed					
One-way analysis of variance					
P value	< 0,0001				
P value summary	***				
Are means signif. different? (P < 0.05)	Yes				
Number of groups	8				
F	4.904				
R square	0.2224				
P value summary	ns				
Do the variances differ signif. (P < 0.05)	No				
ANOVA Table	SS	df	MS		
Treatment (between columns)	585640	7	83663		
Residual (within columns)	2047000	120	17061		
Total	2633000	127			
Bonferroni's Multiple Comparison Test	Mean Diff,	t	Significant? P < 0,05?	Summary	95% CI of diff
control vs 1 min	-90.68	1.964	No	ns	-238,2 to 56,88
control vs 10 min	-161.4	3.495	Yes	*	-309,0 to -13,84
control vs 20 min	-174.6	3.782	Yes	**	-322,2 to -27,09
control vs 30 min	-189.1	4.095	Yes	**	-336,6 to -41,53
control vs 40 min	-204.3	4.423	Yes	***	-351,8 to -

					56,70
control vs 50 min	-220.3	4.771	Yes	***	-367,9 to -72,76
control vs 60 min	-171.2	3.707	Yes	**	-318,7 to -23,62

8.5 Viability

Spectrofluorimetric experiments of intracellular Zn^{2+} distribution are based on at least 3 independent experiments. For the statistical analysis of cellular viability after treatment with ZnO NP (0.1, 10 and 100 µg/mL) the one-way analysis of variance (ANOVA) with Bonferroni´s multiple comparison test was carried out to compare all points in time within a group (* for $p<0.05$ is significant, ** for $p<0.01$ is highly significant, *** for $p<0.001$ is extremely significant).

8.5.1 ZnO NP (4-5 nm)

Table 31: Viability analysis of three different concentrations of ZnO NP (4-5 nm)

	A549 cells					
	Viability [%] of control					
	0.1 µg/mL ZnO NP (4-5 nm)					
	control	1 min	15 min	30 min	1 h	4 h
N=1	100.00	110.05	104.15	102.24	95.27	97.60
N=2	100.00	96.82	70.70	106.40	141.36	100.77
N=3	100.00	98.58	99.44	94.00	92.60	102.68
mean	100.00	101.81	91.43	100.88	109.74	100.35
SD	0.00	7.18	18.11	6.31	27.41	2.56
	Viability [%] of control					
	10 µg/mL ZnO NP (4-5 nm)					
	control	1 min	15 min	30 min	1 h	4 h
N=1	100.00	90.67	84.53	93.93	164.16	147.25
N=2	100.00	94.57	88.86	93.33	86.46	96.77
N=3	100.00	114.50	100.26	96.46	92.24	82.21
mean	100.00	99.91	91.22	94.57	114.29	108.75

SD	0.00	12.78	8.12	1.66	43.29	34.13
	Viability [%] of control					
	100 µg/mL ZnO NP (4-5 nm)					
	control	1 min	15 min	30 min	1 h	4 h
N=1	100.00	32.62	37.53	31.35	33.13	33.96
N=2	100.00	84.94	91.23	52.77	59.39	47.55
N=3	100.00	46.90	58.84	65.21	48.68	43.92
mean	100.00	54.82	62.53	49.78	47.07	41.81
SD	0.00	27.04	27.04	17.13	13.20	7.04

Table 32: Statistical analysis of viability in A549 cells treated with 100 µg/mL ZnO NP (4-5 nm)

	A549 cells				
	100 µg/mL ZnO NP (4-5nm)				
Table Analyzed					
One-way analysis of variance					
P value	0.0217				
P value summary	*				
Are means signif. different? (P < 0.05)	Yes				
Number of groups	6				
F	4.061				
R square	0.6286				
ANOVA Table	SS	df	MS		
Treatment (between columns)	6700	5	1340		
Residual (within columns)	3959	12	329.9		
Total	10659	17			
Bonferroni's Multiple Comparison Test	Mean Diff,	t	Significant? P < 0,05?	Summary	95% CI of diff
control vs 1 min	45.18	3.046	No	ns	-8,936 to 99,30
control vs 15 min	37.47	2.526	No	ns	-16,65 to 91,58
control vs 30 min	50.22	3.386	No	ns	-3,895 to

					104,3
control vs 1 h	52.93	3.569	No	ns	-1,185 to 107,0
control vs 4 h	58.19	3.924	Yes	*	4,075 to 112,3
1 min vs 15 min	-7.715	0.5202	No	ns	-61,83 to 46,40
1 min vs 30 min	5.041	0.3399	No	ns	-49,08 to 59,16
1 min vs 1 h	7.751	0.5226	No	ns	-46,37 to 61,87
1 min vs 4 h	13.01	0.8773	No	ns	-41,11 to 67,13
15 min vs 30 min	12.76	0.8601	No	ns	-41,36 to 66,87
15 min vs 1 h	15.47	1.043	No	ns	-38,65 to 69,58
15 min vs 4 h	20.73	1.397	No	ns	-33,39 to 74,84
30 min vs 1 h	2.71	0.1827	No	ns	-51,41 to 56,83
30 min vs 4 h	7.97	0.5374	No	ns	-46,15 to 62,09
1 h vs 4 h	5.26	0.3547	No	ns	-48,86 to 59,38

8.5.2 ZnO NP (15-18 nm)

Table 33: Viability analysis of three different concentrations of ZnO NP (15-18 nm)

	A549 cells					
	Viability [%] of control					
	0.1 µg/mL ZnO NP (15-18 nm)					
	control	1 min	15 min	30 min	1 h	4 h
N=1	100.00	52.23	99.84	123.21	118.17	131.28
N=2	100.00	136.92	164.49	182.17	160.90	227.90
N=3	100.00	103.03	194.96	131.08	120.23	132.17
N=4	100.00	147.42	53.64	112.93	85.72	146.63
mean	100.00	109.90	128.23	137.35	121.25	159.49
SD	0.00	42.86	63.61	30.79	30.79	46.14
	Viability [%] of control					
	10 µg/mL ZnO NP (15-18 nm)					
	control	1 min	15 min	30 min	1 h	4 h
N=1	100.00	157.40	127.39	88.18	78.37	161.56
N=2	100.00	114.37	156.64	245.13	119.88	198.31
N=3	100.00	88.99	129.45	147.26	103.74	156.64
N=4	100.00	214.71	196.92	231.45	157.16	205.22
Mean	100.00	143.87	152.60	178.00	114.79	180.43
SD	0.00	55.03	32.42	73.89	33.01	24.88
	Viability [%] of control					
	100 µg/mL ZnO NP (15-18 nm)					
	control	1 min	15 min	30 min	1 h	4 h
N=1	100.00	62.23	37.32	26.37	23.34	26.95
N=2	100.00	119.21	107.30	79.93	86.55	83.37
N=3	100.00	72.08	77.74	46.83	30.40	80.63
N=4	100.00	72.11	81.30	17.81	124.73	85.65
Mean	100.00	81.41	75.91	42.74	66.25	69.15
SD	0.00	25.63	28.91	27.62	48.16	28.21

Table 34: Statistical analysis of viability in A549 cells treated with 100 µg/mL ZnO NP (15-18 nm)

Table Analyzed	ZnO NP (15-18 nm)
Column A	control
vs	vs
Column D	30 min
Paired t test	
P value	0,0255
P value summary	*
Are means signif. different? (P < 0.05)	Yes
One- or two-tailed P value?	Two-tailed
t, df	t=4,146 df=3
Number of pairs	4
How big is the difference?	
Mean of differences	57,26
95% confidence interval	13,31 to 101,2
R square	0,8514

8.6 ROS assay

Spectrofluorimetric measurements of intracellular ROS-levels are based on at least 3 independent experiments. For the statistical analysis the one-way analysis of variance (ANOVA) with Bonferroni´s multiple comparison test was carried out to compare the group of ZnO NP with $ZnCl_2$, ZnO NP + BSA, ZnO NP + NAC and ZnO NP + DTPA (* for $p<0.05$ is significant, ** for $p<0.01$ is highly significant, *** for $p<0.001$ is extremely significant).

8.6.1 Positive controls

Table 35: Control and positive controls of ROS assay

	A549 cells								
	ROS [%] of control								
	control			500 µM H_2O_2			1 mM H_2O_2		
	N=1	N=2	N=3	N=1	N=2	N=3	N=1	N=2	N=3
control	100.00	100.00	100.00	100.00	100.00	100.00	100.00	100.00	100.00

1 min	108.00	109.00	102.67	165.00	167.08	227.02	180.92	169.18	287.83
15 min	107.00	107.00	109.01	328.00	319.48	353.12	400.68	337.69	418.92
30 min	110.00	111.00	117.71	399.00	396.56	370.00	527.61	463.87	451.35
1 h	110.00	113.00	130.55	428.00	411.83	376.73	602.71	520.37	466.76
2 h	123.00	128.00	144.24	446.00	433.45	386.61	647.93	592.45	474.57
3 h	127.00	132.00	172.54	446.00	432.06	406.03	644.74	591.24	486.78
4 h	137.00	142.00	193.22	444.00	443.19	421.12	639.86	600.56	499.53
5 h	152.00	155.00	210.37	454.00	454.04	431.66	651.41	605.11	510.36
6 h	158.00	160.00	232.44	455.00	461.26	442.70	647.96	607.19	518.68

8.6.2 ZnO NP (4-5 nm)

Table 36: Time-dependent generation of ROS after treatment with ZnO NP (4-5 nm)

	A549 cells				
	ROS [%] of control				
	100 µg/mL ZnO NP (4-5 nm)				
	N=1	N=2	N=3	mean	SD
control	100.00	100.00	100.00	100.00	0.00
1 min	102.24	124.78	175.93	134.32	37.76
15 min	105.92	128.38	161.78	132.03	28.11
30 min	106.28	129.73	162.48	132.83	28.23
1 h	103.42	127.16	152.87	127.82	24.73
2 h	97.77	121.70	136.78	118.75	19.67
3 h	98.39	123.11	132.77	118.09	17.73
4 h	99.23	105.16	132.02	112.14	17.47
5 h	65.38	104.94	141.55	103.96	38.10
6 h	104.90	65.21	140.50	103.54	37.66
	ROS [%] of control				
	100 µg/mL ZnO NP (4-5 nm) + 5 mM NAC				
	N=1	N=2	N=3	mean	SD
control	100.00	100.00	100.00	100.00	0.00
1 min	107.00	108.00	109.00	108.00	1.00
15 min	119.00	108.00	113.00	113.33	5.51

30 min	119.00	109.00	113.00	113.67	5.03
1 h	121.00	109.00	114.00	114.67	6.03
2 h	127.00	108.00	115.00	116.67	9.61
3 h	125.00	110.00	115.00	116.67	7.64
4 h	126.00	110.00	115.00	117.00	8.19
5 h	127.00	108.00	115.00	116.67	9.61
6 h	127.00	109.00	115.00	117.00	9.17
	ROS [%] of control				
	100 µg/mL ZnO NP (4-5 nm) + 0.06 mM DTPA				
	N=1	N=2	N=3	mean	SD
control	100.00	100.00	100.00	100.00	0.00
1 min	94.87	108.21	175.72	126.27	43.35
15 min	96.61	110.58	152.09	119.76	28.86
30 min	91.01	108.03	151.91	116.98	31.42
1 h	90.23	106.88	148.18	115.10	29.83
2 h	81.03	95.92	142.69	106.55	32.18
3 h	69.82	83.40	143.95	99.06	39.47
4 h	77.86	89.69	143.96	103.84	35.25
5 h	103.55	90.90	154.39	116.28	33.60
6 h	108.48	92.75	157.29	119.51	33.66
	ROS [%] of control				
	100 µg/mL ZnO NP (4-5 nm) + BSA				
	N=1	N=2	N=3	mean	SD
control	100.00	100.00	100.00	100.00	0.00
1 min	119.54	112.23	142.14	124.64	15.59
15 min	120.96	115.24	128.37	121.52	6.58
30 min	119.87	117.90	126.96	121.58	4.76
1 h	115.60	115.77	118.71	116.69	1.75
2 h	108.05	110.48	98.69	105.74	6.22
3 h	108.06	112.04	94.95	105.02	8.94
4 h	108.39	101.79	93.38	101.19	7.52
5 h	95.97	101.94	102.84	100.25	3.74

6 h	101.58	95.43	101.86	99.62	3.63

Table 37: Statistical analysis of intracellular ROS-levels after ZnO NP (4-5 nm) treatment

	A549 cells			
	100 µg/mL ZnO NP (4-5 nm)			
Two-way ANOVA				
Source of Variation	% of total variation	P value		
Interaction	26.35	0.0002		
Column Factor	38.23	< 0,0001		
Row Factor	6.35	0.0155		
Source of Variation	P value summary	Significant?		
Interaction	***	Yes		
Column Factor	***	Yes		
Row Factor	*	Yes		
Source of Variation	Df	Sum-of-squares	Mean square	F
Interaction	36	37773	1049	2.516
Column Factor	4	54806	13702	32.86
Row Factor	9	9098	1011	2.425
Residual	100	41697	417	
Number of missing values	0			
Bonferroni posttests				
ZnO NP (4-5 nm) vs ZnO NP (4-5 nm) + NAC				
Row Factor	ZnO NP (4-5 nm)	ZnO NP (4-5 nm) + NAC	Difference	95% CI of diff,
control	100	100	0	-55,38 to 55,38
1 min	134.3	108	-26.32	-81,70 to 29,07
15 min	132	113.3	-18.69	-74,07 to 36,69
30 min	132.8	113.7	-19.16	-74,55 to 36,22
1 h	127.8	114.7	-13.15	-68,53 to 42,23
2 h	118.8	116.7	-2.085	-57,47 to 53,30

3 h	118.1	116.7	-1.422	-56,80 to 53,96
4 h	112.1	117	4.864	-50,52 to 60,25
5 h	104	116.7	12.71	-42,67 to 68,09
6 h	103.5	117	13.46	-41,92 to 68,85
Row Factor	Difference	t	P value	Summary
control	0	0	P > 0,05	ns
1 min	-26.32	1.578	P > 0,05	ns
15 min	-18.69	1.121	P > 0,05	ns
30 min	-19.16	1.149	P > 0,05	ns
1 h	-13.15	0.7888	P > 0,05	ns
2 h	-2.085	0.1251	P > 0,05	ns
3 h	-1.422	0.08526	P > 0,05	ns
4 h	4.864	0.2917	P > 0,05	ns
5 h	12.71	0.7623	P > 0,05	ns
6 h	13.46	0.8076	P > 0,05	ns
ZnO NP (4-5 nm) vs ZnO NP (4-5 nm) + BSA				
Row Factor	ZnO NP (4-5 nm)	ZnO NP (4-5 nm) + BSA	Difference	95% CI of diff,
control	100	100	0	-55,38 to 55,38
1 min	134.3	124.6	-9.68	-65,06 to 45,70
15 min	132	121.5	-10.5	-65,88 to 44,88
30 min	132.8	121.6	-11.26	-66,64 to 44,13
1 h	127.8	116.7	-11.12	-66,51 to 44,26
2 h	118.8	105.7	-13.01	-68,39 to 42,37
3 h	118.1	105	-13.07	-68,45 to 42,31
4 h	112.1	101.2	-10.95	-66,33 to 44,43
5 h	104	100.3	-3.704	-59,09 to 51,68
6 h	103.5	99.62	-3.913	-59,30 to 51,47
Row Factor	Difference	t	P value	Summary
control	0	0	P > 0,05	ns
1 min	-9.68	0.5806	P > 0,05	ns
15 min	-10.5	0.6299	P > 0,05	ns
30 min	-11.26	0.6751	P > 0,05	ns

1 h	-11.12	0.6672	P > 0,05	ns
2 h	-13.01	0.7803	P > 0,05	ns
3 h	-13.07	0.784	P > 0,05	ns
4 h	-10.95	0.6566	P > 0,05	ns
5 h	-3.704	0.2222	P > 0,05	ns
6 h	-3.913	0.2347	P > 0,05	ns
ZnO NP (4-5 nm) vs ZnO NP (4-5 nm) + DTPA				
Row Factor	ZnO NP (4-5 nm)	ZnO NP (4-5 nm) + DTPA	Difference	95% CI of diff,
control	100	100	0	-55,38 to 55,38
1 min	134.3	126.3	-8.048	-63,43 to 47,33
15 min	132	119.8	-12.27	-67,65 to 43,11
30 min	132.8	117	-15.85	-71,23 to 39,53
1 h	127.8	115.1	-12.72	-68,10 to 42,66
2 h	118.8	106.5	-12.21	-67,59 to 43,18
3 h	118.1	99.06	-19.03	-74,41 to 36,35
4 h	112.1	103.8	-8.299	-63,68 to 47,08
5 h	104	116.3	12.32	-43,06 to 67,70
6 h	103.5	119.5	15.97	-39,41 to 71,35
Row Factor	Difference	t	P value	Summary
control	0	0	P > 0,05	ns
1 min	-8.048	0.4827	P > 0,05	ns
15 min	-12.27	0.7359	P > 0,05	ns
30 min	-15.85	0.9505	P > 0,05	ns
1 h	-12.72	0.7629	P > 0,05	ns
2 h	-12.21	0.732	P > 0,05	ns
3 h	-19.03	1.141	P > 0,05	ns
4 h	-8.299	0.4978	P > 0,05	ns
5 h	12.32	0.7389	P > 0,05	ns
6 h	15.97	0.9579	P > 0,05	ns
ZnO NP (4-5 nm) vs $ZnCl_2$				
Row Factor	ZnO NP (4-5 nm)	$ZnCl_2$	Difference	95% CI of diff,
control	100	100	0	-55,38 to 55,38

1 min	134.3	125.1	-9.189	-64,57 to 46,19
15 min	132	126.4	-5.612	-60,99 to 49,77
30 min	132.8	134.9	2.104	-53,28 to 57,49
1 h	127.8	157.6	29.83	-25,56 to 85,21
2 h	118.8	184.3	65.59	10,21 to 121,0
3 h	118.1	186.2	68.07	12,69 to 123,5
4 h	112.1	192.3	80.16	24,78 to 135,5
5 h	104	199.6	95.69	40,31 to 151,1
6 h	103.5	200.2	96.7	41,32 to 152,1
Row Factor	Difference	t	P value	Summary
control	0	0	P > 0,05	ns
1 min	-9.189	0.5512	P > 0,05	ns
15 min	-5.612	0.3366	P > 0,05	ns
30 min	2.104	0.1262	P > 0,05	ns
1 h	29.83	1.789	P > 0,05	ns
2 h	65.59	3.934	P<0,01	**
3 h	68.07	4.083	P<0,001	***
4 h	80.16	4.808	P<0,001	***
5 h	95.69	5.739	P<0,001	***
6 h	96.7	5.8	P<0,001	***

8.6.3 ZnO NP (15-18 nm)

Table 38: Time-dependent generation of ROS after treatment with ZnO NP (15-18 nm)

	A549 cells				
	ROS [%] of control				
	100 µg/mL ZnO NP (15-18 nm)				
	N=1	N=2	N=3	mean	SD
control	100.00	100.00	100.00	100.00	0.00
1 min	124.00	114.58	111.62	116.73	6.47
15 min	131.00	124.18	116.67	123.95	7.17
30 min	136.00	125.55	121.36	127.64	7.54
1 h	144.00	137.04	122.58	134.54	10.93

2 h	144.00	156.61	125.34	141.98	15.74
3 h	149.00	160.45	131.19	146.88	14.75
4 h	154.00	165.97	130.29	150.09	18.16
5 h	158.00	177.77	137.50	157.76	20.14
6 h	160.00	153.89	151.78	155.22	4.27
	ROS [%] of control				
	100 µg/mL ZnO NP (15-18 nm) + 5 mM NAC				
	N=1	N=2	N=3	mean	SD
control	100.00	100.00	100.00	100.00	0.00
1 min	111.00	111.05	109.39	110.48	0.94
15 min	109.00	119.77	111.82	113.53	5.58
30 min	107.00	118.32	114.45	113.26	5.75
1 h	112.00	125.02	114.22	117.08	6.97
2 h	112.00	125.07	114.71	117.26	6.90
3 h	112.00	124.95	117.27	118.07	6.51
4 h	114.00	126.76	115.27	118.68	7.03
5 h	114.00	119.34	114.81	116.05	2.88
6 h	112.00	119.35	117.55	116.30	3.83
	ROS [%] of control				
	100 µg/mL ZnO NP (15-18 nm) + BSA				
	N=1	N=2	N=3	mean	SD
control	100.00	100.00	100.00	100.00	0.00
1 min	91.26	122.83	164.07	126.06	36.51
15 min	94.06	127.09	172.45	131.20	39.36
30 min	95.44	130.62	177.73	134.60	41.28
1 h	94.28	129.37	167.20	130.28	36.47
2 h	91.33	124.57	139.53	118.47	24.67
3 h	92.04	124.51	134.11	116.89	22.05
4 h	92.38	116.82	131.19	113.46	19.62
5 h	92.01	116.61	122.72	110.45	16.26
6 h	116.49	91.68	121.45	109.87	15.95

	ROS [%] of control				
	100 µg/mL ZnO NP (15-18 nm) + 0.06 mM DTPA				
	N=1	N=2	N=3	mean	SD
control	100.00	100.00	100.00	100.00	0.00
1 min	93.39	97.70	125.92	105.67	17.67
15 min	97.85	102.49	136.02	112.12	20.82
30 min	96.88	104.15	144.27	115.10	25.52
1 h	96.01	101.25	147.04	114.77	28.07
2 h	93.61	98.03	137.85	109.83	24.36
3 h	78.64	83.88	137.13	99.88	32.36
4 h	82.69	86.60	137.35	102.21	30.49
5 h	83.97	87.14	134.30	101.80	28.18
6 h	85.50	88.86	133.91	102.75	27.03

Table 39: Statistical analysis of ROS after treatment with ZnO NP (15-18 nm)

	A549 cells			
	100 µg/mL ZnO NP (15-18 nm)			
Table Analyzed				
Two-way ANOVA				
Source of Variation	% of total variation	P value		
Interaction	22.86	< 0,0001		
Column Factor	41.91	< 0,0001		
Row Factor	15.46	< 0,0001		
Source of Variation	P value summary	Significant?		
Interaction	***	Yes		
Column Factor	***	Yes		
Row Factor	***	Yes		
Source of Variation	Df	Sum-of-squares	Mean square	F
Interaction	36	48336	1343	3.212
Column Factor	4	88637	22159	53.01

Row Factor	9	32694	3633	8.69
Residual	100	41804	418	
Number of missing values	0			
Bonferroni posttests				
	100 µg/mLZnO NP (15-18nm) vs ZnO NP (15-18nm) + NAC			
Row Factor	ZnO NP (15-18nm)	ZnO NP (15-18nm) + NAC	Difference	95% CI of diff,
Row Factor	Difference	t	P value	Summary
control	0	0	P > 0,05	ns
1 min	-9.968	0.5971	P > 0,05	ns
15 min	-13.61	0.8155	P > 0,05	ns
30 min	-25.11	1.504	P > 0,05	ns
1 h	-54.12	3.242	P < 0,05	*
2 h	-72.88	4.366	P<0,001	***
3 h	-71.37	4.275	P<0,001	***
4 h	-75.83	4.542	P<0,001	***
5 h	-85.12	5.099	P<0,001	***
6 h	-86.41	5.176	P<0,001	***
	100 µg/mL ZnO NP (15-18nm) vs ZnO NP (15-18nm) + BSA			
Row Factor	ZnO NP (15-18nm)	ZnO NP (15-18nm) + BSA	Difference	95% CI of diff,
Row Factor	Difference	t	P value	Summary
control	0	0	P > 0,05	ns
1 min	5.61	0.3361	P > 0,05	ns
15 min	4.059	0.2431	P > 0,05	ns
30 min	-3.769	0.2258	P > 0,05	ns
1 h	-40.92	2.451	P > 0,05	ns
2 h	-71.67	4.293	P<0,001	***
3 h	-72.55	4.346	P<0,001	***
4 h	-81.05	4.855	P<0,001	***
5 h	-90.73	5.435	P<0,001	***
6 h	-92.84	5.561	P<0,001	***

	100 µg/mL ZnO NP (15-18nm) vs ZnO NP (15-18nm) + DTPA			
Row Factor	ZnO NP (15-18nm)	ZnO NP (15-18nm) + DTPA	Difference	95% CI of diff,
Row Factor	Difference	t	P value	Summary
control	0	0	P > 0,05	ns
1 min	-14.78	0.8851	P > 0,05	ns
15 min	-15.02	0.8999	P > 0,05	ns
30 min	-23.27	1.394	P > 0,05	ns
1 h	-56.44	3.381	P < 0,05	*
2 h	-80.31	4.811	P<0,001	***
3 h	-89.56	5.365	P<0,001	***
4 h	-92.3	5.529	P<0,001	***
5 h	-99.37	5.952	P<0,001	***
6 h	-99.96	5.988	P<0,001	***

	ZnO NP (15-18nm) vs $ZnCl_2$			
Row Factor	ZnO NP (15-18nm)	$ZnCl_2$	Difference	95% CI of diff,
Row Factor	Difference	t	P value	Summary
control	0	0	P > 0,05	ns
1 min	4.681	0.2804	P > 0,05	ns
15 min	-0.729	0.04367	P > 0,05	ns
30 min	-3.431	0.2055	P > 0,05	ns
1 h	-13.56	0.8122	P > 0,05	ns
2 h	-5.801	0.3475	P > 0,05	ns
3 h	-3.278	0.1964	P > 0,05	ns
4 h	-2.211	0.1325	P > 0,05	ns
5 h	-1.523	0.09125	P > 0,05	ns
6 h	-2.478	0.1484	P > 0,05	ns

8.6.4 $ZnCl_2$

Table 40: Time-dependent generation of ROS after treatment with $ZnCl_2$

	A549 cells
	ROS [%] of control

	100 µg/mL $ZnCl_2$				
	N=1	N=2	N=3	mean	SD
control	100.00	100.00	100.00	100.00	0.00
1 min	126.46	129.36	119.56	125.13	5.03
15 min	128.39	131.42	119.43	126.41	6.23
30 min	136.71	140.48	127.61	134.93	6.62
1 h	151.49	159.99	161.46	157.64	5.38
2 h	175.11	186.65	191.28	184.34	8.33
3 h	170.05	190.80	197.64	186.16	14.37
4 h	169.47	199.36	208.06	192.30	20.24
5 h	176.38	206.59	215.98	199.65	20.69
6 h	177.41	207.38	215.92	200.24	20.23

8.7 Mitochondrial membrane potential (ΔΨm)

Spectrofluorimetric measurements of mitochondrial membrane potential after treatment with ZnO NP (4-5 nm), ZnO NP (15-18 nm), and $ZnCl_2$ are based on at least 3 independent experiments. For the statistical analysis a one-way analysis of variance (ANOVA) with Bonferroni´s multiple comparison test was carried out to compare the group of ZnO NP (15-18 nm) to the groups of ZnO NP (4-5 nm) and $ZnCl_2$ (* for $p<0.05$ is significant, ** for $p<0.01$ is highly significant, *** for $p<0.001$ is extremely significant).

Table 41: Measurement of ΔΨm after treatment with ZnO NP (4-5 nm), ZnO NP (15-18 nm) and $ZnCl_2$

	A549 cells									
	ΔΨm [%] of control									
	100 µg/mL ZnO NP (4-5 nm)									
	control	5 min	15 min	30 min	1 h	2 h	3 h	4 h	5 h	6 h
N=1	100.00	96.36	85.38	98.38	77.47	82.44	78.51	72.81	68.84	66.64
N=2	100.00	173.46	143.69	176.69	116.42	127.10	125.47	118.63	110.00	111.78
N=3	100.00	70.99	63.98	64.73	59.17	70.47	71.29	69.17	68.90	73.81
N=4	100.00	83.46	87.04	87.57	86.29	107.50	109.54	103.64	109.66	104.17
N=5	100.00	76.93	80.81	81.17	80.84	98.56	100.45	92.29	98.05	94.03
N=6	100.00	102.33	106.48	107.74	108.27	136.07	139.39	132.35	141.22	132.31

mean	100.00	100.59	94.56	102.71	88.08	103.69	104.11	98.15	99.45	97.12
SD	0.00	37.58	27.64	39.12	21.05	25.27	26.37	25.04	27.69	24.43
	ΔΨm [%] of control									
	100 µg/mL ZnO NP (15-18 nm)									
	control	5 min	15 min	30 min	1 h	2 h	3 h	4 h	5 h	6 h
N=1	100.00	89.43	87.24	84.55	78.23	63.60	49.75	42.62	38.12	33.72
N=2	100.00	58.85	56.35	55.28	53.04	44.87	35.82	31.07	28.84	25.34
N=3	100.00	63.96	61.77	61.66	58.01	48.07	39.38	34.77	31.15	28.92
mean	100.00	70.75	68.45	67.16	63.10	52.18	41.65	36.16	32.70	29.33
SD	0.00	16.38	16.50	15.39	13.34	10.02	7.24	5.90	4.83	4.21
	ΔΨm [%] of control									
	$ZnCl_2$									
	control	5 min	15 min	30 min	1 h	2 h	3 h	4 h	5 h	6 h
N=1	100.00	93.29	83.54	98.06	78.40	85.17	79.03	73.86	70.05	69.39
N=2	100.00	108.18	91.94	118.30	83.37	95.60	96.19	95.08	96.46	101.54
N=3	100.00	111.01	97.52	101.61	93.54	126.98	126.23	117.97	115.85	117.44
N=4	100.00	82.88	86.41	86.42	87.47	112.58	117.08	109.23	119.61	113.04
N=5	100.00	78.72	80.98	81.62	82.05	101.43	104.54	92.99	103.28	98.21
N=6	100.00	101.03	104.74	105.79	107.15	136.68	142.01	132.85	143.06	135.65
mean	100.00	95.85	90.85	98.64	88.66	109.74	110.85	103.66	108.05	105.88
SD	0.00	13.25	9.05	13.31	10.43	19.51	22.42	20.80	24.58	22.27

Table 42: Statistical analysis of ΔΨm after treatment with ZnO NP and $ZnCl_2$

		A549 cells		
Table Analyzed				
Two-way ANOVA				
Source of Variation	% of total variation	P value		
Interaction	12,01	0,0414		
Column Factor	39,15	< 0,0001		
Row Factor	4,70	0,2134		
Source of Variation	P value summary	Significant?		
Interaction	*	Yes		
Column Factor	***	Yes		
Row Factor	ns	No		
Source of Variation	Df	Sum-of-squares	Mean square	F
Interaction	18	14227	790,4	1,739
Column Factor	2	46390	23195	51,04
Row Factor	9	5567	618,5	1,361
Residual	120	54538	454,5	
Number of missing values	30			
Bonferroni posttests				
ZnO NP (15-18 nm) vs ZnO NP (4-5 nm)				
Row Factor	ZnO NP (15-18 nm)	ZnO NP (4-5 nm)	Difference	95% CI of diff,
Row Factor	Difference	t	P value	Summary
control	0,0	0,0	P > 0,05	ns
1 min	29,84	1,980	P > 0,05	ns
15 min	26,11	1,732	P > 0,05	ns
30 min	35,55	2,358	P > 0,05	ns
1 h	24,98	1,657	P > 0,05	ns
2 h	51,51	3,417	P<0,01	**
3 h	62,46	4,143	P<0,001	***
4 h	61,99	4,112	P<0,001	***
5 h	66,74	4,427	P<0,001	***
6 h	67,80	4,497	P<0,001	***
	ZnO NP (15-18 nm) vs $ZnCl_2$			

Row Factor	ZnO NP (15-18 nm)	$ZnCl_2$	Difference	95% CI of diff,
Row Factor	Difference	t	P value	Summary
control	0,0	0,0	P > 0,05	ns
1 min	25,10	1,665	P > 0,05	ns
15 min	22,40	1,486	P > 0,05	ns
30 min	31,47	2,088	P > 0,05	ns
1 h	25,57	1,696	P > 0,05	ns
2 h	57,56	3,818	P<0,01	**
3 h	69,20	4,590	P<0,001	***
4 h	67,51	4,478	P<0,001	***
5 h	75,35	4,998	P<0,001	***
6 h	76,55	5,078	P<0,001	***
	ZnO NP (4-5 nm) vs $ZnCl_2$			
Row Factor	ZnO NP (4-5 nm)	$ZnCl_2$	Difference	95% CI of diff,
Row Factor	Difference	t	P value	Summary
control	0,0	0,0	P > 0,05	ns
1 min	-4,741	0,3852	P > 0,05	ns
15 min	-3,713	0,3016	P > 0,05	ns
30 min	-4,078	0,3314	P > 0,05	ns
1 h	0,5869	0,04768	P > 0,05	ns
2 h	6,048	0,4914	P > 0,05	ns
3 h	6,741	0,5477	P > 0,05	ns
4 h	5,517	0,4483	P > 0,05	ns
5 h	8,607	0,6993	P > 0,05	ns
6 h	8,756	0,7114	P > 0,05	ns

8.8 γH2A.X immunofluorescence Assay

Immunofluorescences staining with γH2A.X, detecting DNA DSB, after ZnO NP, ZnO bulk, $ZnCl_2$, ZnO NP + BSA, ZnO NP + NAC, ZnO NP + DTPA are based on at least 3 independent experiments. For the statistical analysis the one-way analysis of variance (ANOVA) with Bonferroni´s multiple comparison test or student´s t-test (paired) was carried out to compare the groups with the untreated control of each treatment (* for

p<0.05 is significant, ** for p<0.01 is highly significant, *** for p<0.001 is extremely significant).

8.8.1 Concentration-dependent ZnO NP (4-5 nm) induced DNA DSB

Table 43: ZnO NP (4-5 nm) induced DNA DSB in A549, HNSCCUM-02T, and NIH/3T3 cells

	A549 cells				HNSCCUM-02T cells				NIH/3T3 cells			
	ZnO NP (4-5 nm)				ZnO NP (4-5 nm)				ZnO NP (4-5 nm)			
	1 min				1 min				1 min			
		µg/mL				µg/mL				µg/mL		
	control	0.1	10	100	control	0.1	10	100	control	0.1	10	100
N=1	100.00	551.52	927.27	278.79	100.00	566.18	629.43	352.45	100.00	27.40	51.21	33.77
N=2	100.00	168.13	50.55	98.35	100.00	63.45	45.46	94.64	100.00	186.87	123.23	257.07
N=3	100.00	82.91	170.03	94.26	100.00	40.95	15.92	171.57	100.00	178.26	265.22	460.87
mean	100.00	267.52	382.62	157.13	100.00	223.53	230.27	206.22	100.00	130.84	146.55	250.57
SD	0.00	249.61	475.45	105.38	0.00	296.96	346.00	132.35	0.00	89.68	108.89	213.62
	ZnO NP (4-5 nm)				ZnO NP (4-5 nm)				ZnO NP (4-5 nm)			
	15 min				15 min				15 min			
		µg/mL				µg/mL				µg/mL		
	control	0.1	10	100	control	0.1	10	100	control	0.1	10	100
N=1	100.00	296.30	192.59	629.63	100.00	21.57	37.25	9.80	100.00	86.80	254.95	150.80
N=2	100.00	54.60	56.90	198.28	100.00	71.51	126.88	41.94	100.00	143.44	140.86	62.33
N=3	100.00	184.42	115.58	185.71	100.00	67.07	78.66	45.12	100.00	100.00	171.43	242.86
mean	100.00	178.44	121.69	337.87	100.00	53.38	80.93	32.29	100.00	110.08	189.08	152.00
SD	0.00	120.96	68.05	252.75	0.00	27.64	44.86	19.54	0.00	29.63	59.06	90.27
	ZnO NP (4-5 nm)				ZnO NP (4-5 nm)				ZnO NP (4-5 nm)			
	1 h				1 h				1 h			
		µg/mL				µg/mL				µg/mL		
	control	0.1	10	100	control	0.1	10	100	control	0.1	10	100
N=1	100.00	75.00	111.49	161.49	100.00	58.33	10.98	98.48	100.00	19.37	64.18	223.57
N=2	100.00	87.83	153.91	103.48	100.00	34.54	60.31	50.26	100.00	349.21	1014.29	609.52
N=3	100.00	157.89	19.06	103.83	100.00	55.48	29.68	43.23	100.00	458.33	1100.00	416.67

mean	100.00	106.91	94.82	122.93	100.00	49.45	33.66	63.99	100.00	275.64	726.15	416.59
SD	0.00	44.62	68.95	33.39	0.00	13.00	24.90	30.08	0.00	228.54	574.89	192.98
	ZnO NP (4-5 nm)				ZnO NP (4-5 nm)				ZnO NP (4-5 nm)			
	4 h				4 h				4 h			
		µg/mL				µg/mL				µg/mL		
	control	0.1	10	100	control	0.1	10	100	control	0.1	10	100
N=1	100.00	116.00	52.29	16.00	100.00	40.00	1720.00	3600.00	100.00	44.00	10.00	978.00
N=2	100.00	30.87	39.37	91.13	100.00	300.00	4000.00	2100.00	100.00	105.75	177.53	338.08
N=3	100.00	99.06	51.76	32.71	100.00	25.00	225.00	275.00	100.00	51.85	11.11	9381.48
mean	100.00	81.98	47.81	46.61	100.00	121.67	1981.67	1991.67	100.00	67.20	66.22	3565.85
SD	0.00	45.06	7.31	39.45	0.00	154.62	1901.05	1665.15	0.00	33.62	96.41	5046.63
	ZnO NP (4-5 nm)				ZnO NP (4-5 nm)				ZnO NP (4-5 nm)			
	24 h				24 h				24 h			
		µg/mL				µg/mL				µg/mL		
	control	0.1	10	100	control	0.1	10	100	control	0.1	10	100
N=1	100.00	380.00	865.00	dead	100.00	36.11	91.67	dead	100.00	256.41	492.31	dead
N=2	100.00	108.41	175.91	dead	100.00	100.00	733.33	dead	100.00	149.97	179.40	dead
N=3	100.00	229.50	210.81	dead	100.00	10.17	64.41	dead	100.00	180.00	360.00	dead
mean	100.00	239.30	417.24		100.00	48.76	296.47		100.00	195.46	343.90	
SD	0.00	136.06	388.16		0.00	46.23	378.58		0.00	54.88	157.07	

Table 44: Statistical analysis of DNA DSB in A549 and HNSCCUM-02T cells

	A549 cells	**HNSCCUM-02T cells**		
Table Analyzed	ZnO (4-5nm) 4 h	ZnO NP (4-5nm) 15 min	ZnO NP (4-5nm) 1 h	ZnO NP (4-5nm) 1 h
Column	control	control	control	control
vs	vs	vs	vs	vs
Column	10 µg/mL	100 µg/mL	0,1 µg/mL	10 µg/mL
Paired t test				
P value	0.0064	0.0266	0.0213	0.0439
P value summary	**	*	*	*

Are means signif. different? (P < 0.05)	Yes	Yes	Yes	Yes
One- or two-tailed P value?	Two-tailed	Two-tailed	Two-tailed	Two-tailed
t, df	t=12,40 df=2	t=6,003 df=2	t=6,740 df=2	t=4,614 df=2
Number of pairs	3	3	3	3
How big is the difference?				
Mean of differences	52.14	67.71	50.55	66.34
95% confidence interval	34,04 to 70,24	19,17 to 116,3	18,28 to 82,82	4,473 to 128,2
R square	0.9872	0.9474	0.9578	0.9141

8.8.2 Concentration-dependent induced DNA DSB after ZnO NP (15-18 nm)

Table 45: ZnO NP (15-18 nm) induced DNA DSB in A549, HNSCCUM-02T, and NIH/3T3 cells

	A549 cells				HNSCCUM-02T cells				NIH/3T3 cells			
	ZnO NP (15-18 nm)				ZnO NP (15-18 nm)				ZnO NP (15-18 nm)			
	1 min				1 min				1 min			
		µg/mL				µg/mL				µg/mL		
	control	0.1	10	100	control	0.1	10	100	control	0.1	10	100
N=1	100.00	16.67	4.17	70.83	100.00	100.00	150.00	5850.00	100.00	123.56	123.01	218.08
N=2	100.00	33.33	11.11	55.56	100.00	1300.00	100.00	2800.00	100.00	279.08	245.85	299.71
N=3	100.00	135.00	30.00	125.00	100.00	134.29	62.35	121.10	100.00	79.73	90.79	42.38
mean	100.00	61.67	15.09	83.80	100.00	511.43	104.12	2923.70	100.00	160.79	153.22	186.73
SD	0.00	64.05	13.37	36.49	0.00	683.14	43.97	2866.45	0.00	104.76	81.82	131.50
	ZnO NP (15-18 nm)				ZnO NP (15-18 nm)				ZnO NP (15-18 nm)			
	15 min				15 min				15 min			
		µg/mL				µg/mL				µg/mL		
	control	0.1	10	100	control	0.1	10	100	control	0.1	10	100
N=1	100.00	27.59	3.45	727.59	100.00	1350.00	1100.00	100.00	100.00	537.72	711.84	748.68
N=2	100.00	40.00	40.00	120.00	100.00	46.15	69.23	15.38	100.00	98.28	147.84	205.60
N=3	100.00	20.00	40.00	500.00	100.00	282.91	165.81	256.41	100.00	124.63	203.98	90.05
mean	100.00	29.20	27.82	449.20	100.00	559.69	445.01	123.93	100.00	253.54	354.56	348.11
SD	0.00	10.10	21.10	306.96	0.00	694.59	569.29	122.28	0.00	246.46	310.69	351.68
	ZnO NP (15-18 nm)				ZnO NP (15-18 nm)				ZnO NP (15-18 nm)			

	1 h				1 h				1 h			
		µg/mL				µg/mL				µg/mL		
	control	0.1	10	100	control	0.1	10	100	control	0.1	10	100
N=1	100.00	98.94	190.43	146.81	100.00	20.00	20.00	220.00	100.00	112.80	119.98	82.12
N=2	100.00	110.28	114.02	106.54	100.00	33.33	100.00	666.67	100.00	157.00	194.36	178.40
N=3	100.00	135.00	125.00	170.00	100.00	288.00	231.00	227.00	100.00	81.23	90.36	84.36
mean	100.00	114.74	143.15	141.12	100.00	113.78	117.00	371.22	100.00	117.01	134.90	114.96
SD	0.00	18.44	41.31	32.11	0.00	151.03	106.52	255.89	0.00	38.06	53.58	54.96
	ZnO NP (15-18 nm)				ZnO NP (15-18 nm)				ZnO NP (15-18 nm)			
	4 h				4 h				4 h			
		µg/mL				µg/mL				µg/mL		
	control	0.1	10	100	control	0.1	10	100	control	0.1	10	100
N=1	100.00	33.33	100.00	266.67	100.00	33.33	100.00	266.67	100.00	158.18	70.19	119.08
N=2	100.00	70.28	81.78	130.37	100.00	184.09	214.20	341.48	100.00	100.16	30.93	53.11
N=3	100.00	49.86	60.05	63.97	100.00	53.33	107.32	114.31	100.00	136.81	94.94	83.35
mean	100.00	51.16	80.61	153.67	100.00	90.25	140.51	240.82	100.00	131.72	65.35	85.18
SD	0.00	18.51	20.00	103.34	0.00	81.88	63.93	115.77	0.00	29.34	32.28	33.02
	ZnO NP (15-18 nm)				ZnO NP (15-18 nm)				ZnO NP (15-18 nm)			
	24 h				24 h				24 h			
		µg/mL				µg/mL				µg/mL		
	control	0.1	10	100	control	0.1	10	100	control	0.1	10	100
N=1	100.00	25.71	20.00	dead	100.00	700.00	625.00	dead	100.00	128.33	107.43	dead
N=2	100.00	52.00	16.00	dead	100.00	2300.00	1800.00	dead	100.00	284.77	257.00	dead
N=3	100.00	58.33	233.33	dead	100.00	72.12	92.31	dead	100.00	82.87	85.40	dead
mean	100.00	45.35	89.78		100.00	1024.04	839.10		100.00	165.33	149.94	
SD	0.00	17.30	124.34		0.00	1148.75	873.75		0.00	105.91	93.36	

Table 46: Statistical analysis of DNA DSB in A549 cells

	A549 cells	
Table Analyzed	ZnO (15-18nm) 15 min	ZnO (15-18nm) 24 h
Column	control	control
vs	vs	vs
Column	10 µg/ml	10 µg/ml
Paired t test		
P value	0.037	0.0438
P value summary	*	*
Are means signif. different? (P < 0.05)	Yes	Yes
One- or two-tailed P value?	Two-tailed	Two-tailed
t, df	t=5,056 df=2	t=4,621 df=2
Number of pairs	3	3
How big is the difference?		
Mean of differences	69.81	-149.7
95% confidence interval	10,39 to 129,2	-289,1 to -10,29
R square	0.9274	0.9143

8.8.3 Concentration-dependent $ZnCl_2$ induced DNA DSB

Table 47: DNA DSB in A549 cells induced by $ZnCl_2$

	A549 cells			
	$ZnCl_2$			
	1 min			
	control	0.1 µg/mL	10 µg/mL	100 µg/mL
N=1	100	33.33	66.67	66.67
N=2	100	287.5	1275	387.5
N=3	100	462.5	625	781.25
mean	100.00	261.11	655.56	411.81
SD	0.00	215.80	604.74	357.91
	$ZnCl_2$			
	15 min			
	control	0.1 µg/mL	10 µg/mL	100 µg/mL

N=1	100	200	100	42.86
N=2	100	20	61.67	55
N=3	100	229.3	202.55	71.97
mean	100.00	149.77	121.41	56.61
SD	0.00	113.33	72.84	14.62
	$ZnCl_2$			
	1 h			
	control	0.1 µg/mL	10 µg/mL	100 µg/mL
N=1	100	14.29	42.86	28.57
N=2	100	4.76	9.52	47.62
N=3	100	203.3	2.2	28.57
mean	100.00	74.12	18.19	34.92
SD	0.00	111.98	21.67	11.00
	$ZnCl_2$			
	4 h			
	control	0.1 µg/mL	10 µg/mL	100 µg/mL
N=1	100	100	100	300
N=2	100	2.63	14.47	48.68
N=3	100			
mean	100.00	51.32	57.24	174.34
SD	0.00	68.85	60.48	177.71
	$ZnCl_2$			
	24 h			
	control	0.1 µg/mL	10 µg/mL	100 µg/mL
N=1	100	700		dead
N=2	100	8.25	41.75	dead
N=3	100	80.95	8.1	dead
mean	100.00	263.07	24.93	
SD	0.00	380.14	23.79	

Table 48: Statistical analysis of DNA DSB in A549 cells induced by $ZnCl_2$

	A549 cells
Table Analyzed	$ZnCl_2$ 15 min
Column	control
vs	vs
Column	100 µg/ml
Paired t test	
P value	0.0358
P value summary	*
Are means signif. different? (P < 0.05)	Yes
One- or two-tailed P value?	Two-tailed
t, df	t=5,140 df=2
Number of pairs	3
How big is the difference?	
Mean of differences	43.39
95% confidence interval	7,065 to 79,72
R square	0.9296

8.8.4 Time-dependent measurement of ZnO NP (4-5 nm)

Table 49: Time-dependent induced DNA DSB after treatment with ZnO NP (4-5 nm)

	A549 cells					
	ZnO NP (4-5 nm)					
	100 µg/mL					
	control	1 min	15 min	30 min	1 h	4 h
N=1	100.00	282.31	623.82	90.55	161.39	15.91
N=2	100.00	98.13	197.98	86.76	102.93	91.10
N=3	100.00	94.30	186.83	21.58	103.84	32.66
mean	100.00	158.25	336.21	66.30	122.72	46.56
SD	0.00	107.46	249.14	38.77	33.49	39.47
	ZnO NP (4-5 nm) + NAC					

	100 µg/mL					
	control	1 min	15 min	30 min	1 h	4 h
N=1	100.00	23.10	47.93	51.60	20.60	19.76
N=2	100.00	151.81	40.19	233.38	160.43	81.61
N=3	100.00	67.90	87.24	163.81	22.69	22.15
mean	100.00	80.94	58.45	149.60	67.91	41.18
SD	0.00	65.34	25.23	91.72	80.13	35.04
	ZnO NP (4-5 nm) + DTPA					
	100 µg/mL					
	control	1 min	15 min	30 min	1 h	4 h
N=1	100.00	148.77	308.70	332.37	132.69	127.30
N=2	100.00	43.10	11.41	66.26	45.55	23.17
N=3	100.00	45.88	58.95	110.69	15.33	14.97
mean	100.00	38.10	60.43	37.22	13.33	37.73
SD	0.00	16.76	38.94	20.36	7.43	31.80

8.8.5 Time-dependent measurement of DNA DSB after ZnO NP (4-5 nm)

Table 50: Time-dependent induced DNA DSB after treatment with ZnO NP (15-18 nm)

	A549 cells					
	ZnO NP (15-18 nm)					
	100 µg/mL					
	control	1 min	15 min	30 min	1 h	4 h
N=1	100.00	70.53	730.75	72.42	145.75	266.67
N=2	100.00	52.29	116.36	92.22	106.42	130.37
N=3	100.00	121.17	517.61	25.23	168.77	63.97
mean	100.00	81.33	454.91	63.29	140.31	153.67
SD	0.00	35.69	311.96	34.42	31.53	103.34
	ZnO NP (15-18 nm) + NAC					
	100 µg/mL					
	control	1 min	15 min	30 min	1 h	4 h
N=1	100.00	0.67	132.64	75.49	23.18	19.88

N=2	100.00	232.85	261.46	80.71	146.44	158.41
N=3	100.00	30.34	89.56	20.54	131.87	9.77
mean	100.00	87.95	161.22	58.91	100.50	62.69
SD	0.00	126.36	89.44	33.34	67.35	83.05
	ZnO NP (15-18 nm) + DTPA					
	100 µg/mL					
	control	1 min	15 min	30 min	1 h	4 h
N=1	100.00	57.39	59.88	58.02	5.35	28.67
N=2	100.00	27.08	21.76	17.33	20.03	11.44
N=3	100.00	29.83	99.64	36.30	14.62	73.08
mean	100.00	38.10	60.43	37.22	13.33	37.73
SD	0.00	16.76	38.94	20.36	7.43	31.80

Table 51: Statistical analysis of DNA DSB after treatment with ZnO NP (15-18 nm) + DTPA

	A549 cells			
	ZnO NP (15-18 nm) + DTPA			
Table Analyzed				
One-way analysis of variance				
P value	0,0121			
P value summary	*			
Are means signif. different? (P < 0.05)	Yes			
Number of groups	6			
F	4,809			
R square	0,6671			
ANOVA Table	SS	df	MS	
Treatment (between columns)	13139	5	2628	

Residual (within columns)	6557	12	546,5		
Total	19696	17			
Bonferroni's Multiple Comparison Test	Mean Diff,	t	Significant? P < 0,05?	Summary	95% CI of diff
DTPA vs 1 min	61,90	3,243	No	ns	-7,744 to 131,5
DTPA vs 15 min	39,57	2,073	No	ns	-30,07 to 109,2
DTPA vs 30 min	62,78	3,289	No	ns	-6,865 to 132,4
DTPA vs 1 h	86,67	4,541	Yes	*	17,02 to 156,3
DTPA vs 4 h	62,27	3,262	No	ns	-7,377 to 131,9
1 min vs 15 min	-22,33	1,170	No	ns	-91,97 to 47,32
1 min vs 30 min	0,8787	0,04604	No	ns	-68,77 to 70,52
1 min vs 1 h	24,77	1,298	No	ns	-44,88 to 94,41
1 min vs 4 h	0,3668	0,01922	No	ns	-69,28 to 70,01
15 min vs 30 min	23,21	1,216	No	ns	-46,44 to 92,85
15 min vs 1 h	47,09	2,467	No	ns	-22,55 to 116,7
15 min vs 4 h	22,69	1,189	No	ns	-46,95 to 92,34
30 min vs 1 h	23,89	1,252	No	ns	-45,76 to 93,53
30 min vs 4 h	-0,5120	0,02682	No	ns	-70,16 to 69,13
1 h vs 4 h	-24,40	1,278	No	ns	-94,04 to 45,25

8.8.6 Time-dependent measurement of DNA DSB after treatment with BSA coated ZnO NP (4-5 nm)

Table 52: Time-dependent induced DNA DSB after treatment with BSA coated ZnO NP (4-5 nm)

	A549 cells					
	ZnO NP (4-5 nm) + BSA [%]					
	100 µg/mL					
	control	1 min	15 min	30 min	1 h	4 h
N=1	100.00	82.21	76.08	110.83	79.22	51.91
N=2	100.00	66.50	216.75	52.29	71.80	44.07
N=3	100.00	392.53	221.75	398.65	415.52	63.43
mean	100.00	54.99	76.12	133.93	60.47	49.28
SD	0.00	22.86	90.56	12.20	9.28	39.84

8.8.7 Time-dependent measurement of DNA DSB after BSA coated ZnO NP (15-18 nm)

Table 53: Time-dependent induced DNA DSB after treatment with BSA coated ZnO NP (15-18 nm)

	A549 cells					
	ZnO NP (15-18 nm) + BSA [%]					
	100 µg/mL					
	control	1 min	15 min	30 min	1 h	4 h
N=1	100.00	75.82	179.11	144.22	54.58	25.60
N=2	100.00	30.54	8.93	137.13	55.67	95.27
N=3	100.00	58.60	40.32	120.45	71.17	26.96
mean	100.00	54.99	76.12	133.93	60.47	49.28
SD	0.00	22.86	90.56	12.20	9.28	39.84

8.8.8 Time-dependent measurement of DNA DSB after $ZnCl_2$ treatment

Table 54: Time-dependent induced DNA DSB after treatment with $ZnCl_2$

	A549 cells					
	$ZnCl_2$ [%]					
	100 µg/mL					
	control	1 min	15 min	30 min	1 h	4 h
N=1	100.00	66.67	42.86	28.57	28.57	300.00
N=2	100.00	387.50	55.00	100.00	47.62	48.68
N=3	100.00	781.25	71.97	54.88	28.57	1320.00
mean	100.00	411.81	56.61	61.15	34.92	556.23
SD	0.00	357.91	14.62	36.13	11.00	673.28

8.8.9 Time-dependent measurement of DNA DSB after ZnO bulk material

Table 55: Time-dependent induced DNA DSB after treatment with ZnO bulk material

	A549 cells					
	ZnO bulk [%]					
	100 µg/mL					
	control	1 min	15 min	30 min	1 h	4 h
N=1	100	18.08	51.75	171.12	74.57	14.83
N=2	100	64.14	22.31	571.69	262.14	281.66
N=3	100	154.88	139.02	258.54	180.49	157.32
mean	100	79.03	71.03	333.78	172.40	151.27
SD	0	69.61	60.70	210.62	94.05	133.52

8.9 Measurement of pATM level using ELISA

8.9.1 ZnO NP (15-18 nm)

Table 56: Measurement of phosphorylated ATM after ZnO NP (15-18 nm) treatment

	A549 cells					
	100 µg/mL ZnO NP (15-18 nm)					
	pATM [%] of control					
	control	1 min	15 min	30 min	1 h	4 h

N=1	100.00	179.00	50.00	132.00	179.00	45.00
N=2	100.00	61.11	86.58	115.33	145.23	169.71
N=3	100.00	144.07	117.00	369.49	358.47	375.42
mean	100.00	128.06	84.53	205.61	227.57	196.71
SD	0.00	60.55	33.55	142.17	114.62	166.86

8.9.2 $ZnCl_2$

Table 57: Measurement of phosphorylated ATM after $ZnCl_2$ treatment

	A549 cells					
	100 µg/mL $ZnCl_2$					
	pATM [%] of control					
	control	1 min	15 min	30 min	1 h	4 h
N=1	100.00	119.00	101.00	78.00	150.00	63.00
N=2	100.00	26.80	157.73	37.11	71.13	256.70
N=3	100.00	131.77	365.73	508.56	86.11	326.85
mean	100.00	92.52	208.15	207.89	102.41	215.52
SD	0.00	57.28	139.38	261.19	41.89	136.66

8.10 Western blotting

8.10.1 Analysis of ATR

Table 58: Measurement of phosphorylated ATR after treatment with ZnO NP (15-18 nm)

	A549 cells					
	100 µg/mL ZnO NP (15-18 nm)					
	pATR referred to ATR and in [%] of control					
	control	1 min	15 min	30 min	1 h	4 h
N=1	100.00	94.81	118.13	102.19	95.09	118.80
N=2	100.00	85.96	90.13	91.14	116.73	107.55
N=3	100.00	65.32	55.54	16.00	10.7	11.00
mean	100.00	90.39	104.13	69.78	74.17	79.72
SD	0.00	6.26	19.80	46.90	56.02	59.26

8.10.2 Analysis of Chk1

Table 59: Measurement of phosphorylated Chk1 after treatment with ZnO NP (15-18 nm)

	A549 cells					
	100 µg/mL ZnO NP (15-18 nm)					
	pChk1 referred to ß-actin and in [%] of control					
	control	1 min	15 min	30 min	1 h	4 h
N=1	100.00	111.34	165.99	92.88	91.11	81.87
N=2	100.00	84.38	83.26	25.73	20.33	6.41
N=3	100.00	54.76	56.75	36.15	10.22	97.39
mean	100.00	83.49	102.00	51.59	40.55	61.89
SD	0.00	28.30	56.98	36.14	44.07	48.67

8.10.3 Analysis of Chk2, p53 and p21 after ZnO NP (15-18 nm) exposure

Table 60: Measurement of ATM downstream signaling after treatment with ZnO NP (15-18 nm)

	A549 cells					
	100 µg/mL ZnO NP (15-18 nm)					
	pChk2 referred to ß-actin and in [%] of control					
	control	1 min	15 min	30 min	1 h	4 h
N=1	100.00	71.87	118.68	127.42	115.25	106.74
N=2	100.00	113.92	109.04	117.98	116.31	119.83
N=3	100.00	105.97	151.09	175.31	210.12	294.63
mean	100.00	97.25	126.27	140.24	147.23	173.73
SD	0.00	22.34	22.03	30.74	54.47	104.90
	100 µg/mL ZnO NP (15-18 nm)					
	p53 referred to ß-actin and in [%] of control					
	control	1 min	15 min	30 min	1 h	4 h
N=1	100.00	98.02	114.01	103.75	110.18	206.82
N=2	100.00	164.13	146.66	139.00	127.75	105.41
N=3	100.00	89.91	80.98	84.00	89.05	136.81
mean	100.00	117.35	113.88	108.92	108.99	149.68
SD	0.00	40.71	32.84	27.86	19.38	51.92
	100 µg/mL ZnO NP (15-18 nm)					

	p21 referred to ß-actin and in [%] of control					
	control	1 min	15 min	30 min	1 h	4 h
N=1	100.00	137.59	111.52	180.87	170.44	182.24
N=2	100.00	85.79	91.18	42.62	134.83	69.65
N=3	100.00	293.55	317.69	14.86	80.77	137.17
mean	100.00	172.31	173.46	79.45	128.68	129.69
SD	0.00	108.14	125.32	88.92	45.15	56.67

8.10.4 Analysis of Chk2, p53 and p21 after $ZnCl_2$ exposure

Table 61: Measurement of ATM downstream signaling after treatment with $ZnCl_2$

	A549 cells					
	100 µg/mL $ZnCl_2$					
	pChk2 referred to ß-actin and in [%] of control					
	control	1 min	15 min	30 min	1 h	4 h
N=1	100.00	95.86	97.14	89.41	86.04	112.30
N=2	100.00	77.74	77.97	69.17	70.44	77.78
N=3	100.00	120.79	164.16	87.28	131.00	260.90
mean	100.00	98.13	113.09	81.95	95.83	150.33
SD	0.00	21.61	45.25	11.12	31.44	97.30
	100 µg/mL $ZnCl_2$					
	p53 referred to ß-actin and in [%] of control					
	control	1 min	15 min	30 min	1 h	4 h
N=1	100.00	91.72	105.00	92.90	80.89	138.03
N=2	100.00	75.67	81.66	74.13	80.23	124.84
N=3	100.00	54.91	63.57	80.15	58.01	84.32
mean	100.00	74.10	83.41	82.39	73.04	115.73
SD	0.00	18.46	20.77	9.58	13.02	27.99
	100 µg/mL $ZnCl_2$					
	p21 referred to ß-actin and in [%] of control					
	control	1 min	15 min	30 min	1 h	4 h
N=1	100.00	140.06	106.53	118.79	136.66	160.79
N=2	100.00	102.51	98.80	48.14	81.82	64.62

N=3	100.00	134.41	67.73	57.77	58.66	257.35
mean	100.00	125.66	91.02	74.90	92.38	160.92
SD	0.00	20.25	20.54	38.31	40.06	96.37

8.10.5 Analysis of Chk2, p53 and p21 after ZnO NP (15-18 nm) + NAC

Table 62: Measurement of ATM downstream signaling after treatment with ZnO NP (15-18 nm) + NAC

	A549 cells					
	100 µg/mL ZnO NP (15-18 nm) + 5 mM NAC					
	pChk2 referred to ß-actin and in [%] of control					
	control	1 min	15 min	30 min	1 h	4 h
N=1	100.00	161.43	142.66	181.62	164.78	238.67
N=2	100.00	84.95	67.57	97.24	99.85	93.80
N=3	100.00	153.91	106.01	109.95	96.97	86.51
mean	100.00	133.43	105.41	129.60	120.53	139.66
SD	0.00	42.15	37.55	45.49	38.35	85.82
	100 µg/mL ZnO NP (15-18 nm) + 5 mM NAC					
	p53 referred to ß-actin and in [%] of control					
	control	1 min	15 min	30 min	1 h	4 h
N=1	100.00	128.79	251.04	187.75	165.24	250.36
N=2	100.00	83.13	46.97	83.48	99.98	235.99
N=3	100.00	104.45	73.68	104.05	173.24	116.03
mean	100.00	105.46	123.90	125.09	146.15	200.79
SD	0.00	22.85	110.92	55.23	40.19	73.76
	100 µg/mL ZnO NP (15-18 nm) + 5 mM NAC					
	p21 referred to ß-actin and in [%] of control					
	control	1 min	15 min	30 min	1 h	4 h
N=1	100.00	134.47	70.29	121.28	153.22	200.07
N=2	100.00	151.29	117.14	124.71	158.40	202.21
N=3	100.00	126.15	121.61	106.76	95.78	57.37
mean	100.00	137.30	103.01	117.58	135.80	153.22
SD	0.00	12.81	28.43	9.53	34.75	83.01

8.10.6 Analysis of Chk2, p53 and p21 after ZnO NP (15-18 nm) + DTPA

Table 63: Measurement of ATM downstream signaling after treatment with ZnO NP (15-18 nm) + DTPA

	A549 cells					
	100 µg/mL ZnO NP (15-18 nm) + 0.06 mM DTPA					
	pChk2 referred to ß-actin and in [%] of control					
	control	1 min	15 min	30 min	1 h	4 h
N=1	100.00	84.99	28.55	53.55	17.42	17.91
N=2	100.00	89.46	58.58	81.38	21.37	87.33
N=3	100.00	114.06	53.99	34.80	30.13	44.76
mean	100.00	96.17	47.04	56.58	22.97	50.00
SD	0.00	15.65	16.18	23.44	6.50	35.01
	100 µg/mL ZnO NP (15-18 nm) + 0.06 mM DTPA					
	p53 referred to ß-actin and in [%] of control					
	control	1 min	15 min	30 min	1 h	4 h
N=1	100.00	46.74	29.28	166.14	101.81	158.54
N=2	100.00	95.11	100.53	103.91	94.68	101.43
N=3	100.00	82.62	103.56	112.15	93.62	101.79
mean	100.00	74.82	77.79	127.40	96.70	120.59
SD	0.00	25.11	42.04	33.80	4.45	32.87
	100 µg/mL ZnO NP (15-18 nm) + 0.06 mM DTPA					
	p21 referred to ß-actin and in [%] of control					
	control	1 min	15 min	30 min	1 h	4 h
N=1	100.00	51.79	85.53	45.21	65.94	77.76
N=2	100.00	134.14	110.65	125.84	175.32	129.33
N=3	100.00	20.37	28.42	33.56	82.61	36.43
mean	100.00	68.77	74.87	68.20	107.96	81.17
SD	0.00	58.75	42.14	50.25	58.93	46.54

Table 64: Statistical Analysis of pChk2 after treatment with ZnO NP (15-18 nm) + DTPA

	A549 cells	
	100 µg/mL ZnO NP (15-18 nm) + DTPA	
Table Analyzed	pChk2	pChk2
Column	control	control
vs	vs	vs
Column	15 min	1 h
Paired t test		
P value	0.0297	0.0024
P value summary	*	**
Are means signif. different? (P < 0.05)	Yes	Yes
One- or two-tailed P value?	Two-tailed	Two-tailed
t, df	t=5,672 df=2	t=20,51 df=2
Number of pairs	3	3
How big is the difference?		
Mean of differences	52.96	77.03
95% confidence interval	12,78 to 93,14	60,87 to 93,19
R square	0.9415	0.9953

8.10.7 Analysis of Erk and Akt

8.10.7.1 pErk after ZnO NP (15-18 nm)

Table 65: Measurement of pErk after treatment with ZnO NP (15-18 nm)

	A549 cells			
	pErk referred to ß-actin and in [%] of control			
	control	EGF	100 µg/mL ZnO NP (15-18 nm)	EGF + 100 µg/mL ZnO NP (15-18 nm)
N=1	100.00	382.86	718.71	899.47
N=2	100.00	532.32	643.44	675.64
N=3	100.00	299.79	538.12	783.11
mean	100.00	404.99	633.42	786.07
SD	0.00	117.83	90.71	111.94

Table 66: Statistical analysis of Erk after treatment with ZnO NP (15-18 nm)

A549 cells					
	100 µg/mL ZnO NP (15-18 nm)				
Table Analyzed	pErk				
One-way analysis of variance					
P value	< 0,0001				
P value summary	***				
Are means signif. different? (P < 0.05)	Yes				
Number of groups	4				
F	30.85				
R square	0.9204				
ANOVA Table	SS	df	MS		
Treatment (between columns)	801723	3	267241		
Residual (within columns)	69290	8	8661		
Total	871013	11			
Bonferroni's Multiple Comparison Test	Mean Diff,	t	Significant? P < 0,05?	Summary	95% CI of diff
control vs EGF	-305	4.014	Yes	*	-569,3 to -40,64
control vs ZnO NP (15-18 nm)	-533.4	7.02	Yes	***	-797,8 to -269,1
control vs EGF + ZnO NP (15-18 nm)	-686.1	9.029	Yes	***	-950,4 to -421,7
EGF vs ZnO NP (15-18 nm)	-228.4	3.006	No	ns	-492,8 to 35,92
EGF vs EGF + ZnO NP (15-18 nm)	-381.1	5.015	Yes	**	-645,4 to -116,7
ZnO NP (15-18 nm) vs EGF + ZnO NP (15-18 nm)	-152.7	2.009	No	ns	-417,0 to 111,7

8.10.7.2 pAkt after ZnO NP (15-18 nm)

Table 67: Measurement of pAkt after treatment with ZnO NP (15-18 nm)

	A549 cells			
	pAkt referred to ß-actin and in [%] of control			
	control	EGF	100 µg/mL ZnO NP (15-18 nm)	EGF + 100 µg/mL ZnO NP (15-18 nm)
N=1	100.00	202.06	1003.62	809.18
N=2	100.00	463.64	1239.35	1220.51
N=3	100.00	198.97	972.82	1129.04
mean	100.00	288.22	1071.93	1052.91
SD	0.00	151.92	145.81	215.97

Table 68: Statistical analysis of pAkt after treatment with ZnO NP (15-18 nm)

A549 cells					
	100 µg/mL ZnO NP (15-18 nm)				
Table Analyzed	pAkt				
One-way analysis of variance					
P value	< 0,0001				
P value summary	***				
Are means signif. different? (P < 0.05)	Yes				
Number of groups	4				
F	33.93				
R square	0.9271				
ANOVA Table	SS	df	MS		
Treatment (between columns)	2316000	3	771854		
Residual (within columns)	181970	8	22746		
Total	2498000	11			
Bonferroni's Multiple Comparison Test	Mean Diff,	t	Significant? P < 0,05?	Summary	95% CI of diff
control vs EGF	-188.2	1.528	No	ns	-616,6 to 240,2
control vs ZnO NP (15-18 nm)	-971.9	7.893	Yes	***	-1400 to -543,5
control vs EGF + ZnO NP (15-18 nm)	-952.9	7.738	Yes	***	-1381 to -

					524,5
EGF vs ZnO NP (15-18 nm)	-783.7	6.364	Yes	**	-1212 to -355,3
EGF vs EGF + ZnO NP (15-18 nm)	-764.7	6.21	Yes	**	-1193 to -336,3
ZnO NP (15-18 nm) vs EGF + ZnO NP (15-18 nm)	19.02	0.1545	No	ns	-409,4 to 447,4

8.10.7.3 pErk after $ZnCl_2$

Table 69: Measurement of pErk after treatment with $ZnCl_2$

	A549 cells			
	pERK referred to ß-actin and in [%] of control			
	control	EGF	100 µg/mL $ZnCl_2$	EGF + 100 µg/mL $ZnCl_2$
N=1	100.00	445.63	1491.89	1699.89
N=2	100.00	1750.10	1742.64	2001.51
N=3	100.00	554.11	778.87	853.84
mean	100.00	916.61	1337.80	1518.41
SD	0.00	723.86	500.02	594.97

8.10.7.4 pAkt after $ZnCl_2$

Table 70: Measurement of pAkt after treatment with $ZnCl_2$

	A549 cells			
	pAkt referred to ß-actin and in [%] of control			
	control	EGF	100 µg/mL $ZnCl_2$	EGF + 100 µg/mL $ZnCl_2$
N=1	100.00	668.15	4892.53	6204.97
N=2	100.00	4332.53	4482.90	5121.63
N=3	100.00	1084.32	1659.37	1874.24
mean	100.00	2028.33	3678.27	4400.28
SD	0.00	2006.31	1760.37	2253.68

8.11 FACS analysis of apoptosis and necrosis

Table 71: Measurement of apoptosis and necrosis after ZnO NP (15-18 nm) treatment

	A549 cells					
	100 µg/mL ZnO NP (15-18 nm)					
	live in [%] of control					
	N=1	N=2	N=3	N=4	mean	SD
control	100.00	100.00	100.00	100.00	100.00	0.00
1 min	101.88	0.00	103.63	114.66	80.04	53.66
15 min	93.92	108.83	100.85	108.46	103.01	7.09
30 min	103.21	94.48	107.63	114.78	105.02	8.49
1 h	96.79	95.11	103.51	113.47	102.22	8.33
2 h	99.12	108.68	105.93	90.82	101.14	7.96
3 h	99.78	108.36	99.64	86.05	98.46	9.22
4 h	91.15	96.69	105.69	91.06	96.15	6.88
5 h	95.02	105.05	86.92	0.00	71.75	48.40
6 h	103.65	85.02	97.46	73.42	89.89	13.44
	100 µg/mL ZnO NP (15-18 nm)					
	early apoptosis in [%] of control					
	N=1	N=2	N=3	N=4	mean	SD
control	100.00	100.00	100.00	100.00	100.00	0.00
1 min	103.65	0.00	98.68	111.89	78.55	52.65
15 min	118.73	148.47	101.59	209.43	144.55	47.39
30 min	0.00	214.54	77.25	0.00	72.95	101.18
1 h	113.38	179.34	65.08	63.93	105.43	54.39
2 h	139.90	146.68	55.03	108.20	112.45	41.80
3 h	0.00	298.47	60.05	198.36	139.22	134.79
4 h	282.24	727.04	90.74	69.67	292.42	305.12
5 h	148.66	244.64	328.04	0.00	180.34	140.80
6 h	0.00	887.76	58.99	183.20	282.49	410.67
	100 µg/mL ZnO NP (15-18 nm)					
	apoptosis in [%] of control					
	N=1	N=2	N=3	N=4	mean	SD

control	100.00	100.00	100.00	100.00	100.00	0.00
1 min	19.13	0.00	94.35	9.03	30.63	43.19
15 min	196.25	75.11	110.87	32.04	103.57	69.69
30 min	0.39	101.81	70.00	0.00	43.05	51.16
1 h	150.69	100.00	87.50	27.08	91.32	50.80
2 h	89.55	81.45	82.72	184.07	109.45	49.88
3 h	0.59	62.44	99.13	200.00	90.54	83.54
4 h	114.40	32.17	83.70	186.73	104.25	64.61
5 h	147.73	77.38	146.74	304.42	169.07	96.06
6 h	0.79	37.87	101.41	294.69	108.69	130.78
	100 µg/mL ZnO NP (15-18 nm)					
	necrosis in [%] of control					
	N=1	N=2	N=3	N=4	mean	SD
control	100.00	100.00	100.00	100.00	100.00	0.00
1 min	427.42	0.00	37.94	1.63	116.75	207.85
15 min	41.94	80.47	51.95	9.51	45.96	29.28
30 min	1072.58	86.60	33.66	139.54	333.10	494.88
1 h	30.65	99.06	78.21	8.75	54.16	41.67
2 h	0.00	69.15	55.45	12.93	34.38	33.14
3 h	1567.74	55.38	123.35	13.69	440.04	753.16
4 h	0.00	28.96	30.54	32.32	22.96	15.37
5 h	0.00	64.34	45.14	52.85	40.58	28.18
6 h	1016.13	28.02	154.09	0.00	299.56	482.39

8.12 Analysis of primary cells of mucosa

8.12.1 yH2A.X immunofluorescence analysis in primary cells of mucosa

Table 72: Analysis of DNA DSB in primary cells of mucosa after treatment with ZnO NP (15-18 nm)

	Primary cells of Mucosa						
	ZnO NP (15-18 nm)						
	Foci/cell in [%] of control						
	100 µg/mL						
	control	1 min	15 min	30 min	1 h	4 h	

PMT1	100.00	345.66	943.56	132.20	63.74	130.53	N=1
PMT2	100.00	563.05	153.27	19.66	187.55	86.68	N=1
PMT3	100.00	181.22	216.16	193.32	218.30	324.13	N=1
PMT4	100.00	601.56	569.82	277.41	380.95	176.07	N=1

8.12.2 Western blotting of lysates from primary cells of mucosa

Table 73: Measurment of ATM downstream signaling in primary cells of mucosa

	Primary cells of mucosa					
	100 µg/mL ZnO NP (15-18 nm)					
	pChk2 referred to ß-actin in [%] of control					
	control	ZnO NP (15-18 nm)	DTPA	DTPA + ZnO NP (15-18 nm)	NAC	NAC + ZnO NP (15-18 nm)
N=1	100.00	1430.05	100.00	104.64	100.00	98.08
N=2	100.00	161.59	100.00	189.54	100.00	51.63
N=3	100.00	1985.13	100.00	151.24	100.00	103.99
N=4	100.00	201.85	100.00	168.76	100.00	52.63
mean	100.00	944.66	100.00	153.54	100.00	76.58
SD	0.00	909.79	0.00	36.17	0.00	28.34
	100 µg/mL ZnO NP (15-18 nm)					
	p21 referred to ß-actin in [%] of control					
	control	ZnO NP (15-18 nm)	DTPA	DTPA + ZnO NP (15-18 nm)	NAC	NAC + ZnO NP (15-18 nm)
N=1	100.00	202.28	100.00	98.15	100.00	132.26
N=2	100.00	88.75	100.00	106.64	100.00	104.79
N=3	100.00	1.44	100.00	9.81	100.00	96.36
N=4	N/A	N/A	N/A	N/A	N/A	N/A
mean	100.00	97.49	100.00	71.54	100.00	111.14

SD	0.00	100.71	0.00	53.62	0.00	18.77
	100 µg/mL ZnO NP (15-18 nm)					
	p53 referred to ß-actin in [%] of control					
	control	ZnO NP (15-18 nm)	DTPA	DTPA + ZnO NP (15-18 nm)	NAC	NAC + ZnO NP (15-18 nm)
N=1	100.00	305.03	100.00	97.45	100.00	42.46
N=2	100.00	23.10	100.00	137.07	100.00	17.83
N=3	100.00	231.90	100.00	183.04	100.00	422.48
N=4	100.00	4.58	100.00	279.05	100.00	113.70
mean	100.00	141.15	100.00	174.15	100.00	149.12
SD	0.00	150.20	0.00	78.19	0.00	186.72

Publications

Wurde für die Online-Version entfernt.

Wurde für die Online-Version entfernt.

Conference contributions

Wurde für die Online-Version entfernt.

Wurde für die Online-Version entfernt.

Acknowledgement

Wurde für die Online-Version entfernt.

Wurde für die Online-Version entfernt.

Curriculum Vitae

Wurde für die Online-Version entfernt.

Wurde für die Online-Version entfernt.

Declaration of the Authorship

I hereby declare that I wrote the dissertation submitted without any unauthorized external assistance and used only sources acknowledged in the work. All textual passages which are appropriated verbatim or paraphrased from published and unpublished texts as well as all information obtained from oral sources are duly indicated and listed in accordance with bibliographical rules. In carrying out this research, I complied with the rules of standard scientific practice as formulated in the statutes of Johannes Gutenberg-University Mainz to insure standard scientific practice.

Mainz, den 6. November 2015

Dipl. Biologin Julia Heim

Declaration

Here I declare that the scientific thesis I am handling in has not yet been published at any other German University, or any university abroad, or any comparable institution, with the aim of attaining a scientific degree.

Here I also declare that I have not yet finished any other doctoral PhD or any similar graduation program in any of the subjects represented by the MPGC-JOGU without success.

Mainz, den 6. November 2015

Dipl. Biologin Julia Heim